5-2016

Fundamental physics with cold neutron beams

Kyle Brandon Grammer
University of Tennessee - Knoxville, kgrammer@vols.utk.edu

To the Graduate Council:

I am submitting herewith a dissertation written by Kyle Brandon Grammer entitled "Fundamental physics with cold neutron beams." I have examined the final electronic copy of this dissertation for form and content and recommend that it be accepted in partial fulfillment of the requirements for the degree of Doctor of Philosophy, with a major in Physics.

Geoffrey L Greene, Major Professor

We have read this dissertation and recommend its acceptance:

Kate Jones, Yuri Efremenko, Thomas Papenbrock, Erik Iverson

Accepted for the Council:

Carolyn R. Hodges

Vice Provost and Dean of the Graduate School

(Original signatures are on file with official student records.)

Fundamental physics with cold neutron beams

A Dissertation Presented for the

Doctor of Philosophy

Degree

The University of Tennessee, Knoxville

Kyle Brandon Grammer

May 2016

Acknowledgements

I would like to thank my advisor, Geoff Greene, for his support and guidance during my time as a graduate student. I had the pleasure of working on two experiments, NPDGamma and Beam Lifetime, at two first-class facilities, Oak Ridge National Laboratory and the National Institute of Standards and Technology.

I am greatful to David Bowman and Seppo Pentilla of the NPDGamma collaboration and Jeff Nico, Scott Dewey, and Shannon Hoogerheide of the Beam Lifetime collaboration for thoughtful advice they gave me on analysis and carrying out experiments. I would like to thank Nadia Fomin for converting me to Linux and whom I worked with very closely on both NPDGamma and the Beam Lifetime experiment. I would also like to thank Jonathan Mulholland for keeping Beam Lifetime meetings focused and short.

I would like to thank my parents for their support and encouragement. Finally, my wife, Georgia, whose unending love and support has helped us through this chapter in our lives together.

Abstract

The neutron exhibits rich physics both as a tool for studying materials, particle and nuclear physics, as well as the object of experimental study. The neutron lifetime is an important input to Big Bang Nucleosynthesis models and is currently known only to approximately 0.3% with the most precise measurements from two different experimental techniques in disagreement by more than 3σ [sigma]. Parity violation has been the subject of study since its discovery in 1957. Parity violation experiments provide access to studying the hadronic weak interaction, which is otherwise suppressed by several orders of magnitude below that of the strong interaction. It is the hadronic weak interaction that the NPDGamma experiment accesses via studying the asymmetry in gamma ray emission from the capture of polarized neutrons on liquid parahydrogen. Finally, as part of the NPDGamma experiment, the opportunity arose to use the well known and characterized apparatus for conducting a measurement of the liquid parahydrogen scattering cross section which has important implications in the design of neutron sources and moderators at cold neutron research facilities.

Table of Contents

Chapter 1

Introduction

Since the discovery of the neutron by Chadwick [Chadwick, 1932], the neutron has been a valuable tool as a probe for studying other systems as well as itself being an interesting system to study. The neutron interacts with via known forces, thus making it valuable in studying the Standard Model. The neutron is a spin-$\frac{1}{2}$ baryon composed of three quarks, udd, and its interactions provide information about the first quark family. The free neutron decays to a proton via emission of an electron and an electron antineutrino via the exchange of a W-boson, a process in which a down quark transforms to an up quark. The quark flavor change involved indicates that the β-decay of the neutron is a process mediated by the weak interaction. The neutron β-decay is the prototype of semi-leptonic weak decay, coupling hadrons to leptons, and the simplest nuclear β-decay system because it does not involve nuclear effects corrections that a composite nucleus does. The weak interaction was discovered to violate parity [Wu et al., 1957], thus making the neutron a tool for investigating parity violating processes, often in the form of β-decay product correlations in the polarized neutron decay rate [Jackson et al., 1957; Abele, 2009],

$$dW \propto F(E_e)\left[1 + a\frac{\vec{p}_e \cdot \vec{p}_\nu}{E_e E_\nu} + b\frac{m_e}{E_e} + A\frac{\vec{\sigma}_n \cdot \vec{p}_e}{E_e} + B\frac{\vec{\sigma}_n \cdot \vec{p}_\nu}{E_n u} + D\frac{\vec{\sigma}_n \cdot (\vec{p}_e \times \vec{p}_\nu)}{E_e E_\nu} + \cdots\right], \quad (1.1)$$

where $\vec{p}_e$ and $\vec{p}_\nu$ are the outgoing electron and neutrino momenta, $\vec{\sigma}_n$ is the neutron spin, E_e and E_ν are the electron and neutrino energies, and $F(E_e)$ is the beta energy spectrum, and other correlation terms have been emitted. This set of correlation coefficients is colloquially

known as the "neutron alphabet". The neutron β-decay lifetime is the least well known input to Big Bang Nucleosynthesis models which predict the primordial abundances of the light elements as the universe cooled during the first seconds and minutes after the Big Bang.

There are currently two primary methods for measuring the neutron β-decay lifetime with one method involving the storage of very low energy neutrons and the other involving measuring the decay rate using a beam of neutrons. These methods are complimentary to each other and developing each method is valuable because each method has completely different systematic effects to consider. At present, there is a discrepancy between the most precise storage experiments and the most precise beam experiments. A collaboration at the National Institute of Standards and Technology (NIST) has a long history in the development of the beam method and last carried out this measurement in the early 2000s [Dewey et al., 2003] and later updated due to improvements in the determination of the neutron counting efficiency [Yue et al., 2013]. The updated result agreed with the previously published one and also decreased the systematic uncertainty due to the neutron counting uncertainty. This merits performing the experiment again with the focus on improving the proton counting aspect of the experiment. The current work on this new measurement has been focused on commissioning the apparatus and testing it without neutrons.

While nucleons interact via the strong interaction, the strong interaction does not violate parity and therefore parity violation observed in a purely hadronic system probes the hadronic weak interaction. The NPDGamma experiment studies the $\vec{n} + p \rightarrow d + \gamma$ reaction, in which polarized neutrons capture on liquid parahydrogen. This interaction is predicted to have a parity-violating asymmetry, A_γ, in the γ-ray emission and this interaction isolates the $\Delta I = 1$ component of the hadronic weak interaction. The NPDGamma experiment was previously performed at the Institut LaueLangevin (ILL) [Cavaignac et al., 1977] and the Los Alamos Neutron Science Center (LANSCE) [Gericke et al., 2011], with the latter setting an upper limit on parity violating γ-ray asymmetry of 2×10^{-7}. Higher statistical precision was not achievable at LANSCE and the experiment was performed again at the Spallation Neutron Source (SNS), which provides a higher intensity neutron beam in order to achieve better statistical precision. The main components of the experimental apparatus are a polarizer, a spin rotator to flip the spin of the neutrons in an alternating pattern,

an aluminum vessel and cryostat for the liquid hydrogen target, 48 cesium iodide detectors arranged in 4 rings surrounding the target vessel, as well as upstream and downstream beam monitors.

Significant Monte Carlo calculations that required modifications of the MCNPX [Pelowitz, 2011] source code were performed in order to predict the relative sensitivity of each of the 48 cesium iodide γ detectors, which are known as the geometrical factors. The sensitivity to a γ-ray asymmetry within each ring is expected to be an approximately sinusoidal function of the detector angle, but a Monte Carlo model is required due to finite geometry effects. Along with the idealistic model in MCNPX, measurements were done with a cesium source in order to measure deviations of the center of response of each detector. This work produced the adjusted geometrical factors which are used in the final analysis of the raw asymmetry data for the NPDGamma experiment as well as for auxiliary measurements that were performed throughout the experimental run period.

The NPDGamma experiment also requires a measurement of the polarization of the neutron beam using ^{3}He. However, this measurement does not account for the average polarization of neutrons upon capture within the liquid parahydrogen. The NPDGamma experiment requires the liquid hydrogen to be very close to 100% parahydrogen, with the thermal equilibrium concentration of parahydrogen at 16 K being greater than 99.9%. The $J = 1$ orthohydrogen state can cause a spin flip of a scattered neutron and this effect must be accounted for with models. This was performed using an MCNPX simulation modified in a manner similar to the geometrical factors.

The slow conversion of normal hydrogen, which is 75% orthohydrogen and 25% parahydrogen, to thermal equilibrium parahydrogen concentration at 16 K takes on the order of months. This is catalyzed in the NPDGamma apparatus by using a circulation loop such that evaporated hydrogen is re-condensed and flows through an ortho-para converter filled with iron oxide. The parahydrogen concentration was determined using neutron transmission and the known absorption and orthohydrogen and parahydrogen scattering cross sections [Barrón-Palos et al., 2011], with that result being approximately 99.98% parahydrogen in the vessel. This process was repeated for the SNS iteration of the experiment and a non-physical result was found. A decision was made to change approaches from

using transmission to determine the parahydrogen concentration to instead determining the neutron cross section for parahydrogen. This approach led to the realization that the previously accepted measurement of the parahydrogen scattering cross section [Seiffert et al., 1970] suffered from some orthohydrogen contamination that was not accounted for and a new measurement of the parahydrogen scattering cross section was performed [Grammer et al., 2015].

1.0.1 Contributions

In my time working on the NPDGamma experiment, I participated construction of the apparatus and more general apparatus tests including calibration of the cesium iodide detectors, assembling the detector array, data acquisition system maintenance, and taking shifts on the hydrogen target. My major contributions to the NPDGamma experiment were participating in the initial development of analysis algorithms (section 6.9), the development of numerous Monte Carlo models for the experiment(chapter 7), and the analysis that led to and then the planning and analysis of the parahydrogen cross section measurement (chapter 8) which led to a publication [Grammer et al., 2015]. The Monte Carlo model that I developed began as a simple program for the detector array that rather quickly migrated to MCNPX and developed further into modifications to the MCNPX source code in order to implement the infrastructure to calculate the geometrical factors and beam depolarization as well as to implement an estimate of fast neutron production in the apparatus.

Just before the transmission measurements for the parahydrogen cross section took place near the end of 2012, I moved in order to begin working on the neutron lifetime experiment. Since that time, I've participated in numerous tests in preparation for installing the lifetime apparatus on a beamline. I participated in the investigation, analysis, and modeling of the neutron beam halo in section (section 5.2). I wrote most of the data acquisition code that couldn't be borrowed and updated from the previous measurement since some of the hardware is shared, as well as planning the data stream format and writing a ROOT library for reading the data on the collaboration analysis server (section 5.4).

1.1 Discovery of the Neutron

In 1904 shortly after the discovery of the electron, J. J. Thompson proposed the "plum-pudding" model for the atom. In this model, a neutral atom consisted of corpuscles (electrons) distributed throughout a large, diffuse "cloud" of positive charge. In 1909, Geiger and Marsden performed the gold-foil experiment [Geiger and Marsden, 1909], which disproved this model. The gold-foil experiment showed that alpha particles incident on a metal foil were reflected back to the source, which could not happen with Thompson's model. Rutherford [Rutherford, 1911] interpreted this result to mean that the atom must have a centrally concentrated charge and worked out the theory of Rutherford scattering. Rutherford determined that the number of alpha particles striking a screen per unit area per second, y, is given by

$$y = \frac{Qnt \csc^4(\phi/2)}{16r^2}\left(\frac{2Z_1 Z_\alpha e^2}{m v_\alpha^2}\right)^2, \tag{1.2}$$

where Q is the number of alpha particles per second in the initial beam, n is the number density of the foil, t is the thickness of the foil, Z_1 and Z_α are the atomic number of the incident particle and nucleus respectively, e is the elementary charge, v_0 is the velocity of the alpha particle, and ϕ is the scattering angle. More experiments by Geiger and Marsden [Geiger and Marsden, 1913] were performed in order to verify Rutherford's scattering formula. In his 1920 Bakerian Lecture [Rutherford, 1920], Rutherford noted that atoms seem to have a charge equal to approximately half of the atomic weight and that the nucleus should therefore also contain neutral components. Rutherford theorized that while the neutral hydrogen atom has a single proton and a distant electron, there may also be a closely bound "doublet" of a proton and an electron.

In 1930, Bothe and Becker bombarded beryllium, boron, and lithium with polonium alpha particles and observed that a penetrating, neutral radiation was emitted that they attributed to photons [Bothe and Becker, 1930]. They posited that either nuclei absorbed the alpha particles and emitted a photon in decaying to a ground state or that the nuclei inelastically scattered the alpha particles and were excited in the process and then decayed to a ground state. Bothe and Becker preferred the former [Amaldi, 1984], since they had

observed that the energy of the emitted radiation was greater than the energy of the incident alpha particle.

In 1932 [Joliot-Curie and Joliot-Curie, 1932], a paper by I. Curie and F. Joliot was presented in which Bothe and Becker's neutral radiation was incident on various other materials with the hypothesis being that high energy photons could transmute nuclei. In the case of paraffin, they observed that the neutral radiation caused the emission of protons with an energy of 4.5 MeV. Thinking that this process might be similar to Compton scattering, they estimated that the energy of the incident photons should be approximately 50 MeV. However, due to the Klein-Nishina formula this cross section goes like the inverse square of the recoiling process which meant that the calculated proton rate should have been much smaller than observed. The Klein-Nishina formula, derived in 1929 [Klein and Nishina, 1929], describes the differential cross section for scattering of photons from electrons,

$$\frac{d\sigma}{d\Omega} = \alpha^2\big(\frac{\alpha^2\hbar^2}{2m_e^2c^2}\big) f(E_\gamma,\theta)^2\big[f(E_\gamma,\theta) + \frac{1}{f(E_\gamma,\theta)} - 1 + \cos^2\theta\big], \tag{1.3}$$

where α is the fine structure constant, m_e is the electron mass, c is the speed of light, θ is the scattering angle, and $f(E_\gamma,\theta)$ is the ratio of the incoming and outgoing photon energy given by

$$f(E_\gamma,\theta) = \frac{1}{1+\frac{E_\gamma}{m_ec}(1-\cos\theta)}. \tag{1.4}$$

These initial measurements by Curie and Joliot prompted James Chadwick to make several more observations [Chadwick, 1932]. Chadwick notes that in the reaction

$$^9\mathrm{Be} + \alpha \rightarrow ^{13}\mathrm{C} + \text{quantum}, \tag{1.5}$$

the maximum energy available to the quantum is 14 MeV, much less than the 50 MeV required for the process to be Compton scattering. Chadwick further investigated the process by observing the recoil of atoms from the interaction with this neutral radiation. Chadwick states that if this neutral radiation is a massive particle with a mass close to that of the proton rather than a photon, all of the issues above vanish. Chadwick reports that an ejected proton has a maximum velocity of 3.3×10^9 cm/sec and a recoiling nitrogen atom

has a velocity of 4.7×10^8 cm/sec. Using these two measurements, energy conservation, and momentum conservation gives the following set of equations:

$$\frac{1}{2} m_{\mathrm{n}} v_{\mathrm{n,i}}^2 = \frac{1}{2} m_{\mathrm{N}} v_{\mathrm{N,f}}^2 + \frac{1}{2} m_{\mathrm{n}} v_{\mathrm{n,f2}}^2 \tag{1.6}$$

$$m_{\mathrm{n}} v_{\mathrm{n,i}} = m_{\mathrm{N}} v_{\mathrm{N}} + m_{\mathrm{n}} v_{\mathrm{n,f2}} \tag{1.7}$$

$$\frac{1}{2} m_{\mathrm{n}} v_{\mathrm{n,i}}^2 = \frac{1}{2} m_{\mathrm{p}} v_{\mathrm{p}}^2 + \frac{1}{2} m_{\mathrm{n}} v_{\mathrm{n,f1}}^2 \tag{1.8}$$

$$m_{\mathrm{n}} v_{\mathrm{n,i}} = m_{\mathrm{n}} v_{\mathrm{n,f1}} 1 + m_{\mathrm{p}} v_{\mathrm{p}} \tag{1.9}$$

where v_{p} is the proton velocity, v_{N} is the nitrogen velocity, m_{n} is the neutron mass, and v_{n} is the neutron velocity. Rearranging these four equations gives

$$\frac{m_{\mathrm{n}} + 14}{m_{\mathrm{n}} + 1} = \frac{v_{\mathrm{p}}}{v_{\mathrm{N}}} = \frac{3.3 \times 10^9}{4.7 \times 10^8}, \tag{1.10}$$

and solving for the neutron mass in units of the proton mass gives

$$M_{\mathrm{n}} = 1.15, \tag{1.11}$$

a rough estimate to which Chadwick attributes an uncertainty of 10%. Chadwick goes on to state that the mass of the neutron could be deduced from a reaction in which all constituent masses are known. Fortunately, the boron mass was known at the time and the reaction that Chadwick investigated was

$$^{11}\mathrm{B} + \alpha \rightarrow ^{14}\mathrm{N} + ^{1} n. \tag{1.12}$$

Given the known masses and the measured velocities of the recoiling particles, the measured mass of the neutron is 1.0067 in units of the proton mass, and "that it probably lies between 1.005 and 1.008". Since the sum of the electron and proton masses is 1.0078, this result supported the idea that the neutron is composed of a closely bound proton and electron. Heisenberg [Heisenberg, 1932] and Iwanenko [Iwanenko, 1932] suggested that the neutron is an elementary particle with half integer spin. However, Chadwick [Chadwick, 1932] remarks

> It is, of course, possible to suppose that the neutron may be an elementary particle. This view has little to recommend it at present, except the possibility of explaining the statistics of such nuclei as ^{14}N.

Using the 2.62 MeV gamma rays from ^{208}Tl, Chadwick and Goldhaber [Chadwick and Goldhaber, 1934] performed experiments on the photo-disassociation of the deuteron,

$$^{2}\mathrm{H} + h\nu \rightarrow ^{1}\mathrm{H} + ^{1}\mathrm{n}. \tag{1.13}$$

Coupled with precise mass spectrograph measurements of the hydrogen and deuteron masses by Bainbridge [Bainbridge, 1933], they were able to extract the neutron mass as 1.0080 $\pm$ 0.0005 mass units, with the mass of the hydrogen atom in these units being 1.0078. This was not conclusive proof yet that the neutron could not be a bound state of the proton and the electron.

Fermi proposed the idea that the free neutron must be unstable and that it can spontaneously decay into a proton, electron, and a neutrino [Fermi, 1934]. Further measurements [Chadwick and Goldhaber, 1935] showed that the neutron had a mass of 1.009, compared to the accepted hydrogen atom mass at the time of 1.0081. This conclusively showed that the neutron was heavier than the hydrogen atom and therefore that the neutron could not be a bound state of a proton and an electron.

1.2 Neutron Sources

1.2.1 Spallation Neutron Source

The Spallation Neutron Source (SNS) is a neutron science facility for materials/condensed matter research and fundamental neutron physics located at Oak Ridge National Laboratory [Mason et al., 2006] [Henderson, 2005]. SNS provides an intense 60 Hz pulsed source of neutrons to several experimental beamlines, including the Fundamental Neutron Physics Beamline.

First, H^- ions are created at the ion source and then accelerated along a 331 m linac consisting of room-temperature and superconducting sections to a final energy of 1 GeV. Ions

then pass through a thin carbon stripper foil with the remaining negative ions and neutral atoms being lost and the protons are captured in the proton accumulator ring, which has a radius of 248 m consisting of 4 curved and 4 straight sections. The accumulator ring frequency is approximately 1 MHz. Protons are then kicked out of the accumulator ring at a rate of 60 Hz and are incident on the liquid mercury spallation target. The maximum power is limited to 1.4 MW by facility design, however the power ranged from approximately 750 kW to 1.0 MW over the course of the NPDGamma experiment. In the spallation process [Fraser et al., 1965] [Carpenter, 1977], high energy protons bombard a liquid mercury target releasing on the order of 30 high energy neutrons per proton. These several-MeV-energy neutrons are then moderated by scattering with materials such as beryllium, water, or liquid hydrogen, producing cold neutrons with energies of meV and velocities on the order of 1 km/s that are then transported to experimental areas by neutron guides. The pulsed nature of the SNS along with the use of time of flight choppers allows for a simple conversion of neutron time of flight to neutron energy.

1.2.2 NIST Center for Neutron Research

The National Institute for Standards and Technology operates a 20 MW research reactor at the NIST Center for Neutron Reasearch (NCNR) at the Gaithersburg, MD site [Williams and Rowe, 2002]. The reactor went critical in 1967 and operated at 10 MW until a 1985 upgrade to 20 MW. The reactor is cooled and moderated with D_2O. There are several thermal neutron beam lines as well as cold neutron beam lines. The original liquid hydrogen cold source was installed in 1995 and was upgraded in 2001 after new developments in MCNP suggested more optimized parameters. Figure 1.1 depicts the NCNR floor layout, with the previous beam lifetime measurement having taken place on NG-6. The guide hall expansion project [Cook, 2009] was completed in recent years, and takes advantage of newer guide technology to provide higher neutron intensity at the beam exit. The next iteration of the beam lifetime measurement is planned for NG-C in the new guide hall expansion.

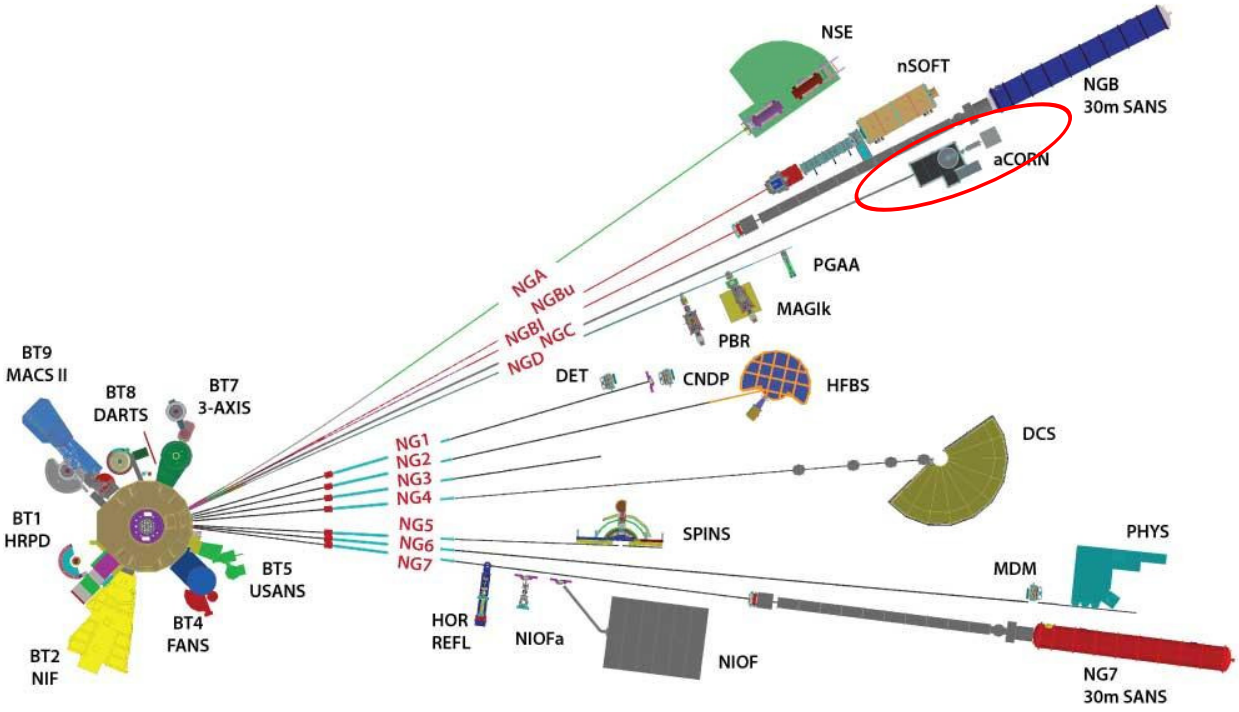

Figure 1.1: NIST Center for Neutron Research Layout

1.2.3 Neutron Guides

Neutrons are not charged and cannot easily be guided to the experimental area by magnetic or electric fields. Instead, cold neutrons can be reflected from polished surfaces, as found by Fermi [Fermi and Zinn, 1946], which serve to translate the neutron source from the moderator to the experimental area. Since cold neutrons have a wavelength on the order of a few Angstroms, their behavior is similar to X-rays in that they reflect at glancing angles of incidence. The neutron beam can be treated as a plane wave incident on a guide surface composed of many scattering potentials. The neutron wavefuction is given by

$$\Psi(\vec{r}) = e^{ikz} + \frac{f(\theta)}{r} e^{i\vec{k}\cdot\vec{r}}, \tag{1.14}$$

very far from the scattering center, where $\vec{k}$ is the wave number of the incident beam, $\vec{r}$ is position. The scattering amplitude, $f(\theta)$, is given by

$$f(\theta) = \frac{1}{2ik} \sum_l (2l+1) P_l(\cos\theta)(e^{2i\delta_l(k)} - 1), \tag{1.15}$$

where l is the angular momentum, δ_l is the phase shift, and P_l are the Legendre polynomials of order l. In the low energy limit, only s-wave scattering is considered and the wave function is given by

$$\Psi(\vec{r}) = e^{ikz} + \frac{b}{r}e^{i\vec{k}\cdot\vec{r}}, \tag{1.16}$$

where b is the scattering length of the nucleus.

For a bulk material, the effective nuclear protential is approximately

$$V_{\text{eff}}(\vec{r}) = \frac{2\pi\hbar^2}{m_n}b_j N, \tag{1.17}$$

where m_n is the neutron mass, b_j is the scattering length, and N is the atomic number density. For many materials, the neutron index of refraction is slightly less than unity which allows the total external reflection of neutrons from the pseudopotential, V_{eff}, of the surface, analogous to how light is totally internally reflected in a fiber optic cable. Total external reflection occurs when the angle of incidence on the surface is below the critical angle θ_{c}. Neutron guides are composed of such materials, one of which is natural nickel.

Consider the scattering of a wave k to k' by a crystal [Goldberger and Seitz, 1947], in the case that the difference between k^2 and k'^2 is small then

$$k'^2 - k^2 = \frac{4\pi N}{k}\Big(\pm \Big[\frac{k^2\sigma_{\text{s}}}{4\pi} - \Big(\frac{k^2\sigma_{\text{a}}}{4\pi}\Big)^2\Big] + i\frac{k^2\sigma_{\text{a}}}{4\pi}\Big), \tag{1.18}$$

where σ_{s} and σ_{a} are the scattering and absorption cross sections, respectively. The magnitude of the scattering amplitude is found by $b_{\text{coh}} = (\sigma_{\text{s}}/4\pi)^{\frac{1}{2}}$. If σ_{a} is zero, then equation 1.18 becomes

$$k'^2 - k^2 = \pm N(4\pi\sigma_{\text{s}})^2 = N(4\pi b_{\text{coh}})^2, \tag{1.19}$$

with the $\pm$ determined from the sign of the coherent scattering amplitude. Since the index of refraction, n, is defined by the relation

$$k' = kn, \tag{1.20}$$

the index of refraction is determined by,

$$1 - n^2 = \frac{N(4\pi\sigma_{\rm s})^{\frac{1}{2}}}{k^2} = \frac{V_{\rm eff}(\vec{r})}{E_{\rm n}} = \frac{2\pi\hbar^2 N b_{\rm coh}}{m_{\rm n} E_{\rm n}} = \frac{N b_{\rm coh}\lambda^2}{\pi}, \tag{1.21}$$

with λ being the neutron wavelength determined by

$$\lambda = \frac{2\pi\hbar}{(2m_{\rm n}E_{\rm n})^{\frac{1}{2}}}. \tag{1.22}$$

Then, total external reflection will occur when

$$\sin^2(\theta) \leq \sin^2(\theta_{\rm crit}) = 1 - n^2, \tag{1.23}$$

where θ is the angle of incidence for the neutron. The total external reflection occurs when the neutron kinetic energy perpendicular to the surface is less than the nuclear potential of the material, or $E_\perp < V_{\rm eff}$. The kinetic energy perpendicular to the surface is given by

$$E_\perp = \frac{1}{2} m_{\rm n} v_\perp^2 = \frac{2\pi^2\hbar^2}{m_{\rm n}\lambda_\perp^2} = \frac{2\pi^2\hbar^2 \sin^2\theta}{m_{\rm n}\lambda^2}. \tag{1.24}$$

The critical angle, $\theta_{\rm crit}$ is the angle for which $E_\perp = V_{\rm eff}$, and is equal to

$$\theta_{\rm crit} = \sin^{-1}\left(\sqrt{\frac{bN\lambda^2}{\pi}}\right). \tag{1.25}$$

For natural nickel, the critical angle is 1.73 mrad/($\mathring{A}$) and the critical angle for other materials is specified by the parameter m in multiples of the critical angle for natural nickel.

By taking advantage of Bragg scattering, the performance of a neutron mirror can be improved to large m factors. Neutrons that satisfy the Bragg condition,

$$n\lambda = 2d\sin\theta, \tag{1.26}$$

interfere constructively and reflect from a periodic crystal lattice. Where a single mirror neutron guide consists of a vacuum with walls composed of a single material coating, nickel for instance, a neutron mirror can also be constructed of multilayer surfaces such that an

artificial crystal lattice is formed. This multilayer surface will reflect neutrons up to the critical angle for the material, as well as reflecting neutrons that satisfy the Bragg condition.

If the thickness of the layers is varied, the Bragg condition is satisfied for a wide range of wavelengths and the surface is called a supermirror, which can have m values up to 7, allowing for higher neutron flux at the guide exit at the cost of increased divergence.

Chapter 2

Weak Interactions and the Standard Model

The standard model of particle physics describes the strong, electromagnetic, and weak interactions. The strong interaction acts on particles with color, quarks and gluons, and is responsible for the binding force of nuclei. The electromagnetic interaction describes the interaction of particles with charge and is mediated by photons. The weak interaction is mediated by the charged W bosons and neutral Z bosons and is responsible for changing particles of one type into another type. The weak interaction can be separated into purely leptonic interactions, semi-leptonic interactions, and hadronic interactions. Unlike the strong and electromagnetic interactions, the weak interaction violates parity symmetry. In comparison to decay via the strong interaction with lifetimes on the order of 10^{-23} seconds and via the electromagnetic interaction with lifetimes on the order of 10^{-16} seconds, decays via the weak interaction are unusually long on the order of 10^{-8} seconds or more.

2.1 Parity

The parity transformation is a coordinate transformation that changes the sign of all coordinates:

$$\begin{pmatrix} x \\ y \\ z \end{pmatrix} \rightarrow \begin{pmatrix} -x \\ -y \\ -z \end{pmatrix}. \tag{2.1}$$

Parity is commonly explained by an analogy of looking into a mirror, which does not flip the sign of all three axes but rather flips the sign of the axis normal to the mirror. It turns out that after flipping all three axes, a rotation by π about one of the axes still preserves the same properties of the coordinate system. Therefore, it is equivalent to flip only one axis:

$$\begin{pmatrix} x \\ y \\ z \end{pmatrix} \rightarrow \begin{pmatrix} -x \\ y \\ z \end{pmatrix}, \tag{2.2}$$

which is the same as the mirror analogy.

A tensor is a quantity that can be expressed by a magnitude and multiple directions in an N-dimensional space. Physical observables are described by their tensor rank and can be expressed by N^R numbers, where R is the rank. A tensor of rank zero is a scalar, for instance, the speed of a particle which has magnitude and no direction. A tensor of rank one is a vector, the velocity of the particle, which has a magnitude and a direction. Rank two is an NxN matrix, and so on. Furthermore, each of these is separated according to how they behave under coordinate transformations. A quantity that behaves like a scalar(vector) under a proper rotation but changes sign under parity is called a pseudoscalar(pseudovector). All axial vectors, like magnetic field, torque, and angular momentum, are pseudovectors. Similarly, the dot product of a vector, which is even under parity, and a pseUdovector, which is odd under parity, is also odd under parity and is a psuedoscalar.

2.2 History of the Weak Interaction

Beta decay is the process by which the quark flavor inside a nucleon changes, ie. an up quark becomes a down quark. This process happens via the charged-current weak interaction

$$n \rightarrow p^{+} + e^{-} + \overline{\nu}_{e} + 782\,\mathrm{keV}. \tag{2.3}$$

Historically, beta decay was first written as a point interaction involving the 4 fermions in

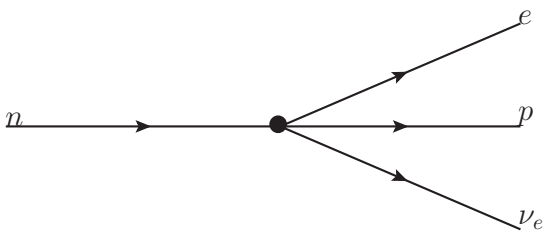

Figure 2.1: β decay of the free neutron under the point interaction Fermi model.

equation (2.3) with a coupling constant G_F (figure 2.1). Fermi [Fermi, 1934][Wilson, 1968] proposed that the matrix elements for beta decay are given by

$$\mathcal{M} = G_F \langle n|\mathcal{O}|p\rangle \langle \nu_e|\mathcal{O}|e\rangle. \tag{2.4}$$

The operator, $\mathcal{O}$, was taken to be purely vector in nature and written as γ_μ. This explained some features of beta decay but not others. The purely vector form of the interaction implied that beta decay would not violate parity. Later work [Gamow and Teller, 1936][Jackson et al., 1957] generalized the Fermi Hamiltonian to include scalar, pseudoscalar, tensor, axial vector, and vector terms, which have coupling constants C_S, C_P, C_T, C_A, and C_V, respectively, given

by

$$
\begin{aligned}
H_{\rm int} =&(\hat{\mathbf{\Psi}}_{\rm p}\Psi_{\rm n})(C_{\rm S}\hat{\mathbf{\Psi}}_{\rm e}\Psi_{\nu} + C'_{\rm S}\hat{\mathbf{\Psi}}_{\rm e}\gamma_5\Psi_{\nu}) \\
&+ (\hat{\mathbf{\Psi}}_{\rm p}\gamma_{\mu}\Psi_{\rm n})(C_{\rm V}\hat{\mathbf{\Psi}}_{\rm e}\gamma_{\mu}\Psi_{\nu} + C'_{\rm V}\hat{\mathbf{\Psi}}_{\rm e}\gamma_{\mu}\gamma_5\Psi_{\nu}) \\
&+ \frac{1}{2}\hat{\mathbf{\Psi}}_{\rm p}\sigma_{\lambda\mu}\Psi_{\rm n}(C_{\rm T}\hat{\mathbf{\Psi}}_{\rm e}\sigma_{\lambda\mu}\Psi_{\nu} + C'_{\rm T}\hat{\mathbf{\Psi}}_{\rm e}\sigma_{\lambda\mu}\gamma_5\Psi_{\nu}) \\
&+ (\hat{\mathbf{\Psi}}_{\rm p}\gamma_{\mu}\gamma_5\Psi_{\rm n})(C_{\rm A}\hat{\mathbf{\Psi}}_{\rm e}\gamma_{\mu}\gamma_5\Psi_{\nu} + C'_{\rm A}\hat{\mathbf{\Psi}}_{\rm e}\gamma_{\mu}\Psi_{\nu}) \\
&+ (\hat{\mathbf{\Psi}}_{\rm p}\gamma_5\Psi_{\rm n})(C_{\rm P}\hat{\mathbf{\Psi}}_{\rm e}\gamma_5\Psi_{\nu} + C'_{\rm P}\hat{\mathbf{\Psi}}_{\rm e}\Psi_{\nu}) \\
&+ \text{Hermitian conjugate.}
\end{aligned}
\tag{2.5}
$$

By the mid-1950s, decays of two different particles with the same mass and charge were observed to have different parities in the final state. This was referred to as the $\Theta - \tau$ problem, in which the following reactions were observed

$$
\begin{aligned}
\Theta^+ &\rightarrow \pi^+ + \pi^0. \\
\tau^+ &\rightarrow \pi^+ + \pi^+ + \pi^-.
\end{aligned}
\tag{2.6}
$$

Since the parity of each pion is $P = -1$ and the total parity is multiplicative, the parity of the Θ^+ was taken to be $+1$ and the parity of the τ^+ was taken to be -1. Lee and Yang [Lee and Yang, 1956] argued that the weak interaction may not conserve parity and that the Θ^+ and τ^+ particles were actually the same particle, which we now call the $K+$. The first experiment that showed that parity is violated in the weak interaction was the Wu-Ambler experiment at the National Bureau of Standards (NBS) [Wu et al., 1957], in which the beta decay of polarized ^{60}Co showed asymmetry in the emission direction for electrons. Lee and Yang also suggested that the successive decays

$$\pi^+ \rightarrow \mu^+ + \nu, \tag{2.7}$$

$$\mu^+ \rightarrow e^+ + 2\nu, \tag{2.8}$$

should result in a spin polarization of the muon and that the positron would have an angular distribution and serve as an analyzer of the muon polarization, which was confirmed in another experiment shortly after the ^{60}Co experiment [Garwin et al., 1957]. Evidence from

these and more experiments showed that the weak interaction involves only right-handed antiparticles and left-handed particles.

2.3 Semi-Leptonic Weak Interaction - Neutron Decay

The β decay of the free neutron addresses important questions in particle physics and astrophysics [Dubbers and Schmidt, 2011][Wietfeldt and Greene, 2011]. The decay is described by the transformation of a d quark into a u quark with the emission of a virtual W^- boson that decays to an electron and an electron antineutrino (figure 2.2). The β decay of the neutron is the simplest semi-leptonic decay and its study tests the charged-current sector of the standard model. The neutron lifetime is also important for determining the relative abundance of helium in the early universe. There are three distinct methods for measuring the neutron lifetime, τ_n: the bottle method, the beam method, and direct measurement of the exponential decay. Each independent method has different systematics and accurate measurements with each are important to reliably measure τ_n. The descriptions below describe the most recent precise in-beam neutron lifetime measurement published in 2005 [Nico et al., 2005]. Improvements will be implemented for this measurement with the goal of achieving a 1s measurement of the neutron lifetime.

There has been no experimental evidence for scalar, psuedoscalar, or tensor terms in the weak interaction Hamiltonian. Experimentally, the correct matrix element for beta decay includes a parity violating axial vector contribution. The beta decay of the neutron is observed as the mixing of two types of decay depending on the alignment of the spins of the electron and neutrino: $\Delta J = 0$ (Fermi decay), and $\Delta J = 0, \pm 1$ (Gamow-Teller decay). Experimentalists continue to search for violations to the Standard Model, such as a tensor contribution, for the weak interaction through precise measurements of decay observables. At the quark level, G_V and G_A are equal and the matrix element can be written [Dubbers and Schmidt, 2011]

$$\mathcal{M}_{quark} = \frac{G_F}{\sqrt{2}} \langle u|\gamma_\mu(1-\gamma_5)|d\rangle \langle \nu_e|\gamma_\mu(1-\gamma_5)|e\rangle. \tag{2.9}$$

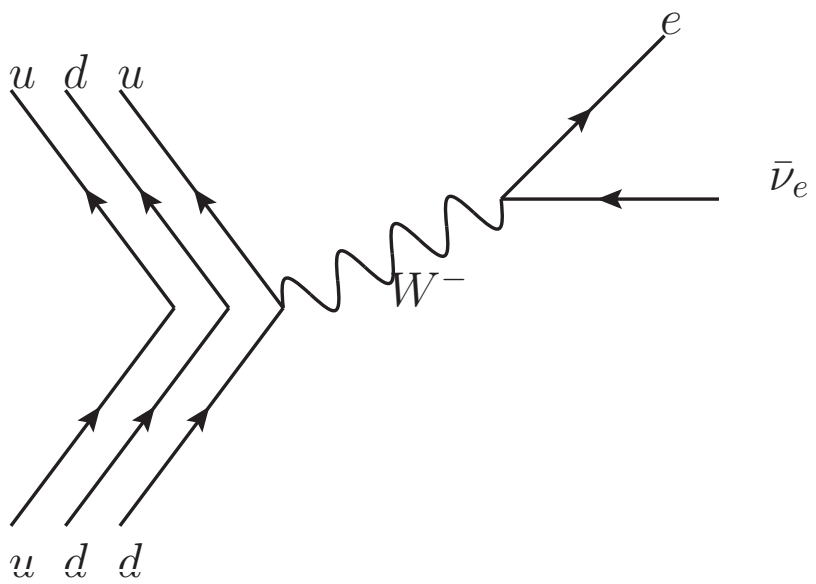

Figure 2.2: β decay of the free neutron into a proton and emitting an electron and an antineutrino.

However, at the nucleon level the coupling strengths of the vector and axial vector components are different. This is written [Wietfeldt and Greene, 2011] so that the vector and axial vector coupling constants are explicitly separated

$$\mathcal{M} = \langle n|\gamma_\mu(G_V - G_A\gamma_5)|p\rangle\langle\nu_e|\gamma_\mu(1-\gamma_5)|e\rangle. \tag{2.10}$$

The vector and axial vector coupling constants are written as

$$\begin{aligned} G_V &= G_F V_{ud} C_V \\ G_A &= G_F V_{ud} C_A, \end{aligned} \tag{2.11}$$

where G_F is Fermi's constant, V_{ud} is the first element in the CKM matrix, $C_V = 1$, and C_A is subject to corrections. Under conserved vector current (CVC) hypothesis, the vector current is analogous to the electromagnetic vector current and C_V is conserved in the same way that the electric charge is conserved. Experimentally, $\lambda = G_A/G_V = -1.2701$ [Beringer,

2012]. The neutron lifetime can be expressed as

$$\tau_n = \frac{2\pi^3\hbar^7}{(G_V^2 + 3G_A^2)m_e^5c^4f(1+RC)}, \tag{2.12}$$

where f is an integral over the Fermi energy spectrum, and $(1+RC)$ corresponds to radiative corrections [Marciano and Sirlin, 2006].

$$\tau_n = \frac{4908.7 \pm 1.9\text{s}}{|V_{ud}|^2(1+3\lambda^2)}. \tag{2.13}$$

The vector coupling constant C_V is best measured in superallowed $0^+ \rightarrow 0^+$ nuclear beta decays since these are pure vector decays. The axial coupling constant C_A, or the ratio λ, is best determined from the neutron decay either from the lifetime or a beta decay asymmetry measurement. Precision measurements of the neutron lifetime are important for obtaining precise and reliable values for the weak coupling constants G_A and G_V and by extension V_{ud} and estimates of unitarity.

2.4 Hadronic Weak Interaction

Hadrons, neutrons and protons for instance, are composed of quarks and are sensitive to gravity, electromagnetism, the strong interaction, and the weak interaction. The least well studied of these is the hadronic weak interaction (HWI), in which composite hadrons are coupled via the weak interaction.

The electroweak theory alone is not sufficient to describe the interaction of hadrons due to contributions from the strong interaction with the weak contribution suppressed by a factor of $\approx 10^{-7}$. Furthermore, the range of the $W^{\pm}$ and Z^0 bosons is far too small for direct interaction between two hadrons and thus between quarks within two hadrons.

The first widely used theory for the HWI is the meson-exchange model proposed by Desplanques, Donaghue, and Holstein (DDH) [Desplanques et al., 1980] in order to explain the strangeness-conserving $\Delta S = 0$ HWI. The DDH model interprets the HWI as a strong vertex with the exchange of a virtual meson, a quark-antiquark pair, and a weak vertex that couples one of the hadrons to a $W^{\pm}$ or Z^0 that couples to a quark in the other hadron

(figure 2.3). The NPDGamma experiment aims to probe the hadronic weak interaction by investigating the $\vec{n} + p \rightarrow d + \gamma$ reaction in which polarized neutrons capture on liquid parahydrogen.

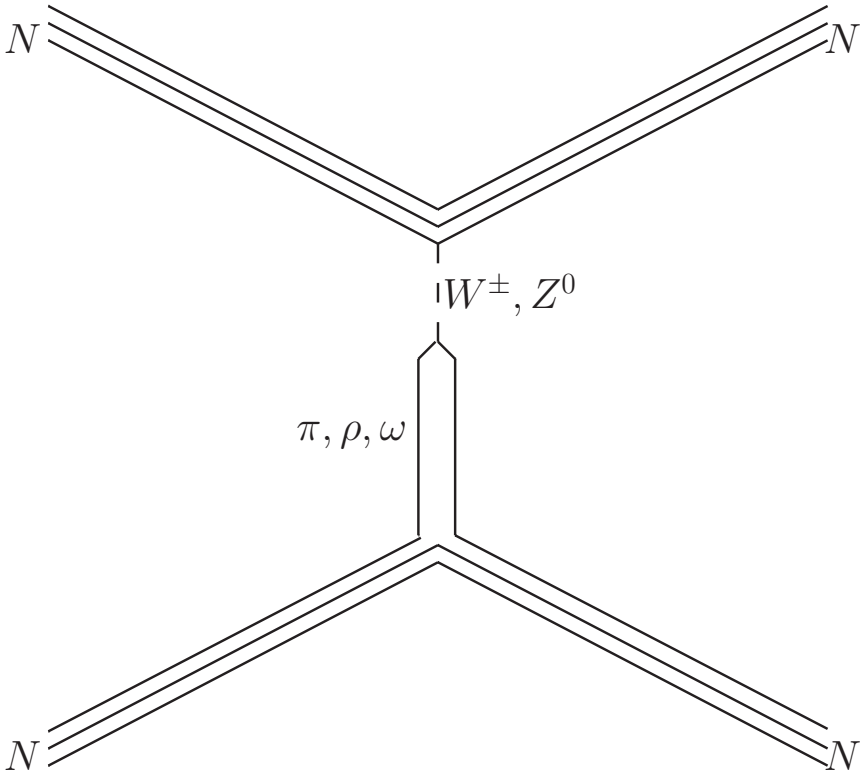

Figure 2.3: Meson exchange model of the hadronic weak interaction, in which two nucleons are coupled by a meson and a short range $W^{\pm}$ or Z^0 boson.

2.4.1 Meson Exchange Model

The strong force describes the binding the the atomic nucleus and is mediated by the exchange of gluons with a range of approximately 2 fm. The strong interaction becomes insignificant at greater distances. Therefore, at low energy, the strong interaction is mediated by the exchange of a virtual meson. The range of the virtual meson is determined from the uncertainty principle, such that energy conservation requires the virtual particle exists for a time $t = \frac{\hbar}{mc^2}$ corresponding to a range of approximately ct. This range is approximately 2 fm for the lighest mesons, the pions π^0 and $\pi^{\pm}$ with masses of 135 MeV/c^2 and 139 MeV/c^2

Table 2.1: Weak meson couplings as calculated by DDH [Desplanques et al., 1980] in units of $G_F F_\pi^2/2\sqrt{(2)} \sim 3.8\text{x}10^{-8}$, where G_F is Fermi's constant and F_π is the pion decay constant.

Constant	Reasonable Range	"Best" Value
h_π^1	$0 \rightarrow 30$	$+12$
h_ρ^0	$30 \rightarrow -81$	-30
h_ρ^1	$-1 \rightarrow 0$	-0.5
h_ρ^2	$-20 \rightarrow -29$	-25
h_ω^0	$15 \rightarrow -27$	-5
h_ω^1	$-5 \rightarrow -2$	-3

respectively. For low energies with conserved strangeness, the strong interaction is carried by the lightest mesons (π, ρ, and ω).

The virtual $W^\pm$ and Z^0 that mediate the weak interaction are much heavier, with masses of 80 GeV/c^2 and 91 GeV/c^2 respectively. This results in the weak interaction having a range of $2\text{x}10^{-3}$ fm, significantly smaller than the separation between nucleons. Therefore, for the weak interaction to participate, a virtual light meson is emitted from one nucleon and comes close enough to the other nucleon that a virtual $W^\pm$ or Z^0 couples the meson to the nucleon. Compared to the strong interaction, the weak interaction is suppressed by a factor of the weak coupling constant of approximately $10^{-6} - 10^{-7}$, however the direct interaction between two nucleons with the exchange of a $W^\pm$ or Z^0 goes as the square of the weak coupling constant and is therefore not observed. The DDH model expresses observables in terms of six meson-nucleon coupling constants, h_π^1, h_ρ^0, h_ρ^1, h_ρ^2, h_ω^0, h_ω^1, where the subscripts are the exchanged meson and the superscripts are the change in isospin. The DDH reasonable ranges and best values are shown in table 2.1.

There is not exceptional overall agreement between various parity violation experiments under the DDH model [Haxton, 2008]. A more recent development in the theory for describing few nucleon systems in the low energy regime is to use effective field theories [Savage, 2001] in which the pion is integrated out as low energy constants [Schindler and Springer, 2010].

2.5 Neutron Decay and Cosmology

The early universe was a very hot soup of particles, and the neutron lifetime is important in determining the composition of the universe at the time when events of interest stopped happening. Big-Bang Nucleosynthesis (BBN) is a critically important probe of physics in the early universe. BBN models predict the primordial abundances of the light elements, and observations of these abundances plays a role in contraining cosmological models. The predicted abundances are affected by the neutron lifetime. First, the neutron lifetime is determined by the weak interaction coupling constant,

$$\tau_{\mathrm{n}}^{-1} = \frac{G_F^2}{2\pi^3}(1 + 3G_A^2)m_e^5\lambda_0, \tag{2.14}$$

where G_F is the Fermi coupling constant, G_A is the axial-vector coupling constant, m_e is the electron mass, and λ_0 is the phase space integral. A different neutron lifetime implies a different weak interaction rate. To a good approximation, weak reactions cease once the weak interation rate

$$\Gamma = \frac{7}{60}\pi(1 + 3G_A^2)G_F^2T^5, \tag{2.15}$$

becomes smaller than the Hubble expansion rate

$$H \approx [\frac{8}{3}\pi G\rho_\gamma]^{\frac{1}{2}}, \tag{2.16}$$

where ρ_γ is the energy density of relativisitc particles [Izotov and Thuan, 2010]. During this time, neutrons and protons are in equilibrium,

$$\begin{aligned} p + e^- &\longleftrightarrow n + \nu_e. \\ n + e^+ &\longleftrightarrow p + \bar{\nu}_e. \end{aligned} \tag{2.17}$$

As long as the interconversion rate is faster than the rate of expansion of the universe at this time[Olive et al., 2000], the neutron-to-proton ratio is in equilibrium and determined by the

Maxwell-Boltzmann distribution [Izotov and Thuan, 2010]

$$\frac{N_n}{N_p} = (\frac{m_n}{m_p})^{\frac{3}{2}} e^{-\frac{m_n - m_p}{T}}, \tag{2.18}$$

where T is the temperature of the universe in units of MeV. Setting the weak reaction rate and the expansion rate equal, gives the freezeout temperature $T_f \approx 1$ MeV and a freezeout time when the universe is approximately 1 s old, and the neutron to proton ratio freezes out at approximately $\frac{1}{6}$. A longer lifetime implies a smaller G_F and therefore a slower weak reaction rate which results in a higher freezeout temperature and freezeout time.

After freeze out and before nucleosynthesis, the only process that changes the relative concentrations is neutron beta decay. Neutron decay before nucleosynthesis leads to a decrease in the number of neutrons available to form helium. Due to the large photon-to-baryon ratio at this time, the photodissociation rate of the deuteron is larger than the production rate until the universe has cooled to about 80 keV. The time for the universe to cool to 80 keV is on the order of a few hundred seconds and neutron decay is not negligible on this time scale. The ratio of neutrons to protons at the time when the universe cools enough to fuse nucleons into light nuclei is approximately $\frac{1}{7}$, and all of the remaining free neutrons at this time become bound in light elements (mostly ^{4}He). The estimated ^{4}He mass fraction, $\mathrm{Y_P}$ is given by,

$$Y_{\mathrm{P}} \approx \frac{2n}{p(1 + \frac{n}{p})} = 0.25. \tag{2.19}$$

Together, the weak interaction rate and the neutron decay period imply that a longer neutron lifetime leads to a higher predicted helium abundance.

The "effective number of neutrino species" has become an interesting probe of the early universe. The standard model predicts an effective number of neutrino species of $N_{\mathrm{eff}} = 3.046$[Mangano et al., 2001], which expresses the expansion rate of the universe in terms of the number of ideally thermalized neutrinos. The effective number of neutrinos need not be an integer if there exist non-thermally populated species. Recent observations of the cosmic microwave background indicate $N_{\mathrm{eff}} = 3.30 \pm 0.27$[Ade et al., 2014]. Using the current Particle Data Group (PDG) value of the neutron lifetime, 880.3s $\pm$ 1.1[Olive, 2014], BBN models predict $N_{\mathrm{eff}} = 3.56 \pm 0.23$[Nollett and Steigman, 2014].

Uncertainties in the astrophysical observations of the baryon density still dominate the BBN field. Astrophysical observations can be used to provide a determination of the neutron lifetime by combining temperature and polarization anisotropies from the Planck satellite with recent measurements of the primordial helium abundance, with a result of $\tau_n = 905.7\text{s} \pm 7.8$ [Salvati et al., 2015]. At present, the largest uncertainty for inputs into primordial nucleosynthesis models is that of the neutron lifetime, providing an impetus to measure it more precisely.

Chapter 3

Measurement of the Neutron Lifetime

The free neutron typically decays via the process

$$\mathrm{n} \rightarrow \mathrm{p}^{+} + \mathrm{e}^{-} + \bar{\nu}_{\mathrm{e}}, \tag{3.1}$$

with 782 keV of energy available for the decay products by comparing the masses of the neutron, proton, and electron, though there is also a radiative mode in which a γ-ray is also emitted with a branching ratio of $(3.09 \pm 0.32) \times 10^{-3}$[Cooper et al., 2010]. The recoiling proton has an endpoint energy of 751 eV. The β-decay of the free neutron follows the usual exponential decay law:

$$N(t) = N_0 e^{-\frac{t}{\tau_{\mathrm{n}}}} \tag{3.2}$$

where $N(t)$ is the number of neutrons at a given time t and τ_{n} is the mean lifetime of the free neutron. Equivalently, the decay law can be expressed in a differential form:

$$\dot{N}(t) = \frac{\mathrm{d}}{\mathrm{dt}} N(t) = \frac{\mathrm{d}}{\mathrm{dt}} N_0 e^{-\frac{t}{\tau_{\mathrm{n}}}} = -\tau_{\mathrm{n}}^{-1} N(t). \tag{3.3}$$

The fact that the lifetime is long, on the order of 880 s [Olive, 2014], means that multiple methods of measuring the lifetime are possible. For very long lived isotopes, for instance ^{238}U with a lifetime of the order of the age of the Earth, the activity of the sample does not measurably change during the measurement period and thus experimental methods that access equation 3.3 must be used. Such a rate experiment requires an absolute measurement

of the quantity of ^{238}U and an absolute measurement of the rate of decay products. For short lived isotopes with lifetimes of the order of the measurement period, ^{137m}Ba with a lifetime on the order of a few minutes, the activity does change quickly and the decay curve from equation 3.2 can be mapped out via a relative counting measurement of the decay products over time which translates directly to the number of remaining particles in the sample as a function of time. Similarly, the number of remaining particles in the sample could be directly measured as a function of time. In this way, neutron lifetime measurements fall into three categories based on the apparatus and detection method: storage bottle, in-beam, and direct exponential decay. The storage bottle experiments store ultracold neutrons (UCN) and detect the number of remaining neutrons after some storage time. The in-beam measurements use a cold neutron beam and detect either the electron or proton from decays while simultaneously measuring the neutron fluence. The direct exponential decay experiments also store UCN but directly measure the decay products such that the exponential decay curve is directly observed.

3.1 Historical Neutron Lifetime Experiments

After the suggestion that the free neutron should be unstable [Chadwick and Goldhaber, 1935] as a result of being more massive than the proton, experimentalists set out to measure the decay lifetime. The first nuclear reactor entered operation in 1943. The Snell measurement [Snell et al., 1950] at the Oak Ridge reactor used a proton-electron coincidence method in order to overcome very large backgrounds and gave a conservative estimate of the neutron lifetime between 14 and 43 minutes.

The first proper measurement of the neutron lifetime was performed by Robson [Robson, 1951]. This measurement was performed at the Chalk River reactor using an electron-proton coincidence method for measuring the decay rate and a manganese foil to determine the neutron fluence. The capture cross section of manganese is inversely proportional to the velocity [Fermi, 1934], the $1/v$ law, and the probability that a neutron of a given velocity decays within the decay volume is similarly proprotional to $1/v$. This $1/v$ dependence is

used to cancel the energy dependence of the decay probability and the neutron capture flux. The Robson experiment gave a result of 18.5 min with an uncertainty of 18%.

The first precision measurements of the neutron lifetime were performed in the coming decades, first [Sosnovsky et al., 1959] at 16.8 min ± 0.4, followed by [Christensen et al., 1972] at 15.3 min $\pm\, 0.2$, and [Bondarenko et al., 1978] at 14.6 min $\pm\, 1.3$. Only the Sosnovsky experiment agreed with the previous measurements and each of these three experiments was in disagreement. This "first lifetime problem" led to new measurements and the development of new techniques.

3.2 Storage in a Bottle

Ultracold neutrons have kinetic energies on the order of 100 neV, corresponding to velocities of a few $\mathrm{m\,s^{-1}}$. The gravitational potential, mgh, for neutrons at the Earth's surface is approximately 100 $\mathrm{neV\,m^{-1}}$, allowing UCN to be trapped vertically. Neutrons are reflected by the wall as a result of the strong interaction with nuclei in the wall such that neutrons below a material specific threshold energy are always reflected. Materials are typically characterized by their critical reflection angles or momentum transfers. The Fermi potential of the bottle walls is of order a few 100 neV, which allows UCN to be confined to a material bottle since all neutrons are below the critical threshold. The magnetic dipole moment of the neutron is 60 $\mathrm{neV\,T^{-1}}$, so UCN can have a kinetic energy less than $\mu \cdot \vec{B}$ potential energy in a magnetic field. Since the direction of the magnetic moment depends on the spin orientation of the neutron, UCN with 100% spin polarization can be trapped indefinitely in a magnetic field minimum until they beta decay.

The first UCN confinement lifetime experiment used a toroidal magnet to trap spin polarized UCN [Paul et al., 1989]. Most other UCN confinement experiments have relied on material bottles with gravitational confinement vertically.

The idea behind this method is rather simple. UCN are created and allowed to enter a bottle. The bottle is designed so that neutrons are confined to the bottle materially, gravitationally, or magnetically. After storing the neutrons for a long time, Δt, the remaining neutrons are allowed to flow out of the bottle and are counted. The experiment is repeated for

different storage times, but with the same initial number of neutrons or with normalization to a loading monitor. Assuming the only neutron loss mechanism is neutron beta decay, the neutron lifetime can be determined from the relative neutron counts N_1 and N_2 given different storage times Δt_1 and Δt_2

$$\tau_n = \frac{\Delta t_2 - \Delta t_1}{\log(N_1/N_2)}. \tag{3.4}$$

However, there are always additional neutron loss mechanisms other than β-decay that must be accounted for, such that the storage lifetime is a combination of many loss mechanisms. Imperfections in the bottle walls can lead to inelastic scattering and absorption. Because the temperature of the bottle is much greater than the effective temperature of the UCN, inelastic scattering will increase the neutron kinetic energy well above the effective potential of the material walls leading to escape . These and other loss mechanisms replace the τ_n in equation 3.4 with a neutron storage lifetime τ_{bottle} where

$$\frac{1}{\tau_{\text{bottle}}} = \frac{1}{\tau_n} + \frac{1}{\tau_{\text{inel}}} + \frac{1}{\tau_{\text{abs}}} + \dots \tag{3.5}$$

where τ_{inel} is loss due to inelastic scattering and τ_{abs} is loss due to neutron absorption. Other loss mechanisms contributing to the storage lifetime in the same fashion as long as the loss mechanisms have a constant rate, though this is not strictly true.

Material bottles were significantly improved by coating the walls with Fomblin oil. Fomblin oil is hydrogen free, cryogenically friendly, and has a low vapor pressure. Fomblin coatings provide a renewable, reflective, and smooth surface for material bottles that would otherwise have hydrogen contamination or cracked surfaces. The first use of a Fomblin oil coated material bottle was the MAMBO experiment[Mampe et al., 1989]. In addition to addressing loss mechanisms, improved UCN production and UCN transport allowed storage experiments to be competitive with beam experiments.

For the Serebrov measurement[Serebrov et al., 2005], the storage lifetime was within 5-10 s of the neutron lifetime, but the extrapolation from τ_{bottle} to the neutron lifetime for other bottle experiments is on the order of 100s [Arzumanov et al., 2000][Pichlmaier et al.,

2010]. The interaction of UCN with the material walls of the bottle is very difficult to address [Steyerl et al., 2012].

There are ongoing efforts to develop and perform competitive magnetic trapping experiments [Ezhov et al., 2014; O'Shaughnessy et al., 2009; Salvat et al., 2014]. However, there are disadvantages associated with the magnetic fields. Half of the UCN produced at the source are immediately lost because they are in the wrong spin state and are not trapped. Imperfections in the magnetic field lead to spin flip of the right spin neutrons, which adds a potential loss mechanism. Neutrons with high kinetic energy may persist in the storage apparatus in long lived orbits for times on the order of the neutron lifetime and are considered "marginally trapped neutrons". Additionally, statistical precision capabilities continue to increase as UCN sources are improved to provide higher UCN densities.

3.3 Cold Neutron Beam

Cold beam experiments have a long history, though only a few cold beam experiments remain in development. The beam method measures the neutron decay rate $dN/dt = -N/\tau_n$ and requires simultaneously counting neutrons and neutron decay products, either protons or electrons. This also requires accurate knowledge of detector efficiencies as well as the precise decay volume. The amount of time that a neutron spends in the decay volume is proportional to $1/v$. Likewise, the typical neutron flux monitor will have a detection efficiency proportional to $1/v$, which allows for a clever cancellation. There are three primary challenges that must be addressed in order to perform a beam measurement to high precision: a) measuring a relatively low decay rate in the presence of background b) accurate determination of the decay volume c) the mean number of neutrons within the decay volume. The method of trapping decay protons was first proposed by Byrne et al. [Byrne et al., 1980][Byrne et al., 1989]. The most recent precision in-beam lifetime measurement is described in detail later.

3.4 Current State of the Lifetime

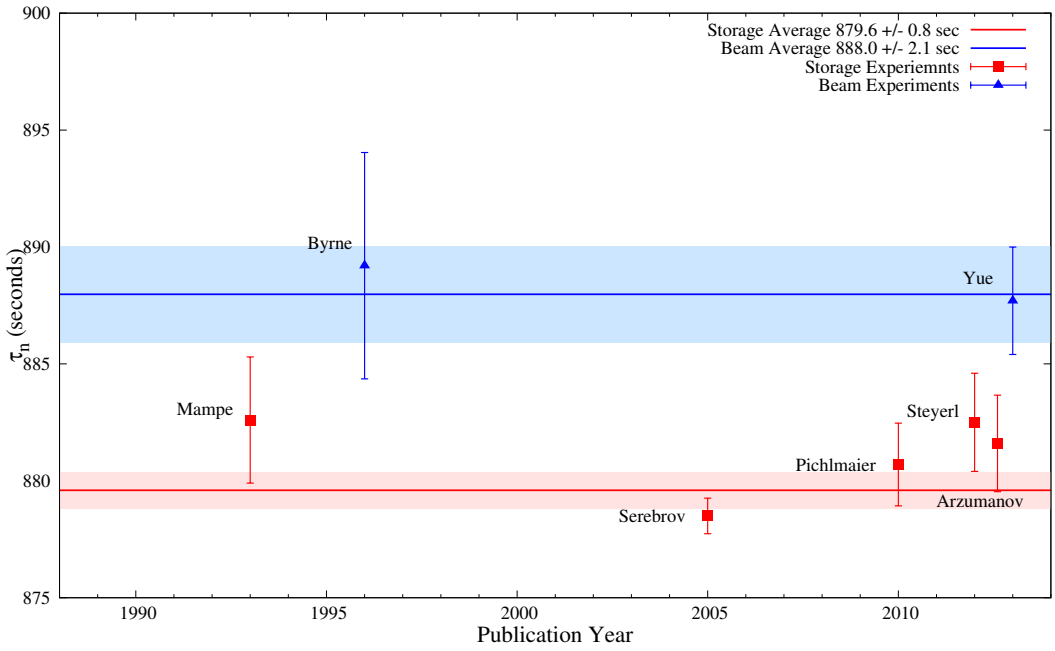

Figure 3.1: Neutron lifetime measurements. The shaded regions indicate beam and bottle averages with 1σ boundaries extracted from taking a weighted average of each experimental technique to illustrate the current discrepancy.

In the last decade, a new neutron lifetime problem has arisen due to the disagreement between two different methods of precision measurements of the neutron lifetime. In 2004, Serebrov and collaborators [Serebrov et al., 2005] published the result from the Gravitrap II experiment, which uses a material bottle. The Gravitrap II result is $\tau_n = (878.5\text{s}) \pm .7$ which was 7 seconds lower than the PDG value at the time of $\tau_n = (885.7 \pm .8\text{s})$. At the time, the PDG [Nakamura, 2010] approached this measurement with caution, stating that the Serebrov result was so far from the other results, that it would not be included in the average but that the present average should be considered suspect.

Since then, more UCN storage experiments have published results or published corrections to previous results that are all in better agreement with the Gravitrap II result. The PDG adjusted the accepted value of the lifetime in 2011 to $\tau_n = (880.1 \pm 1.1\text{s})$ [Beringer, 2012], an adjustment of approximately 5 σ. A reanalysis [Steyerl et al., 2012] of the MAMBO I result [Mampe et al., 1989] has been published that shifts the 1989 result downward by

Table 3.1: Recent neutron lifetime measurements contributing to the PDG world average value [Olive, 2014]. Measurements in the top section are included in the PDG world average, while measurements in the bottom section have been re-analyzed and replaced in the PDG world average.

Value (s) (stat.) (sys.)	Author/Year	Technique
$887.7 \pm 1.2 \pm 1.9$	[Yue et al., 2013]	In-beam n, trapped p
$881.6 \pm 0.8 \pm 1.9$	[Arzumanov et al., 2012]	UCN double bottle
$882.5 \pm 1.4 \pm 1.5$	[Steyerl et al., 2012]	UCN material bottle
$880.7 \pm 1.3 \pm 1.2$	[Pichlmaier et al., 2010]	UCN material bottle
$878.5 \pm 0.7 \pm 0.3$	[Serebrov et al., 2005]	UCN gravitational trap
$889.2 \pm 3.0 \pm 3.8$	[Byrne et al., 1989]	Penning trap
882.6 ± 2.7	[Mampe and Bondarenko, 1993]	UCN material bottle
$885.4 \pm 0.9 \pm 0.4$	[Arzumanov et al., 2000]	see [Arzumanov et al., 2012]
887.6 ± 3.0	[Mampe et al., 1989]	see [Steyerl et al., 2012]
$886.3 \pm 1.2 \pm 3.2$	[Nico et al., 2005]	see [Yue et al., 2013]

approximately 5 s due to a newly developed theory to account for scattering from the material walls. Similarly, reanalysis [Arzumanov et al., 2012] of the previous [Arzumanov et al., 2000] measurement produced a downward by approximately 4 s. An improved determination of the neutron fluence monitor efficiency [Yue et al., 2013] narrows the uncertainty from the previous most precise neutron beam measurement [Nico et al., 2005] while shifting the result upward by 1.4 s, which is within error bars.

During this time, the Particle Data Group has decided to average all of the best seven measurements and to inflate the uncertainty by a scale factor of 1.9, for a PDG world average of $\tau_n = (880.3 \pm 1.1\text{s})$, and again calls on experimenters to resolve the discrepancy[Olive, 2014]. Figure 3.1 depicts the contibuting experiments to the PDG world average neutron lifetime, also listed in table 3.1. In addition, cosmological data from the Planck satellite and helium abundance measurements supports a neutron lifetime that is in disagreement with both the techniques $\tau_n = 905.7\text{s} \pm 7.8$ [Salvati et al., 2015].

In recent years, there has been renewed interest in magnetically trapped UCN bottles. The UCNτ collaboration at Los Alamos National Laboratory has published storage times approaching the neutron lifetime [Salvat et al., 2014] using a permanent magnet bowl-shaped Halbach array that is asymmetric in order to address "marginally trapped neutrons". As yet unpublished, the Ezhov group claims a neutron lifetime of $\tau_n = (878.3 \pm 1.9\text{s})$ with zero

systematic uncertainty using a magneto-gravitational trap using permanent magnets [Ezhov et al., 2014].

The trend appears to be towards a lower lifetime, though several of these measurements are corrections to previous experiments. The bottle experiments are rather similar and depend on similar systematic effects, namely reliance on Monte Carlo of neutron losses in the walls of a material bottle. It is important to perform precise measurements using completely independent methods with different systematic effects in order to address this discrepancy, and it is difficult to trust this trend towards a lower lifetime from ultra-cold neutron storage experiments without corroborating in-beam experiments.

Chapter 4

NIST Beam Lifetime Experiment

4.1 Method and Apparatus

Neutron beam lifetime measurements have a long and developed history. The first neutron lifetime experiment in which decay protons were collected inside a segmented Penning trap and transported along a bent magnetic field to the proton detector were performed by the Byrne group [Byrne et al., 1989, 1990]. The NIST beam lifetime measurement uses the same technique. The in-beam method requires accurate counting of the neutron fluence as well as the rate of neutron decays. There are three primary challenges that must be addressed in order to perform this measurement to high precision: the relatively low decay rate in the presence of background, accurate determination of the decay volume, and the mean number of neutrons within the decay volume. The trapping region of length L intercepts the entire areal cross section of the neutron beam. The neutron beam is characterized by a velocity dependent fluence rate $I(v)$. The mean number of neutrons in the trap is therefore

$$N_n = L \int_A da \int I(v) \frac{1}{v} dv, \tag{4.1}$$

where the beam cross section is A. The proton detection rate is then

$$\dot{N}_p = \tau_n^{-1} \epsilon_p L \int_A da \int I(v) \frac{1}{v} dv, \tag{4.2}$$

where ϵ_p is the proton detection efficiency. After leaving the trapping region the neutron beam passes through a thin detector with a cold neutron detection efficiency proportional to $\frac{1}{v}$. The detector is a thin layer of ^{6}LiF and its efficiency is defined to be ϵ_0 for neutrons with velocity $v_0 = 2200\mathrm{m\,s^{-1}}$ and the velocity dependent efficiency is then $\frac{\epsilon_0 v_0}{v}$. Neutron capture on ^{6}Li produces an alpha and a triton

$$^6\mathrm{Li} + n \rightarrow {}^4\mathrm{He}(2.05\ MeV) + {}^3\mathrm{t}(2.75\ MeV). \tag{4.3}$$

The detection rate is given by

$$\dot{N}_{\alpha+t} = \epsilon_0 v_0 \int_A da \int I(v)\frac{1}{v}\, dv. \tag{4.4}$$

The integrals in equations 4.2 and 4.4 are identical given two assumptions: a) the deposit is thin and absorption is exactly proportional to $\frac{1}{v}$, b) the neutron beam intensity and velocity dependence do not change between the trap and the fluence monitor. [Pritychenko and Mughabghab, 2012] The deviation of the ^{6}Li(n, t)^{4}He cross section from $\frac{1}{v}$ has been shown to be small with a Westcott g-factor, g_w, of 1.001 [Pritychenko and Mughabghab, 2012], and changes in the beam between the trap and the fluence monitor are of order 0.001%. The Westcott g-factor is defined as the ratio of the Maxwellian averaged cross section to the thermal (2200 m/s) cross section

$$g_w = \frac{\sigma_{\mathrm{Maxwell}}}{\sigma_{2200}}. \tag{4.5}$$

The Maxwellian averaged cross section, $\sigma_{\mathrm{Maxwell}}$, can be expressed as

$$\sigma_{\mathrm{Maxwell}}(kT) = \frac{2}{\sqrt{\pi}}\frac{a^2}{(kT)^2}\int_0^\infty \sigma(E_n^L) E_n^L e^{-\frac{aE_n^L}{kT}} dE_n^L, \tag{4.6}$$

where $a = m_{\mathrm{nucleus}}/(m_n + m_{\mathrm{nucleus}})$, E_n^L is the laboratory energy of the neutron, and kT is the usual Boltzmann factor. In terms of measured quantities, the neutron lifetime is given by

$$\tau_n = \frac{L}{v_0}\frac{\dot{N}_{\alpha+t}}{\dot{N}_p}\frac{\epsilon_p}{\epsilon_0}. \tag{4.7}$$

This method, however, ties the experimental result to the currently accepted value of the $^{6}\mathrm{Li}(\mathrm{n},\mathrm{t})^{4}\mathrm{He}$ cross section from ENDF.

4.1.1 Neutron Beamline

The most recent in-beam lifetime experiment was performed at the NIST Center for Neutron Research (NCNR) in 2001-2002. The NCNR operates a 20MW heavy-water reactor. Neutrons are moderated by the D_2O reactor coolant to thermal energies. Cold neutrons are produced by a 20K liquid hydrogen moderator situated near the reactor core. The cold neutrons have a pseudo-Maxwellian spectrum with an effective temperature of 40K. The use of cold neutrons increases the time that a neutron spends in the trap and thus increases the probability that a given neutron decays within the trap. The measurement for the 2005 result took place on NG-6 at the NCNR at the end of a 68m neutron guide coated with ^{58}Ni.

4.1.2 Proton Trapping and Counting

The cylindrical decay volume is defined by the diameter of the neutron beam and the length of the electrostatic proton trap (figure 4.1). The proton trap consists of 16 annular electrodes. The electrostatic trap sits inside a solenoid that provides a 5T magnetic field along the beam axis. Decay protons are emitted with any energy up to 751eV and are confined to helical orbits along the beam axis with a cyclotron radius of about 1mm. Decay protons are trapped along the beam axis by +800 V electrostatic barriers at the upstream and downstream ends of the trap. The trapping efficiency is unity except for the decay protons created near the ends of the trap where edge effects become an issue. After a trapping time on the order of 10ms, the trap door is opened and protons are flushed towards the proton detector and counted.

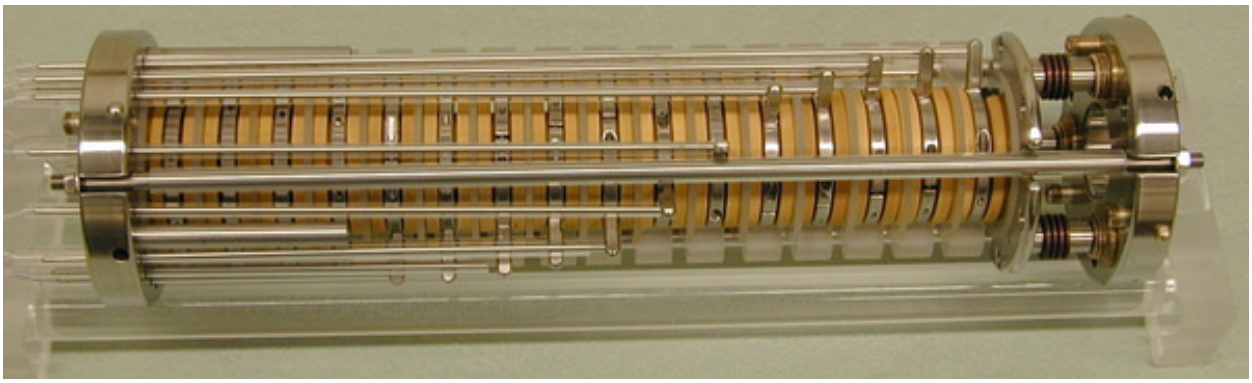

Figure 4.1: Fully assembled segmented proton trap comprised of gold coated fused quartz electrodes.

An ideal proton trap would have a perfectly uniform axial magnetic field and an electrostatic trap with a perfectly square well potential that exceeds the maximum proton energy on both ends. Given these conditions, the neutron lifetime could be measured easily from measuring all the parameters in equation 4.7. However, one cannot realize a square well potential and instead the field is positive and less than the maximum value in the end region near the ends of the trap. Protons created in the middle of the trap are trapped with unit efficiency, but protons created in the end region are trapped with less than 100% efficiency. The use of a trap segmented with 16 electrodes allows the length of the trapping region to be varied in order to probe systematics including the trap end effects. The precise dimensions of the trap must be known to high accuracy for this method, and the trap is designed with this in mind. The electrodes are made of fused quartz and coated with a thin layer of gold. Adjacent electrodes are separated by 3mm fused quartz spacers. The length of the trap is measured at room temperature using metrology to better than 5µm. The change in the length of the electrodes due to temperature is at the 0.01% level. The first 3 upstream electrodes are referred to as the door. There are several electrodes that are grounded during a trapping cycle, ranging from 3 to 10 electrodes in length. Finally, 3 more electrodes after the trapping region are held at the same voltage as the door and referred to as the mirror. During a trapping cycle, the mirror and door confine protons to the trapping region. The end region shape is the same for all trap lengths, and the length of the trap can be written as

$$L = nl + L_{\text{end}}, \tag{4.8}$$

where n is the number of grounded electrodes, l is the total length of 1 electrode and 1 spacer (21.6mm), and L_{end} is the effective length of the two end regions. The effective end region length is proportional to the physical length of the end regions and the probability that a proton created there is trapped. From rearranging equation 4.7, the ratio of the proton to alpha and triton counting rates is measured as a function of the number of electrodes and fit to a straight line in order to extract τ_n.

$$\frac{\dot{N}_p}{\dot{N}_{\alpha+t}} = \tau_n^{-1} \frac{\epsilon_p}{\epsilon_0 v_0}(nl + L_{\text{end}}). \tag{4.9}$$

Because of the symmetry of the trap, the end region is approximately the same for all trap lengths. The electrodes are mounted using a stainless steel frame which is rigidly attached inside the superconducting magnet bore. The bore volume is evacuated to UHV during the running of the experiment and the mirror, door, and trapping region voltages are controlled externally by the DAQ.

There are three trap states during a trapping cycle: trapping protons, counting protons, and clearing the trap. The typical trapping period is 10 ms. It is unlikely that multiple neutrons will decay per cycle because the neutron fluence rate is small, which reduces dead time corrections but these corrections are non-zero and are discussed in a later section. The first trap state is the trapping mode. The door and mirror electrodes are held at 800 V and the other electrodes are grounded. The door and mirror voltages are high enough to confine decay protons along the beam and the magnetic field confines protons radially. After a trapping period of 10 ms, the proton detector is enabled. The door electrodes are then grounded and the central electrodes are placed in a graduated potential in order to flush protons from the trap. Protons follow the magnetic field lines toward the proton detector. The magnetic field lines are bent by approximately 9.5 degrees. The proton detector typically held at a voltage between 20 and 40 kV in order to accelerate the decay protons through the dead layer on the surface barrier detector. Counting mode remains active for a time long enough to detect any protons that may have been in the trap. The trap is then put into clearing mode and the door reset for the next trapping cycle.

4.1.3 Superconducting Magnet

Radial confinement and guiding of decay protons toward the proton detector is provided by a 4.6 T superconducting magnet. The proton trap is placed inside the flat region of the magnetic field. The magnetic field bends towards the proton detector in order to adiabatically guide decay protons. The cyclotron radius for a proton with 700 eV of energy perpendicular to the beam axis is approximately 1 mm. A hall probe was used to measure the magnetic field in the trapping region of the magnet and compared to the manufacturer (figure 4.2).

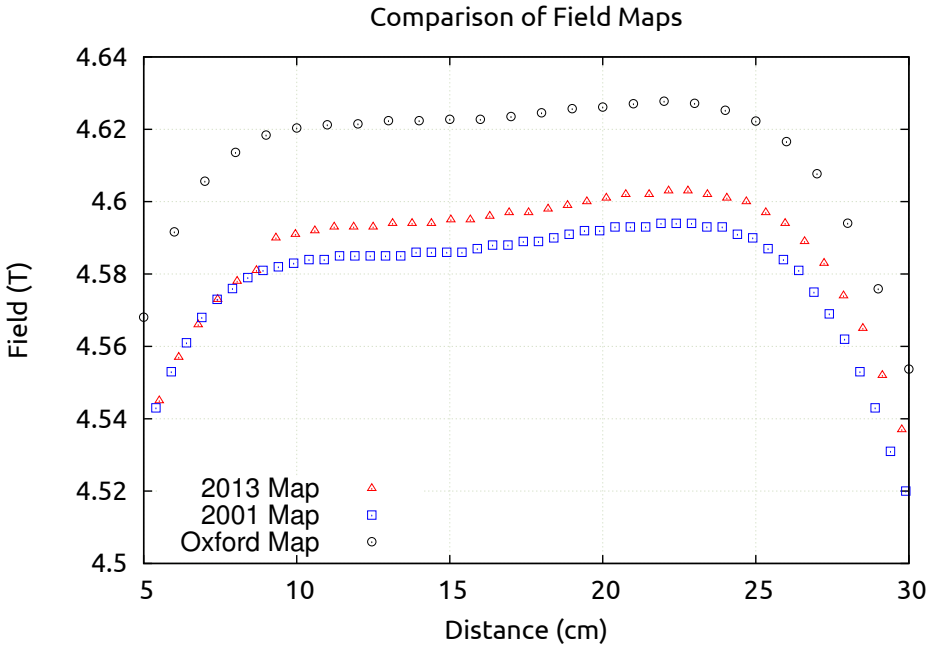

Figure 4.2: Comparison of field maps from 2013, 2001, and the original manufacturer specifications.

4.1.4 Neutron Counting

The neutron monitor is downstream of the magnet and proton trap and the neutron fluence is determined by measuring the ^{6}Li(n,t)^{4}He reaction rate. The detection rate for the α and triton depends on the neutron fluence rate, the detector solid angle, the deposit areal density, and the neutron absorption cross section. The detector consists of a ^{6}LiF deposit on a silicon wafer surrounded by 4 silicon detectors for detecting the reaction products. The 4 silicon detectors have precision-machined apertures in order to have a well defined solid angle. They are arranged so that the solid angle is first order insensitive to the position

of the ^{6}LiF deposit. ^{6}Li has a thermal neutron absorption cross section that is large (940 barns) and well known [Chadwick et al., 2006]. The neutron monitor efficiency for thermal neutrons, ϵ_0, is the ratio of detected reaction products to incident neutrons. It is defined as

$$\epsilon_0 = \frac{2N_A\sigma_0}{4\pi A}\iint \Omega(x,y)\rho(x,y)\phi(x,y)\,dx\,dy, \tag{4.10}$$

where N_A is the Avogadro constant, σ_0 is the absorption cross section at $v_0 = 2200\mathrm{m\,s^{-1}}$, A is the atomic weight of ^{6}Li, $\Omega(x,y)$ is the detector solid angle, $\rho(x,y)$ is the areal density of ^{6}Li in the deposit, and $\phi(x,y)$ is the areal distribution of the neutron beam on the target. The neutron detector solid angle has been measured in two independent ways: contacting metrology and calibration with a ^{239}Pu α source of known activity. Contacting metrology measures precisely the diameter of the apertures and the distance from each aperture center to the center of the target. The ^{239}Pu α source calibration measures the α counting rate in the detectors with the source mounted in the target position. These two results agree to better than 0.1%. There are corrections for the neutron monitor efficiency, such as absorption in lithium and silicon and scattering in silicon. The uncertainty due to neutron counting was 2.7 s and was the dominant uncertainty in the 2005 measurement.

4.2 Data Analysis

4.2.1 Determination of $\dot{N}_{\alpha+t}$

There are 4 silicon detectors for detecting alphas and tritons, with each detector producing 4 single channel analyzer (SCA) windows that are counted in electronics. Window (a) corresponds to alphas, tritons, and high energy events and window (d) to high energy events only. The total number of alpha and triton events is recorded by summing the signals in all 4 detectors in window (a) and subtracting the signals in window (d). The particle rate is then given by

$$\dot{N}_{\alpha+t} = \frac{N_{\mathrm{tot}}}{t_{\mathrm{trap}}N_{\mathrm{open}}}, \tag{4.11}$$

where N_{open} is the number of trap openings and t_{trap} is the trap time. The neutron counting statistics are 0.01% or about 0.1s.

4.2.2 Determination of $\dot{N}_p$

The trapped proton rate is obtained by subtracting the beam-off proton rate from the beam-on proton rate for a given trap length. There are four timing regions shown in figure 4.3: while the trap is closed (I), the trap is opened and trapped protons arrive (II), trap remains open (III), and the trap is being flushed (not labeled). Region II contains the proton peak while regions I and III are background. Region III contains some protons that decay in-flight and the background here is higher than in region I. The beam-off rate is measured following each series of runs.

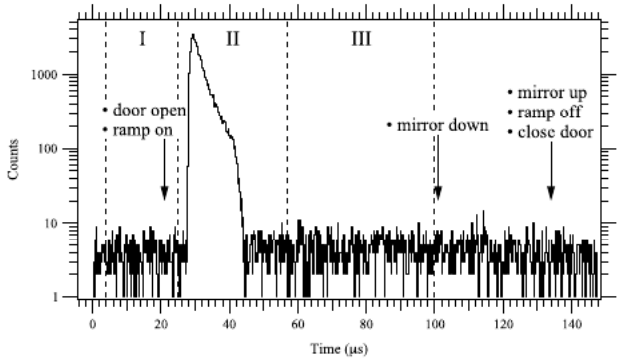

Figure 4.3: Example of TDC Spectrum[Dewey et al., 2003][Nico et al., 2005]

The beam-on proton rate is determined from the timing spectrum from the time-to-digital converter (TDC). This must be corrected for instances when more than one proton arrives at the TDC since the TDC cannot accept more than one event per trapping cycle. The proton rate has to be corrected for missed protons in the case of multiples [Nico et al., 2005]. The experimentally determined time spectrum from the TDC, N_i^{exp}, is corrected for TDC dead time by using

$$N_i = \frac{N_i^{\text{exp}}}{1 - \frac{\sum_{j=1}^{i-1} N_j^{\text{exp}}}{N_{\text{open}}}}, \tag{4.12}$$

where i and j are time bin numbers. The background is determined in two stages, first, regions I and III are assumed to be equal and are averaged together. The average background

is subtracted from region two and the remaining sum in region two is divided by the live time to give an estimate of the trapped proton rate r_p^{one}. Neutrons may also decay in-flight, which may result in a proton that was not trapped but is detected. The number of in-flight decays per channel is $N_{\text{in-flight}} = r_p^{\text{one}} N_{\text{open}} t_{\text{pc}}$, where t_{pc} is the time bin width. $N_{\text{in-flight}}$ is subtracted from each bin in region III, and then subtracted again from region II to yield r_p^{two}. This rate must also be adjusted because the trap is not trapping for the duration it is open ($\Delta t \approx 100\ \mu$s). The number of missed protons, N_{missed}, is given by $\Delta t r_p^{\text{one}} N_{\text{open}} - N_{\text{in-flight}} C$, where C is the number of time bins in region II and $N_{\text{in-flight}} C$ have already been accounted for above. The final proton rate is then

$$\dot{N}_p = r_p^{\text{two}} + \frac{N_{\text{missed}}}{t_{\text{trap}} N_{\text{open}}}, \tag{4.13}$$

where t_{trap} is the trapping time. In the new measurement, the proton signal waveform will be digitized and multiple proton events can be counted directly which provides a separate check on the analysis using the simpler analog system.

4.3 Error Analysis

4.3.1 Neutron Detector Losses

The 2200 $\text{m}\,\text{s}^{-1}$ equivalent fluence rate is given by

$$\dot{N}_n = \int_A da \int I(v) \frac{v_0}{v} \phi(x, y)\, dv, \tag{4.14}$$

and to first order, the observed α and triton rate is

$$\dot{N}_{\alpha+t} = 2 \frac{\Omega(0,0)}{4\pi} \frac{N_A \bar{\rho} \sigma_0}{A} \dot{N}_n, \tag{4.15}$$

where $\phi(x, y)$ is the areal neutron beam distribution, A is the atomic weight of ^{6}Li, $\bar{\rho}$ is the average areal density of ^{6}Li in the deposit, σ_0 is the ^{6}Li absorption cross section at 2200 $\text{m}\,\text{s}^{-1}$, and $\Omega(0,0)/4\pi$ is the fractional solid angle subtended at the center of the ^{6}Li deposit

Table 4.1: Table of systematic corrections and uncertainties for the 2005 measured lifetime

Source of correction	Correction (s)	Uncertainty (s)
^{6}LiF deposit areal density		2.2
^{6}LiF cross section		1.2
Neutron detector solid angle		1.0
Absorption of neutrons by ^{6}Li	+5.2	0.8
Neutron beam profile and detector solid angle	+1.3	0.1
Neutron beam profile and ^{6}Li deposit shape	-1.7	0.1
Neutron beam halo	-1.0	1.0
Absorption of neutrons by Si substrate	+1.2	0.1
Scattering of neutrons by Si substrate	-0.2	0.5
Trap nonlinearity	-5.3	0.8
Proton backscatter calculation		0.4
Neutron counting dead time	+0.1	0.1
Proton counting statistics		1.2
Neutron counting statistics		0.1
Total	-0.4	3.4

by the detector. More accurately, $\Omega(0,0)$ and $\bar{\rho}$ must be replaced by $\Omega(x,y)$ and $\rho(x,y)$ and neutron attenuation must be taken into account inside the integral. These are decomposed into three additive corrections to the lifetime shown in table 4.1. Before neutrons reach the ^{6}Li deposit, they pass through two perfect crystal silicon wafers. There will be absorption and scattering in these wafers which is also accounted for as additive corrections to the lifetime in table 4.1. The neutron beam has a halo defined as the region outside the area defined by collimation and gives another correction to the lifetime.

4.3.2 Trap Corrections

If the proton trap and magnetic field were perfectly uniform, the end effects L_{end} for each electrode would be the same and equation 4.8 would be a straight line, but reality is nonlinear. A proton created in the end regions where the potential is elevated is trapped with less than unit efficiency. The trap is designed so that L_{end} is approximately equal for all trap lengths, but there are three effects that are involved. A Monte Carlo simulation was used to estimate the magnitude of these effects.

The magnetic field inside the trap is nonuniform, which causes the kinetic energy of the protons to change slowly along the trap. The variation is small enough that all protons created in the grounded region are trapped. However, the magnetic field in the end region for the mirror changes with the trap length.

The neutron beam diverges slightly through the length of the trap, meaning the radial distribution of proton creation locations changes with trap length. Since the electrostatic potential has a slight radial dependence, the trapping probability changes as a function of the trap length.

Each electrode has a nominal length of 18.6 mm and an inner radius of 13 mm. Slight deviations from these lengths manifest as small changes in L_{end} for each trap length.

4.3.3 Proton Detector Losses

The efficiency of the proton detection is less than unity for several well-known effects. Some protons lose all of their energy in the dead layer of the detector and never reach the active layer. There is a discriminator threshold on the detector signal due to noise. Some protons do not deposit their full energy in the detector and fall below the discriminator threshold. Some protons also Rutherford scatter from the detector and are not detected, or are possibly return to strike the detector again.

Determination of the proton detector efficiency is difficult because it requires extrapolation to zero backscattering. The neutron lifetime must be measured at different calculated backscattering functions. In order to change the backscattering function, the accelerating voltage and the detector dead layer thickness and composition are all varied. The calculated backscattering function comes from a Monte Carlo simulation using SRIM, a charged particle code. The backscatter fraction is then varied by changing the thickness of the gold layer on the detector and the accelerating voltage. The measured neutron lifetime at each backscattering function is then fit to a linear function and extrapolated to zero backscattering.

4.4 Alpha-Gamma Device

An absolute counter for thermal and cold neutron beams was designed and built at NIST by Gilliam, Greene, and Lamaze in 1989 [Gilliam et al., 1989]. The purpose of this device is to precisely and accurately calibrate a target foil for use in the neutron monitor for the lifetime measurement. The method is based on counting the prompt gamma rays from neutron capture on boron-10 and is used to calibrate the neutron monitor without reference to the cross section, the areal density of the ^{6}Li deposit, or the solid angle. The system can be calibrated without reference to the ^{10}B sample mass or the ^{10}B cross section. When a neutron captures on ^{10}B, an alpha particle and an excited ^{7}Li nucleus are produced

$$n + {}^{10}\mathrm{B} \rightarrow {}^{7}\mathrm{Li}^{*} + \alpha + 2.789\mathrm{MeV}. \tag{4.16}$$

The excited ^{7}Li emits a 477.6 keV gamma ray with a well-known branching ratio of 0.9372 [Deruytter and Pelfer, 1967][Stelts et al., 1979]. The ^{7}Li nucleus is emitted with a speed of $0.016c$. The excited state lifetime as well as the stopping time in the material are both approximately 0.1 fs, such that the photon can be emitted when the ^{7}Li nucleus β can be anything between 0 and 0.016.

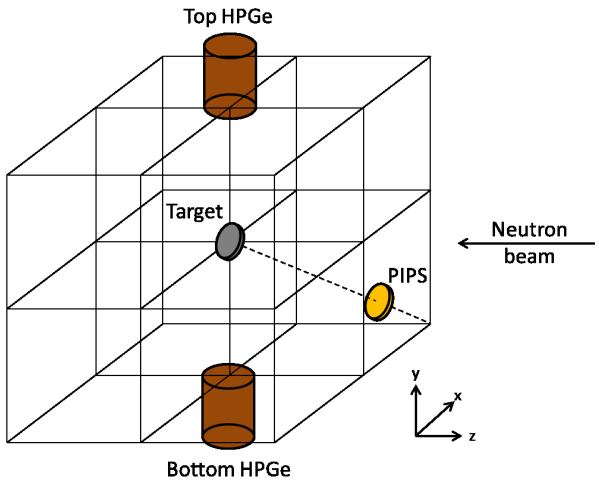

Figure 4.4: Schematic of original alpha-gamma device.

A schematic of the $\alpha - \gamma$ device is shown in figure 4.4, and incorporates two high purity germanium gamma ray detectors (HPGe) and two alpha detectors (PIPS, only one depicted). The gamma counters are positioned on opposite sides of the beam so that the sum of the coincidence counts for either of the two alpha detectors is first order insensitive to β, the speed of the excited ^{7}Li* nucleus. The gamma ray is isotropic in the center of mass system, but is perturbed in the laboratory frame

$$\Phi_{\text{lab}} = \frac{1 - \beta^2}{4\pi(1 + \beta \cos\theta_{\alpha\gamma})^2}, \tag{4.17}$$

where Φ_{lab} is the distribution of coincident α and γ counts. When the alpha counter is located at $\theta_{\alpha\gamma} = \pi/2$ and the sum of the two gamma detectors is used, issues due to the angular correlation and anisotropy due to β are nearly eliminated [Gilliam et al., 1989]. The ^{10}B target is held rigidly in the center of the apparatus with a position reproducibility < 10 μm, which is small relative to the size of the separation between the target and detectors (10 cm). The second alpha counter only has second order sensitivity in the beam centering.

4.4.1 Alpha-Gamma Calibration Technique

The alpha counting is calibrated against a ^{239}Pu alpha source that has an activity known to 0.02%[Denecke et al., 1999]. The ^{239}Pu deposit was prepared on a silicon wafer identical to the thin ^{10}B target. The deposit is placed inside a low solid angle counting stack with a solid angle that is known to better than 0.01% [Gilliam and Yue, 2014]. The disintegration rate of the source is then measured

$$R_{\alpha,\text{Pu}} = \frac{r_{\alpha,\text{stack}}}{\Omega_{\text{stack}}}, \tag{4.18}$$

where $R_{\alpha,\text{Pu}}$ is the activity of the source, $r_{\alpha,\text{stack}}$ is the measured α rate, and Ω_{stack} is the solid angle of the stack.

The ^{239}Pu source is then mounted inside the Alpha-Gamma device and the α rate is measured, $r_{\alpha,\text{Pu}}$. The efficiency of the detector is given by the ratio of this measured rate to

the known rate from the stack

$$\epsilon_\alpha = \frac{r_{\alpha,\mathrm{Pu}}}{R_{\alpha,\mathrm{Pu}}}. \tag{4.19}$$

A thin ^{10}B foil is then mounted in the Alpha-Gamma device in place of the and ^{239}Pu source and a monochromatic neutron beam is incident on the thin foil. The observed alpha rate along with the measured efficiency determine the neutron absorption rate, $r_{n,\mathrm{thin}}$,

$$r_{n,\mathrm{thin}} = \frac{r_\alpha}{\epsilon_\alpha} = r_\alpha \frac{R_{\alpha,\mathrm{Pu}}}{r_{\alpha,\mathrm{Pu}}}, \tag{4.20}$$

assuming that the efficiency for the alpha detector for 5 MeV alphas from ^{239}Pu is the same as for 2 MeV alphas from ^{10}B. This would enter as corrections to the efficiency and has to be modeled. The observed gamma rate is given by

$$r_{\gamma,thin} = \epsilon_\gamma b_\gamma r_{n,\mathrm{thin}}, \tag{4.21}$$

from which the γ detector efficiency can be determined

$$\epsilon_\gamma = \frac{r_{\gamma,\mathrm{thin}} r_{\alpha,Pu}}{b_\gamma r_\alpha R_{\alpha,\mathrm{Pu}}}. \tag{4.22}$$

Finally, the thin ^{10}B target is replaced with a thick ^{10}B that absorbs the entire neutron beam. The observed gamma rate along with the measured gamma efficiency determines the total incident neutron rate

$$r_{\gamma,\mathrm{thick}} = \epsilon_\gamma b_\gamma R_n. \tag{4.23}$$

The $1/v$ fluence monitor using a ^{6}Li foil is operated upstream of the alpha-gamma device simultaneous to the measurement of the total neutron fluence with the alpha-gamma device in order to determine the efficiency of the fluence monitor. Since the absorption in the ^{10}B is $1/v$ (Westcott $g_w = 1.001$ [Pritychenko and Mughabghab, 2012]), the factor of λ_0/λ_{mono} is required. The efficiency of the $\alpha + t$ fluence monitor is given by

$$\epsilon_0 = \frac{r_{\alpha,t}}{r_{\gamma,thick}} \frac{r_{\gamma,thin}}{r_{\alpha,thin}} \frac{r_{\alpha,Pu}}{R_{\alpha,Pu}} \frac{\lambda_0}{\lambda_{mono}}. \tag{4.24}$$

The efficiency of the α+t fluence monitor, along with a correction for wavelength dependence, allows for the determination of the neutron fluence of the white neutron beam for the neutron lifetime measurement without depending on the lithium cross section. This technique has been used to directly measure ϵ_0 to an uncertainty of 0.06%[Yue, 2011], a factor of 5 better than the lithium foil method alone. This corresponds to an uncertainty of approximately 0.5s for the lifetime measurement, and has been used in an improved determination for the neutron lifetime [Yue et al., 2013].

4.5 Proton Counting and Detector

The majority of the 2005 data was taken in the 10 electrode configuration for statistics reasons. It was later found through Monte Carlo simulations that the magnetic field gradient was too large for the 10 electrode configuration and this produced a large correction (5s) to the lifetime [Dewey et al., 2009]. The new experiment will not exceed 9 electrodes in length.

An experiment measuring the radiative decay branching ratio of the neutron used much of the same apparatus as the in-beam lifetime. The surface barrier detector used to detect protons for that experiment had double the surface area of those used in the previous in-beam lifetime experiment. The new measurement will also use larger proton detectors and thus reduce the sensitivity to the alignment of the beam and the beam halo [Dewey et al., 2009].

There was an observed instability issue with the proton trap and detector. The apparatus has a strong magnetic field on the order of 5T, an electric field at the trap of 800V that is moderated at time scales on the order of milliseconds for trap cycles, and an accelerating potential of 30kV at the proton detector. During operation of the experiment, there were sparking or discharge incidents that damaged or degraded the silicon proton detectors. The result was that the leakage current in the detector increased and made decay protons difficult or impossible to detect. This issue will be investigated prior to performing the new measurement by assembling the entire apparatus and operating it without a neutron beam.

The natural extension of the neutron transport model is to use those results as input into a proton tracking model. This model needs to take into account the magnetic and electric

fields in the trap to model the trapping efficiency of the proton trap. The model will also be used to give estimates of the possible beam halo effects at the proton detector location and estimates of the alignment precision required when assembling the apparatus.

4.6 Summary

The goal uncertainty for the new measurement is to reach the 1s level by improving aspects of the previous measurement. Work has begun on a new measurement of the neutron lifetime at NIST using the in-beam technique. The magnet has been cooled down and ramped up near the operating current of 100A and magnetic field of 5T. The data acquisition system code has been written and tested. The Alpha-Gamma apparatus for absolute calibration of the neutron flux apparatus has eliminated the dependence on the neutron cross section and eliminated the most significant uncertainty from the previous measurement. The trap instability problem with the previous measurement will be investigated before installation of the experiment on the beam line. Monte Carlo simulations are currently being used to model the neutron beamline with the goal of producing a collimation scheme for the new experiment. The results will then be used to model the distribution of decay protons in the trap, the trapping efficiency, and the tracking of protons to the proton detector. Table 4.2 shows the projected uncertainty budget along with the 2005 uncertainty budget.

Table 4.2: Projected error budget for the new measurement relative to a nominal value of 880 s

Source of correction	Old Uncertainty (s)	New Uncertainty (s)	Notes
Neutron flux monitor efficiency	2.7	0.5	Alpha-Gamma
Absorption of neutrons by ^{6}Li	0.8	0.8	Thinner ^{6}Li foil
Neutron beam profile and detector solid angle	0.1	0.1	
Neutron beam profile and ^{6}Li deposit shape	0.1	0.1	
Neutron beam halo	1.0	0.1	Larger p-detector, modeling
Absorption of neutrons by Si substrate	0.1	0.1	
Scattering of neutrons by Si substrate	0.5	0.5	New measurement
Trap nonlinearity	0.8	0.1	9 electrodes
Proton backscatter calculation	0.4	0.4	
Neutron counting dead time	0.1	0.1	
Proton counting statistics	1.2	0.5	Longer acquisition, higher n-rate
Neutron counting statistics	0.1	0.1	
Total	3.4	$\sim$1	

Chapter 5

Current Status of the Beam Lifetime Experiment

5.1 Beamline

The design and optimization of the neutron beamline is currently being investigated for the collimation design, with the experiment planned to operate on NG-C in the new NCNR guide hall. The neutron beam halo was a 1s correction to the lifetime for the 2005 result. Protons that reach the proton detector outside the active detector region cause the measured neutron lifetime to be too high and these protons correspond to those produced in the halo region of the neutron beam. The beam halo was measured using a neutron imaging technique using dysprosium. A dysprosium foil is placed in the beam and irradiated for 100s, which turns ^{164}Dy to ^{165}Dy, which beta decays. An imaging film is then placed over the dysprosium foil and the betas from ^{165}Dy causes ionization in the film that can be then read out with a laser probe beam. Less than 0.1% of the neutron beam lies in the halo from these beam images. The image resolution is 100µm per pixel.

Current efforts to understand this beam halo are underway, as well as optimization of the beamline design for a new run of the lifetime experiment. This work is being done in McStas[Lefmann and Nielsen, 1999; Willendrup et al., 2004], a neutron ray-tracing Monte Carlo code. Dysprosium images, from a radiative decay experiment that used much of the

same apparatus as the lifetime, have been compared to Monte Carlo results in order to determine the possible cause of this beam halo.

For the beam collimation design effort, a neutron guide component with a circular cross section had to be written because McStas does not have one. Possible causes for the halo that are being implemented in McStas are surface roughness inside the guide tube, diffuse scattering in the guide tube, and diffuse scattering from collimators. Another possible cause of the beam halo is the method by which images are made and analyzed. The betas from ^{165}Dy decay are approximately 1.2MeV and are emitted isotropically, so the range of electrons in the image plate phosphor layer may cause significant bleeding between pixels. The collimation design as well as the measurement of the beam halo deal in principle with an potential miscounting of protons and this effect must be kept below the 1 s level for the lifetime experiment.

5.2 Beam Halo and Dysprosium Image Method

The neutron beam is imaged using a method to transfer a neutron image to data that lowly humans can interpret. First, a dysprosium foil is mounted in the neutron beam and the beam is turned on. Natural dysprosium is 2.3% ^{160}Dy, 19% ^{161}Dy, 25.5% ^{162}Dy, 24.9% ^{163}Dy, 28.1% ^{165}Dy, and trace amounts ^{156}Dy and ^{158}Dy. Natural dysprosium has a capture cross section of 994 barns and a scattering cross section of 90 barns, and the most absorbent isotopes are ^{161}Dy and ^{164}Dy at 600 and 2840 barns respectively. The ground state of ^{165}Dy has a half life of 2.334 hours and decays by beta emission to ^{165}Ho with an end point energy of approximately 1.2 MeV, there is also a shorter, 1.25 minute decay from ^{165m}Dy to either the ground state ($b = 0.9776$) or by beta emission to ^{165}Ho ($b = 0.0224$). Typical exposure times for the foil in the beam are from 1 minute up to 10 minutes, in order to sufficiently activate dysprosium for transferring to the image plate without being a radiation hazard. The typical dysprosium foil used for this is 25 microns thick.

The activated dysprosium is then mounted inside a cassette along with an image plate and the image plate is exposed to the foil for a few minutes. Betas from the decay of ^{165}Dy ionize the active phosphor layer of the image plate, storing the image for later reading by the image

reader via photo-stimulated luminescence (PSL). The typical composition of the images plates is a protective plastic layer ($\approx 11\mu m$), the phosphor layer ($\approx 140\mu m$), and a support layer ($\approx 300\mu m$), all measurements are for a BAS-III image plate via reference [Taniguchi et al., 1998].

There are artifacts that show up in the resulting PSL data from the image reader. For instance, there is the "galaxy effect", where an image is smeared out along the direction in which the plate is read (figure 5.4). This smearing is purely an artifact of the reader and is not associated with the dysprosium at all. There can also be some blurring of the image due to the isotropic betas from ^{165}Dy if there is a large enough separation between the foil and the phosphor layer of the image plate. In order to properly measure the beam halo, artifacts related to the image reading process have to be separated from any physical neutron beam halo.

5.2.1 Modeling

Early modeling in McStas with partially absorbing collimators, collimators that scatter part of the beam, and a guide tube with a rough surface does not produce a halo in the beam. Anything upstream of the final beam element cannot produce anything outside the line of sight that one would draw for an "ideal" system.

The next step in the model is to assume that there is no beam halo and then use MCNPX to model the response of the dysprosium to neutrons and subsequently the response of the phosphor layer to betas. The neutron profile as a function of depth in the dysprosium was assumed to be constant and the intensity was scaled by an exponential decay due to absorption bypassing an MCNPX calculation step to determine this depth function. The resulting function was used to create a 3-dimensional beta emission source inside a slab of dysprosium and placed above a model of the image plate with the layer thicknesses shown above. The electron energy spectrum is shown in figure 5.1.

The response of an image plate to various particles and energies was found to be proportional to the stopping power of the image plate material [Taniguchi et al., 1998; Tanaka et al., 2005], which implies that an MCNPX model of the energy deposition in the phospher layer should provide a good approximation of the resulting PSL image of the configuration.

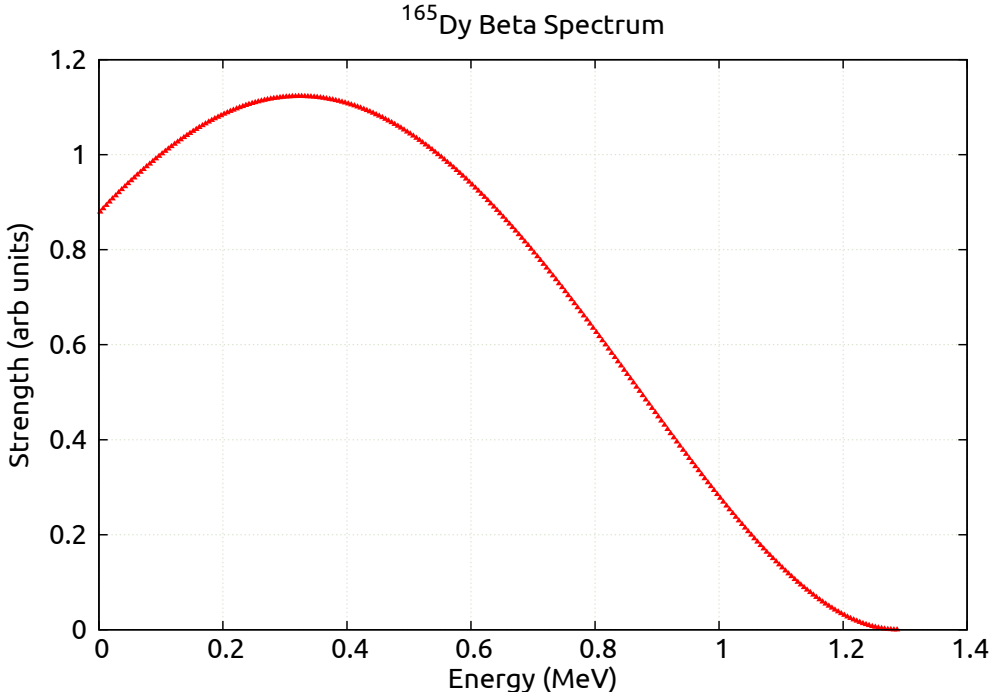

Figure 5.1: Dysprosium beta decay energy spectrum.

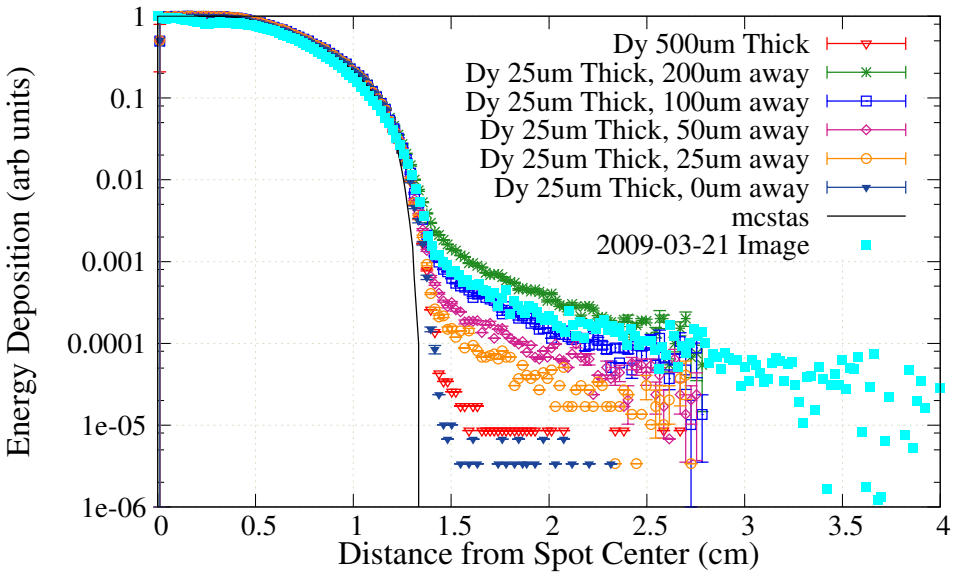

Figure 5.2: Dysprosium beta energy deposition in an image plate as a function of radius from center.

This electron source was then used to model the response of the image plate to betas as a function of the separation between the dysprosium and the image plate and the thickness of the dysprosium foil. The result is shown in figure 5.2. The McStas profile is shown in

yellow and has a hard cut off and no halo. The cyan is the result of an actual image taken in March, 2009, with the background subtracted by eye. The red triangles show a 500 micron thick piece of dysprosium in contact with the image plate, and there is not much of a halo produced. If the betas produce the halo, it instead must be via a separation between the image plate and the dysprosium rather than a thick piece of dysprosium in contact with the plate. The other points show a 25 micron thick piece of dysprosium at various heights above the image plate. The agreement is quite good for a separation of approximately 100 microns. Other blurring effects may occur, such as backscattering from the backing layer within the image plate, and the separation serves as a proxy for these effects.

5.2.2 Results from Cadmium Masks

Data were taken as part of the previous lifetime measurement with cadmium masks placed in front of the dysprosium in order to produce a hard edge in the dysprosium activation and to investigate the artifacts produced by the dysprosium method and the reader. Unfortunately, much of the documentation that was associated with this exercise is not in any of logbooks. The results from two of these images on both linear and log scales is shown in figure 5.3 and 5.4. Each image in these two figures has axes of pixels and the color axis is the converted value of the intensity. Each pixel is 100 microns square.

The image Cd2Dy10min was made by exposing the image plate to the dysprosium shortly after having been in the beam and the image S004Cd10 had a waiting period of 24 hours between exposing the dysprosium to exposing the image plate. Cd2Dy10min is extremely blurred on the log scale and shows significant galaxy effects in the up-down direction as well as an asymmetry left-right for the rectangle. However, S004Cd10 has no blurring to speak of and very little galaxy effect in the up-down direction if one zooms in. S004Cd10 appears to have a hard cut off at the edge of these shapes, while Cd2Dy10min does not.

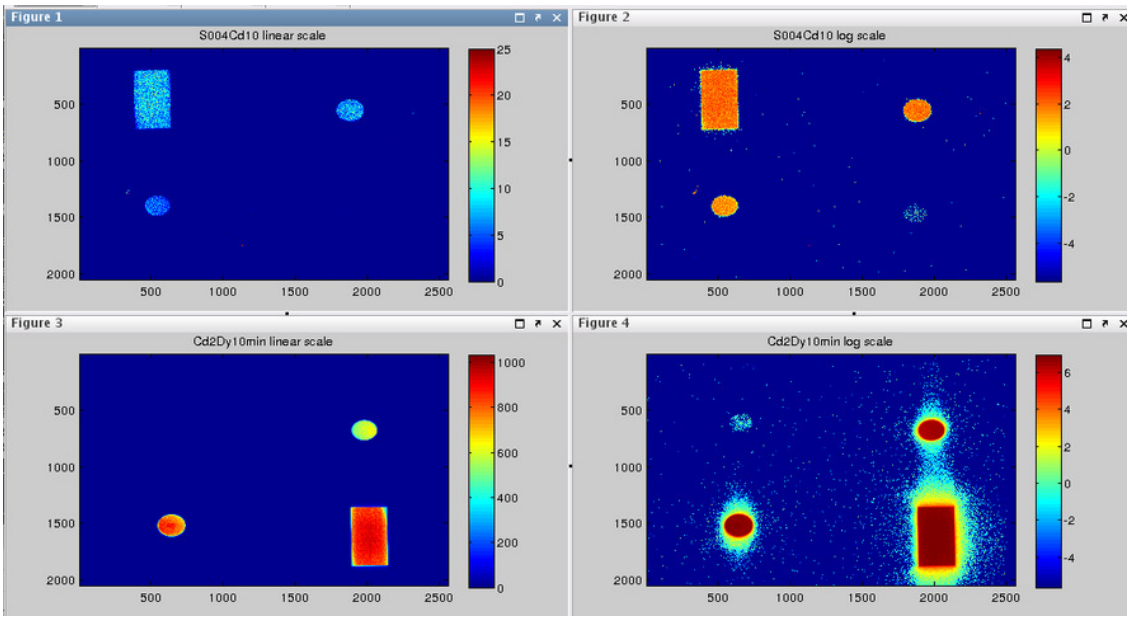

Figure 5.3: Cadmium mask results: top two taken 24 hours after exposure to the beam in linear (left) and logarithmic (right) scales; bottom two taken shortly after exposure to the beam in linear (left) and logarithmic (right) scales.

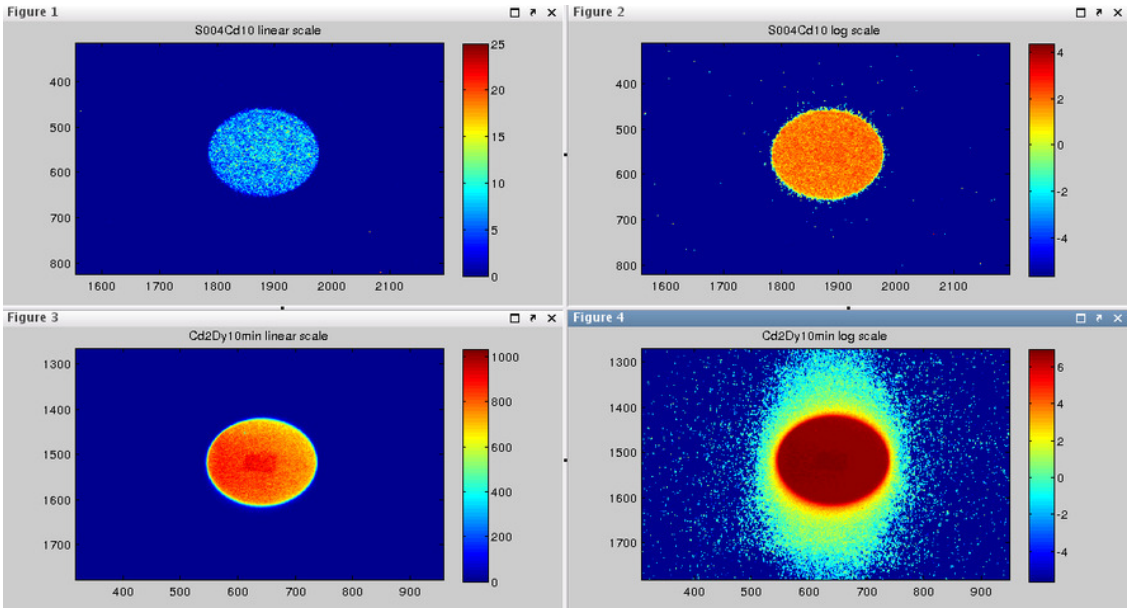

Figure 5.4: Cadmium mask results zoomed in on top right circle (bottom left circle) for S004Cd10.img (Cd2Dy10min.img) from figure 5.3.

Recent tests have been performed with new cadmium masks in both circular and straight edge shapes. Dysprosium was exposed to the neutron beam with a straight edge mask in place in front of the dysprosium. The image plates were then exposed to the dysprosium

for 15 minutes twice, rotating the dysprosium by 90 degrees each time in order to test the galaxy effect. The result is a dramatic difference between the parallel and perpendicular directions visually, figures 5.5 and 5.6, and there is approximately a 4 mm galaxy effect when comparing slices through the two images 5.7. A circular mask was also imaged with the dysprosium method and using a gadolinium oxide (gadox) neutron camera (fig. 5.8) and it clearly shows that there is a significant signal outside the 5 mm cutoff radius of the mask in the dysprosium image that is not present in the gadox image.

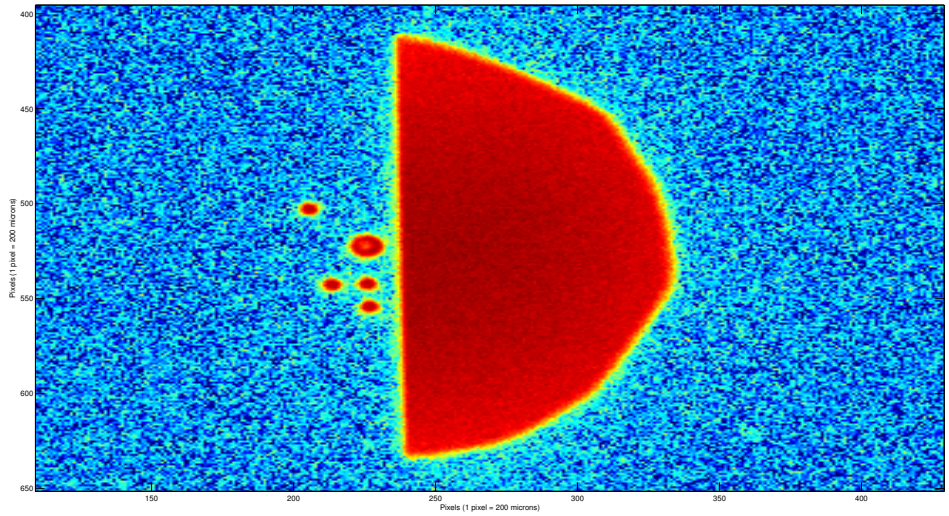

Figure 5.5: Cadmium mask with a straight edge read by image reader with edge parallel to reading direction.

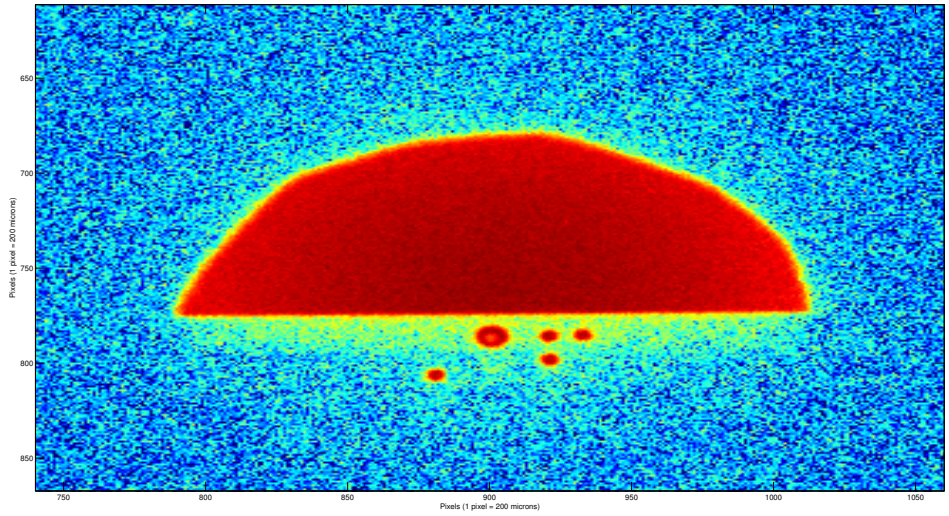

Figure 5.6: Cadmium mask with a straight edge read by image reader with edge perpendicular to reading direction.

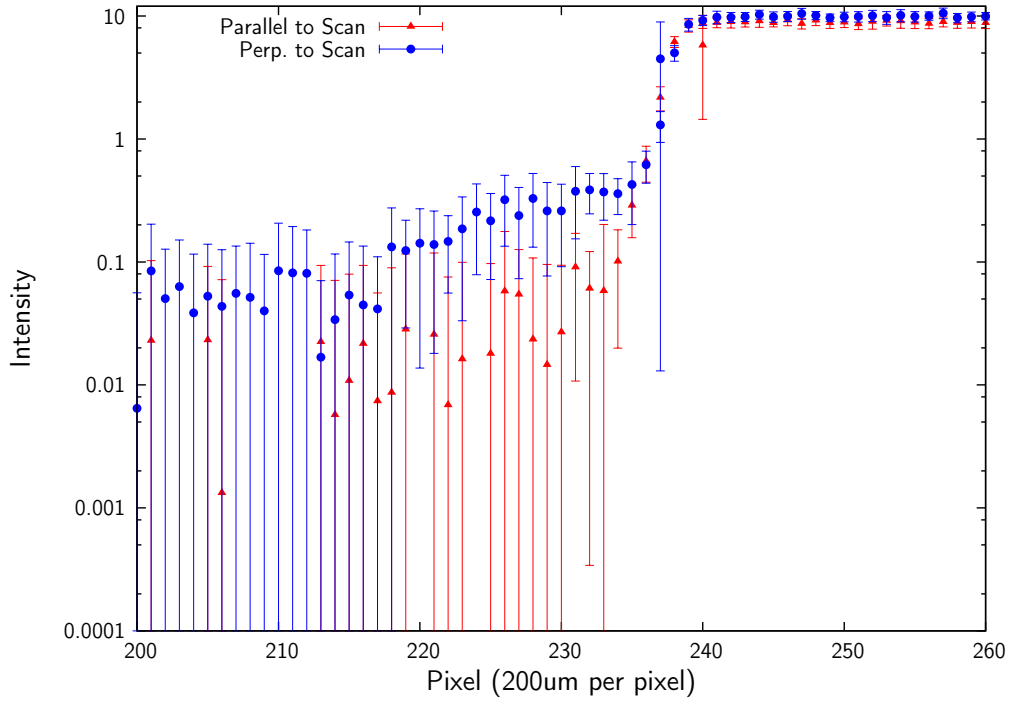

Figure 5.7: Comparison of the image profiles for slices through the straight edge images in figures 5.6 and 5.5, where error bars are from averaging over multiple pixel slices through each image.

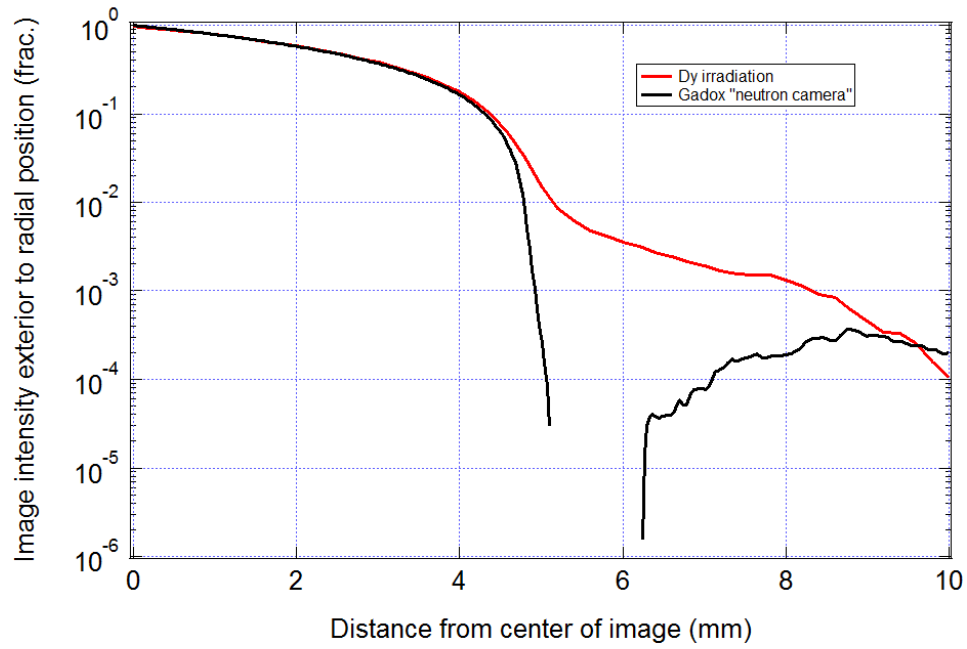

Figure 5.8: Comparison between a 5mm radius cadmium mask imaged with the dysprosium image method and taken with a Gadox camera.

5.2.3 Conclusion

The lack of blooming for the images in figure 5.4 suggests that there must not be a separation between the image plate and the dysprosium during the exposure process. The effect due to betas would be present as long as there is a separation, regardless of how long the dysprosium has been decaying. So, the betas are likely not the culprit. The long waiting period nearly eliminates the galaxy effect, which indicates that the blurring effect is dependent upon the intensity of the image. In the previous lifetime experiment, this method of varying the intensity (by waiting or by short exposures) was used in order to extrapolate the halo. While the previous results using cadmium masks are potentially very illuminating, the documentation for these cadmium images seems to be missing. The more recent images taken in 2014 on NG-6m were rather illuminating and, when combined with the gadox camera measurement, strongly suggest that the beam halo is an artifact of the dysprosium image method.

There is a path forward for handling the determination of the beam halo. The beam halo represents an estimation of the neutron beam that projects onto a non-active region of a 300 mm^2 proton detector. This is not the case if a larger 600 mm^2 proton detector, since a detector of this size is larger in diameter than the inner bore of the trap electrodes and these larger area detectors will be used as part of the neutron lifetime experiment. Furthermore, spare collimators will be manufactured in order to run with a smaller neutron beam.

The collimation system design effort can proceed with beam simulations using 300 mm^2 as the defining beam size without having to worry about lost protons as a result of the neutron halo assuming that the apparatus is aligned properly. With this assumption, 9 mm will be the defining beam radius at the exit of the trap, which was taken to be 1 m from the end of the last beam element. The beam halo issue will also be addressed by performing measurements on the beamline with varying beam sizes as well as a larger proton detector size. Since the beam halo is a proton loss mechanism, if these measurements agree they will give confidence that protons are not being lost due to a beam halo.

5.3 Collimation System Design

McStas is used for simulations for the design and optimization of the collimation system for the new beam lifetime measurement in order to maximize the proton count rate given the physical constraints of the experiment footprint and beam size. Five different designs have been simulated, a system with a circular quartz guide tube only, a system with 2 collimators only, and a system with 2 collimators defining the beam geometrically followed by a circular quartz guide tube with three different guide tube penetration distances into the bore. The collimation system for the previous measurement was also simulated. The beam defining elements involved are a collimator at the exit of the guide (C_1), a collimator several meters downstream (C_2), a fused quartz guide tube approximately 1 m long immediately following C_2 (or the full length of the neutron flight). The beam must then be smaller than the trap (R=13 mm), the neutron monitor deposit (R=19 mm), and the proton detector (R=9.77 mm). For all simulations, the size of the neutron beam at the exit of the trap was restricted to 9 mm, and the position of the end of the trap was taken to be 1 m from the last beam component.

5.3.1 Implementation in McStas

McStas has a library of components for use in instrument models, including guides. There are a number of types of guides implemented already, but none of them have a circular cross section. The source code for the simplest rectangular guide was modified in order to create a guide component with a circular cross section.

McStas traces each particle history through the components in the model by calculating intersection times between the particle and the component and propagating to that time. For each scatter, the intersection between the line

$$\vec{r} = \vec{r_0} + \vec{v}t, \tag{5.1}$$

and the circle

$$dR^2 = |\vec{r}|^2, \tag{5.2}$$

has to be calculated, while neglecting the $\hat{\mathbf{z}}$ coordinate (along the beam) and velocity since the cylinder is not tapered. This simplifies to a quadratic equation in time

$$t^2(v_x^2 + v_y^2) + t(2v_x x_0 + 2v_y y_0) - r^2 + x_0^2 + y_0^2 = 0. \tag{5.3}$$

However, there can be a catastrophic cancellation when using the quadratic formula in a computer. So, the intersection times are calculated as follows for a general quadratic of the form $ax^2 + bx + c = 0$:

$$x_1 = \frac{-b - sgn(b)\sqrt{b^2 - 4ac}}{2a}, \tag{5.4}$$

$$x_2 = \frac{2c}{-b - sgn(b)\sqrt{b^2 - 4ac}}, \tag{5.5}$$

where $sgn(b)$ is the sign of the b term. Since rounding error can result in either 2 positive roots, a positive and a zero root, or a positive and a negative root, the greatest of the two roots is taken to be the next intersection of the cylinder. If the intersection point is beyond the end of the guide, the loop is broken and the particle leaves the guide, otherwise the particle is propagated to its new intersection point. The normal to the surface at the intersection point is simply $\vec{n} = (-x, -y, 0)$. The outgoing vector is then given by

$$\vec{v_f} = \vec{v_i} - \frac{(\vec{n} \cdot \vec{v_i})}{|\vec{n}|^2}\vec{n}, \tag{5.6}$$

and the momentum transfer is

$$q = K\frac{|\vec{n} \cdot \vec{v}|}{\sqrt{|\vec{n}|^2}}. \tag{5.7}$$

The momentum transfer is then sent to a function built into McStas which returns either a given value (0.99 for this case if q is less than the critical momentum transfer Q_c, or a number that quickly dies off above Q_c). This value is then used to adjust the particle weight at each bounce.

Natural nickel has a scattering length of 10.3 fm and a density of 8.9 g/cm^3, which results in an effective potential of

$$V_{\text{eff}} = \frac{2\pi\hbar^2 Nb}{m_{\text{n}}} \approx 250 \text{ neV}, \tag{5.8}$$

and a critical angle of

$$\theta_c = \lambda\sqrt{\frac{Nb}{\pi}} \approx 1.74 \text{ mrad Å}^{-1} \approx 0.1^\circ\text{Å}^{-1}. \tag{5.9}$$

Quartz (SiO_2) has a scattering length of 15.713 fm (4.107 for Si and 5.803 for O), and a density of approximately 2.2 g/cm^3. The resulting effective potential is

$$V_{\text{eff}} = \frac{2\pi\hbar^2 Nb}{m_n} \approx 90 \text{ neV}, \tag{5.10}$$

and a critical angle of

$$\theta_c = \lambda\sqrt{\frac{Nb}{\pi}} \approx 1.05 \text{ mrad Å}^{-1} \approx 0.06^\circ\text{Å}^{-1}. \tag{5.11}$$

Therefore, the quartz guide tube component used in McStas will use m=0.6, with $m = 1$ corresponding to nickel. Internal to McStas, this corresponds to m=1.0 with a critical momentum transfer of 0.6 times that of nickel.

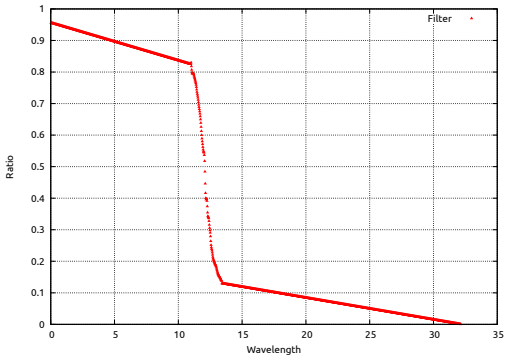

Figure 5.9: Transmission ratio as a function of wavelength in Å for the long wavelength filter.

A filter is in place in the simulation that adjusts the neutron intensity at the exit of the NG-C guide corresponding to the long wavelength filter. The functional form of this was roughly mapped out from the paper[Høghøj et al., 2000]. Images of the beam cross section are taken at the entrance of the trap (0.6 m from the last component), the exit of the trap (0.35 m from the entrance), and at the neutron monitor position (0.83 m from the exit of the

trap). These monitors take the neutron flux integrated over the area (neutrons per second) and scale it by the neutron velocity such that the output has units of neutrons per meter.

5.3.2 A - Quartz Guide Tube

The circular quartz tube has the advantage that it will provide a much higher flux beam to the experiment compared to a simple two collimator system. However, using a circular tube alone allows for the propagation of Garland reflected neutrons through the tube (Fig. 5.10), which skim the internal surface of the guide and emerge as highly divergent neutrons (Fig. 5.11). The $m = 0.6$ guide will also propagate neutrons that are likely too divergent for the constraints of the lifetime experiment, since the neutron beam emitted from the end of a quartz tube will expand in radius by 6 mm per meter of flight and the major constraining component in our experiment is the radius of the proton detector.

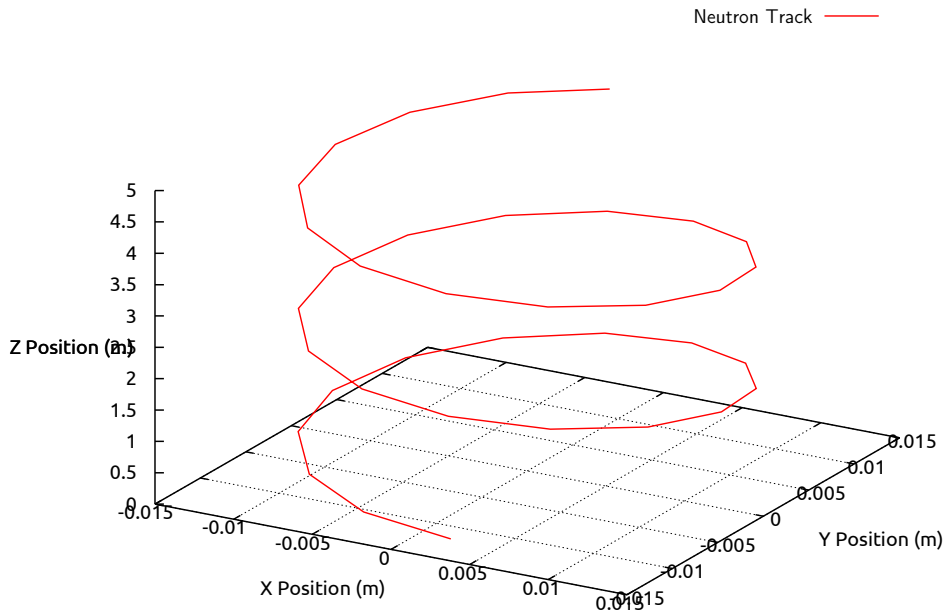

Figure 5.10: Garland reflections inside a 5 m long, 1.27 cm radius m=0.6 circular guide tube, which shows that neutrons can skim the surface inside a circular tube resulting in a highly divergent beam at the end of the tube.

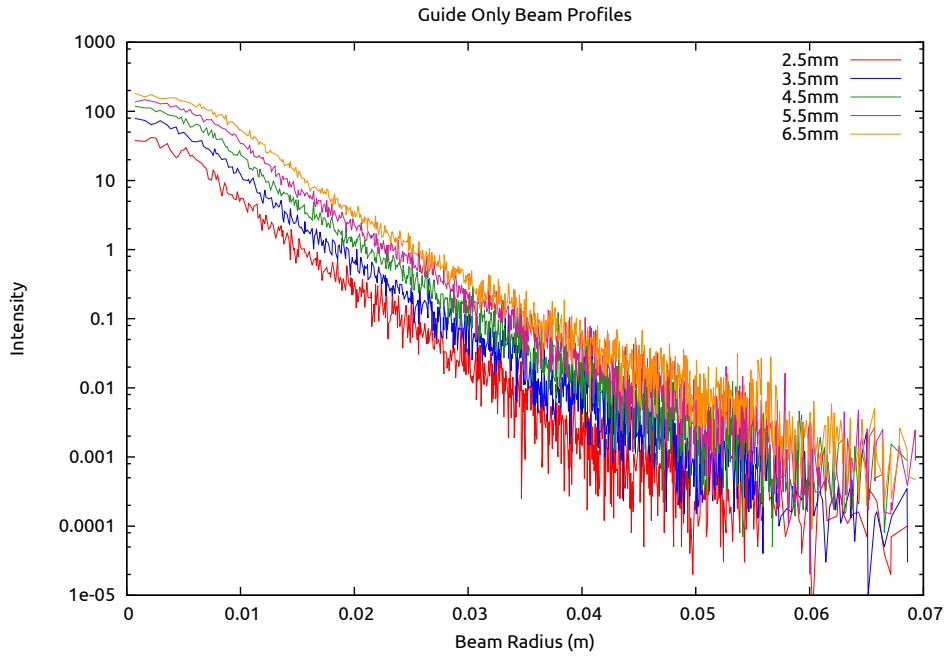

Figure 5.11: Beam profiles at the trap exit for a 5 m pyrex tube as a function of tube radius (legend).

5.3.3 B - Two Collimators Only

The two collimator configuration has the advantage that the size of the beam is geometrically defined, but there is a significant loss in flux compared to the guide tube only configuration. In this configuration, the size of the first collimator, C_1, the position of the second collimator, C_2, and the limiting beam size (9 mm, 1 m from C_2) are used to determine the size of C_2. These parameters are then varied in order to maximize the most relevant quantity to the lifetime experiment, the average number of neutrons in the trap. The right vertical axis (Fig. 5.12) also shows the expected number of neutron decays per second, and is the left axis is an estimate of the proton rate

$$\dot{N}_p = \frac{N_n L}{\tau_n}, \tag{5.12}$$

where N_n is the number of neutrons per meter, L is the length of the trap in meters, and the neutron lifetime is taken to be ≈ 880 s. The corresponding C_2 sizes are shown in figure 5.13.

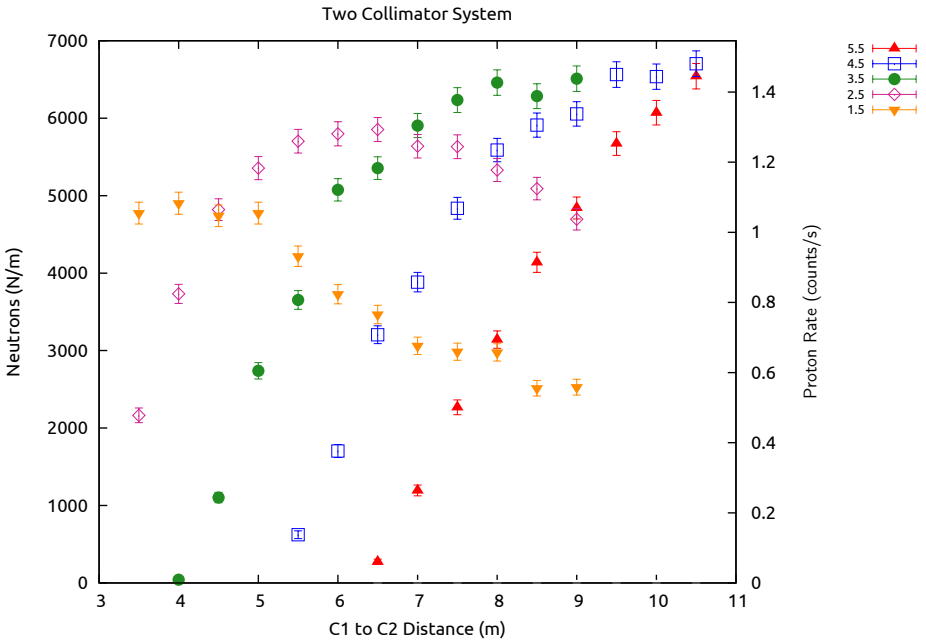

Figure 5.12: Average number of neutrons in the trap for a two collimator setup as a function of the distance between C_1 and C_2 for varying C_1 radius (in cm in the legend).

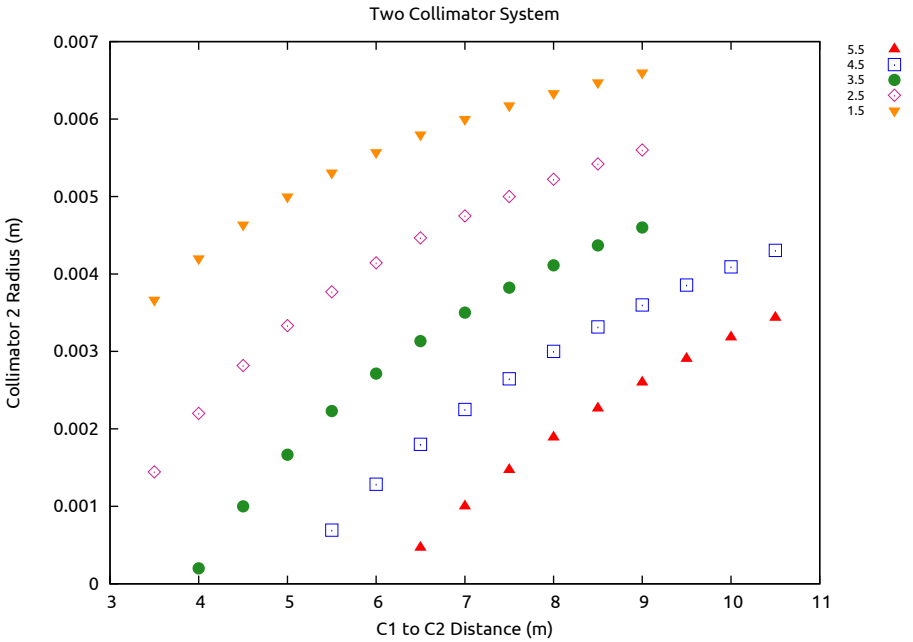

Figure 5.13: C_2 radius as a function of the separation between C_1 and C_2 for different C_1 sizes (in cm in the legend).

5.3.4 C - Two Collimators Followed by a Guide Tube

The collimator plus guide configuration allows us to move the final vacuum entrance window farther away from the trap as well as allowing us to move the exit of the guide tube closer to the trap. This second factor was not taken into account for the current simulations, but it could allow for shortening the distance between the final beam component and the 9 mm limiting factor in the beam size which would permit a slightly larger beam. Results for this configuration are shown in figure 5.14, the beam profiles at the trap exit are shown in figure 5.15, and the C_2 radius is shown in figure 5.16. The length of the guide tube is 1 m. There is not a significant difference in rate between the 2 collimator system and the 2 collimator plus guide system. It may be possible to increase the rate with the hybrid system because it allows moving the end of the guide tube closer to the trap by 20 cm.

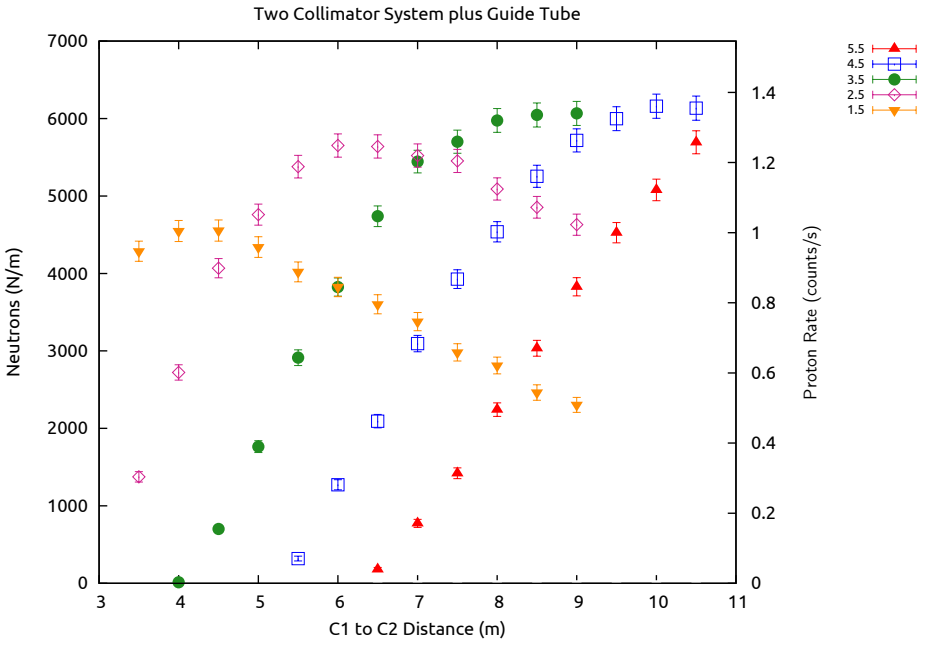

Figure 5.14: Average number of neutrons in the trap for a two collimator setup plus a neutron guide tube beyond C_2 as a function of the distance between C_1 and C_2 for varying C_1 radius (in cm in the legend).

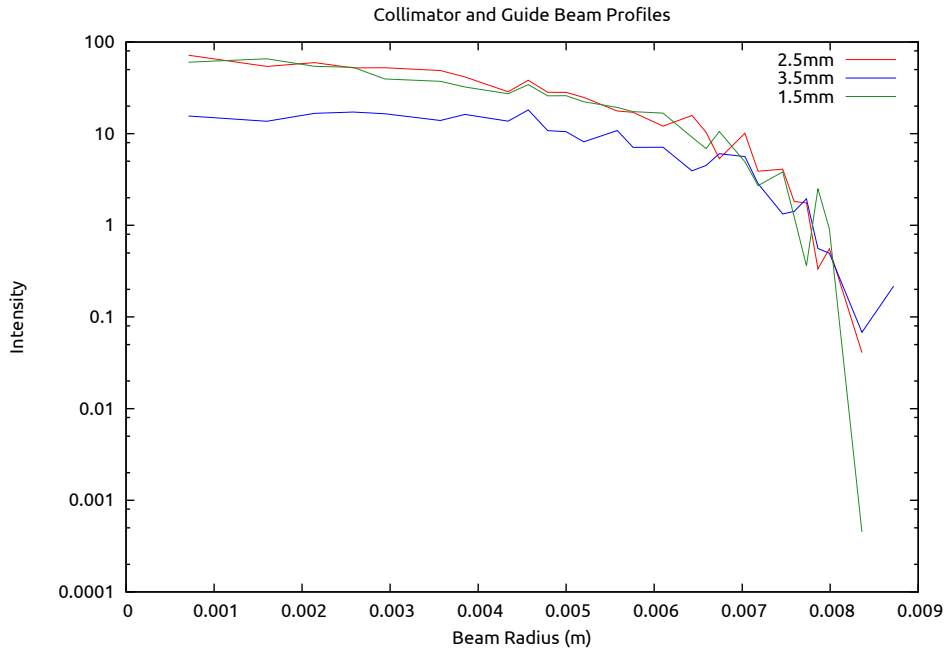

Figure 5.15: Beam profiles at the trap exit for a 1 m pyrex tube following 2 collimators as a function of tube radius (legend). In all three cases, there is a 5 m gap between C_1 and C_2.

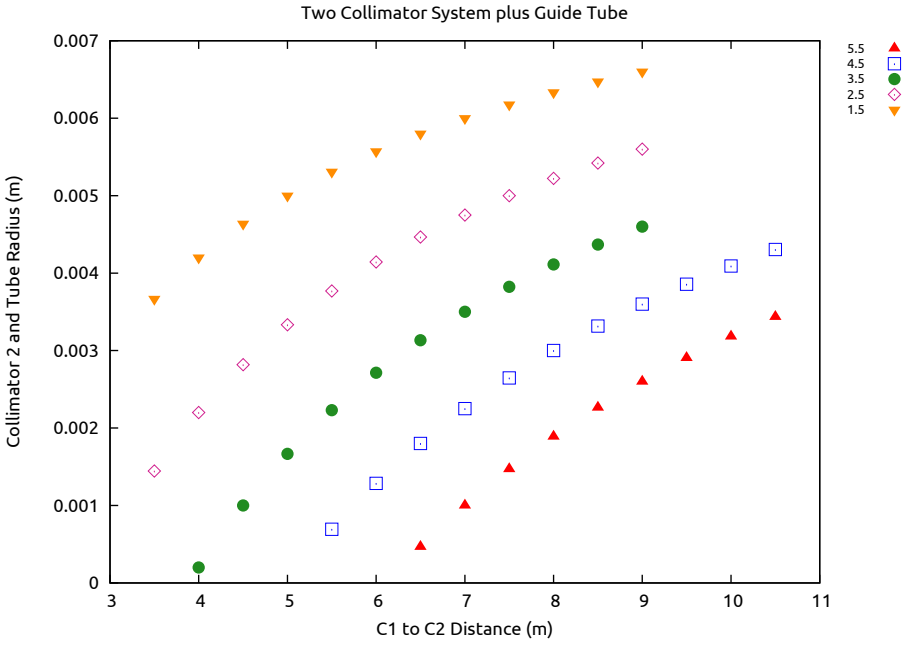

Figure 5.16: C_2 and guide tube radius as a function of the separation between C_1 and C_2 for different C_1 sizes (in cm in the legend).

5.3.5 D - Two Collimators Followed by a Guide Tube - 10 cm into bore

The long wavelength filter is not necessary if the beam is defined geometrically by collimators. Since the guide tube can reach into the magnet bore, the position of the trap relative to the end of the guide tube can be decreased. In this case, the end of the guide tube was 80 cm from the end of the trap. Figure 5.18 shows the beam profile at the trap exit and figure 5.17 shows the number of neutrons in the trap and the expected proton rate. The length of the guide tube is 1 m.

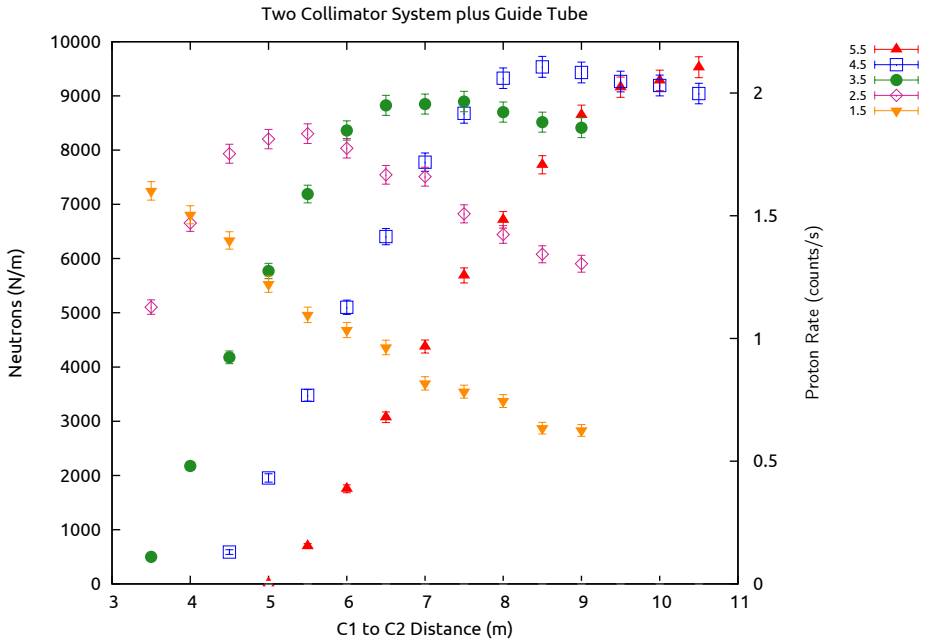

Figure 5.17: Average number of neutrons in the trap for a two collimator setup plus a neutron guide tube beyond C_2 as a function of the distance between C_1 and C_2 for varying C_1 radius (in cm in the legend).

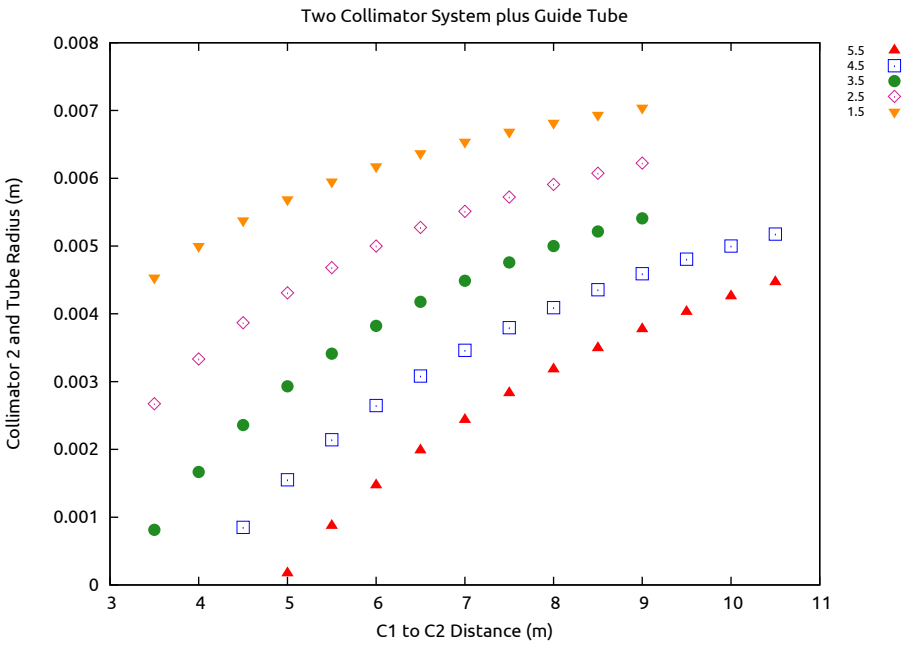

Figure 5.18: C_2 and guide tube radius as a function of the separation between C_1 and C_2 for different C_1 sizes (in cm in the legend).

5.3.6 E - Two Collimators Followed by a Guide Tube - 25 cm into bore

Based on drawings from the previous run of the experiment, the guide tube actually extended 25 cm into the bore from the outside face of the magnet. The upstream flange of the trap is 50 cm from the outside face of the magnet, which puts the downstream end of the trap about 90 cm from the face of the magnet. The result is that the requirement that the beam be less than 9 mm in radius at the exit of the trap is actually about 65 cm from the end of the guide tube, rather than 80 cm from case D or 100 cm in case C. The length of the guide tube is 1 m.

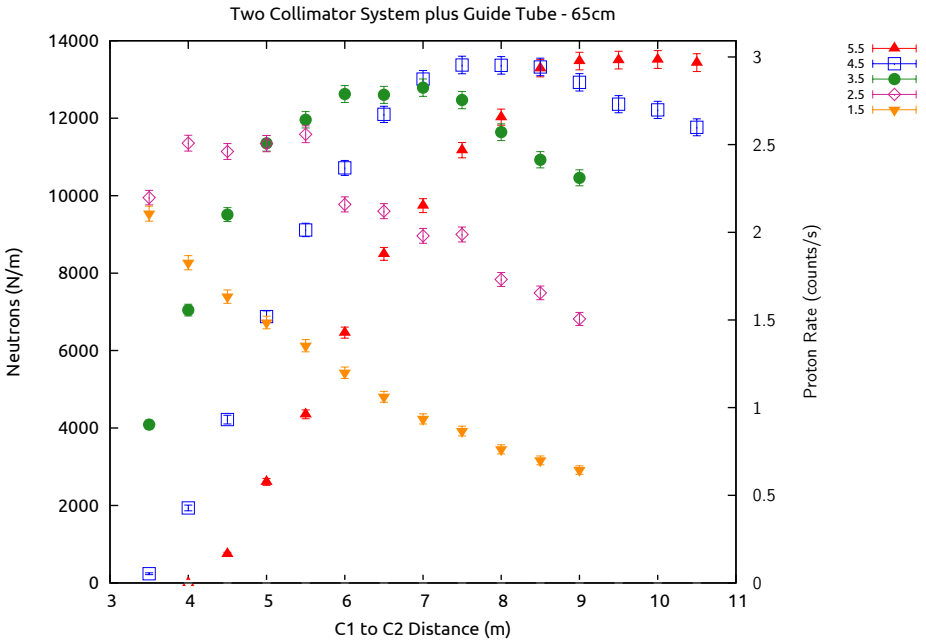

Figure 5.19: Average number of neutrons in the trap for a two collimator setup plus a neutron guide tube beyond C_2 as a function of the distance between C_1 and C_2 for varying C_1 radius (in cm in the legend).

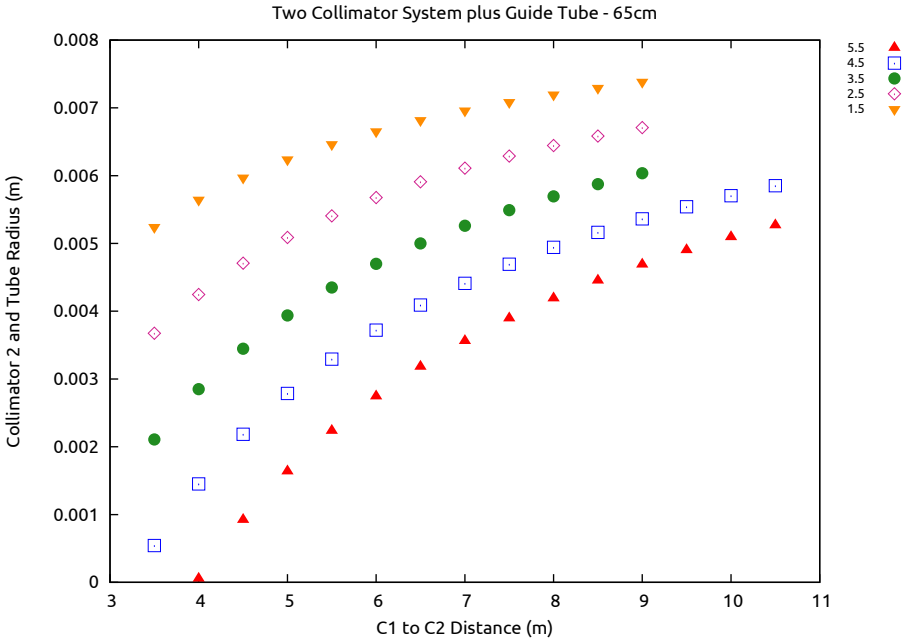

Figure 5.20: C_2 and guide tube radius as a function of the separation between C_1 and C_2 for different C_1 sizes (in cm in the legend).

5.3.7 F - Previous Run Collimation System

The previous run on NG-6 used a collimation system that is slightly different from what is being considered for the NG-C run. First, there was a LiF glass collimator at the guide with a radius of 3 cm. Then a collimator position (C_1) that was 0.9176 m from the LiF glass for which there were 3 interchangeable collimators with radii of A=0.015875 cm, B=0.022225 cm, and C=0.0254 cm. The next collimator (C_2) was 4.9065 m from C_1 and had a radius of 4.19 mm. C_2 is followed by a coated "preguide" with $m \approx 1$, a length of 1.0 m, and a radius of 4.25 mm. There is another collimator following the "preguide" with a radius of 3.5 mm, and it is followed by a quartz guide tube with a radius of 3.75 mm, a length of 0.9 m, and $m \approx 0.6$ (from above). The upstream end of the trap was 25 cm from the end of this tube. The number of neutrons per meter for these configurations plugged into NG-C is A=2357.23, B=4438.51, and C=5452.07. These correspond to proton counts per second for a 9 electrode trap length of A=0.52, B=0.98, and C=1.20.

5.3.8 Conclusions

The maximum physical length of the collimation system is approximately 5.75 m, which is used to estimate the maximum proton rate from the beamline configurations above. The peak proton rate expected based on configurations B or C is approximately 1.3 Hz and approximately 1.75 Hz from configuration D, which is considerably lower than the ≈4 Hz for the previous run of the experiment. This seems to imply that the increased flux at NG-C does not benefit the lifetime experiment because that increased flux is focused and highly divergent due to the curved guide configuration of NG-C.

The predicted optimal configuration from simulation sets B and C is a C_1 radius of 2.5 cm, a C_2 radius of 0.4 cm approximately 6 m from C_1, and a guide tube with a radius of 0.4 cm. Since the use of the guide tube alone is not possible and the beam is being defined geometrically, the long wavelength filter can be removed from the beam and in order to increase the number of neutrons in the trap as well as move the trap closer to the end of the guide tube (configuration D). This configuration has an optimum length slightly longer than B or C with slightly larger C_1 and C_2.

5.4 Data Acquisition System

The data acquisition system (DAQ) consists of three primary sections: the GaGe 1250X CompuScope digitizer card, the CAMAC ADC/TDC and timing system, and the slow monitoring data. The GaGe card digitizes the output of an amplifier. The CAMAC system records pulse heights and arrival times. A schematic of the DAQ is shown in figure C.7. For the previous measurement, the DAQ used a TDC, an ADC, and a histogramming memory module to record the proton detector signal energy and arrival time. This setup was not able to detect multiple protons due to the inability of the TDC to detect and record multiple stop signals. Instead, data was corrected after the fact using an analytic formula for expected multiple triggers within the data acquisition time window.

The new DAQ fully digitizes the proton waveforms for the duration of the trap open period allowing for the possible detection of multiple protons as well as investigation of backgrounds. The digitization uses a 2 channel GaGe card. There are plans to replicate the older CAMAC DAQ and run it in parallel to the new digitizing DAQ. The DAQ code was written entirely in LabWindows CVI using the C programming language.

5.4.1 CAMAC DAQ and Timing System

A Kinetic Systems 3655 timing generator CAMAC module is used to control the trap and detector timing. The 3655 has a crystal clock and the input frequency is tunable in decades from 1 Hz to 1 MHz. The module is set with a 1 MHz frequency and uses 5 output channels with varying delays between pulses. These pulses drive home-built NIM modules that produce outputs corresponding to the 5 main timing signals of the experiment: alpha detector on, proton detector on, trap ramp on, trap door open, and trap mirror open. A trapping cycle has a variable length that is specified in the data acquisition system at run time, with a typical length of 10 ms. When a data acquisition run begins, the alpha counting electronics are gated on and these counters are enabled for the duration of the run. The trap cycles in a pattern in which the trap is in trapping mode for 10 ms with the door and mirror at +800V and the central trapping electrodes grounded, followed by a short period in which the trap voltages are modulated to flush protons out of the trap to the detector.

Timing is as follows, with t=0 corresponding to the end of a trapping period: 0μs proton detector is gated on in ADC and GaGe card, t=21μs door is grounded and ramp applied to trapping region, t=97μs ramp is maintained and the mirror is grounded, t=127μs mirror and door are raised to +800V and the ramp is grounded, t=160μs proton detector is gated off and a new trapping cycle begins. Figure 5.21 depicts these signals, which repeat every trap cycle.

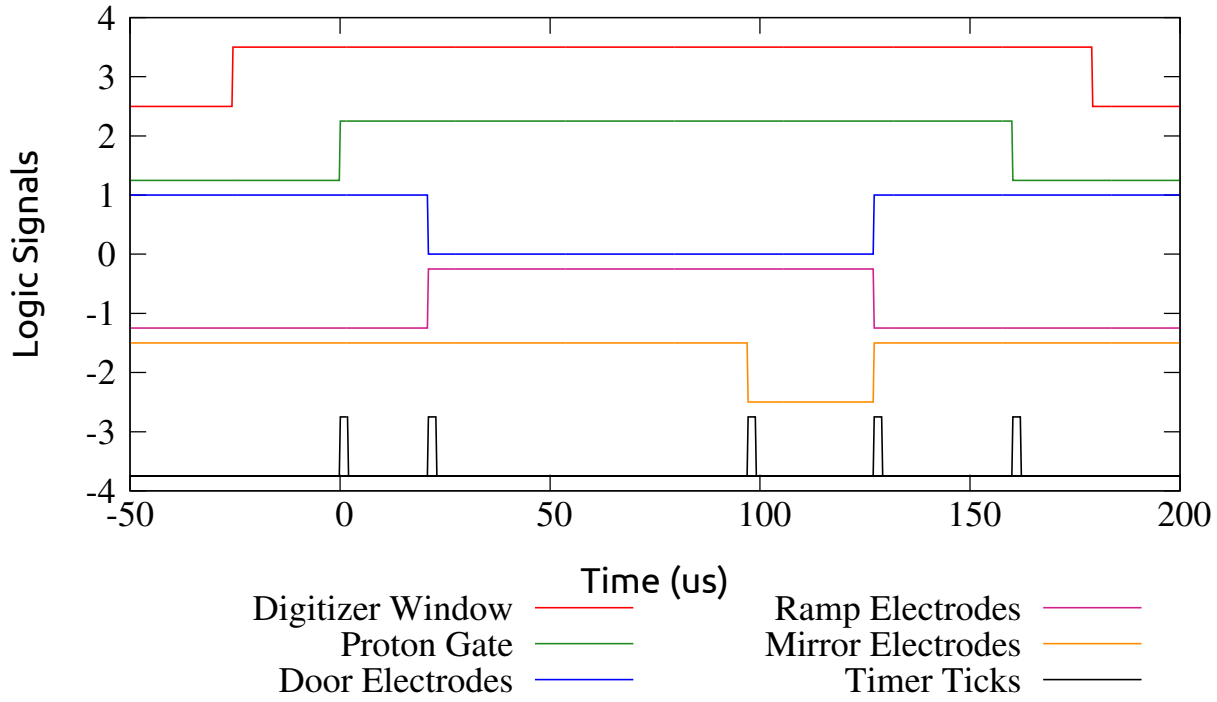

Figure 5.21: Timer triggers and gates for the proton detector and trap voltage levels. This timing sequence repeats every trap cycle, which is nominally 10 ms in duration.

The proton detector gate signal triggers the start of the LeCroy 4204 TDC and gates the LeCroy 3512 ADC. A Kinetic Systems 3063 module controls signals that are always high during running and always low when a run is stopped, in order to set the flipflops inside home-made NIM modules that produce gate signals for the electronics and trap. The alpha detector gate signal is on for the entirety of a run, and the alpha counting electronics counts for the duration of the run. The mirror, door, and ramp timing signals are used as gates for Directed Energy switches for controlling the trap voltages. Two of these switches switch between +800 V and ≈-3 V, and the third applies the high end of the ramp potential between

+20 V and 0 V. The +800 V potential is supplied by an Ortec 556 High Voltage Supply, capable of supplying up to 3000 V at 10 mA. Such high power output is required in order to maintain fast switching between ≈-3 and +800 V in the trap switches. The peak ramp voltage as well as the slightly negative trap voltages are supplied by two separate DC power supplies.

The detector signal preamplifier output is transmitted optically from the high voltage cage to an optical receiver at ground and converted to an analog signal. The analog signal is then shaped in an amplifier, the two separate outputs of which are the LeCroy 3512 ADC input. The LeCroy 3512 ADC has a tunable input threshold and a range from 0 to 8 volts. The 3512 ADC triggers on a coincidence of the input from the amplifier and the proton detector gate timing signal. When the input is above threshold and the proton detector gate signal is high, the ADC produces a "busy" output signal, which is used as the stop signal TDC which causes it to record the arrival time of the signal.

5.4.2 GaGe Digitizer System

The GaGe digitizer operates at 10MHz sampling rate and is gated externally by the proton detector gate signal, such that the GaGe card digitizes a waveform for every trap cycle (figure 5.21). For each trap cycle, the GaGe card digitizes the spectroscopy amplifier output as well as the optical-analog output of the preamplifier signal. The digitizer records 2048 time bins for each waveform, corresponding to 204.8 μs. For each waveform, 256 time bins are recorded before the proton detector is gated on in order to record background data. Following these 256 time bins, the proton detector is gated on for 1600 time bins and the last 192 time bins occur after the proton detector is gated off.

This system serves as a secondary check to the CAMAC system that was used in the previous iteration of the experiment. The CAMAC system is not capable of recording more than one stop signal per trap opening, meaning that multiple protons in a cycle are recorded as a single event. The GaGe digitizer will instead record the full waveforms for the duration of each proton collection cycle, which will record multiple proton events both in the preamplifier signal and the amplifier signal.

5.5 Commissioning the Apparatus

All of the work that has taken place with the apparatus has been performed off of a neutron beam. The primary goals have been to test the trap modulation, magnet, high voltage, and DAQ in preparation for installation on the beamline.

The primary barrier in the previous run of the lifetime experiment was stable operation of the trap, magnet, and high voltage together. Any unstable situation required significant down time because the detector replacement process takes away several days of running time. This also prevented some systematics tests from being fully explored. The apparatus is currently being commissioned offline in order to investigate both what causes these unstable situations and how to prevent the unstable situations from occurring.

The offline apparatus tests have been performed without the neutron fluence monitor in place because it is not necessary for the purposes of the tests. The high voltage system, magnet, and trap have all been in use during the offline tests. The data acquisition system electronics have been instrumented as dummy channels for the neutron counting while the rest of the DAQ is fully instrumented.

5.5.1 Detector Energy Calibration

The proton detector is periodically calibrated for determining the energy resolution as well as to ensure that it is working properly and that the noise properties of the system are adequate. The calibration procedure is performed after allowing the detector to cool radiatively overnight to liquid nitrogen temperatures by inserting it into the bore of the magnet. The detector probe arm has a platinum resistor very close to the detector for determining the temperature of the detector. A background run is performed with the detector inside the bore using the MCA subprogram of the data acquisition system. The detector is then retracted to a position where a weak americium-241 source (10 μCi) can be placed near the detector on the outside of the apparatus, which means that the 59.5 keV γ-rays from ^{241}Am decay go through a stainless steel tube before reaching the detector. Another MCA run is taken with the source in place and this run must be taken soon after retracting the detector because it will begin to warm up and the noise threshold will increase.

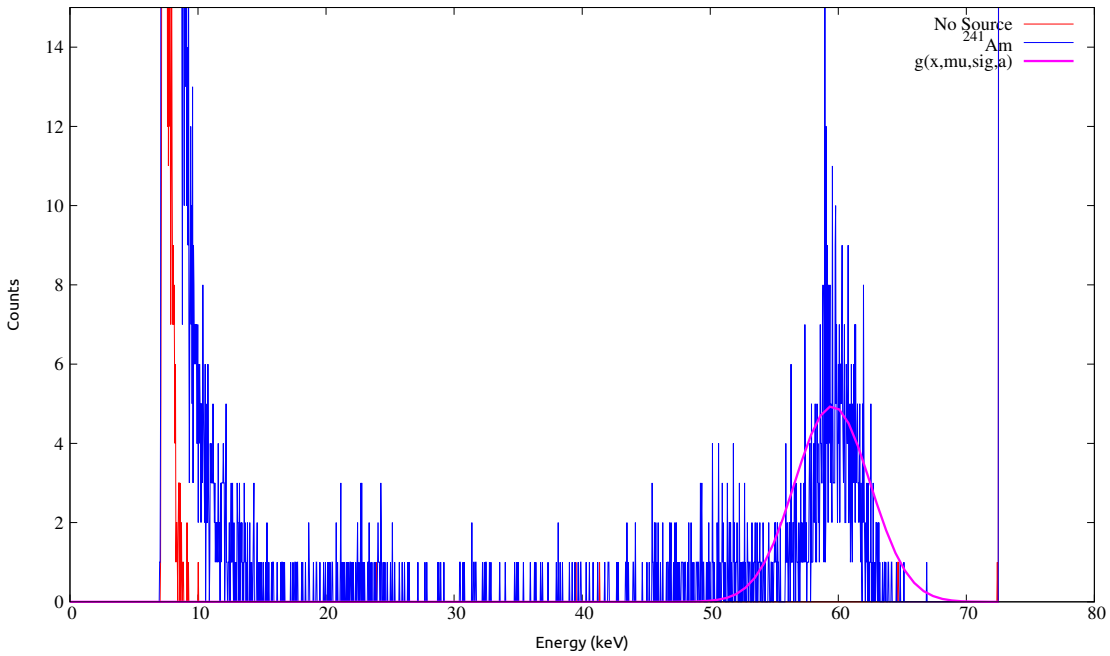

Figure 5.22: Americium-241 source calibration for 300 mm^2 Ortec Ultra ion-implanted-silicon detector with 1 μs shaping time.

The results of a calibration using a new 300 mm^2 Ortec Ultra ion-implanted-silicon detector are shown in figure 5.22. The background and source runs were both 5 minutes in duration, with the MCA program histogramming the peak heights of pulses from a spectroscopy amplifier with 1 μs shaping time. The source run is fit to a Gaussian

$$f(x,) = a \times e^{-\frac{(x-\mu)^2}{2\sigma^2}}, \tag{5.13}$$

with the result being used to scale the plot in figure 5.22 to energy rather than millivolts. The measured full width half maximum is 7 keV. The spectrum also shows a hint of some of the other peaks in the ^{241}Am spectrum at approximately 26 keV and lower. This spectrum is very promising because the noise level of the detector is at or below 10 keV meaning that the detector can detect protons perhaps as low as 15 keV. The apparatus has been more stable in the past when operated at -20 kV compared to -30 kV or more.

5.5.2 Offline Apparatus Tests

Offline tests to date have been fruitful in that they have given potential clues as to what to test next. The magnet has been successfully operated for several months at a time, which had been a concern after the magnet quenched several years ago.

The previous detector electronics incorporated a pre-amplifier that was positioned near the detector and operated at cryogenic temperatures. A new pre-amplifier has been designed by Gerard Visser at Indiana University that is operated at room temperature far away from the detector with the goal to achieve better noise performance and it has performed better than the older pre-amplifier that was in use.

As part of the offline commissioning tests, the apparatus has been operated at voltages varying from -15 kV up to -30 kV with some short excursions at higher voltages. Problems with stability of two existing Bertan high voltage supplies were found which led to acquiring a new Matsusada high voltage supply.

With the end goal being to be able to stably run the experiment and to be able to test systematics, most tests have been to vary the acceleration voltage, vary the trap length, and vary the trapping time in order to find what causes unstable situations. The system has responded well to changes in the trap timing from 5 ms to 20 ms without issues. Similarly, the trap has been operated stably at 3 and 10 electrode lengths.

Most of the problems have been with high voltage sparking that results in a compromised detector which then halts the tests for a few days while swapping detectors. The procedure for swapping detectors involves using a gate valve and keeping the bore volume under vacuum and cryo-pumping while another part of the vacuum system is vented to atmosphere for the detector swap to take place. The final vacuum after this procedure is never quite as good as it was before the detector swap, and a poor vacuum is one possible cause of the sparking instability that fries detectors.

In any case, all of the previous apparatus tests were performed with old surface barrier detectors that had previously been used in other experiments. Interestingly, these old detector surfaces showed significant damage in the form of surface pitting when viewed under a microscope which led to the conclusion that any further tests should be with new

detectors. These old detectors never produced a spectrum as good as figure 5.22 and further tests will be performed with recently purchased pristine detectors. As a sanity check, one of these new detectors was also viewed under a microscope and has no such surface features.

The typical cooldown process begins with a baking process in which all bakable regions of the system are baked to remove water from the vacuum system. The nitrogen jacket is then filled with liquid nitrogen and the detector is extending into the bore and allowed to cool overnight. Noise runs are then taken with the detector at liquid nitrogen temperatures, as well as a quick calibration procedure (figure 5.22). At this stage, the helium volume is pre-cooled with liquid nitrogen in preparation for liquid helium. After approximately one day, the liquid nitrogen is blown out of the helium volume using helium gas and the helium volume is filled with liquid helium. The initial helium fill typically boils off within one day, and the magnet is refilled after one day and is then ready for operation.

This procedure was performed with a new pristine detector for the first time since the last production data run of the experiment. First, the magnet was turned on to 110 A (about 4.6 T). The high voltage was then brought up to -15 kV. Finally, the trap modulation is enabled and the trap voltages are brought up to 800 V for the door and mirror and 15 V for the maximum ramp voltage. This pristine detector has produced some intriguing data beginning with series 102. Detector signals correlated with the trap modulation were apparent immediately once the full apparatus was brought online (figure 5.23). There appears to be a correlated signal centered around 33 μs following the opening of the door that occurs at 22 μs. There is another at approximately 115 μs following the opening of the mirror at 98 μs. Series 102 took place overnight, and the trigger rate (figure 5.25) dropped to nearly zero after a few hours of operation and the correlated signals with the trap ceased. The energy spectrum (figure 5.24) shows only a noise wall with no structure extending down from 15 kV. There was a simultaneous drop in the pressure as measured by a downstream pressure sensor(figure 5.26) , which suggests that that the correlated signal effect is a result of pressure.

This sudden change in the trigger rate was noticed after the apparatus had been allowed to run overnight. The trigger threshold was lowered the next morning from 250 mV to 150 mV, which corresponds to lowering the threshold from approximately 9 keV to 6 keV,

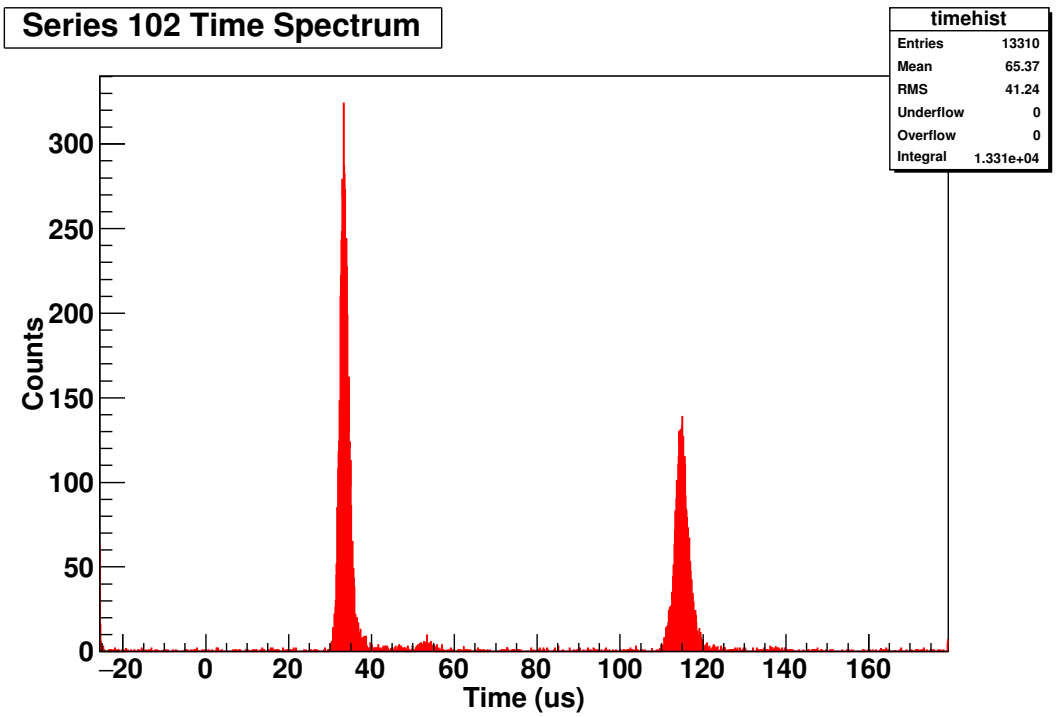

Figure 5.23: Timing spectrum for series 102, with 10 ms trap modulation period, 10 electrode length, and -15 kV acceleration potential. The horizontal axis is time in microseconds since the detector was gated on and the vertical axis is counts per bin.

and series 103 began with the same trap and acceleration potential configuration as series 102. Series 103 ran for several days with no issues and also with no trap correlated signals(figure 5.27). The energy spectrum (figure 5.28) shows a typical noise wall as well as a shoulder that could correspond to "vacuum protons", or hydrogen that is ionized in the apparatus. These protons are expected to come in below 15 keV as a result of energy loss in the dead layer.

This short test has given a lot of promising information. First of all, it is possible that the trap correlated signals are related to the pressure in the apparatus and that more careful UHV techniques and baking are required for future running. A possible way to test this is to make small changes to the pressure in order to see if the correlated signals reappear. Secondly, the noise properties for these runs with this detector have been exceptionally good and have allowed for operation at 15 kV whereas previous runs would have required running at much higher acceleration potential and risked sparking. This is promising because the apparatus has traditionally operated more stably at lower acceleration potentials.

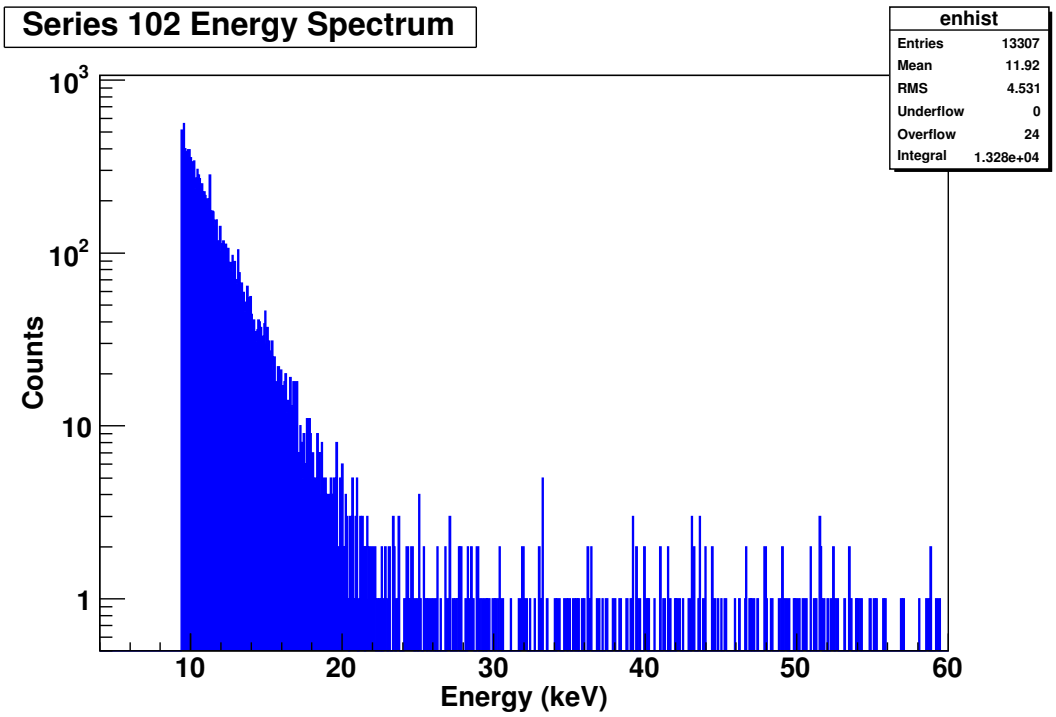

Figure 5.24: Peak height spectrum for series 102, with the horizontal axis in keV and the vertical axis showing counts.

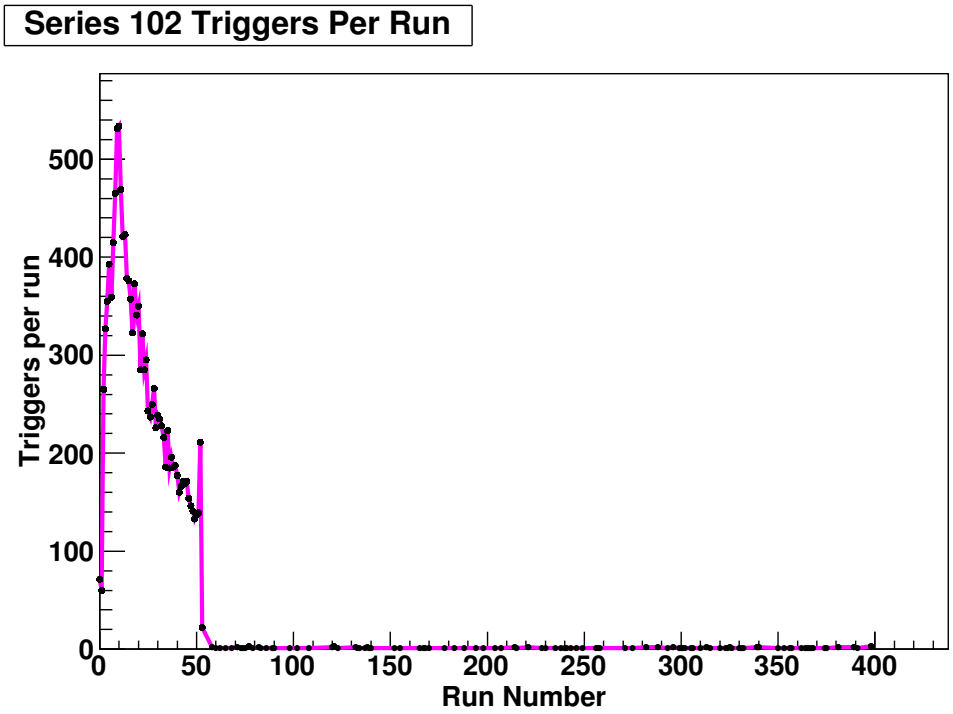

Figure 5.25: Raw number of triggers above threshold for series 102 as a function of run number. There was a sharp drop early in the series followed by a long period of few triggers.

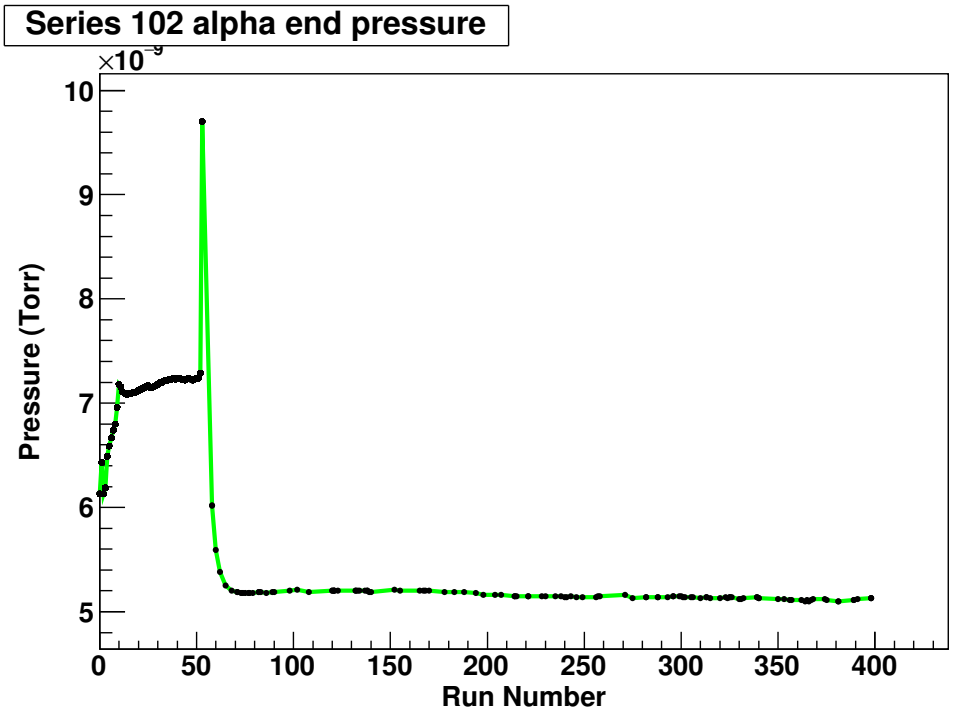

Figure 5.26: Downstream pressure sensor reading as a function of run number. The sharp change in pressure early on correlates perfectly with the dramatic reduction in trigger rate.

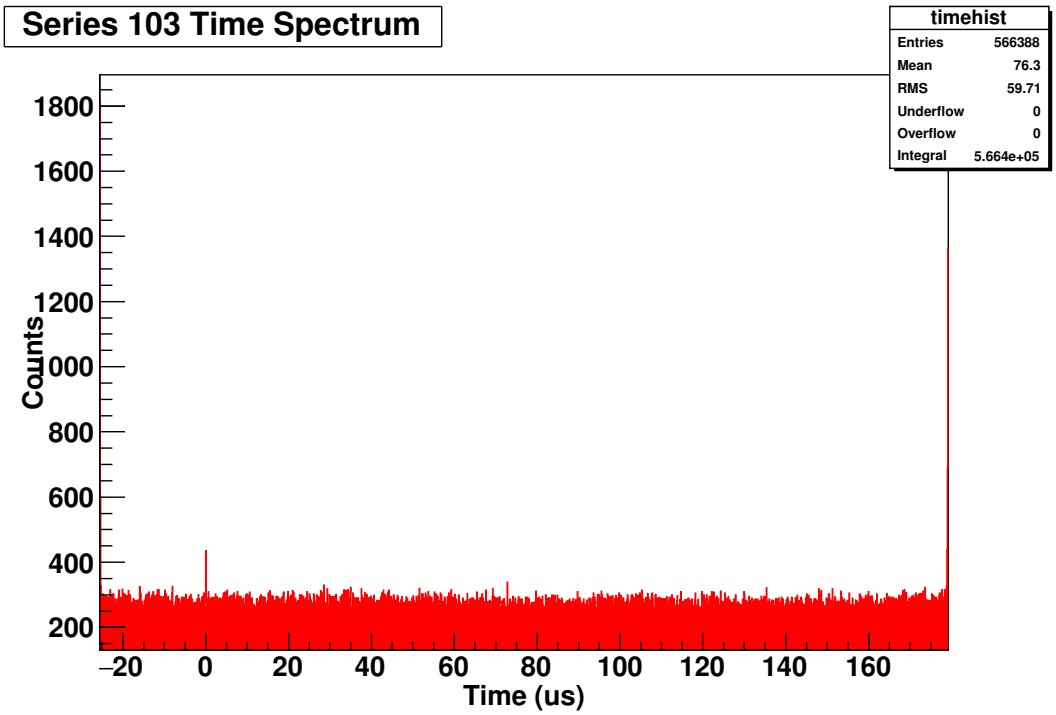

Figure 5.27: Timing spectrum for series 103, with 10 ms trap modulation period, 10 electrode length, and -15 kV acceleration potential. The horizontal axis is time in microseconds since the detector was gated on and the vertical axis is counts per bin.

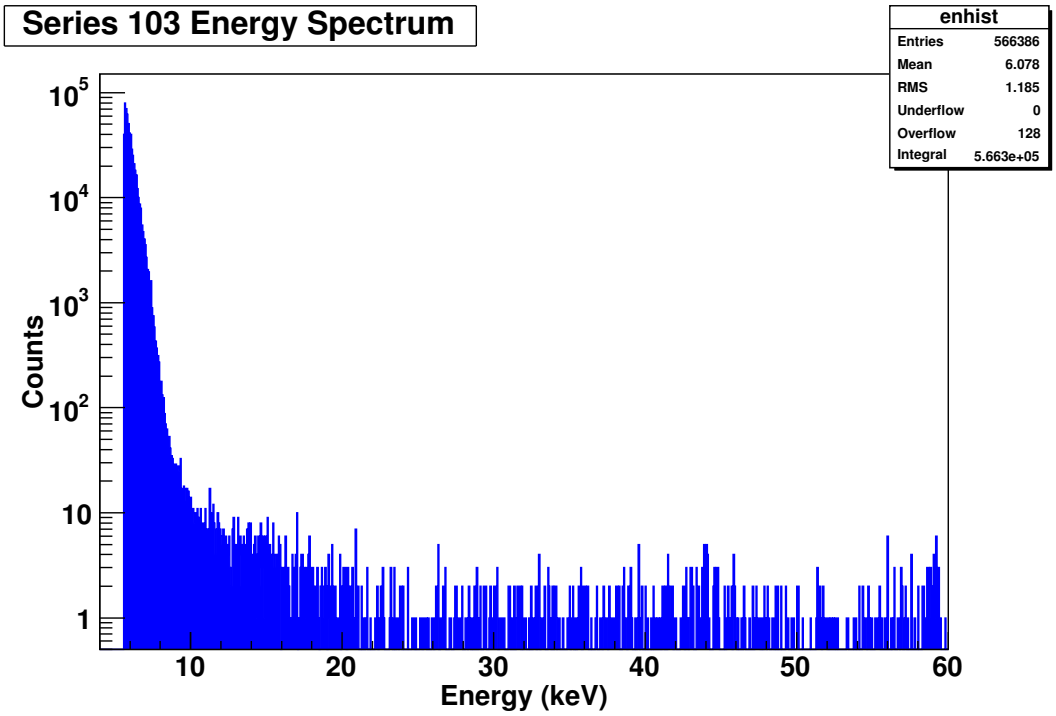

Figure 5.28: Peak height spectrum for series 103, with the horizontal axis in keV and the vertical axis showing counts.

Chapter 6

NPDGamma Experiment

The NPDGamma experiment took place on the Fundamental Neutron Physics Beamline at the Spallation Neutron Source at Oak Ridge National Laboratory. The goal of the NPDGamma experiment is to investigate weak nucleon-nucleon interaction via the reaction $\vec{n}+p \rightarrow d+\gamma$. The NPDGamma experiment is designed to measure the gamma ray directional asymmetry, A_γ, in the capture of polarized cold neutrons on liquid parahydrogen. The size of the measured asymmetry is directly related to the size of the hadronic weak interaction. One model of this interaction, the Desplanques-Donohue-Holstein (DDH) model[Desplanques et al., 1980], approximates the weak nucleon-nucleon coupling as the exchange of a meson between the nucleons.

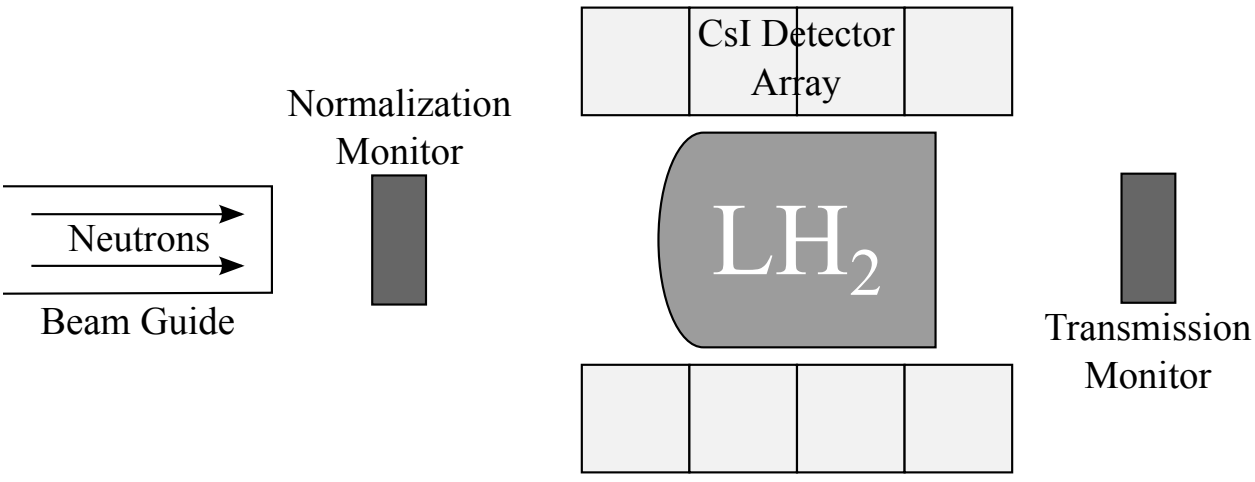

Figure 6.1: Experimental setup showing the cesium iodide detector array, liquid hydrogen target, and beam monitors.

6.1 The NPDGamma Asymmetry, A_γ

As discussed in section 2.4, the weak interaction violates parity and its measurement in a hadronic system gives a probe of the weak vertex of the interaction. This interaction is suppressed by a factor of $10^{-6}-10^{-7}$, and therefore experiments aim to isolate these effects by measuring observables that are parity odd. Pseudoscalars and pseudovectors are odd under parity, and common observables like angular asymmetries and resultant polarizations in these systems are proportional to the pseudoscalar correlation between spin and momentum, $(\vec{\sigma}\cdot\vec{p})$. The NPDGamma experiment investigates the capture of spin polarized neutrons on protons in liquid para-hydrogen, resulting in a 2.2 MeV γ-ray,

$$\vec{n} + \mathrm{p} \rightarrow \mathrm{d} + \gamma \tag{6.1}$$

Parity is violated in this reaction if the nuclear spin and the photon momentum parallel and anti-parallel cross sections are different, that is to say if nature prefers a handedness. The differential cross section is proportional to

$$\frac{d\sigma}{d\Omega} \propto \frac{1}{4\pi}(1 + A_\gamma \cos\theta_{s,\gamma}), \tag{6.2}$$

where A_γ is the observable physics asymmetry, and $\theta_{s,\gamma}$ is the angle between the neutron spin and the γ-ray direction. This violates parity because the correlation between the γ-ray momentum and the neutron spin, $\langle\vec{s}_n \cdot \vec{k}_\gamma\rangle$, is odd under parity. Because the deuteron bound state is at low energy, the asymmetry can be expressed in terms of the DDH coupling constants,

$$A_\gamma = -0.107h^1_\pi - 0.001h^1_\rho - 0.004h^1_\omega, \tag{6.3}$$

which isolates the pion-nucleon, h^1_π, coupling constant, to a good approximation [Bowman et al., 1999] [Snow et al., 2000].

In principle, one could measure this asymmetry using two point detectors, one above and one below a point capture target with the axis between them aligned with the neutron spin,

which allows for an idealized measurement of the asymmetry,

$$A_\gamma = \frac{N_\uparrow - N_\downarrow}{N_\uparrow + N_\downarrow}, \tag{6.4}$$

where $N_\uparrow$ is the number of γ-rays detected in the upper detector and $N_\downarrow$ is the number of γ-rays detected in the lower detector. A detector placed at an angle that is not parallel to the neutron spin is still sensitive to the asymmetry, but is diluted by a cosine. For a ring detector surrounding the target, the asymmetry would be a function of the angle around the target

$$A_{\mathrm{UD}}(\theta) = A_\gamma \sin\theta, \tag{6.5}$$

and the physics asymmetry is extracted by fitting to a cosine function. Furthermore, a cylindrical detector array is sensitive to the physics asymmetry and a function of two angles,

$$A_{\mathrm{UD}}(\theta) = A_\gamma \sin\theta \sin\phi. \tag{6.6}$$

The size of the hydrogen target is chosen for physics and radiological reasons, and the number of required detectors is similarly chosen to maximize the sensitivity to the asymmetry and a run-time determined figure of merit. The final configuration of a 16 l target surrounded by 4 rings of 12 $15.2 \times 15.2 \times 15.2$ cm detectors reflects this.

6.2 Fundamental Neutron Physics Beamline

The Fundamental Neutron Physics Beamline (FnPB) views a 20 K liquid hydrogen moderator at the SNS. The beamline is a 15 m neutron guide with a 10x12 cm cross section[Fomin et al., 2015]. There is an initial neutron bender section so that there is no line of sight from the guide exit and the hydrogen moderator, which serves to decrease the high energy neutron and gamma ray background from the moderator and mercury target.

The beamline has two beam choppers at 5.5 m and 7.5 m from the moderator[Mahurin and Crawford, 2006]. The choppers are 63.7 cm diameter disks rotating at 60 Hz and coated with ^{10}B paint to absorb neutrons, and each has a cutout section to allow neutrons to pass

through when the open section is in the beam path. The opening angle is 131° for chopper 1 and 167° for chopper 2. Without the choppers, a continuous neutron spectrum from approximately 1 Å to 25 Å would be delivered to the experiment. The choppers serve as a neutron velocity selector in order to deliver a specific wavelength frame to the experimental area for each pulse of protons to the mercury target as determined by the relative phase between the two choppers. The NPDGamma experiment utilizes polarized neutrons and a resonant frequency spin rotator (RFSR) that applies a time dependent magnetic field to rotate the spins of the neutrons on alternating pulses.

6.3 Super-mirror Polarizer

The neutron beam is composed of randomly oriented spins and is polarized using a supermirror polarizer. A supermirror polarizer is a supermirror composed of alternating ferromagnetic and nonmagnetic materials. [Schaerpf, 1989b,a][Mezei, 1976]

The NPDGamma supermirror polarizer is 40 cm long and composed of 45 curved channels with a radius of curvature of 9.6 m[Balascuta et al., 2012]. The 0.3 mm thick borated-glass substrates are coated on both sides with reflecting layers of iron and silicon with $m = 3$.

The index of refraction from 1.21 must include a magnetic scattering term and becomes

$$n = \sqrt{1 - \frac{V_{\text{nuc}}(\vec{r}) \; pm\vec{\mu} \cdot \vec{B}}{E_{\text{n}}}}, \tag{6.7}$$

where $\vec{\mu}$ is the neutron magnetic moment, $\vec{B}$ is the magnetic field, and the sign of the $\vec{\mu} \cdot \vec{B}$ is determined by the neutron spin.

The right spin state neutrons are quasi-Bragg reflected, while the wrong spin state neutrons see a uniform index of refraction and are captured on the boron in the glass substrates. The bent configuration of the polarizer ensures that every neutron makes a bounce, that is to say every neutron either Bragg reflects or is absorbed in the substrate, and cannot be transmitted without interacting with the polarizer. The saturation field for the supermirror polarizer is approximately 350 gauss and achieved using 44 NdFeB permanent magnets.

The magnetic field gradients that extend away from the supermirror polarizer can cause Stern-Gerlach steering of the neutrons, which is a systematic effect in the NPDGamma result. The supermirror is therefore placed in a compensation magnet that reduces the portion of the field that can cause Stern-Gerlach steering to 9.4 Gauss so that the gradients between the supermirror and the apparatus guide field.

6.4 Resonant Frequency Spin Rotator

The neutron spins are rotated 180° on a per pulse basis within a specified pattern in order to achieve the desired sensitivity to the gamma ray asymmetry. The apparatus is in a static magnetic field, $\vec{B}_0$ provided by the magnetic guide field coils with the spins aligned to the field. The beam passes through the resonant frequency spin rotator (RFSR), which supplies an RF field parallel to the neutron guide, $\vec{B}_{RF}(t) = B_{RF}\cos(\omega_{RF}t)$. The RFSR is on resonance when the frequency, ω_{RF}, is equal to the Larmor frequency of the neutrons in the guide field, $\omega_0 = \gamma_n B_0$, where γ_n is the neutron gyromagnetic ratio [Seo et al., 2008].

6.5 Magnetic Guide Field

A constant magnetic field maintains the initial polarization of the neutrons as they pass from the supermirror to the apparatus. The guide field is maintained by four rectangular coils surrounding the apparatus. The magnetic field is held at approximately 9.4 Gauss, which was chosen in order to optimize the efficicency of the RFSR by matching the Larmor precession frequency of the guide field to the resonance frequency of the RFSR. The upper and lower coils have 39 windings and the middle two coils have 18 windings. A current of 23 Amps is supplied to the coils. There are auxiliary coils supplied with a current of 3.3 Amps to allow fine tuning of the guide field. The cave walls, floor, and ceiling are lined with steel to shield the experiment from external fields and to provide a flux return that improves the uniformity of the guide field.

6.6 Beam Monitors

There are three neutron beam intensity monitors along the beamline. One is upstream of the supermirror polarizer (M1), the second is downstream of the polarizer (M2). These two beam monitors are used to determine the beam pulse shape and track the stability of the beam power.

These neutron monitors are multi-wire proportional counters that output a current signal proportional to the neutron beam intensity. The chambers have 1 mm thick aluminum windows. There are three wire planes inside each monitor, separated by about 1.2 cm. The wires are soldered to a plastic frame in order to electrically isolate the wires from the aluminum case. The wire planes are held at potentials such that the outer planes are at +1000V and the center plane is at -1000V. The current signal is converted to a voltage by a pre-amplifier and fed to the data acquisition system.

The beam monitors are filled with 10-15 Torr of ^{3}He and about 750 Torr of N_2. Helium-3 has a high neutron capture cross section of 5333 barns for the reaction ^{3}He(n,p)^{3}H libertating 764 keV of energy. The energetic proton and triton ionize the nitrogen gas in the chamber, producing N^+ ions that drift towards the center plane and electrons that drift towards the outer planes. The monitors are operated at sufficiently high voltage that the charge recombination time is long compared to the charge collection time, which manifests as a plateau in the output signal as a function of high voltage.

The third monitor is downstream of the liquid hydrogen target and detector array and serves as the transmission monitor (TM)[Szymanski et al., 1994]. This monitor is a parallel plate ion chamber filled to 760 Torr with helium-3[Barrón-Palos, 2011]. This ion chamber is used monitor the transmission of the neutron beam through the liquid hydrogen target, which is strongly dependent on the ortho:para hydrogen concentrations. It is also used for neutron polarimetry measurements.

6.7 Cesium Iodide Detector Array

The liquid hydrogen target cryostat is surrounded by a gamma detector array. The detector array consists of 48 CsI(Tl) cubic detectors arranged in 4 rings of 12 detectors each.

The detector is segmented due to the angular dependence of the γ-ray asymmetry. The crystals are cubes 15.2 cm on each side, which was chosen such that the size of the crystals is approximately 3 times the mean free path for a 2.2 MeV gamma ray with the detectors absorbing 84% of the energy of a 2.2 MeV γ-ray incident at the center[Gericke et al., 2005]. The simulation of the sensitivity of each detector to the physics asymmetry is described in section 7.2.

The geometry of the detector array is chosen such that the neutron beam can pass through the liquid hydrogen target without activating the CsI. The γ-rays emitted transverse to the neutron beam contribute the most to the physics asymmetry while γ-rays emitted along the beam contribute very little. Monte Carlo simulations were used to determine that 4 detector rings are sufficient for sensitivity to the asymmetry and solid angle acceptance. The predicted peak gamma rate for each detector is approximately 100 MHz. The high gamma rate requires the detectors to operate in current mode, because the decay time of a light pulse in CsI is about 1 μs [Grassman et al., 1985].

Each detector contains two Thallium doped Cesium Iodide crystals. The crystals are wrapped in Teflon and a photoreflector material and housed in a 1 mm thick aluminum case. A vacuum photodiode (VPD) that converts scintillation light into a current is mounted on the rear of each detector package. VPDs were chosen rather than photomultiplier tubes because a 1 G field can change the gain of a PMT by 100%[Gericke et al., 2005]. The sensitivity of the photodiodes was measured to be 10^{-4}/G for a 10 G DC field and less than 10^{-5}/G for an oscillating field [Mitchell et al., 2004].

CsI(Tl) converts γ-rays to 550 nm photons that are detected in vacuum photodiodes. The light yield of CsI(Tl) is 54,000 photons per MeV of γ-ray energy[Knoll, 2010]. Current collected at the VPD anode is amplified by a three stage low noise solid-state preamplifier [Wilburn et al., 2005]. The first stage is a current-to-voltage amplifier with a gain of 5×10^7. The second stage is an inverter with a gain that can be changed by selecting a different resistor

in order to better gain-match the detectors. The third stage provides a low-impedance cable driver.

Because the desired sensitivity to the physics asymmetry is 1×10^{-8}, instrumental false asymmetries must be known to much better than this level. Each detector package has LEDs that can be turned on for beam-off running in order to measure the false asymmetry. The inner faces of the detector packages are covered with an enriched lithium carbonate rubber which acts as neutron shielding due to the high capture cross section of lithium-6 of about 940 barns.

6.8 Liquid Hydrogen Target

The NPDGamma experiment uses a 16 L liquid hydrogen target cooled to 15.5 K. Polarized neutrons capture on the liquid hydrogen in the reaction $\vec{\mathrm{n}} + \mathrm{p} \rightarrow \mathrm{d} + \gamma$, producing 2.2 MeV γ-rays that are detected in the cesium iodide array. Measuring the spatial distribution of these γ-rays gives insight on the parity violating part of the hadronic weak interaction.

The liquid hydrogen in the target vessel must be predominantly parahydrogen in order to maintain the initial neutron polarization. The energy separation between the $J = 0$ parahydrogen ground state and the $J = 1$ orthohydrogen in the first excited state is 14.7 meV. Neutrons with an energy close to or above 14.7 meV can undergo spin-flip scattering from parahydrogen, therefore the neutron energies used are well below this level. Furthermore, a neutron that scatters from orthohydrogen can undergo spin-flip scattering, sharing 14.7 meV of energy between a parahydrogen molecule and a spin-flipped neutron. Maintaining the liquid hydrogen as almost pure parahydrogen is essential to minimizing this effect.

The vessel is initially filled with natural gaseous hydrogen, which has a 75% orthohydrogen concentration. Conveniently, the thermodynamic equilibiurm parahydrogen concentration increases as the temperature decreases, reaching 99.985% parahydrogen at 15.5 K. Less conveniently, this process takes place on a time scale of months but it can be catalyzed. The coldest part of the liquid hydrogen system is the liquefaction chamber, where hydrogen gas condenses and drips down to the ortho-para converter (OPC). The OPC contains an iron-oxide power, which catalyzes the conversion of orthohydrogen to

parahydrogen [Ilisca and Paris, 1999]. Hydrogen molecules are adsorbed onto the surface of the iron-oxide grains, causing the molecules to experience high field gradients which decreases the conversion timescale from months to days.

The vessel is surrounded by a helium jacket for leak detection purposes followed by a vacuum vessel with superinsulation. The vessel is surrounded by a lithium fluoride material which prevents scattered neutrons from activating the cesium iodide crystals. There is a 1.75 inch circulare opening in the lithium shielding to allow neutrons to reach the transmission monitor.

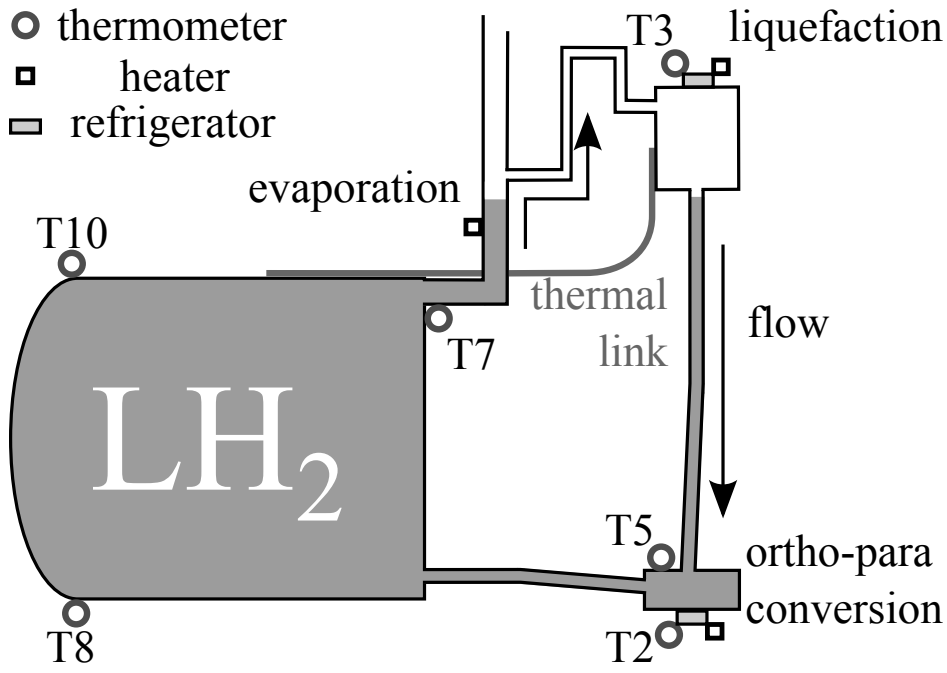

Figure 6.2: Diagram of the circulation loop inside the hydrogen target system. Evaporated hydrogen is re-condensed and is forced to flow through the OPC at a rate of a few millimoles per second. T3, T7, T8, and T10 determine the liquid hydrogen bulk temperature. T2 and T5 determine the temperature of the catalyst in the OPC [Grammer et al., 2015].

6.8.1 Auxiliary Targets

In addition to liquid hydrogen, other capture targets were used to test systematics or other aspects of the apparatus, including water, boron carbide (B_4C), carbon tetrachloride (CCl_4), and aluminum. The water target was used in order to estimate the magnitude of the expected signal from liquid hydrogen before installation. The physical size of these targets is chosen to

intercept a considerable fraction of the 10 x 12 cm beam to not waste neutrons. The targets have to remain below certain radiological limits, while simultaneously providing physics results with statistics realized in a reasonable time.

The boron carbide target was a large slab of B_4C that intercepts the full beam area. The boron carbide target is used for determining the neutron flux at the target position because it captures all incident neutrons due to the large absorption cross section of boron-10 (3835 barns), emitting 478 keV γ-rays with a branching ratio of 93.7% [Stelts et al., 1979] [Deruytter and Pelfer, 1967].

Natural chlorine exhibits a large parity violating asymmetry on γ-rays emitted from capture on chlorine-35 of $29.1 \pm 6.7 \times 10^6$ [Mitchell et al., 2004], which can be measured with the NPDGamma apparatus in under 1 day allowing for a quick check to ensure that the full apparatus is running properly. The chlorine target is a thin shell made of teflon and filled with carbon tetrachloride. Two version of the chlorine target were used, with the first being used inside the array before the target cryostat was installed and the second designed to slide into the spin flipper for apparatus checks while the cryostat was in place.

The target vessel and cryostat are made of 6061-aluminum, and any parity violating asymmetry due to aluminum will be measured simultaneously with the hydrogen asymmetry thus diluting the hydrogen asymmetry. This systematic effect must be measured separately to the hydrogen asymmetry and enters as a correction. The aluminum target was comprised of 35 individual discs with a full length of 45 cm. Each disc has a thickness of 3.175 mm and a radius of 5.715 cm. Each disc is separated by 3.175 mm to allow γ-rays to escape and reach the detectors without scattering in a thick slab of aluminum.

6.9 Data Analysis

The signal in each detector is proportional to

$$Y_{\mathrm{d}} \propto g_{\mathrm{d}}(\theta, \phi, E_{\mathrm{n}}) P_{\mathrm{n}}(E_{\mathrm{n}}) S_{\mathrm{n}}(E_{\mathrm{n}}), \tag{6.8}$$

where $g(\theta, \phi, E_{\rm n})$ is the calculated geometrical factor (section 7.2), $P_{\rm n}$ is the measured neutron polarization, and $S_{\rm n}$ is the calculated spin depolarization factor (section 7.6). The detector gains are matched to approximately 10%.

In order to eliminate effects due to slight misalignment of the detectors relative to the neutron beam, the experiment is not performed with a constant polarization but rather an alternating neutron polarization pattern, $\uparrow\downarrow\downarrow\uparrow\downarrow\uparrow\uparrow\downarrow$, which also cancels second order fluctuations in the per-pulse beam power.

The raw asymmetry can be extracted in multiple different ways, using single detectors or pairs of detectors [Wilburn, 2007]. Each method is detailed below. The signal in a detector at an angle θ about the beam axis for a given spin state ($\uparrow$ or $\downarrow$) is denoted as $N_{\theta}^{\uparrow\downarrow}$, and the signal in the pair detector is denoted as $N_{\theta+\pi}^{\uparrow\downarrow}$ since pairs of detectors are offset by an angle π. The incident neutron flux is given by $N_0^{\uparrow\downarrow}$, and the corresponding signals are determined by

$$N_{\theta}^{\uparrow\downarrow} = N_0^{\uparrow\downarrow}(1 \pm A_{\gamma}\cos\theta \pm B_{\gamma}\sin\theta), \tag{6.9}$$

$$N_{\theta+\pi}^{\uparrow\downarrow} = N_0^{\uparrow\downarrow}(1 \pm A_{\gamma}\cos(\theta+\pi) \pm B_{\gamma}\sin(\theta+\pi)), \tag{6.10}$$

where A_{γ} is the parity violating asymmetry and B_{γ} is the parity conserving asymmetry.

6.9.1 Single Detector Asymmetry

A single detector asymmetry can be constructed by taking the arithmetic mean

$$A_{\rm raw} = \frac{N_{\theta}^{\uparrow} - N_{\theta}^{\downarrow}}{N_{\theta}^{\uparrow} + N_{\theta}^{\downarrow}} = A_{\gamma}\cos\theta + B_{\gamma}\sin\theta, \tag{6.11}$$

with the signals from each spin up and spin down pulse in a spin sequence included in the sums. The pulse to pulse variations, that is variations in $N_0^{\uparrow\downarrow}$ are taken at analysis to be small and therefore replaced by N_0.

6.9.2 Detector Pair Arithmetic Asymmetry

An asymmetry, $\epsilon_{\uparrow\downarrow}$ can be formed for a given pulse using a pair of detectors for a given pulse

$$\epsilon_{\uparrow\downarrow} = \frac{N_{\theta+\pi}^{\uparrow\downarrow} - N_{\theta+\pi}^{\uparrow\downarrow}}{N_{\theta+\pi}^{\uparrow\downarrow} + N_{\theta+\pi}^{\uparrow\downarrow}} = \pm(A_\gamma \cos\theta + B_\gamma \sin\theta). \tag{6.12}$$

The final asymmetry is then given by the mean of the up and down asymmetries and is given by

$$A_{\text{raw}} = \frac{\epsilon_\uparrow - \epsilon_\downarrow}{2} = A_\gamma \cos\theta + B_\gamma \sin\theta. \tag{6.13}$$

6.9.3 Detector Pair Geometric Mean Asymmetry

Define a ratio α as

$$\alpha = \frac{N_\theta^\uparrow}{N_\theta^\downarrow}\frac{N_{\theta+\pi}^\downarrow}{N_{\theta+\pi}^\uparrow}, \tag{6.14}$$

which is equal to

$$\alpha = \left[\frac{1 + A_\gamma \cos\theta + B_\gamma \sin\theta}{1 - A_\gamma \cos\theta - B_\gamma \sin\theta}\right]^2. \tag{6.15}$$

Two quantities can then be formed,

$$\sqrt{\alpha} - 1 = \frac{2(A_\gamma \cos\theta + B_\gamma \sin\theta)}{1 - A_\gamma \cos\theta - B_\gamma \sin\theta}, \tag{6.16}$$

$$\sqrt{\alpha} + 1 = \frac{2}{1 - A_\gamma \cos\theta - B_\gamma \sin\theta}. \tag{6.17}$$

The ratio of these two quantities then determines the raw asymmetry

$$A_{\text{raw}} = \frac{\sqrt{\alpha} - 1}{\sqrt{\alpha} + 1} = A_\gamma \cos\theta + B_\gamma \sin\theta. \tag{6.18}$$

6.9.4 Extracting the Asymmetry in Practice

In practice, the detectors are not aligned perfectly such that a pair is offset by π, and the detectors are finite objects rather than point detectors. The sensitivity to the physics

asymmetry for each detector is therefore not given simply by

$$N_{\theta}^{\uparrow\downarrow} = N_{0}^{\uparrow\downarrow}(1 \pm A_{\gamma}\cos\theta \pm B_{\gamma}\sin\theta), \tag{6.19}$$

but rather by

$$N_{\theta}^{\uparrow\downarrow} = N_{0}^{\uparrow\downarrow}(1 \pm A_{\gamma}G_{\mathrm{UD}} \pm B_{\gamma}G_{\mathrm{LR}}), \tag{6.20}$$

where the terms G_{UD} and G_{LR} are determined from the Monte Carlo simulations detailed in section 7.2. It is a fit to these geometrical factors that are used in the last step of analysis in order to extract the up-down parity violating and left-right parity conserving asymmetries.

There are pathologies that have to be eliminated in the data. Instead of running the experiment with a single spin sequence of $\uparrow\downarrow\downarrow\uparrow\downarrow\uparrow\uparrow\downarrow$ followed by one pulse of non-data taking time in order to read the data from the DAQ, data is analyzed in pairs of two alternating spin sequences of type A $\uparrow\downarrow\downarrow\uparrow\downarrow\uparrow\uparrow\downarrow$ followed by a read pulse and then type B $\downarrow\uparrow\uparrow\downarrow\uparrow\downarrow\downarrow\uparrow$ followed by another read pulse. This is done because a false asymmetry was found to be caused by a transient in the single 8 step spin sequence method and this false asymmetry is canceled by using type A followed by type B pattern spin sequences.

The time of flight window is determined by the beamline choppers. The phasing of these choppers is chosen in order to minimize so called wrap-around neutrons that have very long wavelengths, and therefore very slow velocities, and reach the apparatus several pulses after the main neutron pulse. The composition of these wrap-around neutrons depends on the previous beam stability history. Therefore, three spin sequences are used for the analysis of the asymmetry with spin sequences n and $n+1$ being the analysis unit and spin sequence $n-1$ being used to determine the stability of the beam.

First, the spin sequence state has to be determined, because it can be type A followed by type B or type B followed by type A and the AB or BA sequence is flipped rarely. To determine this, a ratio is formed as follows:

$$R_{\mathrm{SF}} = \frac{\sum_{t=0}^{t=8000} sf_{\uparrow}^{2}(t)}{\sum_{t=0}^{t=8000} sf_{\downarrow}^{2}(t)}, \tag{6.21}$$

which forms a ratio of the square of the ↑-like spin flipper signal to the square of the ↓-like spin flipper signal. The raw spin flipper signal for an 8 step spin sequence has 8000 time bins and is a rapidly oscillating voltage signal with a frequency of 30 kHz. During a spin flipper on signal, this signal has a higher magnitude than spin flipper off. Therefore, the magnitude of this ratio directly determines whether the spin sequence is type A or type B, with $R_{\mathrm{SF}} \gg 1$ signifying type A and $R_{\mathrm{SF}} \ll 1$ signifying type B. If the ratio is not much different from 1, there is an issue with the spin flipper and the run is skipped as a bad run. The ratio is actually expected to be on the order of 100 in the case of type A, but can vary largely with noise levels in the data acqusition system. In any case, this ratio should be very different for type A and type B and should provide an easy way to distinguish between the two. An example of a type B histogram is shown in figure 6.3.

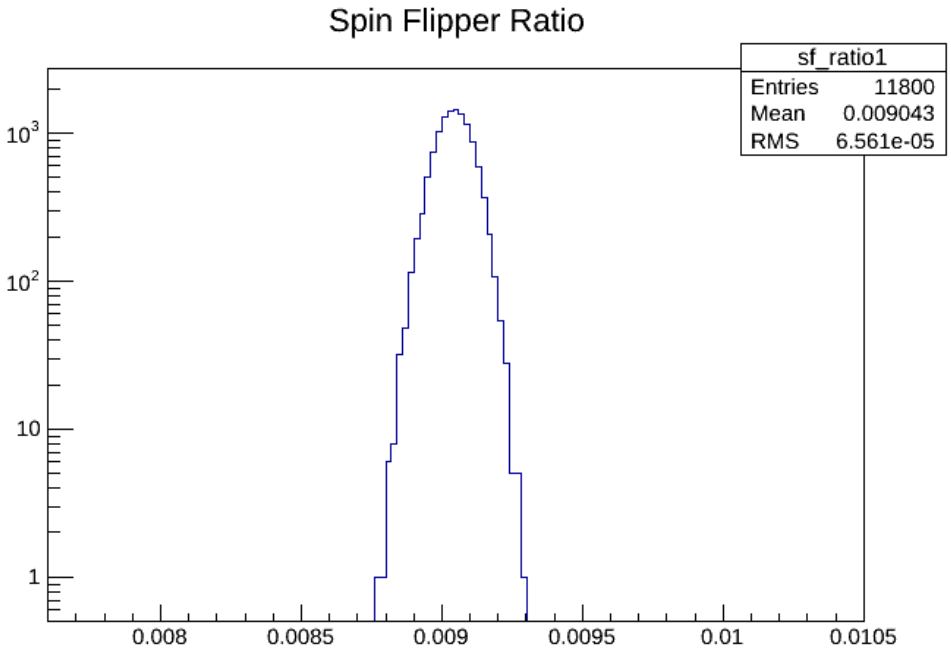

Figure 6.3: Example of the spin flipper ratio histogram, signifying a type B pulse sequence.

Next the upstream beam monitor, called M1 or the normalization monitor, is used to determine the beam stability over the course of a spin sequence. In order to determine the stability of the sequence, a ratio is formed by integrating the M1 signal for each pulse k and

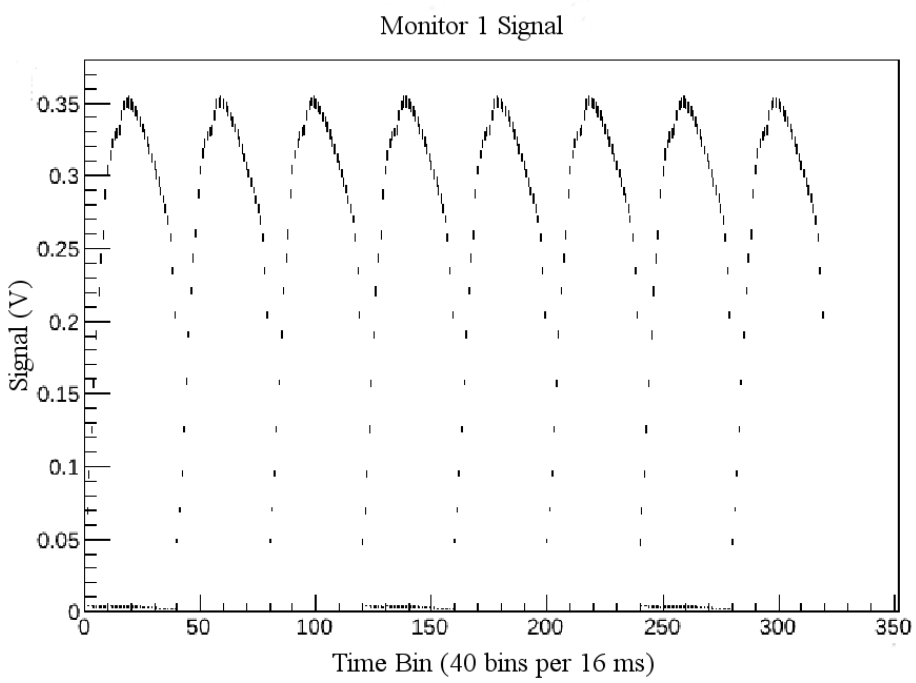

Figure 6.4: Example of the M1 signal for pulses over the course of a single run. The horizontal axis is time bins and the vertical axis is the signal voltage.

comparing it to the average for the full sequence of 16 pulses

$$R_{\mathrm{M1},k} = \frac{16 \sum_{t=0}^{t=39} V_{\mathrm{M1},k}(t)}{\sum_{k=0}^{k=15} \sum_{t=0}^{t=39} V_{\mathrm{M1},k}(t)}. \tag{6.22}$$

If a spin sequence is stable, the 16 $R_{\mathrm{M1},k}$ values for the spin sequence will lie near unity. An example of monitor 1 stability histogram is shown in figure 6.5. There are a number of prominent features depicted here. The stable beam peak is the narrow peak at unity. It is sitting on top of a broad peak at unity corresponding to full 16 step sequences with beam off. There are several short peaks to the right at approximately 1.05, 1.15, 1.25, etc. which correspond to 1, 2, 3, etc. dropped pulses within the 16 step sequence during which protons were not delivered to the mercury target and therefore no neutrons were produced. Sequences with dropped pulses cannot be used for analysis. An example of the spin flipper signal for a run is shown in figure 6.4, depicting low level dropped pulses in pulses 0, 3, and 6. These occur regularly every 600 pulses for accelerator diagnostic reasons.

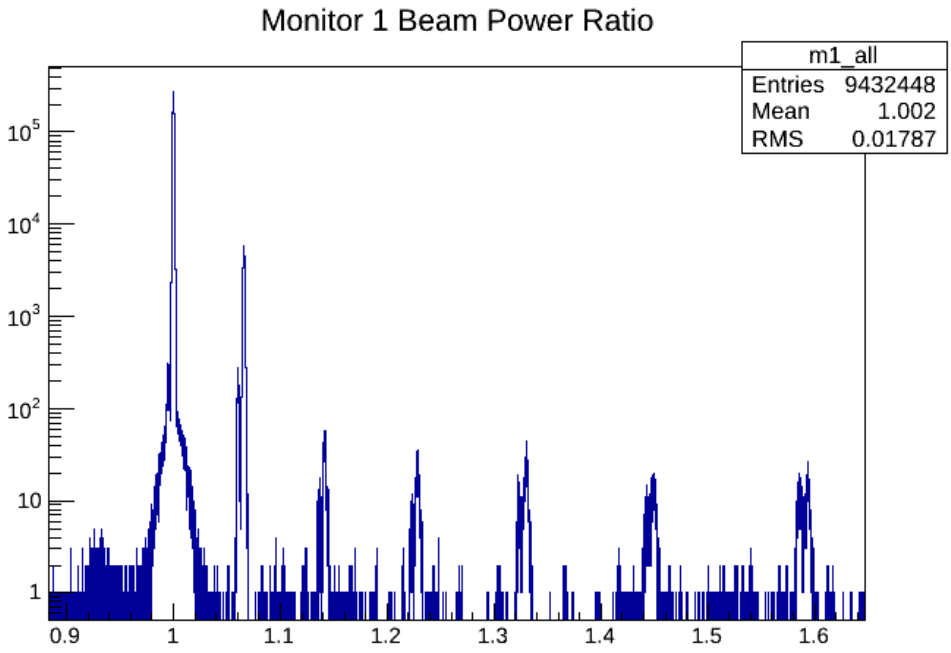

Figure 6.5: Example of the M1 stability histogram without cuts applied.

The first level cut on the monitor signal is to ensure that a neutron pulse was received for every pulse within the 16 step sequence. This is done by checking whether the signal in time bin 20 of each pulse k is greater than 0.01 V, and this bin is chosen because it is near the peak of each pulse in figure 6.4 with magnitude near 0.35 V for full power pulses and should thus be very different from 0.01 V when a neutron pulse arrives. The resulting histogram eliminates much of the structure in figure 6.5 and the result is shown in figure 6.6 zoomed in on the peak at unity. Another structure is now evident in the beam stability histogram, appearing as a smaller peak to the left of the main peak. This secondary peak is due to missing wrap-around neutrons as a result of a dropped pulse in pulse $n-1$. This is illustrated in figure 6.7, which shows the subtle effect of a missing pulse can have on later spin sequences.

This structure isn't completely eliminated by applying the $V_{\mathrm{M1},k}(20) > 0.01$ cut to sequences $n-1$, n, and $n+1$, however. This is due to neglecting the read-out pulses between 8 step spin sequences, from which there are no data recorded from the beam monitor. The detector array is downstream and therefore sees neutrons later than the monitor does, which means that part of a missing readout pulse is visible in the detector data.

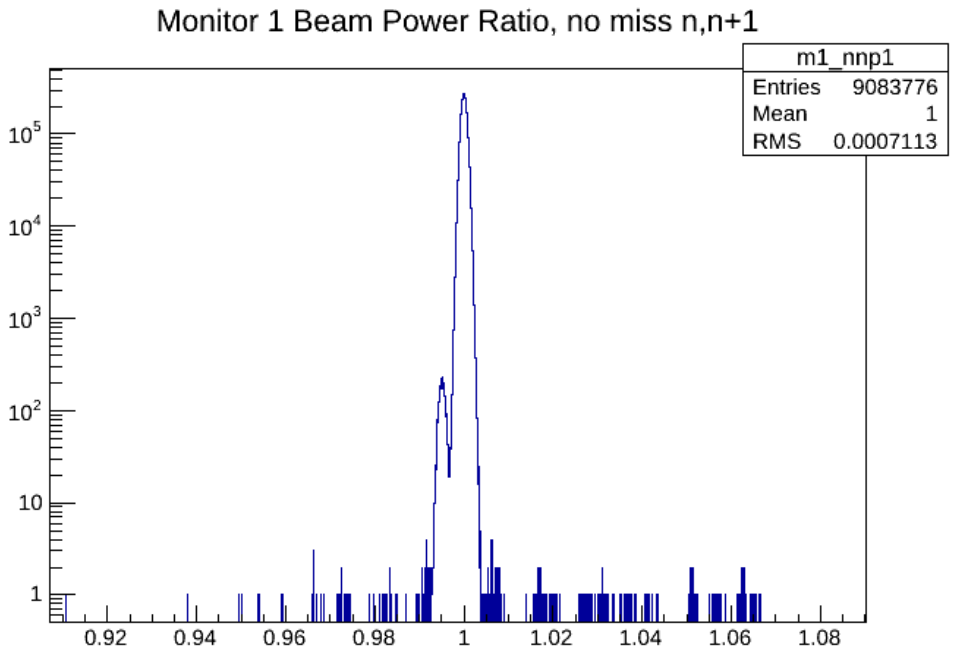

Figure 6.6: Example of the M1 stability histogram after applying the $V_{\mathrm{M1},k}(20) > 0.01$ cut.

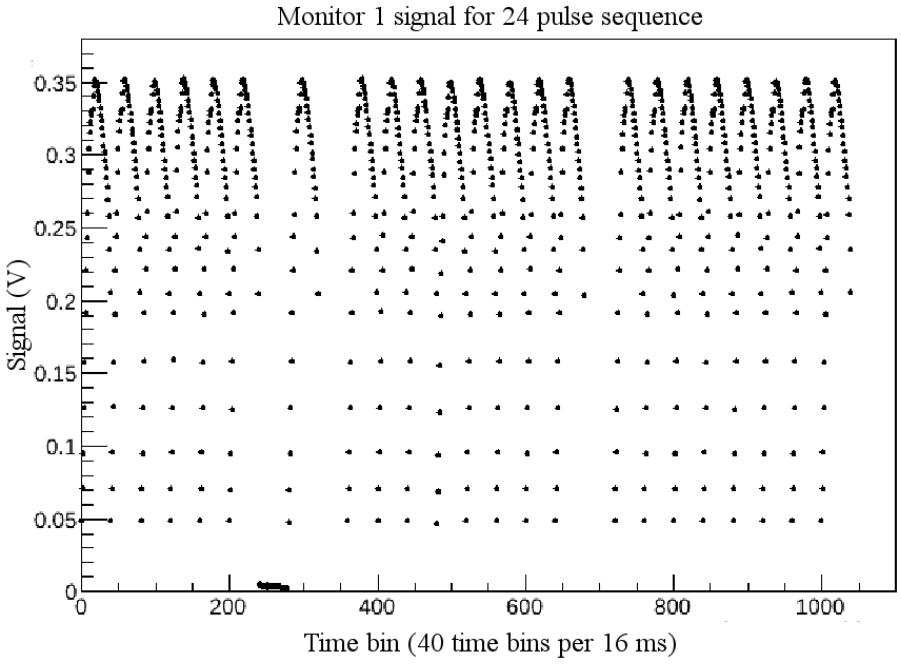

Figure 6.7: An $n-1$(left), n(middle), and $n+1$(right) pulse sequence showing a dropped pulse in pulse 6 of $n-1$ and missing neutrons in pulse 3 of n, where spin sequences are numbered 0 to 7.

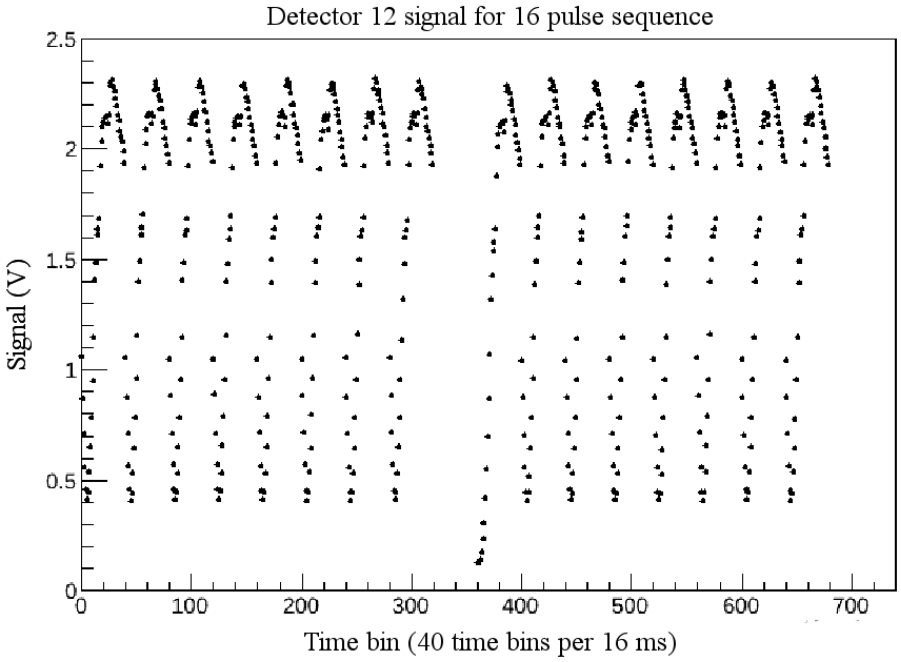

Figure 6.8: An example of spin sequence n and $n+1$ for detector 12. The horizontal axis is time bins and the vertical axis is the detector signal in volts. Notice the dip in pulse 0 of sequence $n+1$, which is the result of a missing readout pulse.

Another ratio is formed using one of the cesium iodide crystals and aims to ensure that the trailing edge of the previous accelerator pulse is similar in magnitude to the leading edge of the next accelerator pulse

$$R_{\mathrm{D12},k} = \frac{16 \sum_{t=0}^{t=3} V_{\mathrm{D12}}(t)}{\sum_{t=8}^{t=11} V_{\mathrm{D12}}(t)}, \tag{6.23}$$

which is expected to be near unity but not necessarily equal to unity for a spin sequence of beam on pulses. The detector ratio cut asserts that $0.8 < R_{\mathrm{D12},k} < 1.2$, which is very broad and far away from the actual good peak involved. The peak at unity in figure 6.9 is eliminated by the monitor 1 beam on cut.

The beam stability cut is the final cut, ensuring that the beam is stable to 1%. The ratio $R_{\mathrm{M1},k}$ is used and the entire 16 step sequence is required to be between 0.99 and 1.01. The beam stability histogram after the beam on and detector ratio cuts is shown in figure 6.10.

A typical detector asymmetry after these cuts should be a gaussian without pathologies. Figure 6.11 shows a typical detector asymmetry for a small number of runs after applying these three simple cuts to the data.

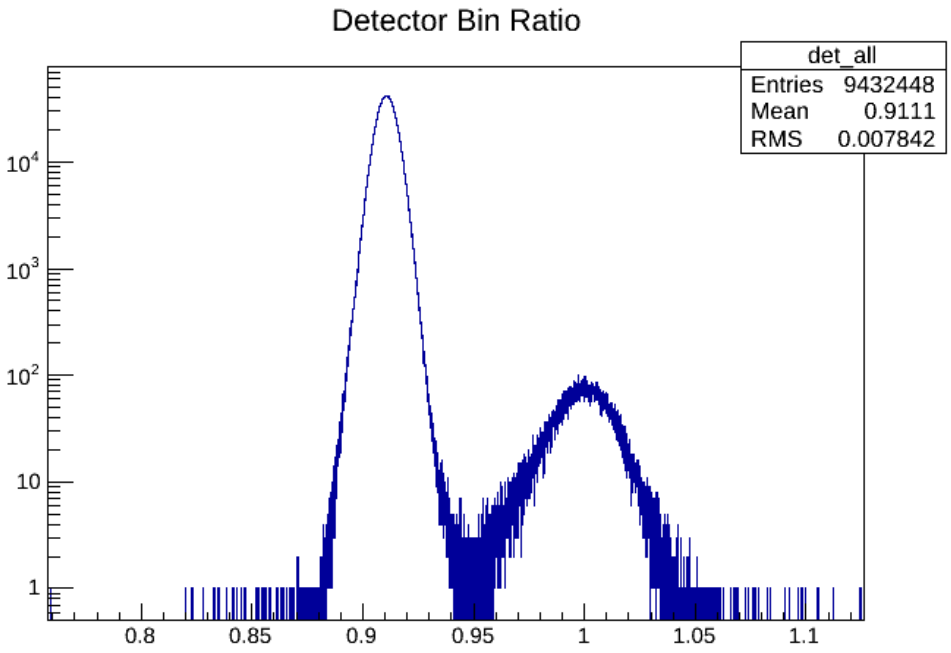

Figure 6.9: The detector ratio histogram, showing a good peak at approximately 0.91 and a noise peak due to beam off signals at unity.

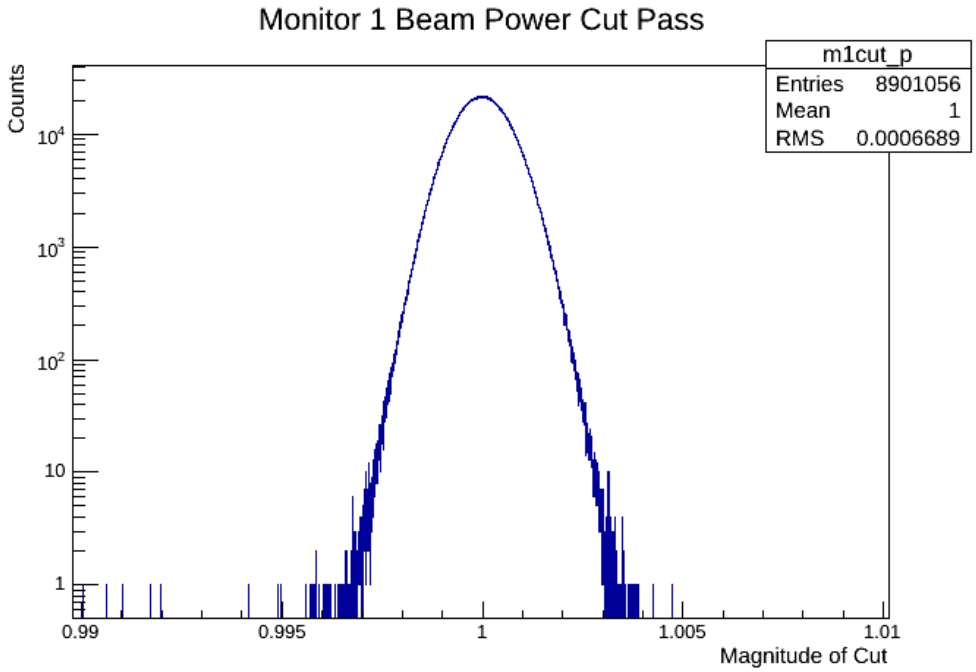

Figure 6.10: Monitor 1 ratio $R_{\mathrm{M1},k}$ after applying beam on and detector ratio cuts. The second peak is eliminated.

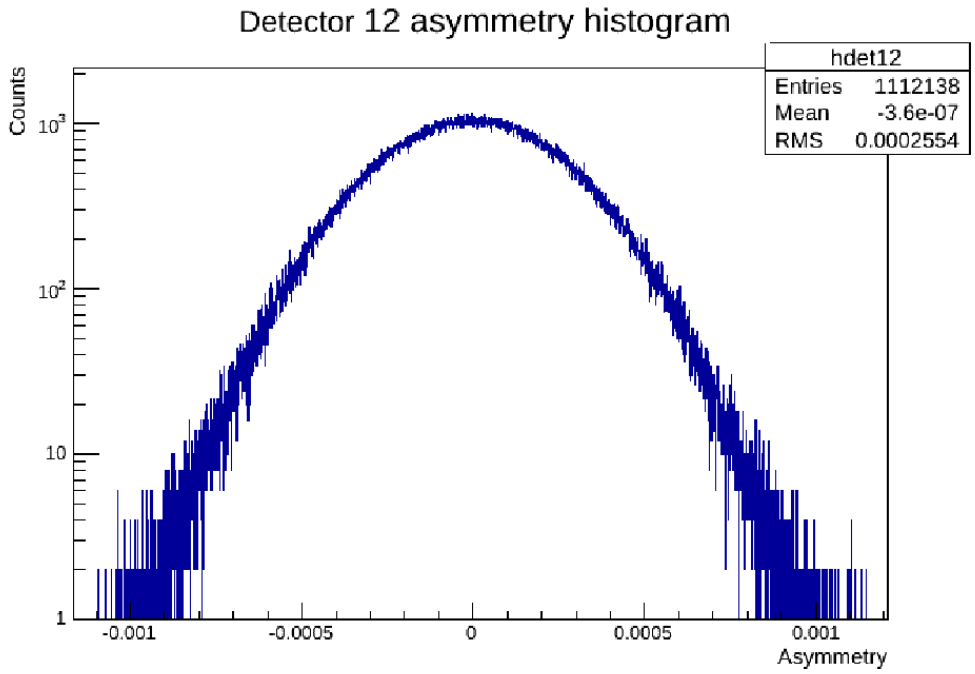

Figure 6.11: Detector asymmetry after $0.99 < R_{\mathrm{M1},k} < 1.01$, $0.8 < R_{\mathrm{D12},k} < 1.2$, and $V_{\mathrm{M1},k}(20) > 0.01$. Showing a gaussian in log scale.

Raw asymmetries are extracted for each detector or pair of detectors, resulting in 48 or 24 results respectively, each with an uncertainty determined according to the σ from a gaussian fit to the histograms depicted in figure 6.11. The sensitivity to the asymmetry for each detector or pair of detectors is modeled and described in section 7.2, such that the expected asymmetry measured by detector i is given by

$$A_{\mathrm{model},i} = A_\gamma G_{\mathrm{UD},i} + B_\gamma G_{\mathrm{LR},i}, \tag{6.24}$$

where $G_{\mathrm{UD},i}$ and $G_{\mathrm{LR},i}$ are the up-down and left-right geometrical factors for detector or pair i. The χ^2 is then written down as

$$\chi^2 = \sum_i^{24 \text{ or } 48} \frac{(A_{\mathrm{raw},i} - A_{\mathrm{model},i})^2}{\sigma_i^2} = \sum_i^{24 \text{ or } 48} \frac{(A_{\mathrm{raw},i} - A_\gamma G_{\mathrm{UD},i} - B_\gamma G_{\mathrm{LR},i})^2}{\sigma_i^2}, \tag{6.25}$$

with the fit parameters being A_γ and B_γ, the up-down parity violating and left-right parity conserving asymmetries respectively.

Chapter 7

Monte Carlo Models for NPDGamma

7.1 NPDGamma Geometry Model in MCNPX

The NPDGamma experiment relies on Monte Carlo simulations for predicting the detector sensitivity to the physics asymmetry, as well as to predict the depolarization of neutrons in materials as they propagate through the experiment. The full geometry of the NPDGamma cave is modeled using MCNPX.

After creation in the source, neutrons pass through approximately 1.5 m of air before striking the target inside the detector array. Air will scatter a small percentage of neutrons out of the beam. There is also a lithium loaded plastic collimator upstream of the spin flipper that absorbs all of the neutrons incident on it. Lithium plastic is also used as neutron shielding. The spin flipper has aluminum windows that scatter and absorb some neutrons and contribute to backgrounds in the detectors. The cesium iodide detectors detect gammas primarily via the photoelectric effect and Compton scattering. The following sections describe elements of the model further.

7.1.1 Detector Geometry and Materials

The version of MCNPX used in these simulations is MCNPX 2.7, released in July 2011[Pelowitz, 2011]. All of the materials in the model are shown in table B.1 and all percentages are normalized to 100% by MCNPX at run time for each material.

Every material uses neutron cross sections from the same library in MCNPX with ZAID ZZZAAA.70c which is an ENDF-B/VII evaluation at 293.6 K and all cross section libraries are standard libraries from the MCNPX disc. The MCNPX geometry model incorporates the CsI detectors of the correct dimensions of 15.2 cm on each side. There is 1 mmof aluminum on each face of the detectors as well as a ^{6}Li loaded plastic neutron shielding on the inner faces of the detectors. Downstream from the source and slightly upstream from the spin flipper is a lithium absorber and collimator. The spin flipper windows are made of aluminum and can contribute to the signal in the detectors. The lithium fluoride material in the table is used inside the hydrogen target cryostat only while the lithium carbonate material is used on the detectors.

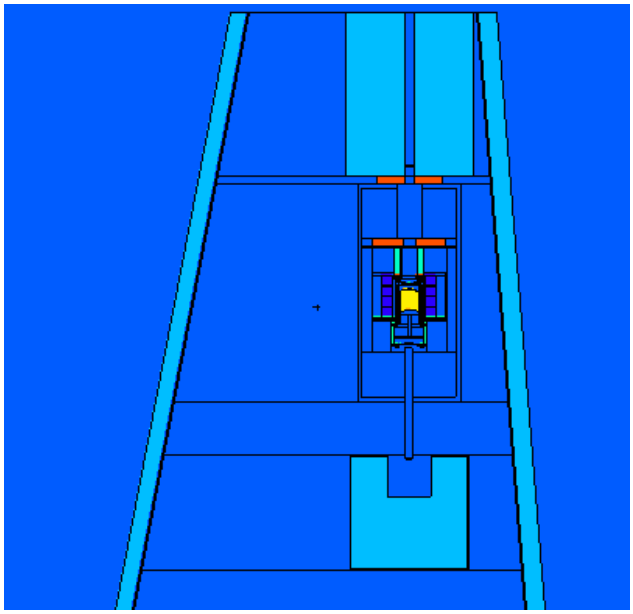

Figure 7.1: MCNPX Geometry projected in the X-Z plane at beam height, depicting the detector array (dark blue), air (dark blue), the hydrogen target (yellow), concrete cave as well as upstream concrete shielding and the downstream beam stop (light blue), and the lead shields (orange).

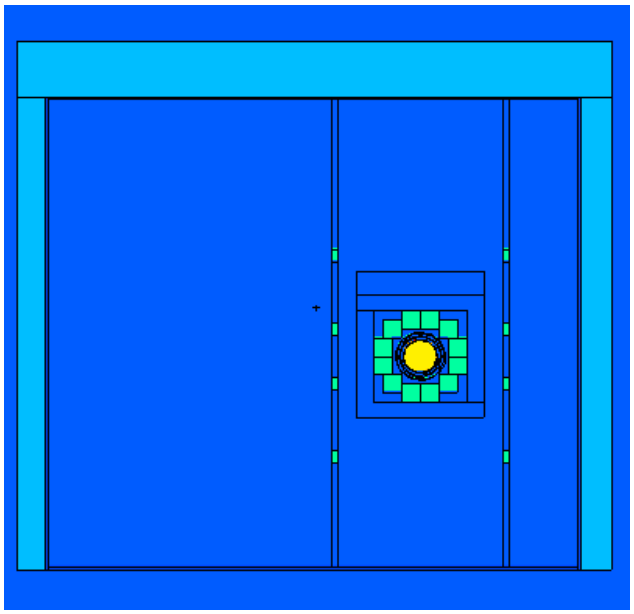

Figure 7.2: MCNPX Geometry projected in the X-Y plane at the center of the detector array (green-blue) and the hydrogen target (yellow). The concrete cave surrounds the apparatus (light blue), and air (dark blue).

The aluminum is modified to use a thermal neutron treatment at 293K and 20K (H-target vessel only) and it scatters as an amorphous powder of crystals rather than a rolled sheet-like crystal. The thermal treatment cross sections for aluminum are al27.10t at 20 K and al27.12t at 293 K from ENDF-VII. The thermal treatment leads to the production of Bragg edges in the transmitted spectrum through an aluminum region. To show this, 10^7 source neutrons for the aluminum target were modeled with the thermal neutron treatment enabled. The neutron energy spectrum was tallied at the source and in a downstream air gap in the aluminum target for an energy range from 1 meV to 20 meV. The spectrum is shown in figure 7.3 in Å (bottom axis) and meV (top axis) and clearly shows that the source input was a flat distribution from 1 meV to 20 meV and that after transmission through the aluminum target there are several obvious drops in neutron flux at specific energies.

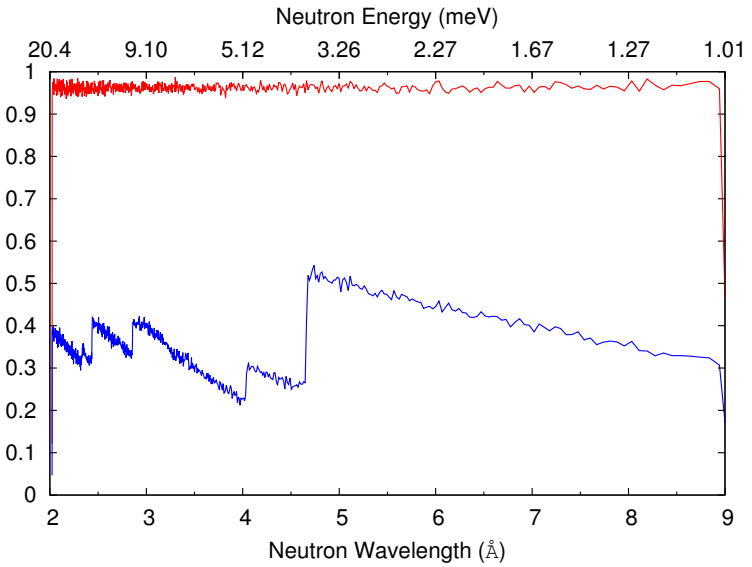

Figure 7.3: Neutron Energy Flux in arbitrary units (red=source, blue=after target)

The MCNPX simulation results for these are shown in both Å and meV in figure 7.3. The reason for these drops is that there is increased scattering of neutrons at certain wavelengths that leads to increased absorption since a scattered neutron sees more aluminum than one that passes straight through. Bragg edges in the NPDGamma pulse window are expected to be at 4.05 Å and 4.67 Å, both of which are visible in figure 7.3.

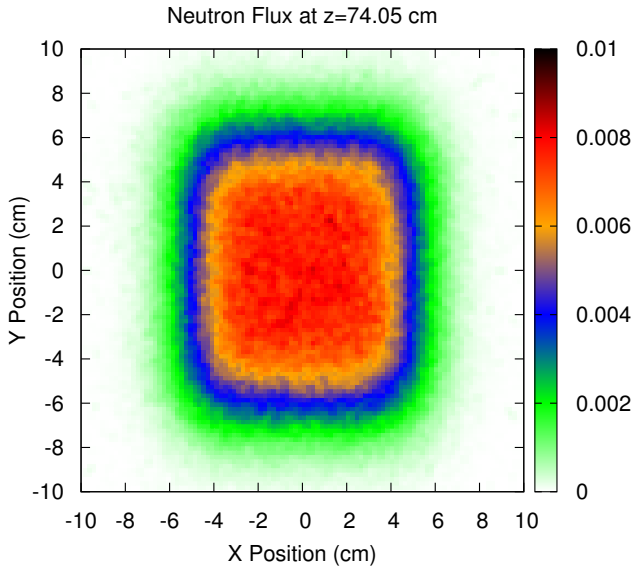

Figure 7.4: 20 cm × 20 cm mesh grid of neutron flux for source with divergence upstream of the main apparatus

The neutron source is modeled as a 10 cm × 12 cm rectangle 1.885 m from the center of the detector array. Beamline 13 at the Spallation Neutron Source has been measured to have a small divergence in the vertical and horizontal directions of 11 and 15 mrad respectively. This divergence is incorporated into the model via a custom source subroutine in the source code of MCNPX. Figure 7.4 shows the cross section of the beam upstream of the apparatus.

The MCNPX model tracks neutrons, photons, and electrons. It is necessary to model the electrons for computational accuracy because it is Compton scattered electrons that deposit energy in the detector array. However, modeling electrons is expensive in computation time because electrons scatter many thousands of times as they lose energy leading to a run time increase by a few orders of magnitude. To manage the run time increase, the electron energy is cut at 100 keV such that all electrons with energy less than 100 keV are terminated and the energy is deposited locally. This brings the run time increase down to a factor of less than 5 compared to tracking photons only. Continuing to track electrons with energy below 100 keV is only a small surface effect because the range of a 100 keV electron in cesium iodide is only 60 μm(figure 7.5, NIST ESTAR Data) compared to the 15.2 cm size of the detectors.

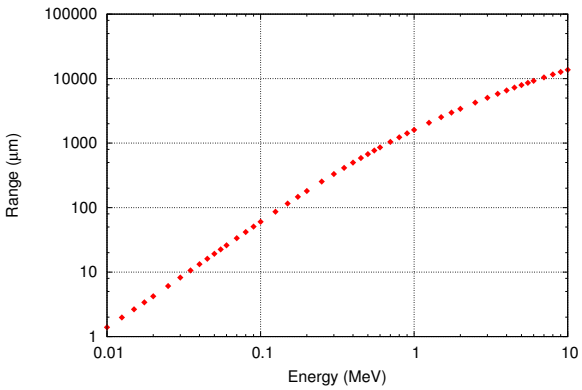

Figure 7.5: Electron range in Cesium Iodide from NIST ESTAR data

7.1.2 Chlorine Target

The chlorine target is a liquid carbon tetrachloride inside an aluminum case. The radius of the cavity holding the liquid is 5.715 cm and the depth of the cavity is 5.588 mm. The outer radius of the case is 6.1468 cm. The upstream face of the aluminum case is thinner than

the downstream face at 0.762 mm compared to 2.667 mm. The cavity was assumed to be completely filled with carbon tetrachloride. The geometrical factors were calculated with the chlorine target placed 4.9 cm downstream from the center of the array inside ring 3. This was the location of the chlorine target for the first run with the chlorine target. The second version of the chlorine target uses a teflon case and is typically placed in the spin flipper.

7.1.3 Aluminum Target

The aluminum target was comprised of 35 individual discs. Each disc has a thickness of 3.175 mm and a radius of 5.715 cm. Each disc is separated by 3.175 mm. The stand was not included in the model. The composition of the aluminum was a complicated mixture of mostly aluminum with small amounts of other elements that comprise 6061 aluminum. This aluminum uses the thermal treatment at 293 K. The aluminum thermal treatment libraries are al27.10t (20 K) and al27.12t (293.6 K).

7.1.4 Hydrogen Target

The hydrogen target model uses para-hydrogen at 20 K with the aluminum target vessel at 20 K as well. The target vessel in the model is hermetically sealed in lithium fluoride. There are two thin layers of copper outside the lithium on the target vessel. The hydrogen target was built from CAD drawings and the position of all components of the hydrogen target was determined relative to the front face of the hydrogen target vacuum box. The position of the front face of the vacuum box was measured to be 2 inches from the lithium neutron shielding on the downstream face of the detector array aluminum frame. The lithium collimator upstream of the spin flipper is removed for the hydrogen target. The hydrogen thermal treatment library is from ENDF7, evaluated at 20 K.

7.1.5 Hydrogen Target Auxiliary Components

The hydrogen target contains a complicated aluminum geometry that can carry an asymmetry and therefore needs to be modeled. In the same manner as the other targets, the geometrical factors can be calculated for auxiliary aluminum as well. Geometrical factors for

neutrons that capture in the CsI crystals and produce gammas are also modeled, though these are dependent on the transmission of neutrons through the lithium blankets and through cracks in the lithium blanket.

7.1.6 Other Targets

Auxiliary configurations used targets located in the spin flipper. These include aluminum, chlorine, and cesium iodide. Geometrical factors have been calculated for these targets as well, but they are not discussed at length in this writeup.

7.2 Modeling the Geometrical Factors

7.2.1 Motivation and Discussion of the Geometrical Factors

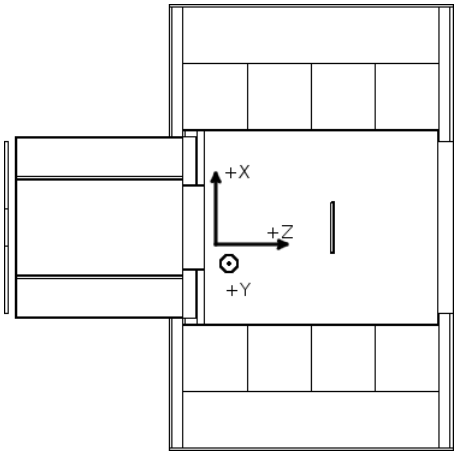

Figure 7.6: MCNPX Detector Model and Coordinate System looking down from ceiling

The goal of the NPDGamma experiment is to measure the asymmetry in γ-ray emission in the capture of polarized neutrons on parahydrogen. The sensitivity of the CsI detector array to the physics asymmetry, known as the geometrical factors, must be modeled and used as a parameter in the analysis of data. To first order, the sensitivity of each detector to the physics asymmetry is a sinusoidal function of the angular position, θ, of the detectors along the beam axis, as was used in the NPDGamma measurement conducted at LANSCE[Gericke et al.,

2011]. The sensitivity should also vary between wings due to dependence on the azimuthal angle, ϕ, for each ring. This requires a more complex model which was accomplished by modifying the MCNPX code and simulating the full geometry of the NPDGamma apparatus.

The neutron beam and upward (polarization) directions define the coordinate system that will be used. The beam travels in the $+\hat{\mathbf{z}}$ direction, the upward neutron polarization is the $+\hat{\mathbf{y}}$ direction, and the $+\hat{\mathbf{x}}$ is the beam left direction in order to make the coordinate system right handed (figure 7.6). Spherical coordinates are defined as usual with ϕ measured from the $\hat{\mathbf{x}}$-axis and θ measured from the $\hat{\mathbf{z}}$-axis.

The geometrical factors are related to the position of the detectors in the detector array. In this sense, the geometrical factors are average energy weighted functions that are a measure of the emission direction of a photon from the target that deposits energy in a given detector. The $\hat{\mathbf{x}}$-direction, or left-right, geometrical factor is proportional to the parity allowed asymmetry and is given by

$$\begin{aligned} G_{\mathrm{LR}} &= \langle \hat{\mathbf{k}}_{\gamma,\mathrm{initial}} \cdot (\hat{\sigma}_n \times \hat{\mathbf{k}}_n) \rangle \\ &= \langle \hat{\mathbf{k}}_{\gamma,\mathrm{initial}} \cdot (\hat{\mathbf{y}} \times \hat{\mathbf{z}}) \rangle \\ &= \langle \hat{\mathbf{k}}_{\gamma,\mathrm{initial}} \cdot \hat{\mathbf{x}} \rangle = \langle \sin(\theta)\cos(\phi) \rangle. \end{aligned} \tag{7.1}$$

The $\hat{\mathbf{y}}$-direction, or up-down, geometrical factor is proportional to the parity violating asymmetry and is given by

$$\begin{aligned} G_{\mathrm{UD}} &= \langle \hat{\mathbf{k}}_{\gamma,\mathrm{initial}} \cdot \hat{\sigma}_n \rangle \\ &= \langle \hat{\mathbf{k}}_{\gamma,\mathrm{initial}} \cdot \hat{\mathbf{y}} \rangle \\ &= \langle \sin(\theta)\sin(\phi). \end{aligned} \tag{7.2}$$

The $\hat{\mathbf{z}}$-direction geometrical factor is not used in the analysis of experimental data but is instead a consistency check on the calculations in this document and is given by

$$\begin{aligned} G_{\mathrm{Z}} &= \langle \hat{\mathbf{k}}_{\gamma,\mathrm{initial}} \cdot \hat{\mathbf{z}} \rangle \\ &= \langle \cos(\theta) \rangle. \end{aligned} \tag{7.3}$$

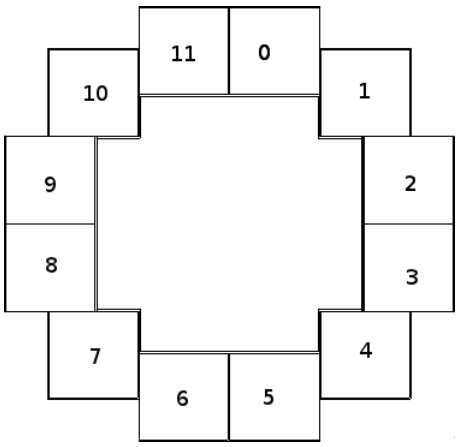

Figure 7.7: Detector Numbering Scheme, looking in +z direction

In a simplified detector configuration with point detectors centered on the axes at ±x and ±y with a point source at the origin. Every detector in this configuration should have $\theta = 0$ and the geometrical factors become functions of ϕ only. For the +x detector, $\phi = 0$ and the up-down geometrical factor should be zero while the left-right geometrical factor should be unity. For the -x detector, the up-down geometrical factor should be zero and the left-right geometrical factor should be -1. The same should be true for the ±y detectors for with the up-down geometrical factor equal to ±1 and the left-right equal to zero. Point detectors at an arbitrary ϕ and θ are expected to behave according to equations (7.1), (7.2), and (7.3).

Instead, there are 4 rings with 12 detectors per ring and two types of detectors: side/top and corner. Each detector in a ring is expected to have roughly the same $\langle\cos(\theta)\rangle$ with some deviations between side/top and corner detectors. The consistency check is then that the $\langle\cos(\theta)\rangle$ geometrical factor should be flat for each ring and it should be positive for rings downstream from the target and negative for upstream rings. The 2 top detectors in each ring should have the same $\sin(\phi)$ angle and therefore should have equal and positive $\langle\sin(\theta)\sin(\phi)\rangle$ but opposite $\cos(\phi)$ and $\langle\sin(\theta)\cos(\phi)\rangle$. The top/bottom detectors should have the maximum magnitude $\langle\sin(\theta)\sin(\phi)\rangle$ and the minimum magnitude $\langle\sin(\theta)\cos(\phi)\rangle$ in each ring and should see the greatest parity violating asymmetries. Side detectors should have the maximum magnitude $\langle\sin(\theta)\cos(\phi)\rangle$ and the minimum magnitude $\langle\sin(\theta)\sin(\phi)\rangle$ and see the smallest parity violating asymmetries. Since the corner detectors are at approximately $\phi = \frac{\pi}{4}$, the $\langle\sin(\theta)\sin(\phi)\rangle$ and $\langle\sin(\theta)\cos(\phi)\rangle$ should be equal in magnitude.

The detectors are non-ideal because each detector is a bulk detector, rather than a point detector, that contains 2 half-crystals of cesium iodide rather than 1 large crystal. Each half-crystal can have different optical properties and slightly different efficiencies. The distance from the center of the detector array to the front faces of the detectors is approximately 25 cm. If one crystal has an efficiency of 110% and the other crystal has an efficiency of 90% the center of detection of the detector shifts by 0.75 cm, or about 35 mrad. Differences in crystal efficiencies are the primary contributor to angle shift therefore the detector misalignment angles are expected to be of order 40 mrad. This angle shift mixes the up-down and left-right geometrical factors. The primary assumption is that detector angle shift, δ, can be cast as a small rotation of the detectors about the beam axis and thus a small correction to the geometrical factors.

Even if the detector crystals were perfectly uniform and in their ideal positions, there are still finite geometry effects. It is rather difficult to assign a θ and ϕ to a single detector. There are shadowing effects that have to be taken into account. The targets used in the experiment are also finite in size. For these reasons, it is necessary to use simulations and auxiliary measurements to calculate the geometrical factors for each detector. With the chlorine asymmetry measured to 1%, the geometrical factors need to be calculated to much better than 1%.

7.2.2 MCNPX Code Modifications

Calculation of the geometrical factors as defined above is not a standard function of MCNPX, and this calculation requires a modification of the source code. The code was modified to save the initial direction, $\hat{\mathbf{k}}_{\gamma,\text{initial}}$, of every photon created by neutron absorption to three elements of an array. As the photon propagates through the model, the initial direction tags remain unchanged even as the photon scatters and changes direction. Furthermore the initial direction tags are inherited for all daughter particles created in the model, such as for Compton electrons. Therefore, as energy is deposited in the detector crystals by Compton electrons, these electrons carry the $\hat{\mathbf{k}}_{\gamma,\text{initial}}$ tags and can be binned accordingly.

MCNPX has built in tallying algorithms to tally the energy deposition in a cell. A tallyx subroutine was added so that MCNPX would tally the product of energy deposition and the

initial photon direction cosines ($\hat{\mathbf{k}}_{\gamma,\text{initial}}$). The tallies are shown in equations (7.4) (7.5) (7.6) (7.7), and are in units of MeV g^{-1} normalized per source particle. The results are tallied for each detector, j, in the array and the geometrical factors can be calculated from these

$$T_{j,\text{total}} = \langle \sum_{i=1}^{N_\gamma} E_{i,j} \rangle, \tag{7.4}$$

$$T_{j,x} = \langle \sum_{i=1}^{N_\gamma} E_{i,j} \times (\hat{\mathbf{k}}_{\gamma,\text{initial}} \cdot \hat{\mathbf{x}})_i \rangle, \tag{7.5}$$

$$T_{j,y} = \langle \sum_{i=1}^{N_\gamma} E_{i,j} \times (\hat{\mathbf{k}}_{\gamma,\text{initial}} \cdot \hat{\mathbf{y}})_i \rangle, \tag{7.6}$$

$$T_{j,z} = \langle \sum_{i=1}^{N_\gamma} E_{i,j} \times (\hat{\mathbf{k}}_{\gamma,\text{initial}} \cdot \hat{\mathbf{z}})_i \rangle. \tag{7.7}$$

The geometrical factors can be viewed as the ratio of initial photon emission direction weighted energy deposition to total energy deposition for each detector. They are found by finding the ratio of the three directional tallies above to the total energy deposition in each detector,

$$G_{\text{LR},j} = \langle \hat{\mathbf{k}}_{\gamma,\text{initial}} \cdot \hat{\mathbf{x}} \rangle = \frac{\langle \sum_{i=1}^{N_\gamma} E_{i,j} \times (\hat{\mathbf{k}}_{\gamma,\text{initial}} \cdot \hat{\mathbf{x}})_i \rangle}{\langle \sum_{i=1}^{N_\gamma} E_{i,j} \rangle} = \frac{T_{j,x}}{T_{j,\text{total}}}, \tag{7.8}$$

$$G_{\text{UD},j} = \langle \hat{\mathbf{k}}_{\gamma,\text{initial}} \cdot \hat{\mathbf{y}} \rangle = \frac{\langle \sum_{i=1}^{N_\gamma} E_{i,j} \times (\hat{\mathbf{k}}_{\gamma,\text{initial}} \cdot \hat{\mathbf{y}})_i \rangle}{\langle \sum_{i=1}^{N_\gamma} E_{i,j} \rangle} = \frac{T_{j,y}}{T_{j,\text{total}}}, \tag{7.9}$$

$$G_{\text{Z},j} = \langle \hat{\mathbf{k}}_{\gamma,\text{initial}} \cdot \hat{\mathbf{z}} \rangle = \frac{\langle \sum_{i=1}^{N_\gamma} E_{i,j} \times (\hat{\mathbf{k}}_{\gamma,\text{initial}} \cdot \hat{\mathbf{z}})_i \rangle}{\langle \sum_{i=1}^{N_\gamma} E_{i,j} \rangle} = \frac{T_{j,z}}{T_{j,\text{total}}}. \tag{7.10}$$

7.3 ^{137}Cs Source Scans and Detector Center of Response

The detector alignment as well as the center of response of the two half crystals in each detector package must be measured, modeled, and accounted for by adjusting the geometrical factors. With a source at some arbitrary position along the beam, the θ and ϕ angles are mixed. With a source centered inside each detector ring, the θ angle is 90 degrees and the ϕ

angle is isolated. To isolate the ϕ angle, a 4 mCi ^{137}Cs source was mounted on an x-y stepper motor scanner and scanned in a grid centered along the beam axis inside each of the four detector rings. Inches are used in this section because the x-y scanner was programmed so that 3200 motor steps corresponded to 1 inch. The scan pattern started at the zero position in x, moved to +1 in, +2 in, repeated +2 in, moved to +1 in, moved to zero, moved to -1 in, and then -2 in twice. This pattern was repeated several times and each data run began 60 seconds after the previous run in order to cancel drifts in the detector pedestals. The same pattern was used in the y-direction and then data were taken at points that mix the x and y directions: at (1,1), (1,-1), (-1,1), and (-1,-1). The ^{137}Cs source scan pattern is depicted in blue in figure 7.8.

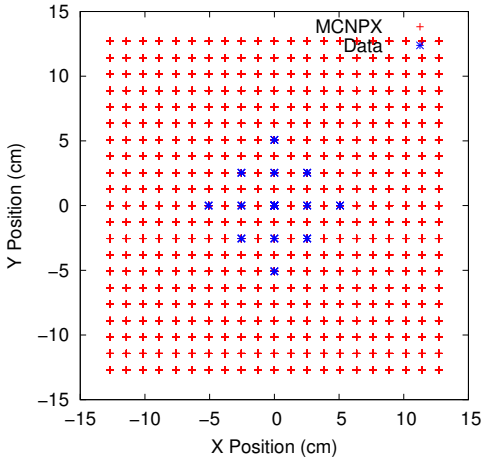

Figure 7.8: Grid scan data points using the 4 mCi ^{137}Cs source are shown in blue. The MCNPX model grid points are shown in red.

Several pedestals were taken at different times during the scan period by removing the source from the detector array. Once a scan was completed for one ring, the source was moved to the center of the next ring and the grid was repeated.

Originally, MCNPX was used to model a much larger grid than the scans, 10 in $\times$ 10 in for 121 total grid points per ring. The MCNPX model initially used a 662 keV gamma point source and was done without changing the starting history number in MCNPX so that each calculation was not independent, but later calculations used a random 48-bit integer to reseed MCNPX for each run and used a more dense grid of 441 grid points per ring as well as adding cross-hair like MCNPX calculations between each ring to fill in the $\hat{\mathbf{z}}$-axis.

The MCNPX simulation scan pattern is depicted in red in figure 7.8. The final simulation uses a small uniform cylindrical source that is 8 mm long and 3 mm in radius. Gammas are emitted from points uniformly inside this volume and isotropically in direction.

The output of the MCNPX simulation is the energy deposition measured in MeV g^{-1} normalized per source particle in each detector, and this should be proportional to the signal in volts for each detector as measured using the ^{137}Cs source up to some arbitrary gain factor. That is to say the x-y distribution in the case of the ^{137}Cs source and the MCNPX simulation should have the same shape and differ only by a scale factor and a small rotation angle, δ_ϕ, that should be of order 35 mrad due to imperfections in the efficiency of the half crystals in each detector unit. The ideal detector response is a function of the (x, y, z) position of the ^{137}Cs source in the MCNPX model. The function is fit to an 8th order polynomial in x and y in GNU Scientific Library, which allows for complicated fitting models in multiple dimensions

$$P(x,y) = \sum_{i=0}^{8} \sum_{j=0}^{8-i} k_{i,j} x^i y^j. \tag{7.11}$$

7.3.1 δ_ϕ Rotation Angles

The δ_ϕ rotation angles affect the ϕ angle in the geometrical factors. The adjusted geometrical factors are then given by a simple transformation of $\phi \to \phi + \delta_\phi$. This allows the adjusted geometrical factors to be expressed in terms of the ideal geometrical factors and the δ_ϕ angles. The derivation is given for the parity allowed geometrical factor, G'_{LR}, using the sum angle identity for the cosine.

$$\begin{aligned}
G'_{\mathrm{LR}} &= \langle \hat{\mathbf{k}}_{\gamma,\mathrm{initial}} \cdot \hat{\mathbf{x}} \rangle' \\
&= \langle \sin(\theta)\cos(\phi + \delta_\phi) \rangle \\
&= \langle \sin(\theta) \times [\cos(\phi)\cos(\delta_\phi) - \sin(\phi)\sin(\delta_\phi)] \rangle \\
&= \langle \sin(\theta)\cos(\phi)\cos(\delta_\phi) - \sin(\theta)\sin(\phi)\sin(\delta_\phi) \rangle \\
G'_{\mathrm{LR}} &= \langle \hat{\mathbf{k}}_{\gamma,\mathrm{initial}} \cdot \hat{\mathbf{x}} \rangle \cos(\delta_\phi) - \langle \hat{\mathbf{k}}_{\gamma,\mathrm{initial}} \cdot \hat{\mathbf{y}} \rangle \sin(\delta_\phi).
\end{aligned} \tag{7.12}$$

Similarly, the adjusted parity violating geometrical factor, G'_{UD}, is given by:

$$G'_{\mathrm{UD}} = \langle \hat{\mathbf{k}}_{\gamma,\mathrm{initial}} \cdot \hat{\mathbf{y}} \rangle' = \langle \hat{\mathbf{k}}_{\gamma,\mathrm{initial}} \cdot \hat{\mathbf{x}} \rangle \sin(\delta_\phi) + \langle \hat{\mathbf{k}}_{\gamma,\mathrm{initial}} \cdot \hat{\mathbf{y}} \rangle \cos(\delta_\phi) \tag{7.13}$$

Recall that the detectors and target have significant finite geometry effects which implies that the corrected geometrical factors will be rather complicated. The expressions in equations (7.12) and (7.13) are surprisingly simple and arise directly from the sum angle identities for sine and cosine. Therefore, all that is needed to apply corrections for the finite geometry effects and imperfections in the detectors is a calculation of the ideal geometrical factors and a measurement and simulation of the detector shift angles.

7.4 Geometrical Factors Results

All three targets used a flat neutron energy spectrum of 3.3 to 13 meV so that energy dependence of the geometrical factors is averaged out. Initial calculations showed that the uncertainty for the G_{Z} factor is greatest for ring 1 in both the chlorine and aluminum simulations. This feature is due to the small signal from capture on the aluminum in the spin flipper which contributes a very different G_{Z} than capture in the target. A similar increase in the uncertainties in the G_{UD} and G_{LR} geometrical factors for ring 1 is also present. A separate set of 200 runs were done with the components of the spin flipper set to air and this feature nearly goes away for the aluminum target. Final calculations of the geometrical factors then isolated the targets themselves so that there is no contribution from other components of the geometry to the geometrical factors.

7.4.1 δ_ϕ Rotation Angles

As expected, the δ_ϕ shift angles are nearly all less than 40 mrad and appear to be somewhat ordered about zero (figure 7.9 and table B.6). There are groups of detectors that have a pattern that repeats in shapes from ring to ring. This can be seen in detectors 17-23 compared to 29-35. These uncertainties come from the fitting algorithm in GSL. Originally, the uncertainties in the δ_ϕ angles for the first ring were approximately a factor of 2 larger

than for the other 3 rings. The initial MCNPX model used for this calculation had been simple and neglected some aspects of the geometry. The downstream end of the spin flipper has a considerable amount of lithium plastic on it as well as 3 mm of lead. A new calculation in MCNPX was done using these new elements of the geometry and the uncertainties for ring 1 came out to be comparable to the other rings. The δ_ϕ angles changed slightly compared to the old MCNPX model, but the error bars overlapped in every case. The change from a point source to a cylindrical source also changed the δ_ϕ angles, but also only slightly. It is reassuring that the incorporation of lead and the cylindrical source still give results that are consistent with simpler models.

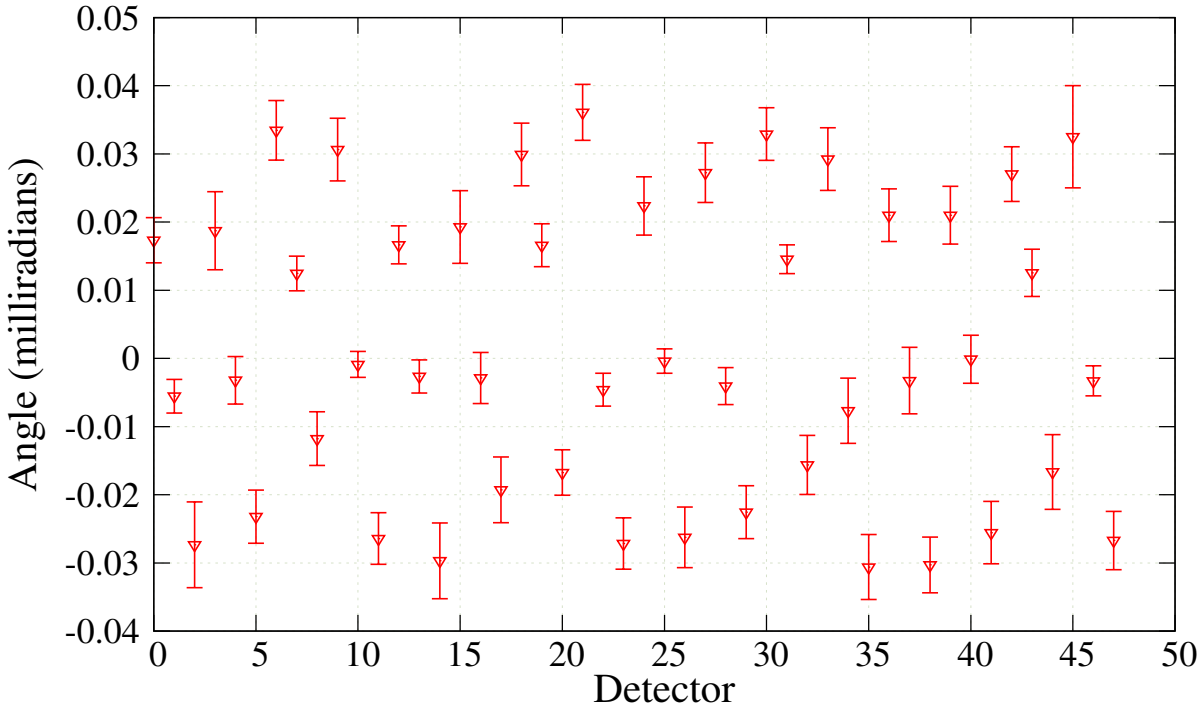

Figure 7.9: δ_ϕ Correction Angles with Uncertainties

7.4.2 Chlorine Target

The uncorrected geometrical factors appear in shape and qualitative magnitude as expected. Detectors 0 and 11 in each ring should have the same parity violating (up-down) geometrical factors and same magnitude but opposite sign parity allowed (left-right) geometrical factors. The G_{LR} factor is least in magnitude for top and bottom detectors and greatest for sides

(figure 7.10). The G_{UD} factor is greatest in magnitude for top and bottom detectors in ring 3, which is expected because the target is inside ring 3. The target is closer to ring 2 than 4 and closer to 4 than 1, so it is expected that the G_{UD} factors for ring 2 will be greater than for ring 4 and that ring 4 will be greater than ring 1. It is also expected that the G_{UD} and G_{LR} factors for each corner detector, like detector 1, should be the same and this is also the case. As mentioned previously, the G_{Z} geometrical factor is a consistency check because it should be a constant for each ring with corner detectors being slightly different than top/side detectors. The statistical uncertainties in the ideal geometrical factors is 0.01% in the case of geometrical factor values near ± 0.9 and 0.1% in the case of geometrical factor values near ± 0.2. The uncertainties in the adjusted geometrical factors are of order 1% for the highest magnitude values, i.e. the geometrical factors that are near 0.9 in value have an uncertainty of about 1%. See table B.2 for the chlorine target ideal geometrical factors and their uncertainties and table B.7 for the adjusted geometrical factors and their uncertainties.

The adjusted geometrical factors do not change significantly compared to the unadjusted factors. The greatest adjustments are found for detectors with small magnitude factors, such as the G_{LR} factor for top/bottom detectors or the G_{UD} factor for side detectors. The maximum factors are roughly 0.9, so the adjustments are of order a few percent.

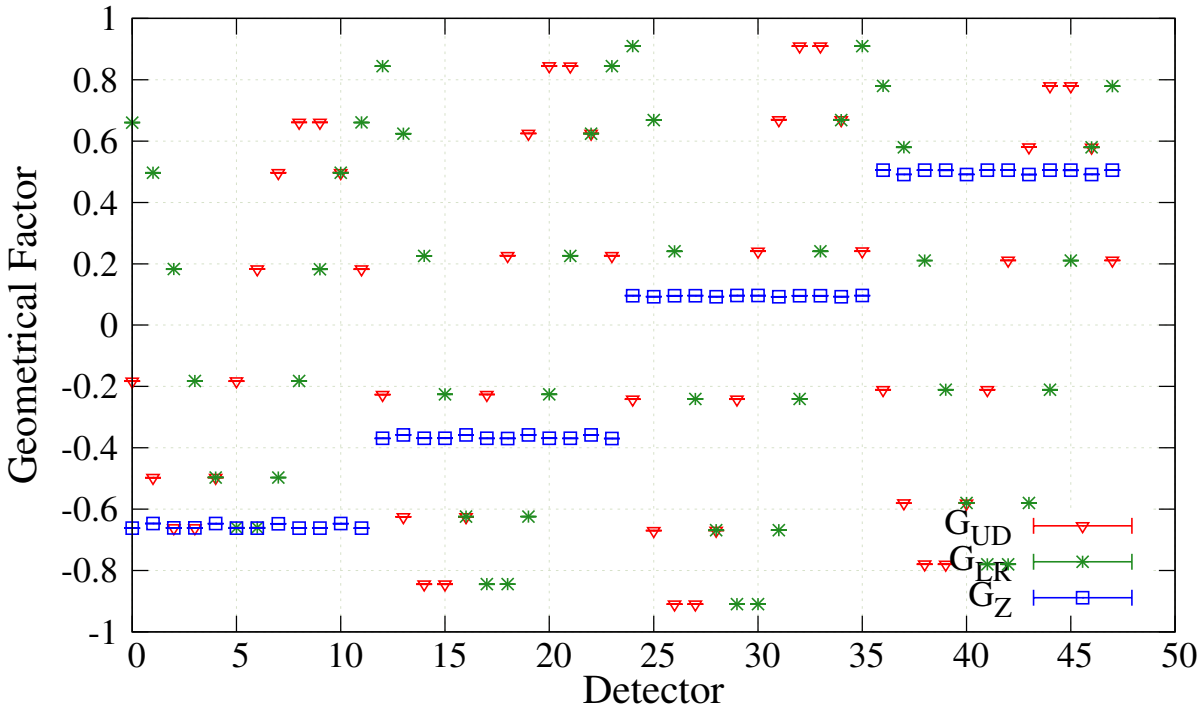

Figure 7.10: G_{UD}, G_{LR}, and G_{Z} Ideal Geometrical Factors, Chlorine Target in Detector Array

7.4.3 Aluminum Target

The aluminum target is a distributed target that is more than 20 cm long. The greatest magnitude geometrical factors are in ring 2 for the aluminum target (figure 7.11), which makes sense because the neutron flux incident on each disc decreases through the target and the upstream end of the target is inside ring 2. The G_{Z} factor is once again nearly a step function with almost constant values for each ring. The adjustments are once again relatively small . The uncertainties in the geometrical factors for aluminum are on the same order as for the chlorine target. The remaining difference in the uncertainty between the rings is due to the increased distance from the target, which lowers the number of photons that reach far away rings. Setting the spin flipper to air also changes the geometrical factors by about 1%. The uncertainties in the adjusted geometrical factors are of order 1% for the highest magnitude values, i.e. the geometrical factors that are near 0.9 in value have an uncertainty

of about 1%. See table B.4 for the aluminum target ideal geometrical factors and their uncertainties and table B.9 for the adjusted geometrical factors and their uncertainties.

There is a systematic uncertainty introduced by the energy dependent absorption and the fact that the aluminum target is distributed in the G_Z direction. Recall that the neutron thermal treatment for aluminum in MCNPX makes the Bragg edges in aluminum visible in the neutron flux. This appears in the geometrical factors for aluminum as dips of order several percent and gives a systematic uncertainty of a few percent to the aluminum geometrical factors. This was found by doing a scan in the energy from 1.5 meV to 20 meV or about 2 Å to 7 Å. Bragg edges are expected to be at 4.05 Å and 4.67 Å and the geometrical factors drop the lowest at about 4.55 Å and 3.95 Å.

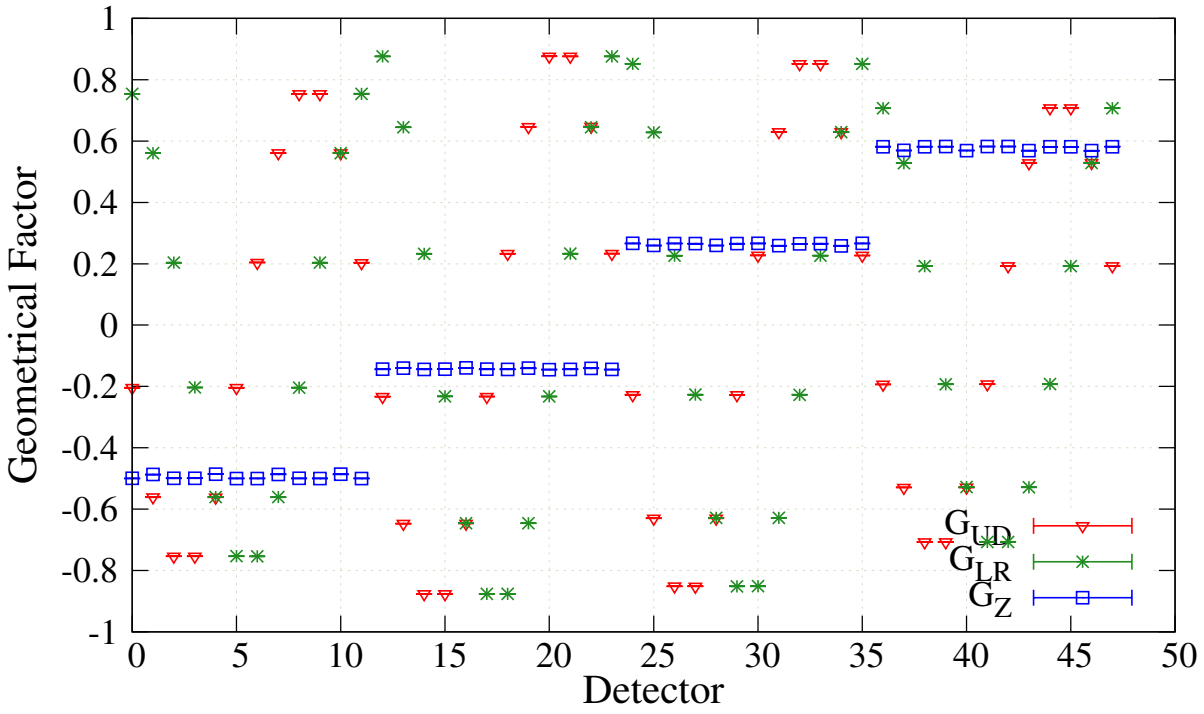

Figure 7.11: G_{UD}, G_{LR}, and G_Z Ideal Geometrical Factors, Aluminum disc target in the detector array.

7.4.4 Hydrogen Target

Runs with the hydrogen target were calculated with photon production disabled in all parts of the geometry except the para-hydrogen. The geometrical factors for rings 2 and 3 are

nearly equal in magnitude and rings 1 and 4 are also nearly equal in magnitude, as seen in figure 7.12. The G_Z factor is once again nearly a step function with almost constant values for each ring. One expects ring 4 to see the fewest gammas, rings 2 and 3 to be roughly equal, and ring 1 to see fewer gammas than rings 2 and 3. The uncertainties in the adjusted geometrical factors are of order 1% for the highest magnitude values, i.e. the geometrical factors that are near 0.9 in value have an uncertainty of about 1%. See table B.5 for the hydrogen target ideal geometrical factors and their uncertainties and table B.10 for the adjusted geometrical factors and their uncertainties.

There is a definite energy dependence that results from the energy dependent scattering cross section on para-hydrogen. This gives a systematic uncertainty to the hydrogen geometrical factors of a few percent. The geometrical factors are also very sensitive to the ortho-para ratio because the ortho-para ratio changes the spatial distribution of gammas emitted from the target. Each detector ring behaves differently as the para concentration changes. For example, G_{UD} for detector 36 increases from 0.67 to 0.73 as the para concentration goes from 90% to 100% and the uncertainty in the up-down geometrical factors is of order a few percent for very high para concentrations near 100%. For detector 0, G_{UD} decreases from 0.76 to 0.74 for the same para concentrations and the uncertainty at the highest concentrations is approximately 0.5%. Detector 12 decreases from 0.885 to 0.868 and the uncertainty at the highest concentrations is approximately 0.25%. For detector 24, there is an increase from 0.83 to 0.855 and the uncertainty at the highest concentrations is approximately 1%. Hydrogen carries along systematic uncertainties each of order 1 or 2 percent due to energy dependence and dependence on the para concentration.

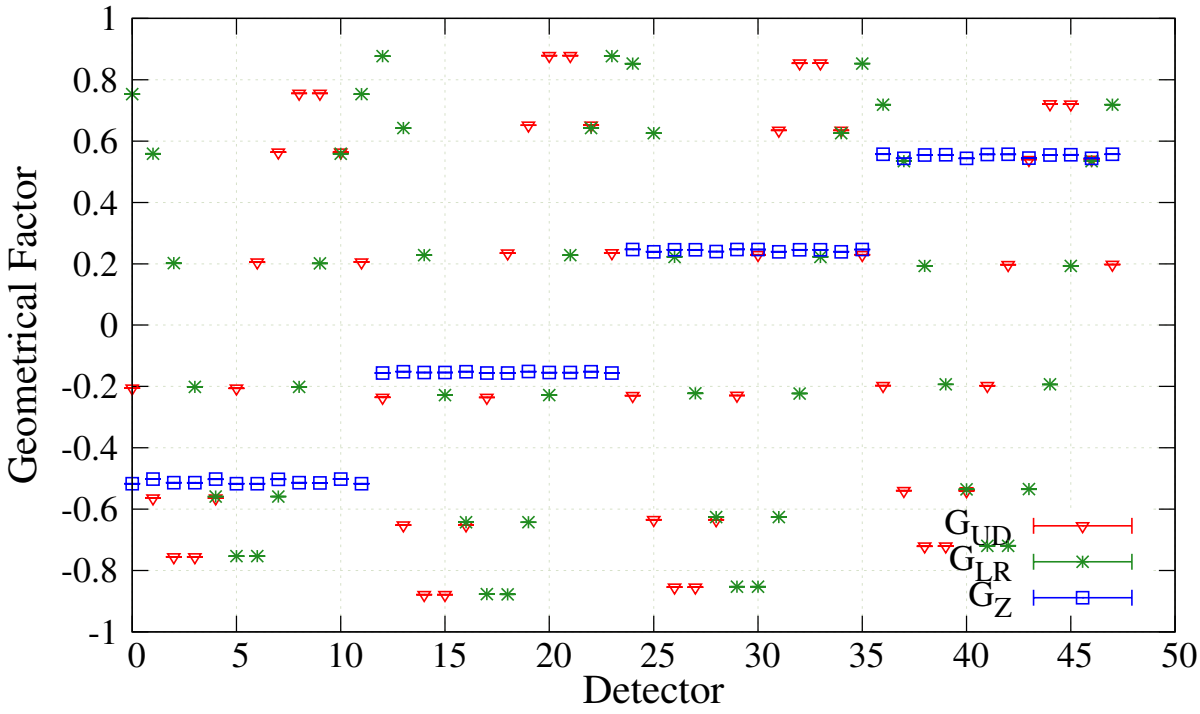

Figure 7.12: G_{UD}, G_{LR}, and G_{Z} Ideal Geometrical Factors, Hydrogen Target

7.4.5 Systematics due to Uncertainty in Position of Targets

The geometrical factors alone are sensitive to the position of the target and beam. The L-R and U-D geometrical factors are dependent on the $\hat{\mathbf{z}}$ geometrical factor, and therefore the $\hat{\mathbf{z}}$ position of the target, through the angle θ. All calculations assumed that targets are in ideal positions, so the position dependence of the geometrical factors is investigated as well.

U-D and L-R shifts - Pairwise Geometrical Factors

A shift of the target/beam in the up-down or left-right directions can produce a significant change in the geometrical factors for individual detectors, but the geometrical factors for a pair of detectors is insensitive to small shifts. Rather than analyzing data for each detector, we can analyze pairs of detectors. It important to note the relative signs of ideal geometrical

factors for pairs of detectors, with the detector pair denoted by $i = 0..5$ and $j = i + 6$,

$$\begin{aligned} G_{\mathrm{UD},i} &\approx -G_{\mathrm{UD},j}, \\ G_{\mathrm{LR},i} &\approx -G_{\mathrm{LR},j}. \end{aligned} \tag{7.14}$$

In the case of analyzing pairs, the difference of two geometrical factors is used in the analysis,

$$\begin{aligned} G_{\mathrm{UD},ij} &= G_{\mathrm{UD},i} - G_{\mathrm{UD},j} \\ G_{\mathrm{LR},ij} &= G_{\mathrm{LR},i} - G_{\mathrm{LR},j}. \end{aligned} \tag{7.15}$$

The pairwise geometrical factors in equations (7.15) are insensitive to small displacements of the target in the x and y directions. Take two point detectors, detector i at coordinates (15 cm,15 cm) and detector j at (-15 cm,-15 cm) with a point source at the origin, approximately the coordinates are a realistic pair of corner detectors in the NPDGamma detector array. The geometrical factors for each will be as follows:

$$\begin{aligned} G_{\mathrm{LR},i} &= \cos(\tfrac{\pi}{4}) = 0.7071067813 \\ G_{\mathrm{UD},i} &= \sin(\tfrac{\pi}{4}) = 0.7071067813 \\ G_{\mathrm{LR},j} &= \cos(\tfrac{5\pi}{4}) = -0.7071067813 \\ G_{\mathrm{UD},j} &= \sin(\tfrac{5\pi}{4}) = -0.7071067813. \end{aligned} \tag{7.16}$$

The pairwise geometrical factors are then given by

$$\begin{aligned} G_{\mathrm{LR},ij} &= G_{\mathrm{LR},i} - G_{\mathrm{LR},j} = 1.414213563 \\ G_{\mathrm{UD},ij} &= G_{\mathrm{UD},i} - G_{\mathrm{UD},j} = 1.414213563. \end{aligned} \tag{7.17}$$

Under a displacement of the source by 1 cm in the $+x$ direction, detector i has new coordinates $(14\text{ cm}, 15\text{ cm})$ and detector j is at coordinates $(16\text{ cm}, 15\text{ cm})$. The geometrical

factors for each detector individually will shift by a significant fraction of approximately 4%,

$$\begin{aligned} G'_{\mathrm{LR},i} &= \cos(\arctan(\tfrac{14}{15})) = 0.7310552682 \\ G'_{\mathrm{UD},i} &= \sin(\arctan(\tfrac{14}{15})) = 0.6823182504 \\ G'_{\mathrm{LR},j} &= \cos(\pi + \arctan(\tfrac{16}{15})) = -0.6839411288 \\ G'_{\mathrm{UD},j} &= \sin(\pi + \arctan(\tfrac{16}{15})) = -.7295372041. \end{aligned} \tag{7.18}$$

However, the pairwise geometrical factor is insensitive to the small displacement,

$$\begin{aligned} G_{\mathrm{LR},ij} &= G_{\mathrm{LR},1} - G_{\mathrm{LR},2} = 1.414996397 \\ G_{\mathrm{UD},ij} &= G_{\mathrm{UD},1} - G_{\mathrm{UD},2} = 1.411855455. \end{aligned} \tag{7.19}$$

In the left-right case, the deviation is 0.055% of the ideal pairwise geometrical factor and the deviation in the up-down case is 0.167% of the ideal pairwise geometrical factor. Pairwise up-down and left-right geometrical factors aren't tabulated, but can be determined directly from the single detector geometrical factors by equaiton 7.15.

Shifts along the Beam Axis

The uncertainty in the geometrical factors for the hydrogen target under shifts along the beam axis was modeled in MCNPX. Shifts of ±1 cm were modeled. The G_{Z} geometrical factor depends only on the θ angle, and a change in the theta angle changes G_{LR} and G_{UD}. The G_{Z} geometrical factor has the strongest sensitivity to beam axis shifts, as expected, and can change by 5% to 15%. The results are symmetric as expected, for instance, ring 1 and 4 shift the same amount but opposite signs, as do rings 2 and 3. The shift for rings 2 and 3 is smaller in magnitude than rings 1 and 4, since the target is physically inside these rings making them less sensitive to small shifts. Under a shift of ±1 cm, G_{LR} and G_{UD} for rings 1 and 4 shift by about 1.5%. Under the same shift, G_{LR} and G_{UD} for rings 2 and 3 shift by about 0.5%. See figure 7.13 for G_{LR}, figure 7.14 for G_{UD}, and 7.15 for G_{Z}. These calculations were performed at ortho/para concentrations corresponding to 15 K, or 99.989% para and 0.011% ortho.

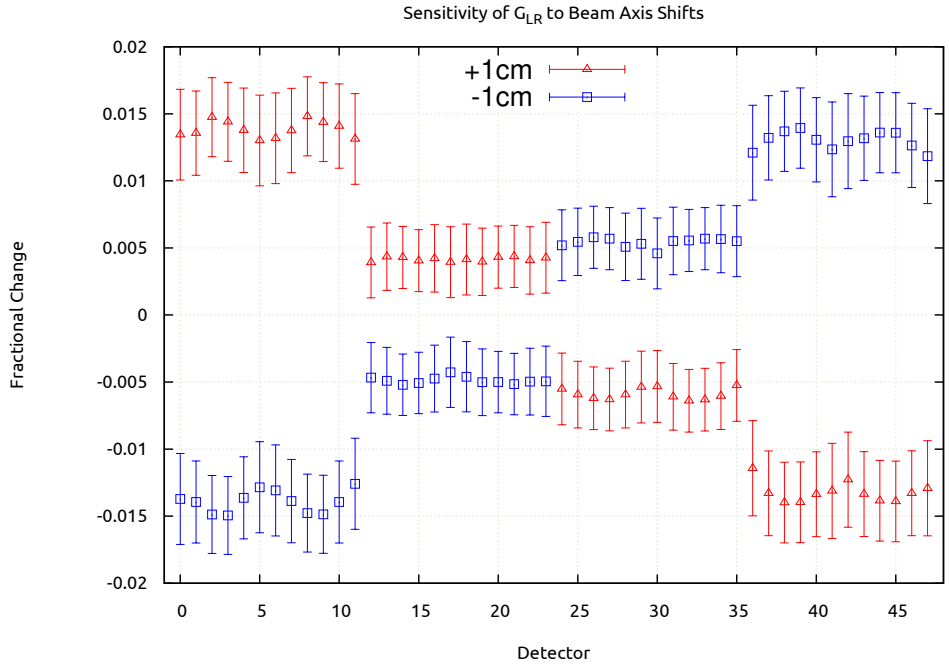

Figure 7.13: Beam Axis Position Dependence, Hydrogen Target, G_{LR}

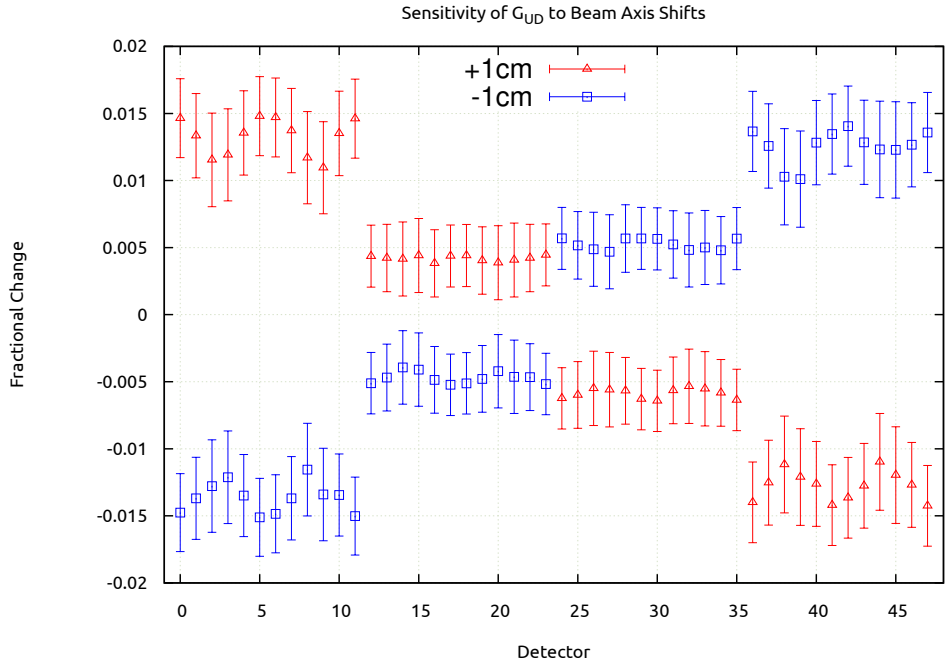

Figure 7.14: Beam Axis Position Dependence, Hydrogen Target, G_{UD}

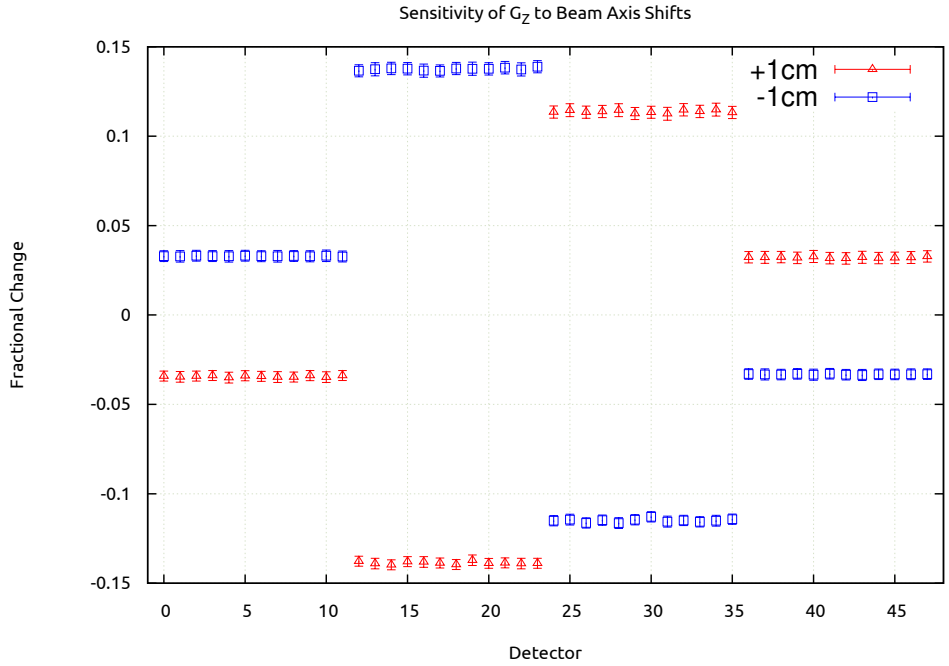

Figure 7.15: Beam Axis Position Dependence, Hydrogen Target, G_Z

7.5 Geometrical factors summary and experimental validation

The geometrical factors are an improvement on the previously used method of extracting the asymmetry for the NPDGamma experiment used in the LANSCE iteration, which described the asymmetry within all four rings as a single sinusoidal function of the detector angles. Because of the complicated distribution of neutron captures within the apparatus, a Monte Carlo model of the apparatus was used to simulate the sensitivity of each detector to the physics asymmetry. The simulation method must also be validated by experiments, which was accomplished using the chlorine target.

The asymmetry for chlorine is very large and the asymmetry can be measured in about 1 day of beam time compared to the several years beam time for hydrogen, which makes chlorine a perfect way to test the geometrical factors. A teflon cased carbon tetrachloride target was placed inside the downstream end of the spin flipper for periodic checks on the apparatus. Ring 1 is most sensitive to the asymmetry in this configuration with the sensitivity decreasing as the distance from the ring to the chlorine target increases. See

figure 7.16 for the expected sensitivity to up-down, left-right, and z asymmetries for this configuration for all 48 detectors. This is the best data set that was taken with the NPDGamma apparatus for validation of the geometrical factors calculation.

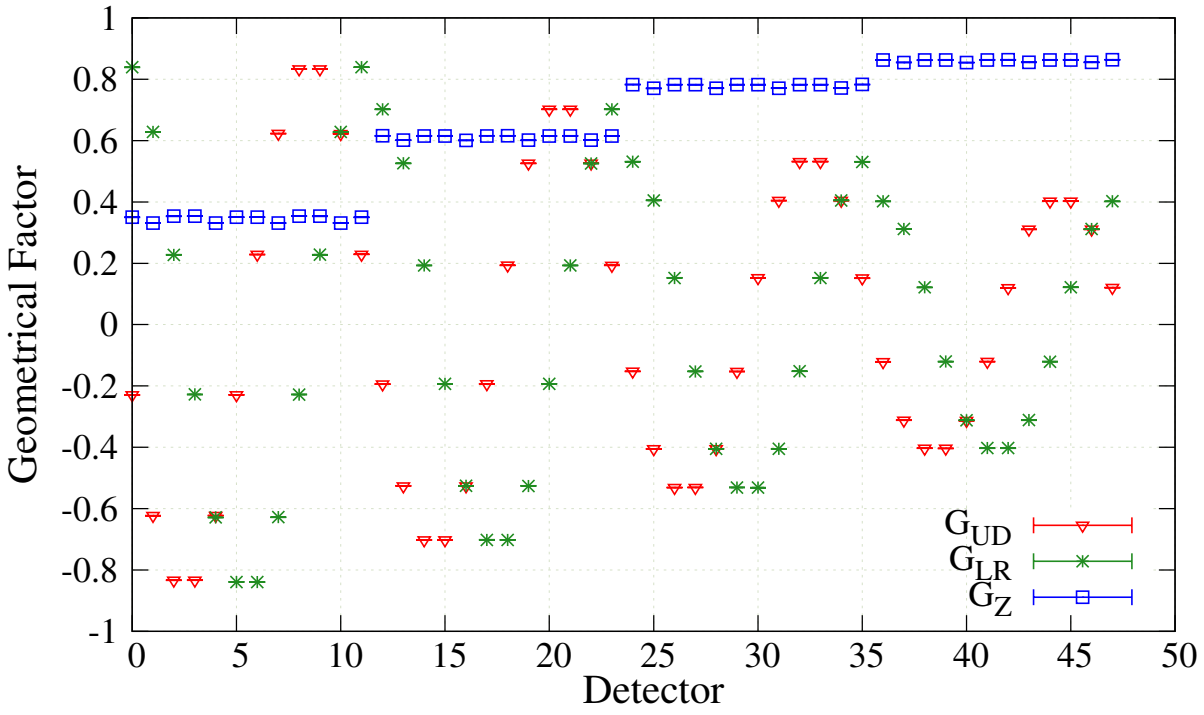

Figure 7.16: G_{UD}, G_{LR}, and G_{Z} Ideal Geometrical Factors, Chlorine Target in Spin Flipper

Unfortunately, ring 1 was not being used when this data were taken because the data acquisition system was being re-designed and only rings 2-4 were functional at the time. The single detector asymmetries are extracted using the arithmetic mean method. The raw asymmetries with uncertainties from fitting each detector to a Gaussian are fit to the following

$$A_{\gamma,raw} = A_{\mathrm{UD}} \times G_{\mathrm{UD}} + A_{\mathrm{LR}} \times G_{\mathrm{LR}}. \tag{7.20}$$

The χ^2 per degree of freedom from this fit is 1.36, indicating a good fit of the data to the model. The resulting up-down asymmetry is 2.07×10^{-5}. The up-down geometrical factors for rings 2, 3, and 4 are shown in figure 7.17 along with the raw asymmetries scaled by G_{UD} such that the asymmetries appear on the same scale as the geometrical factors. The left-right asymmetry here is approximately 2 orders of magnitude smaller than the up-down

asymmetry, so the asymmetries are expected to match the up-down geometrical factors well. The agreement between the two is clear.

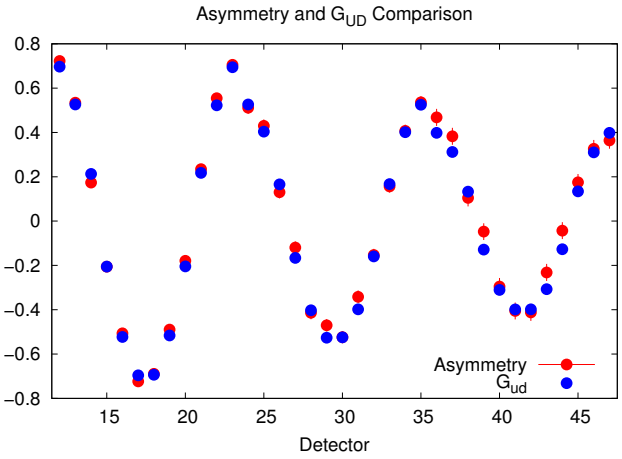

Figure 7.17: Chlorine Asymmetry with geometrical factors using the calculated sensitivity for each ring

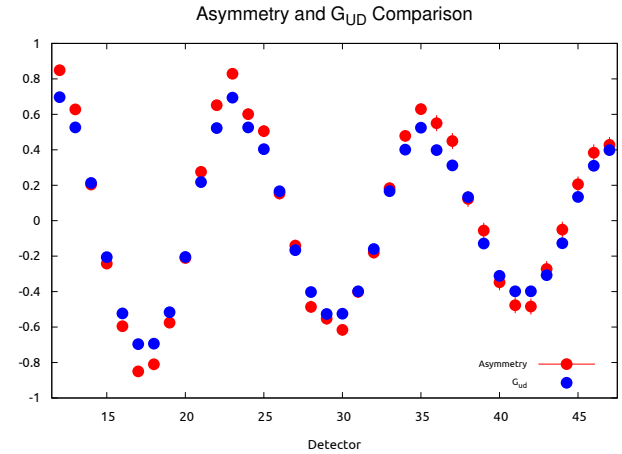

Figure 7.18: Chlorine asymmetry with geometrical factors using the same sinusoidal sensitivity for each ring

The geometrical factors model represents a significant improvement over the method using a sinusoidal shape that doesn't vary between ring. For comparison, figure 7.18 shows the result of fitting the same raw asymmetries with the geometrical factors for ring 2 used for each ring. The asymmetry result becomes 1.785×10^{-5} with a χ^2 per degree of freedom of 13, indicating a very poor fit to the data.

7.6 Polarization Model

The average polarization of the neutron beam upon capture is an important systematic effect in the extraction of the physics asymmetry from the raw asymmetry in NPDGamma and auxiliary experiments. Neutrons can undergo spin-flip scattering in beam windows, shielding, and off of orthohydrogen in the target. The polarization of the beam without the target in place can be measured using ^{3}He spin analysis, but the polarization upon capture must be modeled separately. In order to model this effective polarization, MCNPX must be modified to approximate spin interaction probabilities and this is performed in a manner similar to the geometrical factors.

The isotopic composition of the materials used in the MCNPX model is shown in table B.1. When two isotopes are listed with a single percentage, those isotopes are present in equal proportions. The transmission of neutrons through the hydrogen target is strongly dependent on the relative concentrations of parahydrogen and orthohydrogen, with transmission increasing with the parahydrogen concentration. For pure orthohydrogen, neutrons do not penetrate deeply into the target and are instead scattered back upstream.

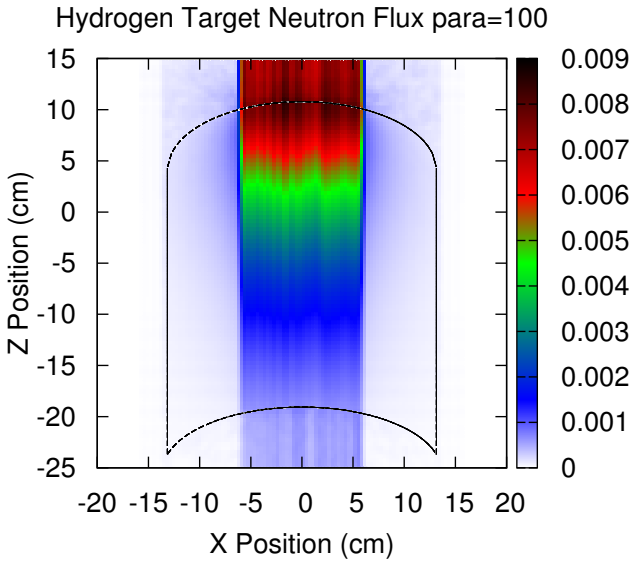

Figure 7.19: Mesh grid of neutron flux for 100% parahydrogen target volume.

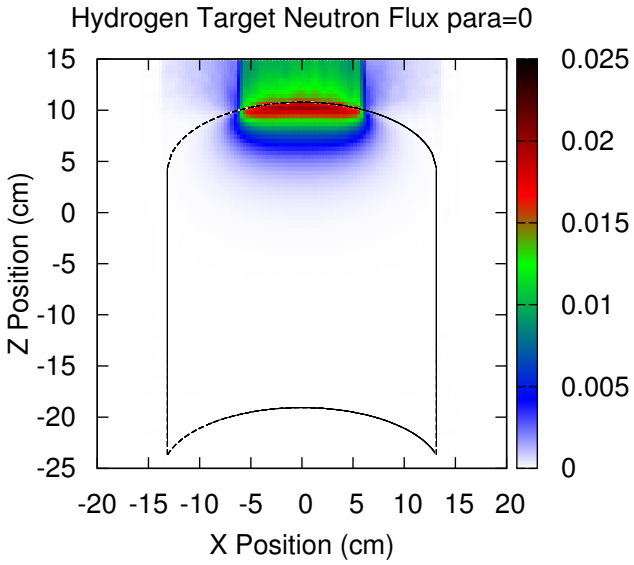

Figure 7.20: Mesh grid of neutron flux for 100% orthohydrogen target volume.

7.6.1 Model

MCNPX does not have built in capabilities to track the spin of particles. A method to track the neutron spin was incorporated by using an array that is banked along with particles that keeps track of spin up (1) and spin down (0). MCNPX does not allow for a native way to mix orthohydrogen and parahydrogen in a single material specification, however this can be done if one of the spin isomers, in this case orthohydrogen, is artificially labeled as ^{4}H. The simulation assumes that all source neutrons are initially have spin 1, which means that the true polarization of the beam as measured with ^{3}He can be applied later as a multiplicative factor.

As neutrons propagate through the model, the scattering material is determined and MCNPX finds the proper cross section tables for that isotope, adjusts the particle momentum and creatures daughter particles, and the calculation would normally continue. Instead, there is an additional step in which the neutron spin tag is flipped probabilistically as described below. Neutrons that have flipped once are able to flip back on subsequent scatters.

The scattering amplitude for scattering from a neutron is shown in equation (7.21), which has 4 terms, shown in equation (7.22)[Blume, 1963]

$$U_i^{ss'} = \langle s'|(b_i - p_i \vec{S_{\perp i}} \cdot \vec{\sigma} + B_i \vec{I_i} \cdot \sigma)|s\rangle. \tag{7.21}$$

$$\begin{aligned} U^{++} &= b - pS_{\perp z} + BI_z, \\ U^{--} &= b + pS_{\perp z} - BI_z, \\ U^{+-} &= -p(S_{\perp x} + iS_{\perp y}) + B(S_{\perp x} + iS_{\perp y}), \\ U^{-+} &= -p(S_{\perp x} - iS_{\perp y}) + B(S_{\perp x} - iS_{\perp y}), \end{aligned} \tag{7.22}$$

where b is the coherent nuclear scattering amplitude, $\hat{\mathbf{z}}$ is the neutron polarization axis, p is the magnetic scattering amplitude, $\vec{S_\perp}$ is the projection of the neutron spin onto the plane perpendicular to the scattering vector, $\vec{I}$ is the nuclear spin, and B is the spin-dependent nuclear scattering amplitude. For nuclear-spin incoherent scattering, only the $B\vec{I}$ term remains from equation (7.21). The calculation of the differential scattering cross section simplifies to the non-spin-flip (equation (7.23)) and spin-flip (equation (7.24)) differential cross sections[Blume, 1963]. Therefore, the probability of a spin-flip incoherent scatter for a particular isotope is $\frac{2}{3}$ for a mono-isotopic sample[Moon et al., 1969],

$$\frac{d\sigma^{++}}{d\Omega} = \frac{d\sigma^{--}}{d\Omega} = \tfrac{1}{3}B^2 I(I+1) \quad \text{(non-spin-flip)}, \tag{7.23}$$

$$\frac{d\sigma^{+-}}{d\Omega} = \frac{d\sigma^{-+}}{d\Omega} = \tfrac{2}{3}B^2 I(I+1) \quad \text{(spin-flip)}. \tag{7.24}$$

The probabilities listed in equation (7.25) are designed to capture the probability of an incoherent scattering event given that a neutron is interacting with that specific isotope. The MCNPX calculation used implicit capture so that capture events do not cause a neutron to stop propagating, but rather capture events produce the appropriate γ-rays and then decrease the weight of a neutron and continue propagating that neutron. MCNPX handles the bookkeeping for the probability of interaction with copper-63 in a material containing aluminum-27, so these factors are not included in the probabilities listed. The reactions that have been incorporated into the model along with their probabilities are shown in equation

(7.25). These reactions are for nuclei with non-zero nuclear spin that are relevant to the NPDGamma MCNPX model that have incoherent cross sections found from [Munter, 2013],

$$
\begin{aligned}
n_{\uparrow} + {}^{1}H_{ortho} &\rightarrow n_{\downarrow} + {}^{1}H_{ortho} & P_{flip} &= 0.6497 \\
n_{\uparrow} + {}^{1}H_{ortho} &\rightarrow n_{\downarrow} + {}^{1}H_{para} & P_{flip} &= 1.0 \\
n_{\uparrow} + {}^{1}H_{para} &\rightarrow n_{\downarrow} + {}^{1}H_{para} & P_{flip} &= 0.0 \\
n_{\uparrow} + {}^{1}H_{para} &\rightarrow n_{\downarrow} + {}^{1}H_{ortho} & P_{flip} &= 1.0 \\
n_{\uparrow} + {}^{1}H_{bound} &\rightarrow n_{\downarrow} + {}^{1}H_{bound} & P_{flip} &= 0.6497 \\
n_{\uparrow} + {}^{6}Li &\rightarrow n_{\downarrow} + {}^{6}Li & P_{flip} &= 0.000489 \\
n_{\uparrow} + {}^{7}Li &\rightarrow n_{\downarrow} + {}^{7}Li & P_{flip} &= 0.3597 \\
n_{\uparrow} + {}^{14}N &\rightarrow n_{\downarrow} + {}^{14}N & P_{flip} &= 0.0372 \\
n_{\uparrow} + {}^{27}Al &\rightarrow n_{\downarrow} + {}^{27}Al & P_{flip} &= 0.00315 \\
n_{\uparrow} + {}^{35}Cl &\rightarrow n_{\downarrow} + {}^{35}Cl & P_{flip} &= 0.0475 \\
n_{\uparrow} + {}^{37}Cl &\rightarrow n_{\downarrow} + {}^{37}Cl & P_{flip} &= 0.0004107 \\
n_{\uparrow} + {}^{55}Mn &\rightarrow n_{\downarrow} + {}^{55}Mn & P_{flip} &= 0.01726 \\
n_{\uparrow} + {}^{63}Cu &\rightarrow n_{\downarrow} + {}^{63}Cu & P_{flip} &= 0.000412 \\
n_{\uparrow} + {}^{65}Cu &\rightarrow n_{\downarrow} + {}^{65}Cu & P_{flip} &= 0.01599 \\
n_{\uparrow} + Zn &\rightarrow n_{\downarrow} + Zn & P_{flip} &= 0.0011.
\end{aligned}
\tag{7.25}
$$

The ${}^{1}H_{ortho}$ implies scattering off of liquid orthohydrogen in the target volume, ${}^{1}H_{para}$ implies parahydrogen in the target volume, and ${}^{1}H_{bound}$ implies scattering off of hydrogen elsewhere in the model, such as in the lithium plastic shielding.

The spin-flip scattering reactions in equation 7.25 for ortho and parahydrogen have to be addressed in a manner different from each other isotope. For all other isotopes, the probability of a possible spin flip reaction is $\frac{2}{3}$ of the ratio of the incoherent scattering cross section to the energy dependent total cross section. For ${}^{1}H_{bound}$ the probability of a spin flip equals the probability of a non-absorption event because incoherent scattering cross sections could not be found.

The average polarization is determined by tallying the energy deposition in each detector from photons binned by the neutron spin state at the capture event for that photon. The average polarization for each detector, i, is found by equation (7.26).

$$P_{i,\text{ave}} = \frac{E_{i,\uparrow} - E_{i,\downarrow}}{E_{i,\uparrow} + E_{i,\downarrow}} \tag{7.26}$$

7.6.2 Hydrogen Kernels

The basis for the hydrogen scattering kernels is the model of Young and Koppel [Young and Koppel, 1964], which addresses the scattering of slow neutrons from gaseous orthohydrogen and parahydrogen incorporating the rotational, vibrational, and spin correlations and allows for free translation of the molecules. This model matches well with experiment and is approximately valid for neutrons with energy above 7 meV scattering from liquid hydrogen. Below this energy, correlations between neighboring molecules in the liquid have to be taken into account and the gas model breaks down. The terms in the scattering cross section are modified in the method described by Keinert and Sax [Keinert and Sax, 1987], which includes hindered translation of the molecules giving the molecules an effective mass of approximately 20 molecular masses [MacFarlane, 1998]. The liquid model better describes the drop in the cross section below 5 meV, where there is intermolecular interference in the liquid that is not seen in the gas.

Since MCNPX does not natively track the spin of the neutrons, it also does not track whether a scattering interaction with orthohydrogen should lead to a spin exchange between the neutron and the molecule. However, the results of the scattering event should carry the signature of the inelastic reactions that transform orthohydrogen into parahydrogen and vice versa, in that there is a kinetic energy change of 14.7 meV shared between the molecule and the neutron with parahydrogen $\rightarrow$ orthohydrogen losing 14.7 meV and orthohydrogen $\rightarrow$ parahydrogen gaining 14.7 meV.

From conservation of energy and momentum, the recoil energy of the molecule is given by

$$E_{\text{recoil}} = \frac{m_{\text{n}}}{m_{\text{m}}}\left(E_{\text{i}} - 2\sqrt{E_{\text{i}}E_{\text{f}}}\hat{\mathbf{k}}_{\text{i}} \cdot \hat{\mathbf{k}}_{\text{f}} + E_{\text{f}}\right), \tag{7.27}$$

where E_{i} and E_{f} are the initial and final neutron energies, $\hat{\mathbf{k}}_{\text{i}}$ and $\hat{\mathbf{k}}_{\text{f}}$ are the initial and final neutron velocity vectors, m_{n} is the neutron mass, and m_{m} is the mass of the molecule. Figures 7.21 and 7.22 show plots of ΔE versus E_{recoil} with the initial mass factor on the

recoil energy dropped. The regions near 14.7 meV were fit to a gaussian in ΔE and the full-width-half-maximum was found for the non-gaussian E_{recoil} in order to determine the ellipses that are shown in black. These ellispses correspond to 1, 2, and 3σ levels for the inelastic scattering peaks near 14.7 meV. The 3σ ellipse is used for the depolarization calculation, such that any ΔE and E_{recoil} inside the ellipse is determined to be an orthohydrogen $\rightarrow$ parahydrogen or parahydrogen $\rightarrow$ orthohydrogen scattering event and therefore has a neutron spin-flip probability of unity. If the event lies outside the ellipse, it is determined to be an parahydrogen $\rightarrow$ parahydrogen event with spin flip probability of zero or orthohydrogen $\rightarrow$ orthohydrogen event with spin flip probability of $\frac{2}{3}$.

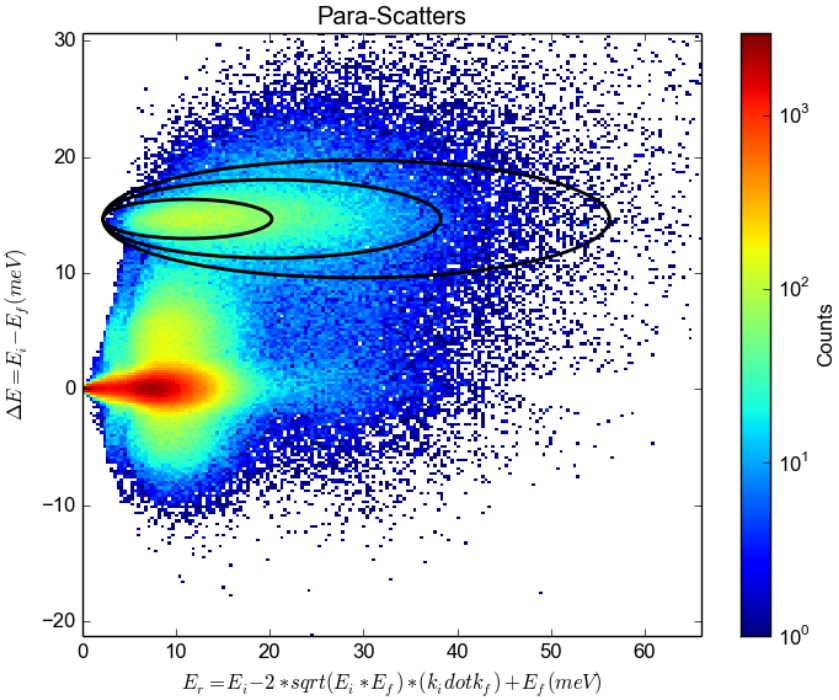

Figure 7.21: Parahydrogen scattering kinematics

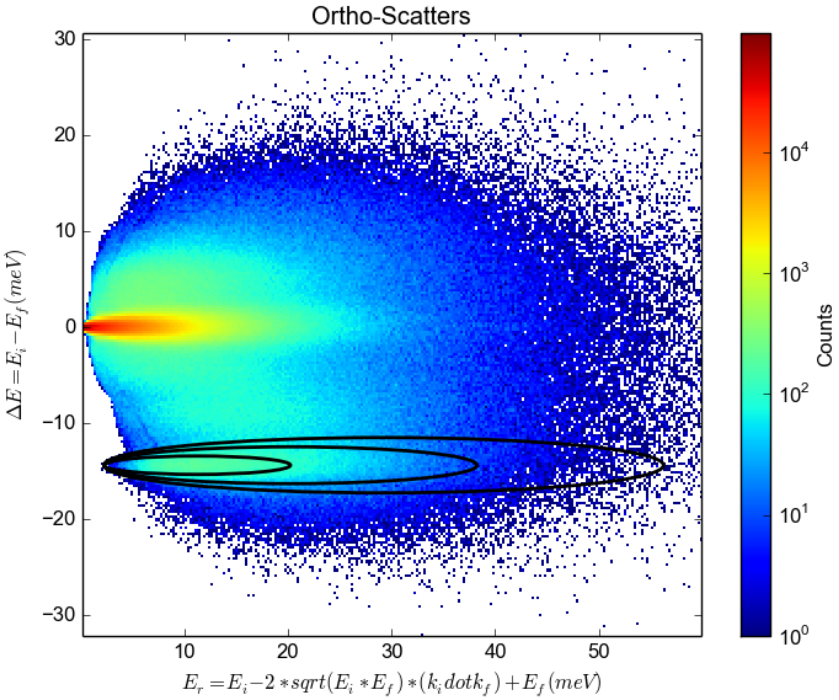

Figure 7.22: Orthohydrogen scattering kinematics

7.6.3 Results

Multiple configurations have been simulated and all simulations first used neutron energies linearly interpolated between 2.3 meV and 13 meV (2.5 Å to 6.0 Å), and later used a more accurate model of the chopped neutron spectrum with correct weights.

The average polarization calculation uses the upper limit orthohydrogen concentration and the thermodynamic orthohydrogen concentration in order to provide an uncertainty, because the orthohydrogen and parahydrogen concentrations in the target vessel are not known. The estimate of the upper limit of the orthohydrogen concentration is described in chapter 8 where it is used to provide an upper bound on the parahydrogen cross section.

The hydrogen target density used in these calculations was 0.0739013 $\mathrm{g\,cm^{-3}}$, corresponding to approximately 17 K. The air material in these simulations was dry air with no humidity. These calculations assume that $\frac{2}{3}$ of incoherent scatters on orthohydrogen produce a flip and allows every isotope to flip spins. Figure 7.23 shows the results for the average polarization on capture on liquid hydrogen in the vessel. The average polarization is found

using equation 7.26, and the uncertainty for detector i is found by

$$\sigma_i^2 = \frac{4(\sigma_{i,\downarrow}^2 E_{i,\uparrow}^2 + \sigma_{i,\uparrow}^2 E_{i,\downarrow}^2)}{(E_{i,\downarrow} + E_{i,\uparrow})^4}. \tag{7.28}$$

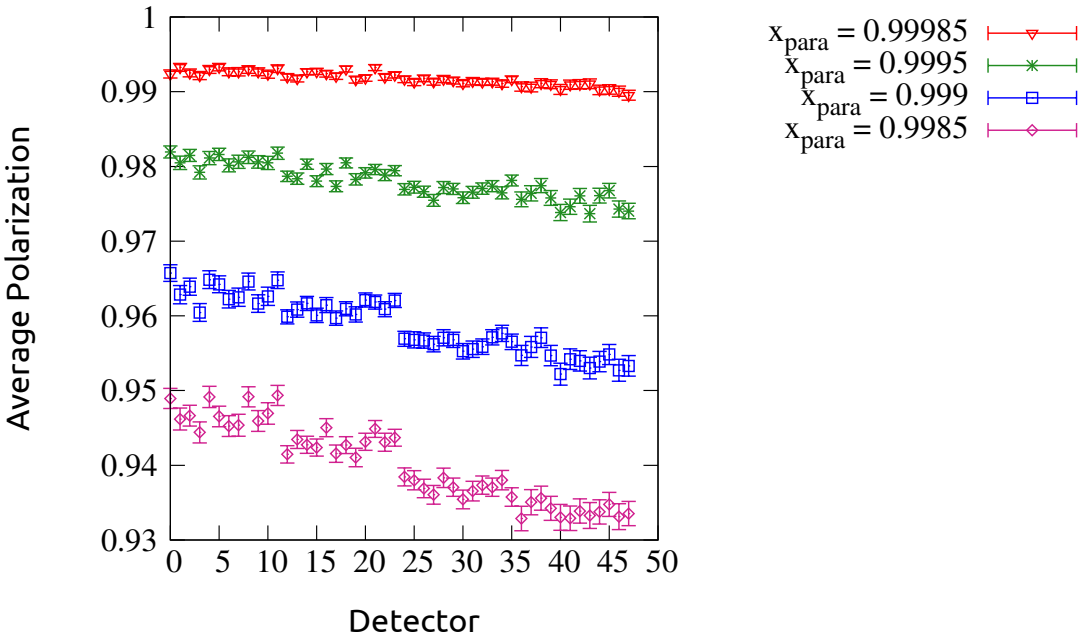

Figure 7.23: Average polarization for neutrons that capture on hydrogen in the vessel as a function of parahydrogen concentration.

The ring j average is then found by taking a weighted average of the 12 detectors in each ring

$$P_{j,\text{ave}} = \frac{\sum_{i=0}^{11} \sigma_i^2 P_i}{\sum_{i=0}^{11} \sigma_i^2}, \tag{7.29}$$

and the uncertainty for each ring is found by

$$\sigma_{j,\text{ave}}^2 = \sum_{i=0}^{11} \sigma_i^2. \tag{7.30}$$

Tables 7.1 and 7.2 contain the ring averaged results for capture on liquid hydrogen in the vessel, and these tables represent the upper and lower bounds on the estimate of the average polarization on capture. As expected, the average polarization decreases as the neutrons

Table 7.1: Average polarization per ring for captures on liquid hydrogen in the vessel with $x_{\text{para}} = 0.99985$, corresponding to thermal equilibrium.

Ring	$P_{j,\text{ave}}$	$\sigma_{j,\text{ave}}$
1	0.992762	0.00015171
2	0.992346	0.000124349
3	0.991442	0.000134414
4	0.990606	0.000182754
Total	0.991911	7.19052e-05

Table 7.2: Average polarization per ring for captures on liquid hydrogen in the vessel with $x_{\text{para}} = 0.9985$, corresponding to the upper limit orthohydrogen concentration.

Ring	$P_{j,\text{ave}}$	$\sigma_{j,\text{ave}}$
1	0.94705	0.000404387
2	0.942939	0.000336016
3	0.937068	0.000361128
4	0.933862	0.000477352
Total	0.94073	0.000192349

reach the rear of the target because neutrons that reach deep within the target are more likely to have interacted and undergone a spin flip.

The average polarization of neutrons on capture with the aluminum in the apparatus is a systematic that requires a separate model, because the aluminum parity violation signal is also included in the measurement on hydrogen. All γ-ray production in MCNPX was turned off in cells that do not contain aluminum. The calculation then proceeded in a manner identical to the previous calculation on hydrogen.

Table 7.3: Average polarization per ring for captures on aluminum 6061 in the apparatus with $x_{\text{para}} = 0.99985$, corresponding to thermal equilibrium.

Ring	$P_{j,\text{ave}}$	$\sigma_{j,\text{ave}}$
1	0.996104	0.000332658
2	0.995561	0.000331825
3	0.993964	0.000482961
4	0.994169	0.000601427
Total	0.995331	0.000199322

Table 7.4: Average polarization per ring for captures on aluminum 6061 in the apparatus with $x_{\text{para}} = 0.9985$, corresponding to the upper limit orthohydrogen concentration.

Ring	$P_{j,\text{ave}}$	$\sigma_{j,\text{ave}}$
1	0.979971	0.000772723
2	0.972275	0.000868999
3	0.958171	0.00134986
4	0.955601	0.00188852
Total	0.972399	0.000511098

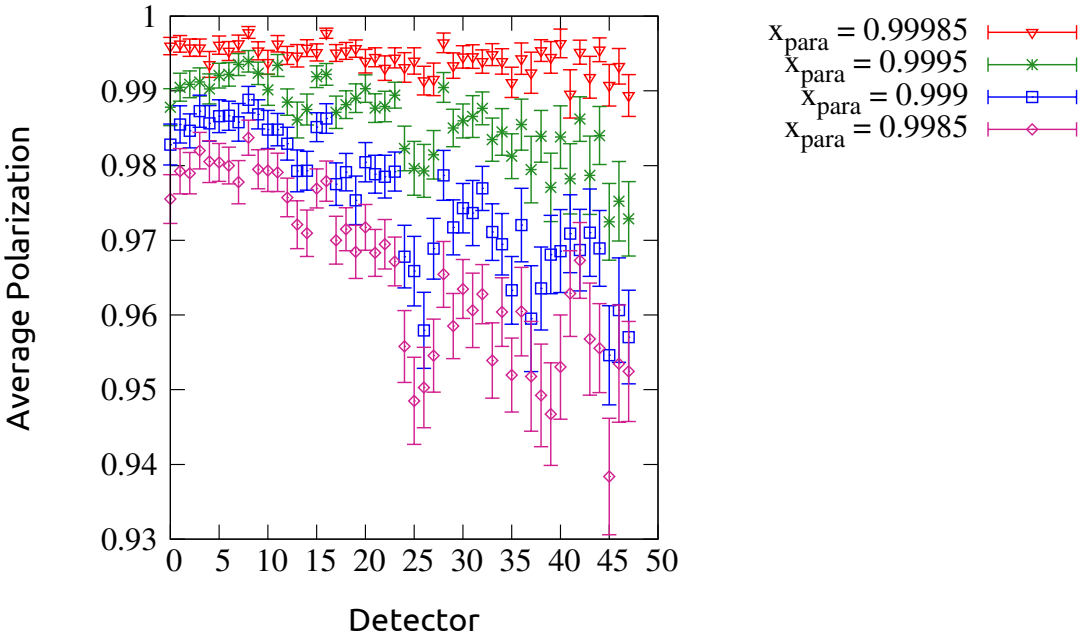

Figure 7.24: Average polarization for neutrons that capture on aluminum 6061 containing cells as a function of parahydrogen concentration.

7.7 Fast Neutron Production in Lithium

For neutron experiments that do not directly measure neutrons, scattered neutrons are a major contributor to the background signal in detectors. The NPDGamma experiment uses ^{6}Li loaded plastic shielding in order to minimize the capture of thermal neutrons in the cesium iodide crystals. The capture reaction,

$$^6\mathrm{Li} + \mathrm{n} \rightarrow \alpha + \mathrm{t} \qquad 4.785 \text{ MeV} \tag{7.31}$$

has a high cross section of 940 b. The alpha and triton from this reaction are high energy and can lead to the production of fast neutrons in the shielding [Lone et al., 1980]. The NPDGamma experiment uses two types of lithium shielding in and around the apparatus, based on Li_2CO_3 and LiF and both are embedded in a plastic/rubber matrix. There are a number of secondary reactions reactions described in the Lone et al. paper, many of which lead to MeV scale energy neutrons as a result of triton or alpha capture on lithium, nitrogen, oxygen, etc. The general result is that approximately 1 in 10^4 thermal neutron captures in the NPDGamma shielding will produce a fast neutron with an energy above 1MeV.

$$\begin{aligned} ^6\mathrm{Li} + \mathrm{t} &\rightarrow {}^9\mathrm{Be} + \gamma & 17.7 \text{ MeV} \\ &\rightarrow {}^8\mathrm{Be} + \mathrm{n} & 16.02 \text{ MeV} \\ &\rightarrow 2\,{}^4\mathrm{He} + \mathrm{n} & 16.115 \text{ MeV} \\ &\rightarrow {}^5\mathrm{He} + {}^4\mathrm{He} & 15.15 \text{ MeV} \end{aligned} \tag{7.32}$$

7.7.1 Calculation and Results

The MCNPX code and libraries do not include incident alpha and triton interactions, so the code was modified in order to estimate the relative magnitude of this signal in the detectors and therefore whether this contribution requires further investigation as a systematic effect. Neutron collisions are checked to see if ^{6}Li is involved. If that collision should produce a charged particle in the MCNPX code as normal, that is to say an alpha or triton, then a fast neutron is also produced. The fast neutrons are produced isotropically and the neutron energy is always 8 MeV, which is a typical energy for the reactions involved and precise

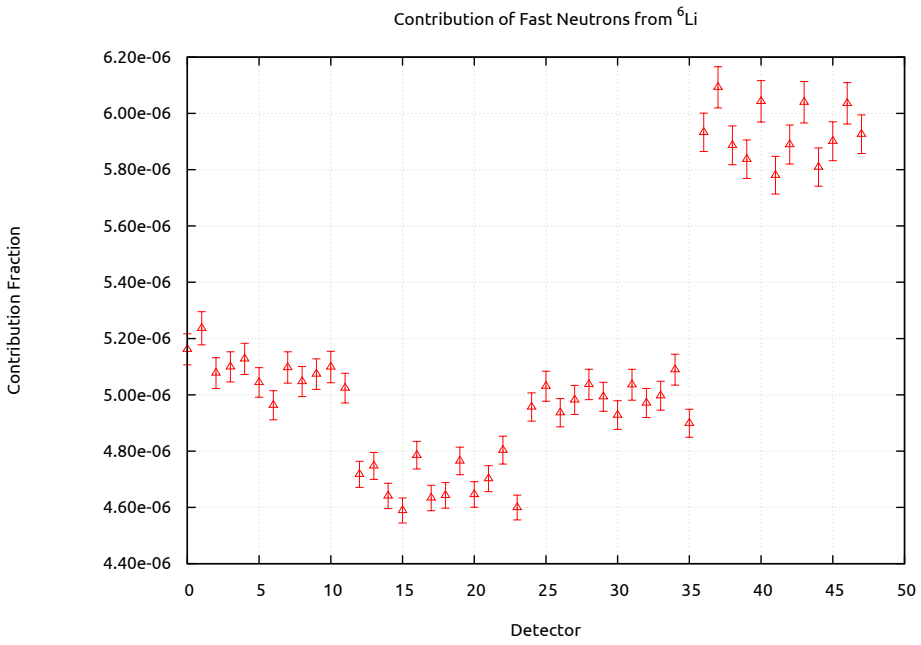

Figure 7.25: Fractional contribution of fast neutrons created in ^{6}Li

kinematics is not necessary for this estimate. In order to get better statistics out of the simulation, the initial particle weight of the fast neutron is not decreased by a factor of 10^{-4} and but is instead given the same weight as the neutron that produced the charged particles. Neutrons do not typicall reach the lithium shielding without having undergone many weight reducing interactions in the hydrogen and other materials, and a low weight product here would be quickly rouletted by MCNPX and not tracked. The fast neutrons are tagged so that the energy deposition by secondary particles created by them can be tracked. The fast neutron is then banked in MCNPX, and queued for calculation as normal.

The calculation enabled neutrons, electrons, photons, alphas, and tritons. The energy deposition in the 48 detectors is tallied in total and for particles with the ^{6}Li fast neutron tag described above. Since the weight was not adjusted by a factor of 10^{-4}, this result is an overestimate of the contribution due to these fast neutrons by 10^4. Figure 7.25 has this factor of 10^4 divided out. The result is that these fast neutrons contribute at the level of 5×10^{-6} level relative to the hydrogen capture signal and therefore that these fast neutrons would have to carry an asymmetry of 1×10^{-2} in order to be comparable to the expected uncertainty goal for the NPDGamma experiment of 1×10^{-8}.

Chapter 8

The Parahydrogen Scattering Cross Section

8.1 Motivation

Since the NPDGamma experiment aims to measure the gamma ray asymmetry from polarized neutron capture on liquid parahydrogen, the average polarization of neutrons is an important factor in the extraction of the final result. The average polarization of neutrons will depend on the initial polarization of neutrons as well as the depolarization of the neutron beam as it passes through air, aluminum windows, and the liquid hydrogen target itself. The depolarization of the neutron beam as it passes through the liquid hydrogen target is dependent on the orthohydrogen concentration within the target due to the large orthohydrogen scattering cross section (fig. 8.1), as described in section 7.6.

In principle, transmission measurements can be used to deduce the parahydrogen concentration when compared to a model in MCNPX. Unfortunately, this depends on using scattering kernels in MCNPX and different kernels disagree on the orthohydrogen and parahydrogen scattering cross sections at these energies (section 8.2), though they are all benchmarked to the Seiffert [Seiffert et al., 1970] measurement. The result of using these kernels for predicting the transmission through the apparatus is unphysical.

The above results led to a change in the philosophy of how the transmission of neutrons through the target would be used. The extracted ortho-para ratio depends on the cross

sections, but there is no reason to prefer the ENDF kernels to the IKE kernels, or vice versa. Since the cross sections are not, in principle, well known, they cannot be used to extract the ortho-para ratio. The fact that doing so results in an extracted parahydrogen concentration greater than unity, led to questioning the cross section kernels and the data used to benchmark the kernels. As a result, measuring the parahydrogen cross section became the focus of the transmission measurements.

Such a measurement is useful to other areas of research, such as in the design of neutron sources. Intense slow neutron sources as well as the increasing phase space acceptance of neutron mirrors has enabled the applications of neutron scattering to encompass many fields. At the heart of the increase in intensity of these neutron sources is the performance of the moderating medium that accepts high energy neutrons from spallation or fission and slows them down to the cold neutron energy range.

Many intense neutron sources commonly use liquid hydrogen as a neutron moderator medium. The near-equality of the neutron and proton mass coupled with the anomalously large s-wave neutron-proton scattering amplitude allow a hydrogen-rich medium to both efficiently lower the incident neutron energy through collisions and also maintain a small neutron mean free path to help conserve the initial source intensity. As the neutron energy is lowered into the cold neutron regime, however, the neutron scattering cross section and therefore the mean free path is sensitive to the interference of the scattering amplitudes from neighboring atoms.

The most recent measurement of the scattering cross section on parahydrogen was performed by Seiffert [Seiffert et al., 1970], which is used as the benchmark for comparison of other hydrogen cross section measurements as well as the models used in ENDF [Chadwick et al., 2011]. The fact that the MCNPX model based on the ENDF scattering kernels gave a negative orthohydrogen concentration for the NPDGamma hydrogen vessel implies that the hydrogen sample in the NPDGamma experiment has less orthohydrogen than Seiffert. The Seiffert measurement used a sample of natural hydrogen gas that was cooled to 15 K and liquefied in a chamber in the presence of a catalyst in the bottom of the chamber, though with no active circulation of the liquid through the catalyst. The transmission of neutrons was monitored through the sample and was seen to level off after approximately one day, at

which point the sample was determined to be converted to parahydrogen with "negligible" orthohydrogen contamination. It must be that the measurement using the NPDGamma apparatus in fact has less orthohydrogen than Seiffert, and that the Seiffert sample had some unaccounted-for orthohydrogen contamination leading to a higher cross section.

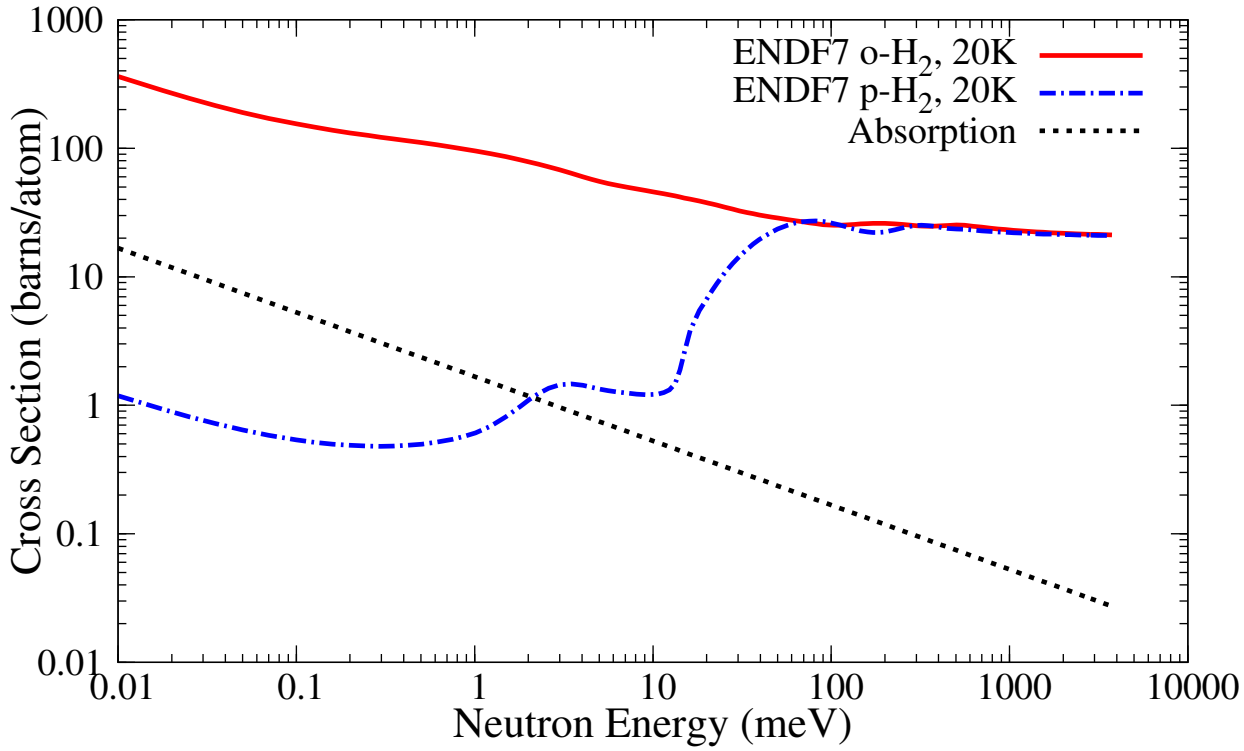

Figure 8.1: Parahydrogen and orthohydrogen scattering cross sections at 20 K from ENDF-VII [Chadwick et al., 2011] and the absorption cross section [Mughabghab, 2006].

8.2 Extracting the Parahydrogen Concentraction from Transmission

The original goal of the NPDGamma transmission measurements was to take the known cross sections for orthohydrogen and parahydrogen and extract the concentrations of each, as was done for the LANSCE iteration of the NPDGamma experiment [Barrón-Palos et al., 2011]. This required a suite of Monte Carlo calculations that were done using MCNPX. Since there is no a priori reason to prefer a certain scattering kernel, multiple evaluations of hydrogen scattering kernels from ENDF7 and IKE were used. These kernels in MCNPX take

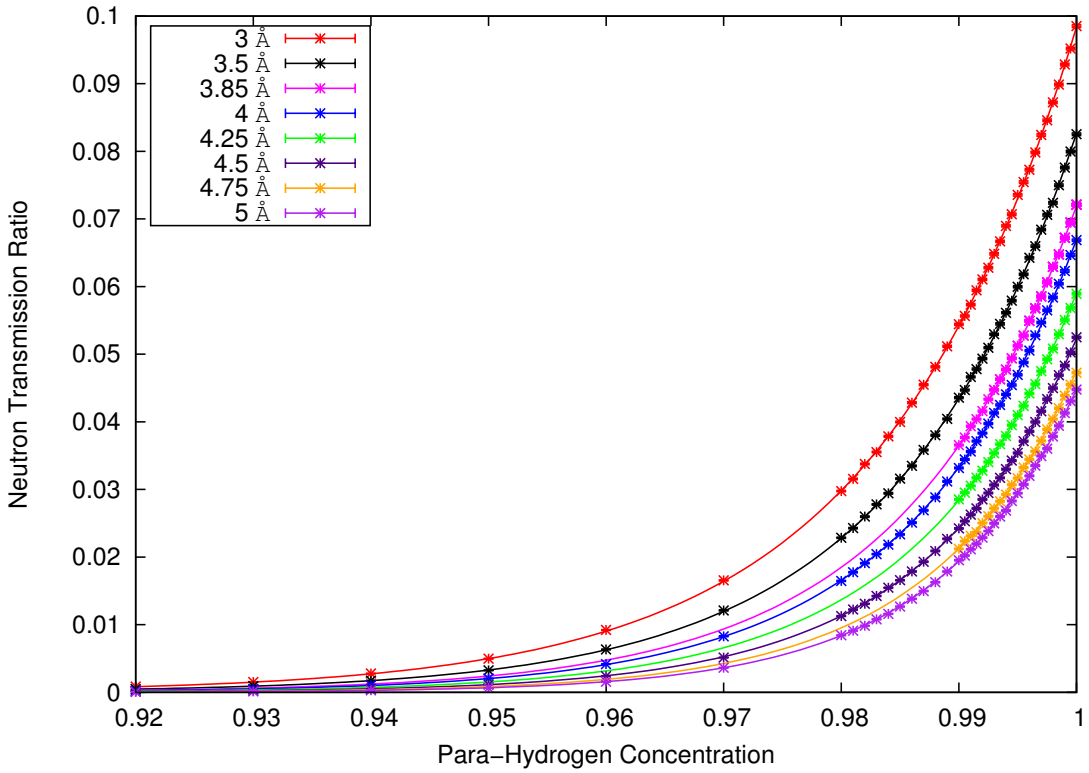

Figure 8.2: Calculation Results and Functional Fits for OPM, for ρ_0

existing cross section tables and modify them in the cold neutron regime with the thermal neutron treatment. Continuous ENDF7 kernels evaluated at temperatures 15, 16, 17, 18, 19, and 20 K were used, as well as IKE kernels at 14, 16, and 20.38 K. The IKE kernels and ENDF7 kernels disagree by up to 10% for the scattering cross section. MCNPX doesn't provide a native way to mix orthohydrogen and parahydrogen, because the thermal neutron tables for orthohydrogen and parahydrogen both modify the hydrogen-1 isotope. In order to mix orthohydrogen and parahydrogen, the hydrogen-4 isotope was replaced with a copy of the normal hydrogen-1 tables and the hydrogen-1 mass, which allows orthohydrogen to be represented by hydrogen-4 while parahydrogen is represented as hydrogen-1.

These initial calculations calculations were performed at 8 different neutron wavelengths (5, 4.75, 4.5, 4.25, 4, 3.85, 3.5, and 3 Å), which provides a wide range of the NPDGamma pulse spectrum. Calculations were also performed with the target vessel volume evacuated in order to predict the transmission through the full target.

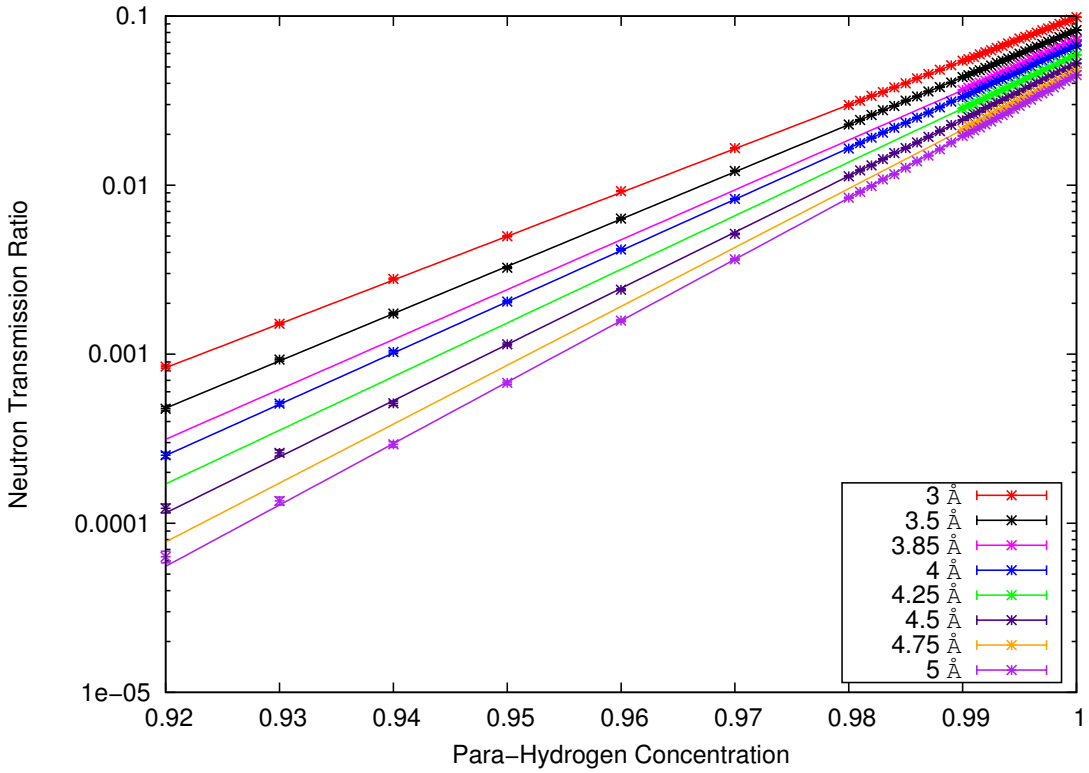

Figure 8.3: Calculation Results and Functional Fits for OPM, Logscale, for ρ_0

In all cases, the cell averaged neutron flux normalized per source particle was tallied in the transmission monitor. These 8 empty target calculations show that approximately 2.2% to 2.5% of neutrons that exit the polarizer reach the transmission monitor (figure 8.4).

The ortho-para ratio was modeled in the range of 92% to 100% parahydrogen. Each calculation used 10^8 source neutrons incident on the hydrogen target. In the case of pure para-hydrogen and 3 $\mathring{A}$ neutrons, the neutron transmission is approximately 10%. The transmission decreases at longer wavelengths, with a transmission of approximately 8%, 6.5%, 5%, and 4.5% for 3.5, 4, 4.5, and 5 $\mathring{A}$ neutrons respectively. The functions fit to an exponential of the fractional parahydrogen concentration (equation 8.1) very well with χ^2 values from 0.87 to 1.01 (table 8.2).

$$T = \frac{\Phi_{full}}{\Phi_{empty}} = e^{(ax_{\text{para}}+b)\frac{\rho}{\rho_0}}, \tag{8.1}$$

where Φ_{full} and Φ_{empty} are the full and empty target neutron flux, x_{para} is the parahydrogen concentration, and a and b are fit parameters. The fit is scaled by a factor $\frac{\rho}{\rho_0}$ to account for

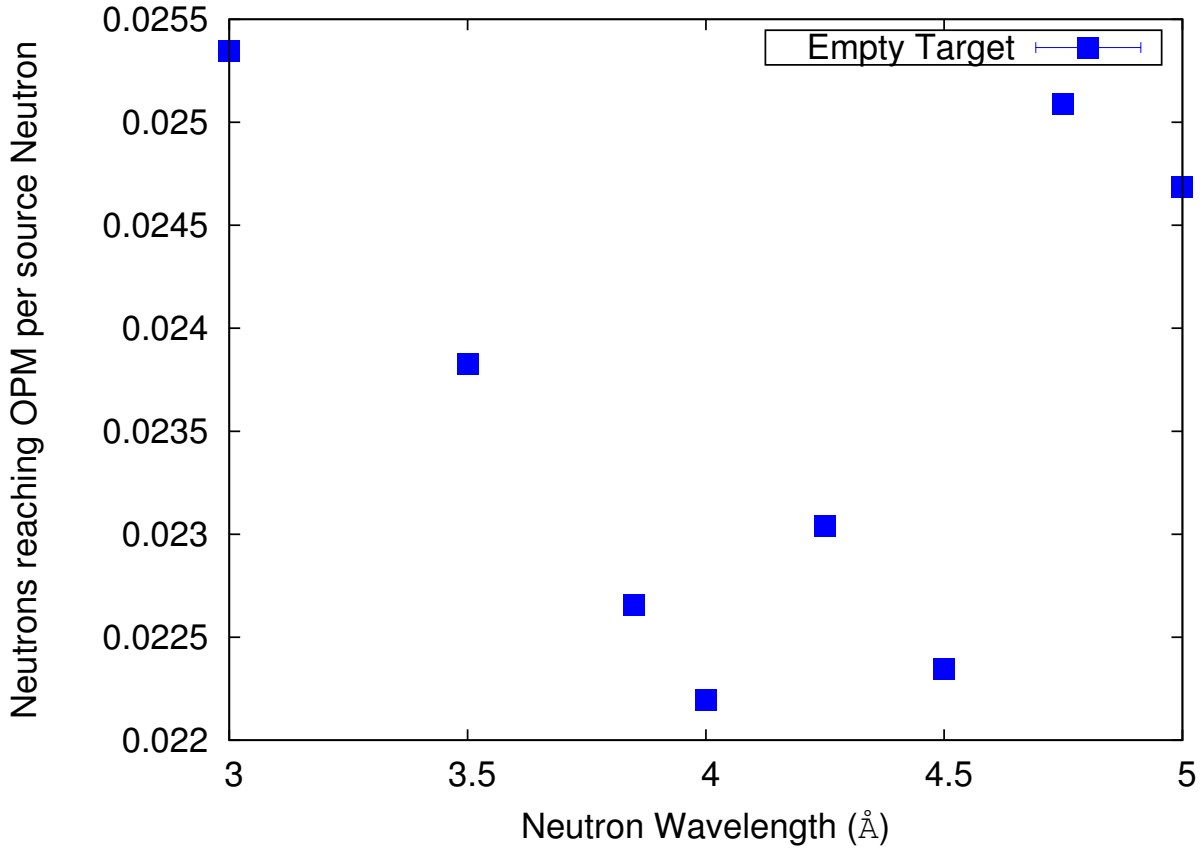

Figure 8.4: Fraction of Neutrons that Reach OPM for an Empty Target Vessel

the variation in transmission as a function of density. The value of ρ_0 is 0.073252 g cm^{-3}, which corresponds to 18 K. See figures 8.2 and 8.3 for a plot of the calculation results and fit functions for all 5 wavelengths. The density as a function of temperature is approximately linear in the range 14 K to 20 K [Leachman et al., 2009].

Table 8.1: Table of Fit Parameters

Wavelength ($\AA$)	a	b	σ_a	σ_b	χ^2
3	59.652	-61.97	0.024345	0.024169	0.99455
3.5	64.374	-66.867	0.029786	0.029577	1.0158
4	69.796	-72.5	0.035997	0.035753	0.99577
4.5	76.476	-79.427	0.038519	0.038268	0.87416
5	83.631	-86.738	0.046319	0.046029	0.95345

A total of 4 measurements were performed to extract the parahydrogen concentration: target full, target empty, pedestal, and room background. The transmission through the target as a function of wavelength, λ, is given by:

$$T(\lambda) = \frac{(S_{full}(\lambda) - S_{pedestal}){N_1}^{-1} - (S_{room} - S_{pedestal}){N_3}^{-1}}{(S_{empty}(\lambda) - S_{pedestal}){N_2}^{-1} - (S_{room} - S_{pedestal}){N_3}^{-1}}. \tag{8.2}$$

The normalization quantities N_1, N_2, and N_3 are the monitor signals for runs target full, target empty, and room background respectively. The parahydrogen concentration extracted for a particular wavelength, λ, is then given by

$$x_p(\lambda) = \frac{1}{a}\left[\log[T(\lambda)]\frac{\rho_0}{\rho} - b\right]. \tag{8.3}$$

The quantities a and b are the fit parameters from table 8.2 and ρ is the fitted density given the temperature of the target vessel.

Table 8.2: Extracted Parahydrogen Concentration

Wavelength ($\AA$)	$T_{\text{Calc.}}$	$T_{\text{Meas.}}$	x_{para}
3	0.09867	0.07673 ± 0.0043	0.9957 ± 0.0013
3.5	0.08292	0.0895 ± 0.0045	1.0012 ± 0.0012
4	0.06714	0.0822 ± 0.0031	1.003 ± 0.001
4.5	0.05246	0.0677 ± 0.00244	1.003 ± 0.001
5	0.04492	0.0632 ± 0.0024	1.004 ± 0.001
Average	—	—	1.0019 ± 0.0005

The results were unphysical, suggesting that the calculations were incorrect due to problems with the scattering kernels. The hydrogen absorption cross section is known well and this implicates the scattering cross section as the culprit. The scattering kernels are benchmarked to a single measurement of the parahydrogen scattering cross section, that of Seiffert [Seiffert et al., 1970], and few other measurements have been performed in this neutron energy regime. Because the NPDGamma experiment features a well defined volume of liquid hydrogen and has an efficient active catalyst to continually convert towards the thermal equilibrium parahydrogen concentration by continuous recirculation, the next approach was to use the apparatus to measure the parahydrogen cross section.

8.3 Extracting the Parahydrogen Scattering Cross Section from Neutron Transmission

The measurement of the cross section eliminates the dependence on scattering kernels that doomed the determination of the concentration, because it is purely based on measuring the transmission. Unfortunately, this means that neutron transmission cannot be used to infer the relative concentrations in the liquid hydrogen target and that the concentration will be a systematic effect in the calculated average polarization on capture in extracting the final result from NPDGamma. Analysis of preliminary data taken at 60 Hz suggested that the Seiffert measurement was in error by as much as 25%, and that the cause for this error could have been due to orthohydrogen contamination on the order of 0.3%.

The preliminary data produced a few percent measurement of the scattering cross section between 3 and 6 Å. A short proposal was drafted with the goal of measuring the parahydrogen cross section while the SNS was operating at lower than 60 Hz in order to run with the beamline choppers parked open in order to increase the energy range of the measurement and to eliminate frame overlap neutrons. The proposed measurement range was 2.5 to 12 Å, and the run time estimate was two periods of 6 hours.

The transmission signal is extracted by making measurements of the signal in the transmission monitor for both an empty and full target vessel in order to determine the transmission through the liquid hydrogen. The cross section data were taken during accelerator physics periods at SNS when the accelerator was operating at 10 Hz rather than 60 Hz. The target full measurement was performed after the vessel had been in steady state operation for four weeks for NPDGamma production data, corresponding to approximately 30 OPC conversion time constants (figure 8.5). The target empty measurement was performed two weeks later. The uncertainty in the preliminary measurement is limited by the uncertainty in the length and density of the hydrogen target.

Conveniently, the SNS accelerator has planned periods of operation at low rate for accelerator tests, known as accelerator physics time. One 10 Hz shift is required for measurements with the target "full" of liquid parahydrogen. This measurement took place during accelerator physics time before the winter shutdown period in late December

2012. The second 10 Hz shift was be used to make target "empty" measurements. This measurement was performed during the accelerator physics time after a winter shutdown period. Each shift acquired beam off pedestals before and after a long run period with the 10 Hz neutron beam on target.

8.3.1 Ortho-Para Conversion Loop Measurements

Transmission measurements were taken throughout the filling process as the OPC catalyzes conversion of the liquid to parahydrogen. The transmission is exquisitely sensitive to the orthohydrogen concentraction due to the large scattering cross section shown in figure 8.1. The vessel is filled with gaseous natural hydrogen (75% orthohydrogen at room temperature) and gaseous hydrogen is liquefied in the liquefaction chamber (shown in figure 8.8) with T3 representing the coldest point in the system. Liquid hydrogen then drips down to the ortho-para conversion chamber (OPC). The slow natural conversion to parahydrogen is accelerated by circulation of the liquid through the OPC which is filled with 150 ml of hydrous iron (III) oxide [Sigma-Aldridge Corp., 3050 Spruce Street, St. Louis, MO 63103, 2010] 30–50 mesh powder catalyst [Barrón-Palos et al., 2011]. The vessel represents the warmest part of the system, and evaporated hydrogen is re-liquefied and passes through the OPC before returning to the vessel thus creating an actively circulating loop that converts orthohydrogen to parahydrogen and approaches the thermal equilibrium concentrations.

The OPC loop circulates continuously while the vessel is in operation, such that the expected thermodynamic equilibrium concentration of orthohydrogen corresponds to the temperature of the OPC, 15.4 K±0.5, which results in an expected orthohydrogen concentration of 0.00015. The orthohydrogen concentration is expected to be near the thermal equilibrium value but there is no way built into the apparatus to determine it directly. The transmission was measured during the filling and conversion process over the course of two weeks of running and was fit to an asymptotic function

$$f(t) = a \times \left[1 - \exp(-\frac{t-c}{\tau})\right], \tag{8.4}$$

where a is the asymptotic fit parameter, c is a time offset in days, and τ is the conversion time in days. Figure 8.5 depicts the conversion as tracked by transmission measurements over the course of two weeks. The conversion fits this function well with a conversion time of 1.13 days. Since the conversion loop operates continually, data taken starting approximately 1-2 weeks after the initial target vessel fill is deemed to be "fully converted" to parahydrogen and expected to be near the thermal equilibrium value because depolarization on the apparatus walls is expected to be negligible.

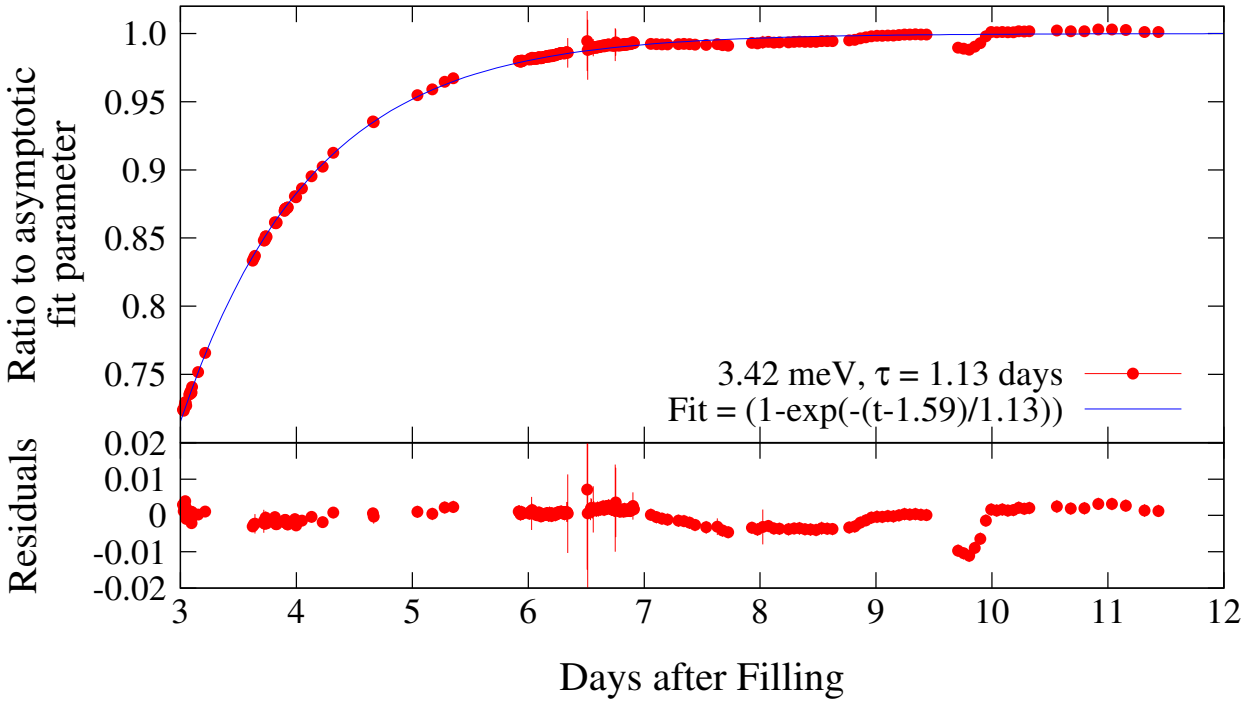

Figure 8.5: Observed ortho-para conversion over time as a fraction of the asymptotic limit for 3.42 meV neutrons shortly after filling the target, with a time constant of approximately one day. Residuals from the exponential fit are shown at the bottom [Grammer et al., 2015].

8.3.2 Cross Section Data Analysis

The neutron transmission is an exponential function of the neutron energy dependent total cross section

$$T(\lambda) = \exp(-nl\sigma_{\text{total}}(\lambda)), \tag{8.5}$$

where n is the number density and l is the length of the hydrogen in the neutron beam. The total cross section can be extracted from measurements of the transmission

$$\begin{aligned} \sigma_{\text{total}}(\lambda) &= \frac{-\log[T(\lambda)]}{nl} && (8.6) \\ &= \sigma_{\text{abs}}(\lambda) + \sigma_{\text{scatter}}(\lambda) \\ &= \sigma_{\text{abs}}(\lambda) + f \times \sigma_{\text{para}} + (1-f)\sigma_{\text{ortho}}, && (8.7) \end{aligned}$$

where f is the parahydrogen fraction, $\sigma_{\text{abs}} = 0.3326 \pm 0.0007$ b at 2200 m/s [Mughabghab, 2006], σ_{scatter} is the total scattering cross section, σ_{ortho} is the orthohydrogen scattering cross section, and σ_{para} is the parahydrogen scattering cross section.

During analysis of the data, it was discovered that the moderator spectrum had shifted and it was later revealed that the moderator had been emptied and refilled with fresh hydrogen between the two run periods. This required a more careful use of the normalization monitor, by wavelength rather than by integration, in order to normalize each measurement and extract the transmission. The transmission monitor exhibits a 240 Hz noise pattern with a small amplitude that is evident at long wavelengths and small signals, which is then fit to a sinusoidal function and subtracted away. Pedestal runs were taken before and after the measurement periods with the FNPB shutter closed. The beam intensity is normalized to a monitor upstream of the supermirror polarizer, which requires a time of flight adjustment when extracting the transmission. The transmission is extracted as follows, with the 240 Hz noise and pedestals subtracted,

$$T(\lambda) = \frac{S_{\text{trans,full}}(\lambda)}{S_{\text{trans,empty}}(\lambda)} \frac{S_{\text{norm,empty}}(\lambda)}{S_{\text{norm,full}}(\lambda)} \frac{g_{\text{norm}}}{g_{\text{trans}}}, \quad (8.8)$$

where the S_{trans} is the signal in the transmission monitor, S_{norm} is the signal in the normalization monitor (M1), and g are monitor gain adjustment factors.

The cold hydrogen moderator viewed by FNPB is a fully coupled, unpoisoned liquid hydrogen volume at 20 K [Fomin et al., 2015]. It is continuously circulated via a jet at the bottom of the vessel. It is initially filled with natural hydrogen that slowly converts to parahydrogen without the aid of a catalyst. The neutron spectrum is dependent on the

relative concentrations of orthohydrogen and parahydrogen of the moderator. The full target measurement for the cross section was performed on December 21, 2012, and the empty target measurement was performed on January 7, 2013. During that 2 week break between measurements, the moderator viewed by FNPB was emptied and refilled with fresh hydrogen which led to a shift in the moderator spectrum that requires a correction using the upstream monitor, M1. The time of flight conversion to neutron energy is used to interpolate with a cubic spline and extract the M1 normalization factors required to adjust the transmission for the moderator spectrum change as a function of wavelength. The functional form of the normalization monitor correction is shown in figure 8.6.

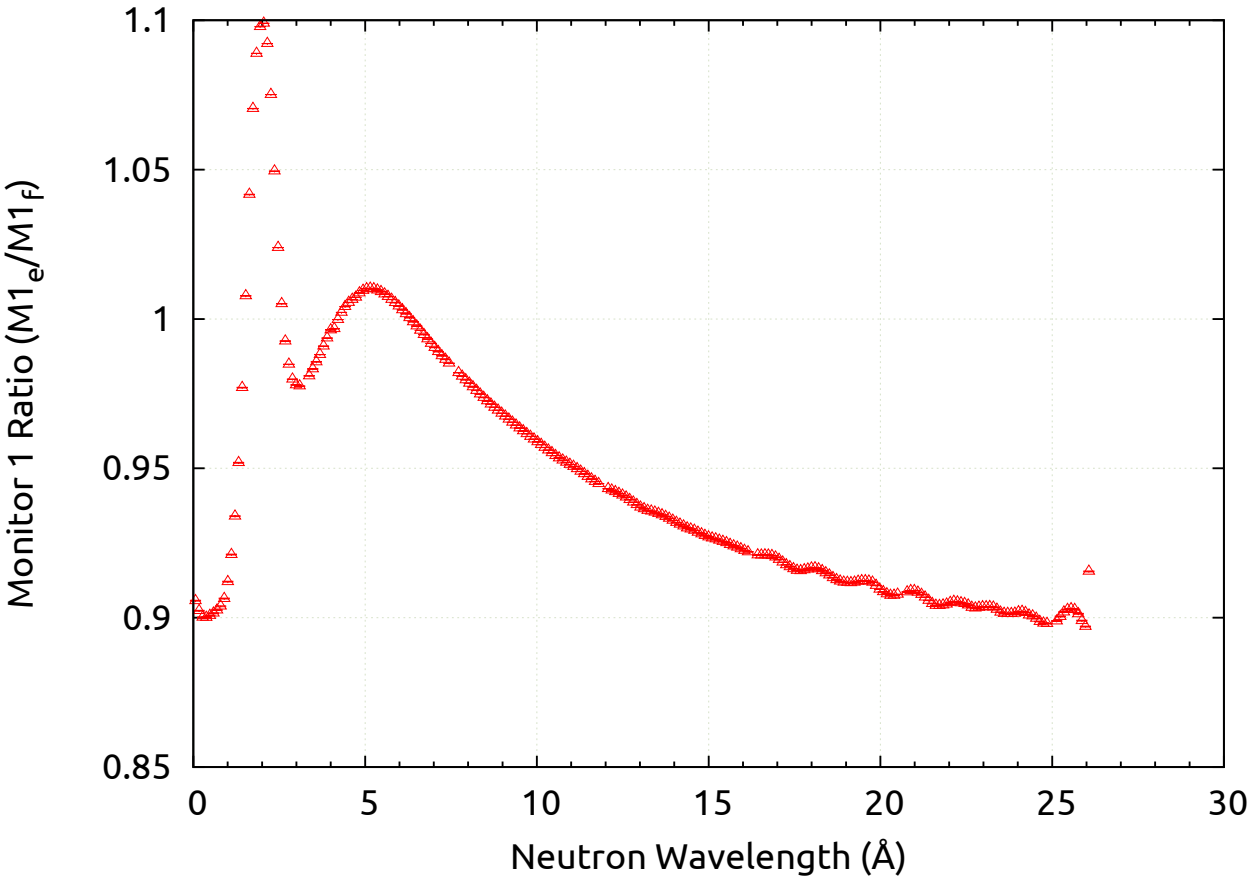

Figure 8.6: Measured ratio of monitor 1 signals for empty and full target measurements, showing the moderator spectrum shift and depicting lower neutron flux for the target empty run corresponding to fresh hydrogen in the moderator and therefore higher orthohydrogen content.

Neutron time of flight is used to determine the position of the neutron monitors relative to the moderator and target in order to convert arrival time in the data acquisition system

to neutron energy. The sharp dips in the pulse shapes in Fig. 8.7 are due to Bragg scattering on aluminum windows along the path of the neutron beam. These dips are visible at neutron energies of 4.98 and 3.74 meV, corresponding to the aluminum (200) and (111) Bragg planes [Wyckoff, 1963], respectively. Data were taken at higher sampling rate in order to pinpoint the arrival time of these Bragg edges in the monitors to within 0.16 ms. The normalization monitor (M1) is located 15.24 m ± 0.12 m from the moderator, the 16-liter liquid hydrogen target [Santra et al., 2010] is centered 17.6 m from the moderator, and the transmission monitor is located 3.44 m ± 0.02 m from the normalization monitor.

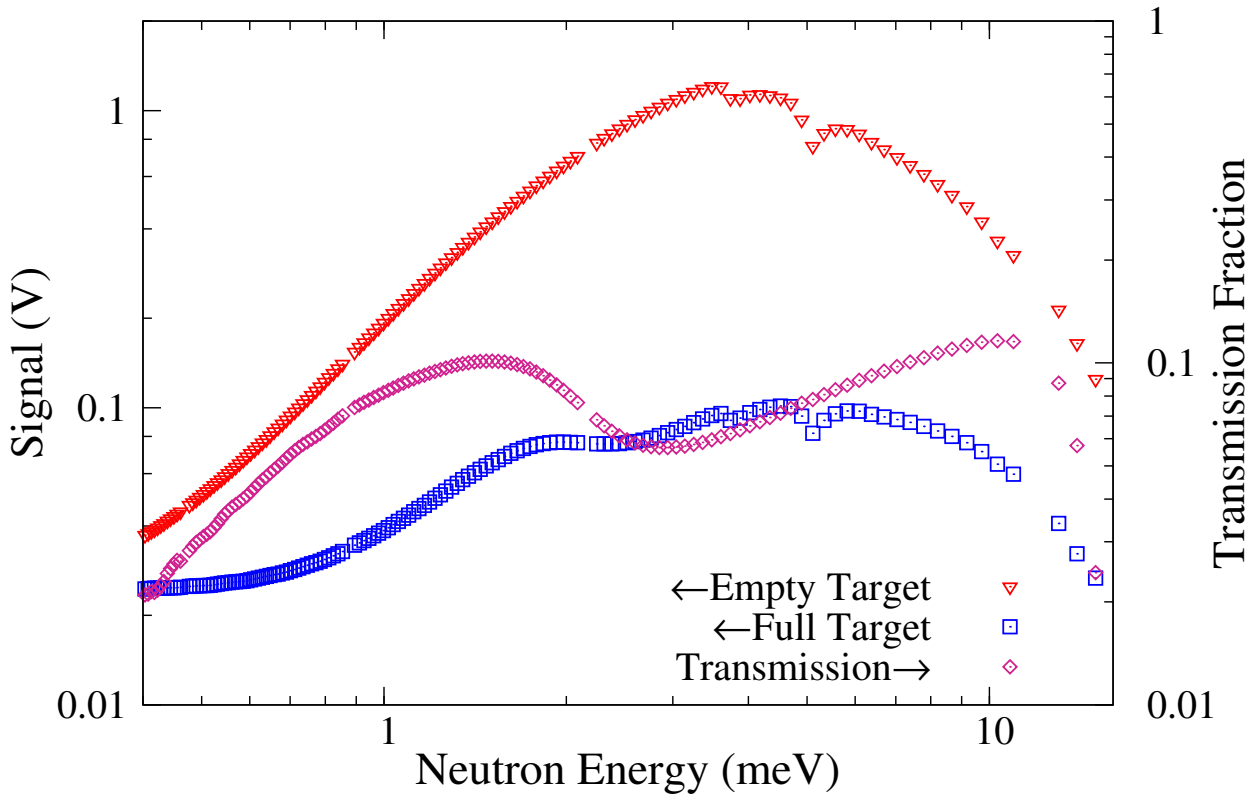

Figure 8.7: Transmission monitor signals (left axis) for empty (triangles) and hydrogen-filled (squares) aluminum target vessel. Dips in the spectra are at the aluminum Bragg edges. Transmission ratio (right axis, diamonds) depicts no transmission for energies above 14.5 meV spin-flip transition [Grammer et al., 2015].

8.3.3 Uncertainty Analysis

The hydrogen target vessel is instrumented with multiple thermometers around the vessel and the OPC. These thermometers are Lakeshore DT-670 silicon diodes and are specified

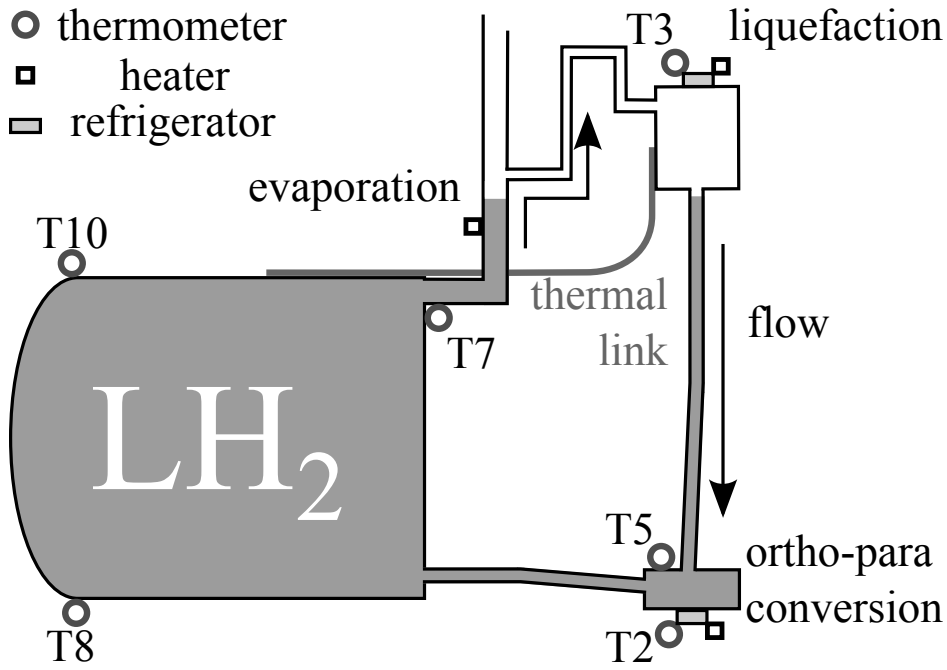

Figure 8.8: Diagram of circulation loop inside the hydrogen target system. Evaporated hydrogen is re-condensed and is forced to flow through the OPC at a rate of a few millimoles per second. T3, T7, T8, and T10 determine the liquid hydrogen bulk temperature. T2 and T5 determine the temperature of the catalyst in the OPC [Grammer et al., 2015].

to have a 0.5 K tolerance, however, they also exhibit drift and some experience radiation damage.

The thermometers T3, T7, T8, and T10, shown in figure 8.8, are used to determine the temperature of the bulk liquid. At the time of the measurement of the full target for the cross section data run, these measured T3 = 15.5 K, T7 = 15.4 K, T8 = 15.78 K, and T10 = 15.84 K for an average of 15.6 K.

The T3 thermometer is attached to the liquefaction chamber and is held fixed by a heater and refrigerator and does not drift over time. The other thermometers do drift over time at a rate of approximately 0.1 K per month. The hydrogen vessel had been in operation for approximately 4-5 months by the time the cross section measurement was performed, making the expected drift not worse than 0.4 K.

At the start of the experiment, T8 and T10 gave measurements equal to or slightly higher than T3. During the measurement period a heater was active meaning that T8 and T10 could only be higher than T3. Since the heater and the drift act in the same direction, the

fact that T8 and T10 are only 0.3 K above T3 implies that the drift could not be worse than 0.3 K and provides a stronger constraint on the drift than the 0.1 K per month argument. Added in quadrature, the expected uncertainty in the temperature measurement is 0.6 K.

The temperature is used to extract the density of the bulk liquid in the vessel. The functional form of the density was determined by combining multiple sources [Leachman et al., 2009; McCarty et al., 1981; Souers, 1986]. A distinction between parahydrogen and orthohydrogen is not made when combining these sources together, providing an uncertainty of the fit to the functional form of the density of 0.5%,

$$\rho(\mathrm{T}) = 0.083658 - 0.000150459\mathrm{T} - 2.3642 \times 10^{-5}\mathrm{T}^2, \tag{8.9}$$

corresponding to a density of 0.07573 g cm$^{-3}\pm$ 0.00044. The vessel temperature is also used to determine the length of the target after thermal contraction using NIST cryogenics data,

$$\begin{aligned} \Delta L(\mathrm{T}) &= \tfrac{L-L_{293}}{L_{293}} \times 10^5 \\ &= -412.77 - 3.0389 \times 10^{-1}\mathrm{T} + 8.7696 \times 10^{-3}\mathrm{T}^2 - 9.9821 \times 10^{-6}\mathrm{T}^3, \end{aligned} \tag{8.10}$$

with a warm length of 30.19 cm$\pm$0.002 as determined from measurements with a coordinate measurement machine, the cold length is therefore 30.065 cm$\pm$0.005.

The linearity of the monitors was determined by performing bias voltage scans in order to eliminate recombination of ions in the chambers, and the monitors were operated at sufficiently high voltage to accomplish this. The linearity is therefore expect to be better than 0.15%. Current injection tests were performed on the preamplifiers to determine that the linearity of the preamplifers is better than 0.1% and to determine the gain shift for the monitors. Additionally, contamination of the transmission signal by small angle scattering was estimated in MCNPX to be less than 0.1%, meaning that the neutrons detected in the transmission monitor are un-scattered neutrons.

The required running time was determined based on the requirement that the neutron counting statistics would not dominate the uncertainty and that the measurement would instead be systematics limited. the two largest contributions are the neutron time of flight and the temperature of the liquid in the vessel. The table 8.3 shows the uncertainty in

Table 8.3: Main uncertainties in the total cross section at 1.92 meV.

Source	Uncertainty
Neutrons	0.02%
Time of flight	0.61%
Monitor gains	0.06%
Monitor linearity	0.12%
Target length	0.007%
Liquid density fit	0.5%
Temperature	0.71%
Total	1.07%

the measured total cross section evaluated at 1.92 meV, since this is actually a function of energy.

8.3.4 Results

The result of the transmission measurement [Grammer et al., 2015] is the total cross section for the particular sample of liquid hydrogen that was in the NPDGamma apparatus at the time, and the total cross section is measured with precision of approximately 1%. In principle, that sample could have some orthohydrogen contamination present. The total scattering cross section can be determined by subtracting the known $1/v$ absorption cross section for hydrogen. If the lowest magnitude point in the total scattering cross section is assumed to be due to orthohydrogen only, that is to say the parahydrogen scattering cross section at this point is 0 barns, then the maximum orthohydrogen contamination can be determined by using the relatively well-known orthohydrogen scattering cross section from ENDF-VII. The lowest point is at 0.8 meV, and this provides an estimate for the orthohydrogen concentration of 0.0015 with a corresponding parahydrogen concentration of 0.9985. This upper limit on the orthohydrogen concentration provides a measurement band in which the parahydrogen scattering section should lie. The total cross section has been determined with an uncertainty of 1% or approximately 0.2b/atom over the energy range 0.43 meV to 16.1 meV. Figure 8.9 shows the total cross section in red and then parahydrogen scattering cross section band in blue, with the upper error bar determined by the uncertainty analysis and the lower error bar determined by the upper limit on the orthohydrogen concentration. This upper limit on the

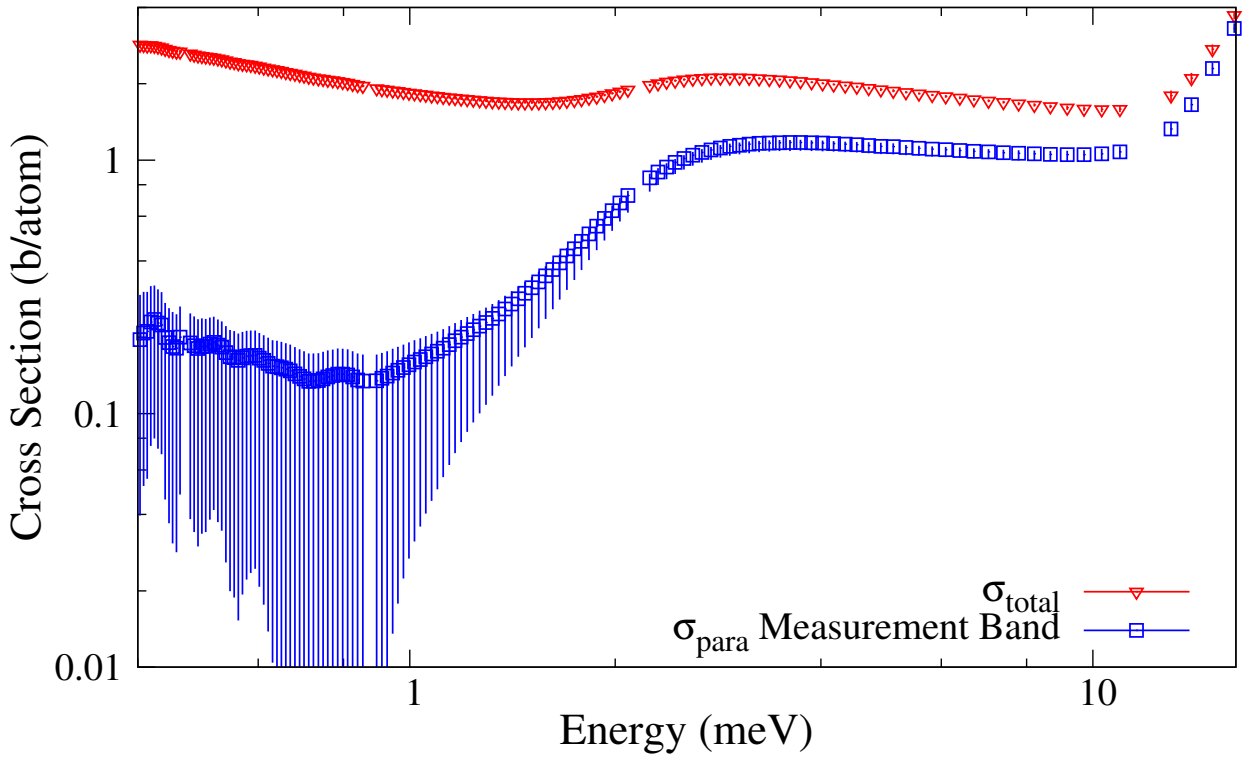

Figure 8.9: Total cross section from this work in b/atom (triangles), parahydrogen scattering cross section (squares). The upper error bar on the parahydrogen cross section comes from Table 8.3 and the lower error bar is given by the upper limit on the orthohydrogen contamination [Grammer et al., 2015].

orthohydrogen concentration is also used in the MCNPX polarization model for determining the polarization on capture.

The spectral shift that was observed during the measurement of the parahydrogen cross section indicates that the spectrum of a moderator depends rather strongly on the isomeric composition of the liquid hydrogen in the moderator vessel. In fact, previous calculations for the design of the J-PARC moderator [Kai et al., 2004], the LANSCE cold source [Ooi et al., 2006], and the design of the planned ESS [Magán et al., 2013] similarly show that the neutronics performance of a liquid hydrogen cold source depends on the parahydrogen and orthohydrogen content of the moderator. This new measurement implies that the contribution to scattering due to parahydrogen was being overestimated and that the moderating properties of pure parahydrogen are in fact lower than previously expected.

The the ENDF-VII kernel [Chadwick et al., 2011] due to being benchmarked to the Seiffert cross section had predicted a transmission through the NPDGamma apparatus

that was approximately 2% less than what was measured. Figure 8.10 shows the comparison between this new measurement and several previous measurements. The

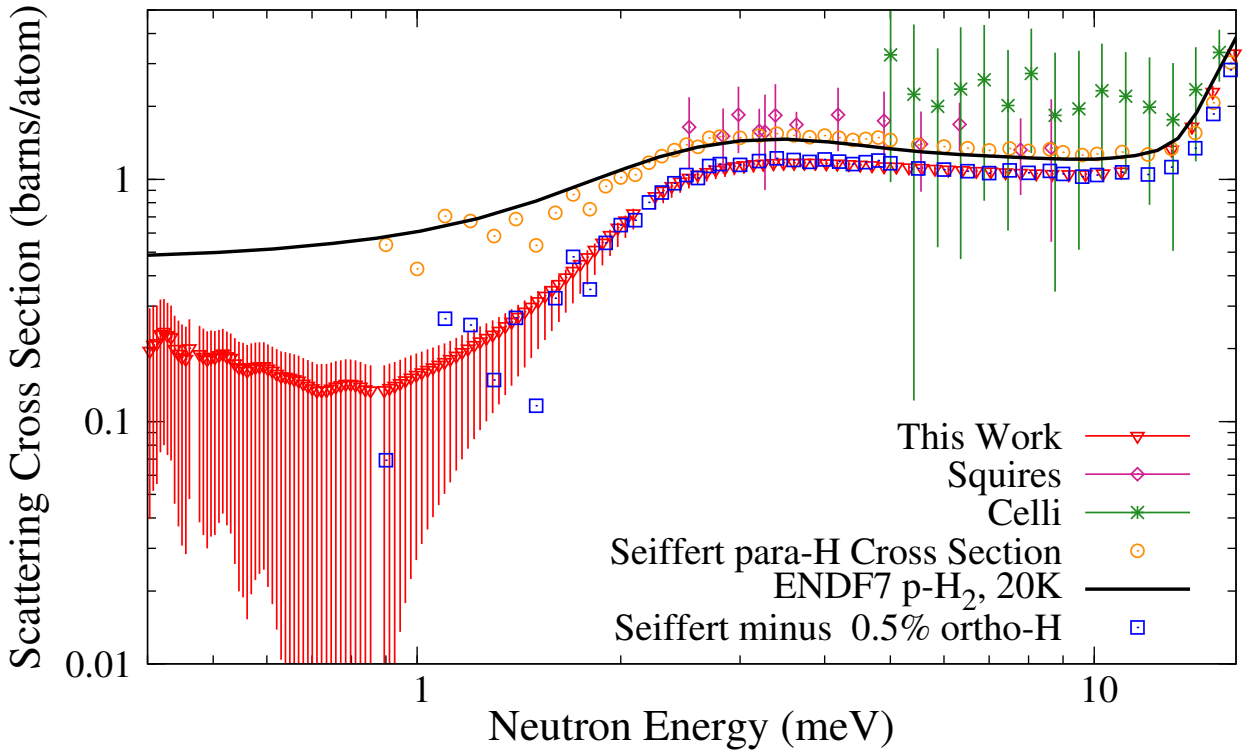

Figure 8.10: (Color online) The scattering cross section extracted in this work [Grammer et al., 2015] (triangles), Squires [Squires and Stewart, 1955] (diamonds), Celli [Celli et al., 1999] (stars, some points omitted), Seiffert [Seiffert et al., 1970] (circles), ENDF-VII (black), and subtraction of a 0.5% admixture of orthohydrogen from Seiffert (squares).

Squires measurement [Squires and Stewart, 1955] was performed using a gaseous mixture of parahydrogen and orthohydrogen with a 0.9979 parahydrogen concentration that was independently measured using thermal conductivity. The Celli [Celli et al., 1999] and Seiffert [Seiffert et al., 1970] were both performed using thin liquid hydrogen samples that were in the presence of a catalyst. Seiffert monitored the transmission of neutrons through the sample for approximately one day before determining that the orthohydrogen concentration was "negligible". Celli inferred that the sample was in thermal equilibrium after approximately 20 hours with an estimated parahydrogen concentration of 0.9996. The Seiffert measurement used a static conversion system rather than a circulating system. By comparison, the NPDGamma system is thick and contains an active conversion loop.

It is clear that the NPDGamma sample has less orthohydrogen contamination than these previous measurements because the result is smaller in magnitude than the previous measurements. If an admixture of 0.5% orthohydrogen via the ENDF-VII cross section is subtracted from the Seiffert measurement, the discrepancy between that measurement and the new measurement using the NPDGamma apparatus is resolved. This implies that the previous measurements should be treated as upper limits on the parahydrogen scattering cross section and that the measurement band result using the NPDGamma apparatus presents the most accurate and highest precision measurement of this cross section.

Bibliography

Abele, H. (2009). The neutron alphabet: Exploring the properties of fundamental interactions. *Nucl. Instrum. Methods Phys. Res., Sect. A*, 611(2-3):193–197. 1

Ade, P. A. R., Aghanim, N., Armitage-Caplan, C., Arnaud, M., Ashdown, M., Atrio-Barandela, F., Aumont, J., Baccigalupi, C., Banday, A. J., Barreiro, R. B., Bartlett, J. G., Battaner, E., Benabed, K., Benoît, A., Benoit-Lévy, A., Bernard, J.-P., Bersanelli, M., Bielewicz, P., Bobin, J., Bock, J. J., Bonaldi, A., Bond, J. R., Borrill, J., Bouchet, F. R., Bridges, M., Bucher, M., Burigana, C., Butler, R. C., Calabrese, E., Cappellini, B., Cardoso, J.-F., Catalano, A., Challinor, A., Chamballu, A., Chary, R.-R., Chen, X., Chiang, H. C., Chiang, L.-Y., Christensen, P. R., Church, S., Clements, D. L., Colombi, S., Colombo, L. P. L., Couchot, F., Coulais, A., Crill, B. P., Curto, A., Cuttaia, F., Danese, L., Davies, R. D., Davis, R. J., de Bernardis, P., de Rosa, A., de Zotti, G., Delabrouille, J., Delouis, J.-M., Désert, F.-X., Dickinson, C., Diego, J. M., Dolag, K., Dole, H., Donzelli, S., Doré, O., Douspis, M., Dunkley, J., Dupac, X., Efstathiou, G., Elsner, F., Enßlin, T. A., Eriksen, H. K., Finelli, F., Forni, O., Frailis, M., Fraisse, A. A., Franceschi, E., Gaier, T. C., Galeotta, S., Galli, S., Ganga, K., Giard, M., Giardino, G., Giraud-Héraud, Y., Gjerløw, E., González-Nuevo, J., Górski, K. M., Gratton, S., Gregorio, A., Gruppuso, A., Gudmundsson, J. E., Haissinski, J., Hamann, J., Hansen, F. K., Hanson, D., Harrison, D., Henrot-Versillé, S., Hernández-Monteagudo, C., Herranz, D., Hildebrandt, S. R., Hivon, E., Hobson, M., Holmes, W. A., Hornstrup, A., Hou, Z., Hovest, W., Huffenberger, K. M., Jaffe, A. H., Jaffe, T. R., Jewell, J., Jones, W. C., Juvela, M., Keihänen, E., Keskitalo, R., Kisner, T. S., Kneissl, R., Knoche, J., Knox, L., Kunz, M., Kurki-Suonio, H., Lagache, G., Lähteenmäki, A., Lamarre, J.-M., Lasenby, A., Lattanzi, M., Laureijs, R. J., Lawrence, C. R., Leach, S., Leahy, J. P., Leonardi, R., León-Tavares, J., Lesgourgues, J., Lewis, A., Liguori, M., Lilje, P. B., Linden-Vørnle, M., López-Caniego, M., Lubin, P. M., Macías-Pérez, J. F., Maffei, B., Maino, D., Mandolesi, N., Maris, M., Marshall, D. J., Martin, P. G., Martínez-González, E., Masi, S., Massardi, M., Matarrese, S., Matthai, F., Mazzotta, P., Meinhold, P. R., Melchiorri, A., Melin, J.-B., Mendes, L., Menegoni, E., Mennella, A., Migliaccio, M., Millea, M., Mitra, S., Miville-Deschênes, M.-A., Moneti, A., Montier, L., Morgante, G., Mortlock, D., Moss, A., Munshi, D., Murphy,

J. A., Naselsky, P., Nati, F., Natoli, P., Netterfield, C. B., Nørgaard-Nielsen, H. U., Noviello, F., Novikov, D., Novikov, I., O'Dwyer, I. J., Osborne, S., Oxborrow, C. A., Paci, F., Pagano, L., Pajot, F., Paladini, R., Paoletti, D., Partridge, B., Pasian, F., Patanchon, G., Pearson, D., Pearson, T. J., Peiris, H. V., Perdereau, O., Perotto, L., Perrotta, F., Pettorino, V., Piacentini, F., Piat, M., Pierpaoli, E., Pietrobon, D., Plaszczynski, S., Platania, P., Pointecouteau, E., Polenta, G., Ponthieu, N., Popa, L., Poutanen, T., Pratt, G. W., Prézeau, G., Prunet, S., Puget, J.-L., Rachen, J. P., Reach, W. T., Rebolo, R., Reinecke, M., Remazeilles, M., Renault, C., Ricciardi, S., Riller, T., Ristorcelli, I., Rocha, G., Rosset, C., Roudier, G., Rowan-Robinson, M., Rubiño-Martín, J. A., Rusholme, B., Sandri, M., Santos, D., Savelainen, M., Savini, G., Scott, D., Seiffert, M. D., Shellard, E. P. S., Spencer, L. D., Starck, J.-L., Stolyarov, V., Stompor, R., Sudiwala, R., Sunyaev, R., Sureau, F., Sutton, D., Suur-Uski, A.-S., Sygnet, J.-F., Tauber, J. A., Tavagnacco, D., Terenzi, L., Toffolatti, L., Tomasi, M., Tristram, M., Tucci, M., Tuovinen, J., Türler, M., Umana, G., Valenziano, L., Valiviita, J., Van Tent, B., Vielva, P., Villa, F., Vittorio, N., Wade, L. A., Wandelt, B. D., Wehus, I. K., White, M., White, S. D. M., Wilkinson, A., Yvon, D., Zacchei, A., and Zonca, A. (2014). Planck 2013 results. XVI. Cosmological parameters. *Astronomy & Astrophysics*, 571:A16. 24

Amaldi, E. (1984). From the discovery of the neutron to the discovery of nuclear fission. *Physics Reports*, 111(1-4):1–331. 5

Arzumanov, S., Bondarenko, L., Chernyavsky, S., Drexel, W., Fomin, A., Geltenbort, P., Morozov, V., Panin, Y., Pendlebury, J., and Schreckenbach, K. (2000). Neutron life time value measured by storing ultracold neutrons with detection of inelastically scattered neutrons. *Physics Letters B*, 483(1-3):15–22. 29, 32

Arzumanov, S. S., Bondarenko, L. N., Morozov, V. I., Panin, Y. N., and Chernyavsky, S. M. (2012). Analysis and correction of the measurement of the neutron lifetime. *JETP Letters*, 95(5):224–228. 32

Bainbridge, K. T. (1933). Comparison of the masses of H2 and helium. *Phys. Rev.*, 44(1):57. 8

Balascuta, S., Alarcon, R., Baeβler, S., Greene, G., Mietke, A., Crawford, C., Milburn, R., Penttila, S., Prince, J., Schädler, J., and Others (2012). The implementation of a super mirror polarizer at the SNS fundamental neutron physics beamline. *Nucl. Instrum. Methods Phys. Res., Sect. A*, 671:137–143. 86

Barrón-Palos, L. (2011). Efficiency of the Triple Monitor. Technical report, NPDGamma Internal Report. 88

Barrón-Palos, L., Alarcon, R., Balascuta, S., Blessinger, C., Bowman, J., Chupp, T., Covrig, S., Crawford, C., Dabaghyan, M., Dadras, J., Dawkins, M., Fox, W., Gericke, M., Gillis, R., Lauss, B., Leuschner, M., Lozowski, B., Mahurin, R., Mason, M., Mei, J., Nann, H., Penttilä, S., Ramsay, W., Salas-Bacci, A., Santra, S., Seo, P.-N., Sharma, M., Smith, T., Snow, W., Wilburn, W., and Yuan, V. (2011). Determination of the parahydrogen fraction in a liquid hydrogen target using energy-dependent slow neutron transmission. *Nucl. Instrum. Methods Phys. Res., Sect. A*, 659(1):579–586. 3, 143, 149

Beringer, J. (2012). Review of Particle Physics. *Physical Review D*, 86(1):010001. 19, 31

Blume, M. (1963). Polarization Effects in the Magnetic Elastic Scattering of Slow Neutrons. *Phys. Rev.*, 130(5):1670–1676. 131

Bondarenko, L. N., Kurguzov, V. V., Prokof'ev, Y. A., Rogov, E. V., and Spivak, P. E. (1978). Measurement of the neutron half-life. *JETP Letters*, 28(5):303. 28

Bothe, W. and Becker, H. (1930). Künstliche Erregung von Kern-γ-Strahlen. *Zeitschrift f{ü}r Physik*, 66(5-6):289–306. 5

Bowman, J. D., Greene, G. L., Hogan, G. E., Knudson, J., Lamoreaux, S., Morgan, G., Morris, C. L., Penttilä, S. I., Smith, D., Smith, T. B., Wilburn, W. S., Yuan, V., Bazhenov, A., Kolomenski, E., Pirozhkov, A., Serebrov, A., Blessinger, C. S., Hansen, G., Nann, H., Rich, D., Snow, W. M., Chupp, T. E., Coulter, K. P., Welsh, R. C., Zerger, J., Freedman, S. J., Fujikawa, B. K., Gentile, T. R., Jones, G. L., Wietfeldt, F. E., Leuschner, M. B., Pomeroy, V., Masaike, A., Matsuda, Y., Ishimoto, S., Masuda, Y., Morimoto, K., and Sharapov, E. I. (1999). Measurement of the Parity-Violating Gamma Asymmetry in the

Capture of Polarized Cold Neutrons by Para-Hydrogen. Technical report, Los Alamos National Laboratory. 84

Brun, R. and Rademakers, F. (1996). ROOT - An Object Oriented Data Analysis Framework. In *Proceedings AIHENP'96 Workshop, Lausanne, Nucl. Inst. & Meth. in Phys. Res. A*, pages 81–86. 203

Byrne, J., Dawber, P., Spain, J., Dewey, M., Gilliam, D., Greene, G., Lamaze, G., Williams, A., Pauwels, J., Eykens, R., VanGestel, J., Lamberty, A., and Scott, R. (1989). Determination of the neutron lifetime by counting trapped protons. *Nucl. Instrum. Methods Phys. Res., Sect. A*, 284(1):116–119. 30, 32, 34

Byrne, J., Dawber, P., Spain, J., Williams, A., Dewey, M., Gilliam, D., Greene, G., Lamaze, G., Scott, R., Pauwels, J., Eykens, R., and Lamberty, A. (1990). Measurement of the neutron lifetime by counting trapped protons. *Phys. Rev. Lett.*, 65(3):289–292. 34

Byrne, J., Morse, J., Smith, K. F., Shaikh, F., Green, K., and Greene, G. (1980). A new measurement of the neutron lifetime. *Physics Letters B*, 92(3-4):274–278. 30

Carpenter, J. M. (1977). Pulsed spallation neutron sources for slow neutron scattering. 9

Cavaignac, J., Vignon, B., and Wilson, R. (1977). Search for parity violation in neutron-proton capture. *Physics Letters B*, 67(2):148–150. 2

Celli, M., Rhodes, N., Soper, A. K., and Zoppi, M. (1999). The total neutron cross section of liquid para-hydrogen. *J. Phys.: Condens. Matter*, 11(50):10229–10242. 158

Chadwick, J. (1932). The Existence of a Neutron. *Proc. R. Soc. A*, 136(830):692–708. 1, 6, 7

Chadwick, J. and Goldhaber, M. (1934). A 'nuclear photo-effect': disintegration of the diplon by g-rays. *Nature*, 134(3381):237–238. 8

Chadwick, J. and Goldhaber, M. (1935). The Nuclear Photoelectric Effect. *Proc. R. Soc. A*, 151(873):479–493. 8, 27

Chadwick, M., Herman, M., Oblozinsky, P., Pritychenko, B., Arbanas, G., Arcilla, R., Brewer, R., Brown, D. A., Capote, R., Carlson, A. D., Cho, Y. S., Derrien, H., Guber, K., Hale, G. M., Hoblit, S., Holloway, S., Johnson, T. D., Kawano, T., Kiedrowski, B. C., Kim, H., Kunieda, S., Larson, N. M., Leal, L., Lestone, J. P., Little, R. C., Mccutchan, E. A., Macfarlane, R. E., Macinnes, M., Mattoon, C. M., McKnight, R. D., Mughabghab, S. F., Nobre, G. P. A., Palmiotti, G., Palumbo, A., Pigni, M. T., Pronyaev, V. G., Vogt, R. L., Marck, S. C. V. D., Wallner, A., White, M. C., Wiarda, D., Young, P. G., Obložinský, P., Dunn, M., Danon, Y., Kahler, A., Smith, D., Sayer, R., Sonzogni, A., Summers, N., Talou, P., Thompson, I., Trkov, A., and van der Marck, S. (2011). ENDF/B-VII.1 Nuclear Data for Science and Technology: Cross Sections, Covariances, Fission Product Yields and Decay Data. *Nucl. Data Sheets*, 112(12):2887–2996. 142, 143, 157

Chadwick, M., Obložinský, P., Herman, M., Greene, N., McKnight, R., Smith, D., Young, P., MacFarlane, R., Hale, G., Frankle, S., Kahler, A., Kawano, T., Little, R., Madland, D., Moller, P., Mosteller, R., Page, P., Talou, P., Trellue, H., White, M., Wilson, W., Arcilla, R., Dunford, C., Mughabghab, S., Pritychenko, B., Rochman, D., Sonzogni, A., Lubitz, C., Trumbull, T., Weinman, J., Brown, D., Cullen, D., Heinrichs, D., McNabb, D., Derrien, H., Dunn, M., Larson, N., Leal, L., Carlson, A., Block, R., Briggs, J., Cheng, E., Huria, H., Zerkle, M., Kozier, K., Courcelle, A., Pronyaev, V., and van der Marck, S. (2006). ENDF/B-VII.0: Next Generation Evaluated Nuclear Data Library for Nuclear Science and Technology. *Nuclear Data Sheets*, 107(12):2931–3060. 40

Christensen, C. J., Nielsen, A., Bahnsen, A., Brown, W. K., and Rustad, B. M. (1972). Free-Neutron Beta-Decay Half-Life. *Physical Review D*, 5(7):1628–1640. 28

Cook, J. C. (2009). Design and estimated performance of a new neutron guide system for the NCNR expansion project. *The Review of scientific instruments*, 80(2):023101. 9

Cooper, R., Chupp, T., and Dewey, M. (2010). Radiative β decay of the free neutron. *Phys. Rev. C*, 035503:1–15. 26

Denecke, B., Eykens, R., and Pauwels, J. (1999). Characterization of actinide targets by low solid-angle alpha particle counting. *Nuclear Instruments and ...*, 438(0168):124–130. 46

Deruytter, A. and Pelfer, P. (1967). Precise determination of the branching ratio and Q-value of the 10B(n, α)7Li reaction and of the Q-value of the 6Li(n, α)3H reaction. *Journal of Nuclear Energy*, 21(11):833–845. 45, 92

Desplanques, B., Donoghue, J. F. J., and Holstein, B. B. R. (1980). Unified treatment of the parity violating nuclear force. *Annals of Physics*, 124(2):449–495. 20, 22, 83

Dewey, M., Coakley, K., Gilliam, D., Greene, G., Laptev, A., Nico, J., Snow, W., Wietfeldt, F., and Yue, A. (2009). Prospects for a new cold neutron beam measurement of the neutron lifetime. *Nucl. Instrum. Methods Phys. Res., Sect. A*, 611(2-3):189–192. 48

Dewey, M. S., Gilliam, D. M., Nico, J. S., Wietfeldt, F. E., Fei, X., Snow, W. M., Greene, G. L., Pauwels, J., Eykens, R., Lamberty, A., and Van Gestel, J. (2003). Measurement of the Neutron Lifetime Using a Proton Trap. *Physical Review Letters*, 91(15):152302. 2, 41

Dubbers, D. and Schmidt, M. G. (2011). The neutron and its role in cosmology and particle physics. *Reviews of Modern Physics*, 83(4):1111–1171. 18

Ezhov, V. F., Andreev, A. Z., Ban, G., Bazarov, B. A., Geltenbort, P., Glushkov, A. G., Knyazkov, V. A., Kovrizhnykh, N. A., Krygin, G. B., Naviliat-Cuncic, O., and Ryabov, V. L. (2014). Measurement of the neutron lifetime with ultra-cold neutrons stored in a magneto-gravitational trap. *arXiv 1412.7434*, pages 18–21. 30, 33

Fermi, E. (1934). Versuch einer Theorie der β-Strahlen. I. *Zeitschrift für Physik*, 88(3-4):161–177. 8, 16, 27

Fermi, E. and Zinn, W. H. (1946). *Reflection of neutrons on mirrors*. Manhattan District. 10

Fomin, N., Greene, G., Allen, R., Cianciolo, V., Crawford, C., Tito, T., Huffman, P., Iverson, E., Mahurin, R., and Snow, W. (2015). Fundamental neutron physics beamline at the spallation neutron source at ORNL. *Nucl. Instrum. Methods Phys. Res., Sect. A*, 773:45–51. 85, 151

Fraser, J. S., Green, R. E., Hilborn, J. W., Milton, J. C. D., Gibson, W. A., Gross, E. E., and Zucker, A. (1965). Neutron production in thick targets bombarded by high energy protons. *Phys. Canada*, 21(2):17–18. 9

Gamow, G. and Teller, E. (1936). Selection Rules for the β-Disintegration. *Phys. Rev.*, 49(12):895–899. 16

Garwin, R. L., Lederman, L. M., and Weinrich, M. (1957). Observations of the Failure of Conservation of Parity and Charge Conjugation in Meson Decays: the Magnetic Moment of the Free Muon. *Physical Review*, 105(4):1415–1417. 17

Geiger, H. and Marsden, E. (1909). On a Diffuse Reflection of the Formula-Particles. 5

Geiger, H. and Marsden, E. (1913). The laws of deflexion of alpha particles through large angles. *Philosophical Magazine*, LXXXIII(1910):604–629. 5

Gericke, M. T., Alarcon, R., Balascuta, S., Barrón-Palos, L., Blessinger, C., Bowman, J. D., Carlini, R. D., Chen, W., Chupp, T. E., Crawford, C., Covrig, S., Dabaghyan, M., Fomin, N., Freedman, S. J., Gentile, T. R., Gillis, R. C., Greene, G. L., Hersman, F. W., Ino, T., Jones, G. L., Lauss, B., Leuschner, M., Lozowski, W. R., Mahurin, R., Masuda, Y., Mei, J., Mitchell, G. S., Muto, S., Nann, H., Page, S. a., Penttilä, S. I., Ramsay, W. D., Salas-Bacci, A., Santra, S., Sharma, M., Seo, P.-N., Sharapov, E. I., Smith, T. B., Snow, W. M., Wilburn, W. S., and Yuan, V. (2011). Measurement of parity-violating γ-ray asymmetry in the capture of polarized cold neutrons on protons. *Phys. Rev. C*, 83(1):015505. 2, 109

Gericke, M. T., Blessinger, C., Bowman, J. D., Gillis, R. C., Hartfield, J., Ino, T., Leuschner, M., Masuda, Y., Mitchell, G. S., Muto, S., Nann, H., Page, S. A., Penttilä, S. I., Ramsay, W. D., Seo, P. N., Snow, W. M., Tasson, J., and Wilburn, W. S. (2005). A current mode detector array for γ ray asymmetry measurements. *Nuclear Instruments and Methods in Physics Research, Section A: Accelerators, Spectrometers, Detectors and Associated Equipment*, 540(2-3):328–347. 89

Gilliam, D., Greene, G., and Lamaze, G. (1989). Absolute neutron counting based on B-10 alpha-gamma coincidence methods. *Nucl. Instrum. Methods Phys. Res., Sect. A*, 284(1):220–222. 45, 46

Gilliam, D. M. and Yue, A. T. (2014). Improvements in the characterization of actinide targets by low solid-angle counting. *Journal of Radioanalytical and Nuclear Chemistry*, 299(2):1061–1065. 46

Goldberger, M. L. and Seitz, F. (1947). Theory of the refraction and the diffraction of neutrons by crystals. *Phys. Rev.*, 71(5):294–310. 11

Grammer, K. B., Alarcon, R., Barr, L., Blyth, D., Bowman, J. D., Calarco, J., Crawford, C., Craycraft, K., Evans, D., Fomin, N., Fry, J., Gericke, M., Gillis, R. C., Greene, G. L., Hamblen, J., Hayes, C., Kucuker, S., and Wilburn, W. S. (2015). Measurement of the scattering cross section of slow neutrons on liquid parahydrogen from neutron transmission. *Phys. Rev. B*, 180301:1–6. 4, 91, 150, 153, 154, 156, 157, 158

Grassman, H., Lorenz, E., and Moser, H. (1985). Properties of CsI(Tl) - Renaissance of an old scintillation material. *Nuclear Instruments and Methods in Physics Research Section A: Accelerators, Spectrometers, Detectors and Associated Equipment*, 228:323–326. 89

Haxton, W. C. (2008). Nuclear Constraints on the Weak Nucleon-Nucleon Interaction. *arXiv 0802.2984*. 22

Heisenberg, W. (1932). Uber den Bau der Atomkerne. I. *Zeitschrift fur Physik*, 77(1-2):1–11. 7

Henderson, S. (2005). SNS Parameters List R13. Technical Report June, Oak Ridge National Laboratory. 8

Høghøj, P., Abele, H., Astruc Hoffmann, M., Baeßler, S., Reich, J., Nesvizhevsky, V., and Zimmer, O. (2000). Neutron long wavelength cut-off filter. *Nucl. Instrum. Methods Phys. Res., Sect. B*, 160(3):431–434. 62

Ilisca, E. and Paris, S. (1999). Magnetic Field Acceleration of the ortho-para H2 Conversion on Transition Oxides. *Physical Review Letters*, 82(8):1788–1791. 91

Iwanenko, D. (1932). The Neutron Hypothesis. *Nature (London)*, 129(3265):798–798. 7

Izotov, Y. I. and Thuan, T. X. (2010). THE PRIMORDIAL ABUNDANCE OF 4 He: EVIDENCE FOR NON-STANDARD BIG BANG NUCLEOSYNTHESIS. *The Astrophysical Journal*, 710(1):L67–L71. 23, 24

Jackson, J., Treiman, S., and Wyld, H. (1957). Possible Tests of Time Reversal Invariance in Beta Decay. *Phys. Rev.*, 106(3):517–521. 1, 16

Joliot-Curie, I. and Joliot-Curie, F. (1932). *Émission de protons de grande vitesse par les substances hydrogénées sous l'influence des rayons lambda tres pénétrants*. Gauthier-Villars. 6

Kai, T., Harada, M., Teshigawara, M., Watanabe, N., and Ikeda, Y. (2004). Coupled hydrogen moderator optimization with ortho/para hydrogen ratio. *Nucl. Instrum. Methods Phys. Res., Sect. A*, 523(3):398–414. 157

Keinert, J. and Sax, J. (1987). Investigation of neutron scattering dynamics in liquid hydrogen and deuterium for cold neutron sources. *Kerntechnik*, 51:19. 133

Klein, O. and Nishina, T. (1929). Über die Streuung von Strahlung durch freie Elektronen nach der neuen relativistischen Quantendynamik von Dirac. *Zeitschrift fur Physik*, 52:853–868. 6

Knoll, G. F. (2010). *Radiation detection and measurement*. John Wiley & Sons. 89

Leachman, J. W., Jacobsen, R. T., Penoncello, S. G., and Lemmon, E. W. (2009). Fundamental Equations of State for Parahydrogen, Normal Hydrogen, and Orthohydrogen. *J. Phys. Chem. Ref. Data*, 38(3):721. 146, 155

Lee, T. and Yang, C. C. (1956). Question of Parity Conservation in Weak Interactions. *Phys. Rev.*, 104(1):254–258. 17

Lefmann, K. and Nielsen, K. (1999). McStas, a general software package for neutron ray-tracing simulations. *Neutron news*, 10(3):20–23. 51

Lone, M., Santry, D., and Inglis, W. (1980). MeV neutron production from thermal neutron capture in Li and B compounds. *Nuclear Instruments and Methods*, 174(3):521–529. 139

MacFarlane, R. (1998). Cold-moderator scattering kernel methods. Technical report, Los Alamos National Laboratory (LANL), Los Alamos, NM. 133

Magán, M., Sordo, F., Zanini, L., Terrón, S., Ghiglino, A., Martínez, F., de Vicente, J., Vivanco, R., Perlado, J., Bermejo, F., Mezei, F., and Muhrer, G. (2013). Neutronic analysis of the bi-spectral moderator such as that proposed for ESS. *Nucl. Instrum. Methods Phys. Res., Sect. A*, 729:417–425. 157

Mahurin, R. and Crawford, C. (2006). Opening angles for the SNS FnPB choppers. Technical report, NPDGamma Internal Report. 85

Mampe, W., Ageron, P., Bates, C., Pendlebury, J., and Steyerl, A. (1989). Neutron lifetime measured with stored ultracold neutrons. *Phys. Rev. Lett.*, 63(6):593–596. 29, 31, 32

Mampe, W. and Bondarenko, L. (1993). Measuring neutron lifetime by storing ultracold neutrons and detecting inelastically scattered neutrons. *. . . C/C OF PIS'MA V . . . .* 32

Mangano, G., Miele, G., Pastor, S., and Peloso, M. (2001). A precision calculation of the effective number of cosmological neutrinos. *Physics Letters B*, 534(February 2008):15. 24

Marciano, W. and Sirlin, A. (2006). Improved Calculation of Electroweak Radiative Corrections and the Value of Vud. *Phys. Rev. Lett.*, 96(3):032002. 20

Mason, T. E., Abernathy, D., Anderson, I., Ankner, J., Egami, T., Ehlers, G., Ekkebus, a., Granroth, G., Hagen, M., Herwig, K., Hodges, J., Hoffmann, C., Horak, C., Horton, L., Klose, F., Larese, J., Mesecar, a., Myles, D., Neuefeind, J., Ohl, M., Tulk, C., Wang, X. L., and Zhao, J. (2006). The Spallation Neutron Source in Oak Ridge: A powerful tool for materials research. *Physica B: Condensed Matter*, 385-386(2006):955–960. 8

McCarty, R., Hord, J., and Roder, H. (1981). Selected Properties of Hydrogen (Engineering Design Data). Technical report, Center for Chemical Engineering, National Engineering Laboratory, National Bureau of Standards, Boulder, CO. 155

Mezei, F. (1976). Novel polarized neutron devices: supermirror and spin component amplifier. *Commun. Phys*, 1:81–85. 86

Mitchell, G. S., Blessinger, C. S., Bowman, J. D., Chupp, T. E., Coulter, K. P., Gericke, M., Jones, G. L., Leuschner, M. B., Nann, H., Page, S. A., Penttilä, S. I., Smith, T. B., Snow, W. M., and Wilburn, W. S. (2004). A measurement of parity-violating gamma-ray asymmetries in polarized cold neutron capture on 35Cl, 113Cd, and 139La. *Nuclear Instruments and Methods in Physics Research, Section A: Accelerators, Spectrometers, Detectors and Associated Equipment*, 521(2-3):468–479. 89, 92

Moon, R., Riste, T., and Koehler, W. (1969). Polarization Analysis of Thermal-Neutron Scattering. *Phys. Rev.*, 181(2):920–931. 131

Mughabghab, S. F. (2006). *Atlas of Neutron Resonances*. Elsevier, New York, 5-th ed. edition. 143, 151

Munter, A. (2013). Neutron scattering lengths and cross sections. Technical report, National Institute of Standards and Technology, Gaithersburg, MD. 132

Nakamura, K. (2010). Review of particle physics. *Journal of Physics G: Nuclear and Particle Physics*, 37:075021. 31

Nico, J., Dewey, M., Gilliam, D., Wietfeldt, F., Fei, X., Snow, W., Greene, G., Pauwels, J., Eykens, R., Lamberty, A., Gestel, J., and Scott, R. (2005). Measurement of the neutron lifetime by counting trapped protons in a cold neutron beam. *Phys. Rev. C*, 71(5):055502. 18, 32, 41

Nollett, K. M. and Steigman, G. (2014). BBN and the CMB constrain light, electromagnetically coupled WIMPs. *Phys. Rev. D*, 89(8):083508. 24

Olive, K. A. (2014). Review of particle physics. *Chin. Phys. C*, 38:90001. 24, 26, 32

Olive, K. A., Steigman, G., and Walker, T. P. (2000). Primordial nucleosynthesis: theory and observations. *Physics Reports*, 333-334:389–407. 23

Ooi, M., Ino, T., Muhrer, G., Pitcher, E., Russell, G., Ferguson, P., Iverson, E., Freeman, D., and Kiyanagi, Y. (2006). Measurements of the change of neutronic performance of a hydrogen moderator at Manuel Lujan Neutron Scattering Center due to conversion from ortho- to para-hydrogen state. *Nucl. Instrum. Methods Phys. Res., Sect. A*, 566(2):699–705. 157

O'Shaughnessy, C., Golub, R., Schelhammer, K., Swank, C., Seo, P.-N., Huffman, P., Dzhosyuk, S., Mattoni, C., Yang, L., Doyle, J., Coakley, K., Thompson, A., Mumm, H., Lamoreaux, S., McKinsey, D., and Yang, G. (2009). Measuring the neutron lifetime using magnetically trapped neutrons. *Nucl. Instrum. Methods Phys. Res., Sect. A*, 611(2-3):171–175. 30

Paul, W., Anton, F., Paul, L., Paul, S., and Mampe, W. (1989). Measurement of the neutron lifetime in a magnetic storage ring. *Zeitschrift für Physik C Particles and Fields*, 45(1):25–30. 28

Pelowitz, D. B. (2011). *MCNPX User's Manual*. Los Alamos National Laboratory. 3, 103

Pichlmaier, A., Varlamov, V., Schreckenbach, K., and Geltenbort, P. (2010). Neutron lifetime measurement with the UCN trap-in-trap MAMBO II. *Physics Letters B*, 693(3):221–226. 29, 32

Pritychenko, B. and Mughabghab, S. F. (2012). Neutron Thermal Cross Sections, Westcott Factors, Resonance Integrals, Maxwellian Averaged Cross Sections and Astrophysical Reaction Rates Calculated from Major Evaluated Data Libraries. *Nuclear Data Sheets*, 113(12):145. 35, 47

Robson, J. M. (1951). The Radioactive Decay of the Neutron. *Physical Review*, 83(2):349–358. 27

Rutherford, E. (1911). The Scattering of α and β Particles by Matter and the Structure of the Atom. *Phil. Mag*, 495(1909):1–24. 5

Rutherford, E. (1920). Bakerian Lecture. Nuclear Constitution of Atoms. *Proceedings of the Royal Society of London*, 97(686):374–400. 5

Salvat, D. J., Adamek, E. R., Barlow, D., Bowman, J. D., Broussard, L. J., Callahan, N. B., Clayton, S. M., Cude-Woods, C., Currie, S., Dees, E. B., Fox, W., Geltenbort, P., Hickerson, K. P., Holley, a. T., Liu, C.-Y., Makela, M., Medina, J., Morley, D. J., Morris, C. L., Penttilä, S. I., Ramsey, J., Saunders, A., Seestrom, S. J., Sharapov, E. I., Sjue, S. K. L., Slaughter, B. a., Vanderwerp, J., VornDick, B., Walstrom, P. L., Wang, Z., Womack, T. L., and Young, a. R. (2014). Storage of ultracold neutrons in the magneto-gravitational trap of the UCN-tau experiment. *Phys. Rev. C*, 89(5):52501. 30, 32

Salvati, L., Pagano, L., Consiglio, R., and Melchiorri, A. (2015). Cosmological constraints on the neutron lifetime. *arXiv 1507.07243*, pages 1–5. 25, 32

Santra, S., Barrón Palos, L., Blessinger, C., Bowman, J., Chupp, T., Covrig, S., Crawford, C., Dabaghyan, M., Dadras, J., Dawkins, M., Gericke, M., Fox, W., Gillis, R., Leuschner, M., Lozowski, B., Mahurin, R., Mason, M., Mei, J., Nann, H., Penttila, S., Salas-Bacci, A., Sharma, M., Snow, W., and Wilburn, W. (2010). A liquid parahydrogen target for the measurement of a parity-violating gamma asymmetry in. *Nucl. Instrum. Methods Phys. Res., Sect. A*, 620(2-3):421–436. 153

Savage, M. J. (2001). Parity violation in low-energy npdγ and the deuteron anapole moment. *Nuclear Physics A*, 695(1-4):365–373. 22

Schaerpf, O. (1989a). Comparison of theoretical and experimental behaviour of supermirrors and discussion of limitations. *Physica B: Condensed Matter*, 156-157:631–638. 86

Schaerpf, O. (1989b). Properties of beam bender type neutron polarizers using supermirrors. *Physica B: Condensed Matter*, 156-157:639–646. 86

Schindler, M. R. and Springer, R. P. (2010). Two parity-violating asymmetries from in pionless effective field theories. *Nuclear Physics A*, 846(1-4):51–62. 22

Seiffert, W. D., Weckermann, B., and Misenta, R. (1970). Messung der Streuquerschnitte von flüssigem und festem Wasserstoff Deuterium und Deuteriumhydrid für thermische

Neutronen. *Z. Naturforsch A, Phys., Phys. Chem., Kosmophys.*, 25:967. 4, 141, 142, 147, 158

Seo, P. N., Barrón-Palos, L., Bowman, J. D., Chupp, T. E., Crawford, C., Dabaghyan, M., Dawkins, M., Freedman, S. J., Gentile, T., Gericke, M. T., Gillis, R. C., Greene, G. L., Hersman, F. W., Jones, G. L., Kandes, M., Lamoreaux, S., Lauss, B., Leuschner, M. B., Mahurin, R., Mason, M., Mei, J., Mitchell, G. S., Nann, H., Page, S. A., Penttilä, S. I., Ramsay, W. D., Salas Bacci, A., Santra, S., Sharma, M., Smith, T. B., Snow, W. M., Wilburn, W. S., and Zhu, H. (2008). High-efficiency resonant rf spin rotator with broad phase space acceptance for pulsed polarized cold neutron beams. *Physical Review Special Topics - Accelerators and Beams*, 11(8):1–15. 87

Serebrov, A., Varlamov, V., Kharitonov, A., Fomin, A., Pokotilovski, Y., Geltenbort, P., Butterworth, J., Krasnoschekova, I., Lasakov, M., Tal'daev, R., Vassiljev, A., and Zherebtsov, O. (2005). Measurement of the neutron lifetime using a gravitational trap and a low-temperature Fomblin coating. *Physics Letters B*, 605(1-2):72–78. 29, 31, 32

Sigma-Aldridge Corp., 3050 Spruce Street, St. Louis, MO 63103, U. (2010). Product No. 371254-250G. 149

Snell, A. H., Pleasonton, F., and McCord, R. V. (1950). Radioactive Decay of the Neutron. *Physical Review*, 78(3):310–311. 27

Snow, W., Bazhenov, A., Blessinger, C., Bowman, J., Chupp, T., Coulter, K., Freedman, S., Fujikawa, B., Gentile, T., Greene, G., Hansen, G., Hogan, G., Ishimoto, S., Jones, G., Knudson, J., Kolomenski, E., Lamoreaux, S., Leuschner, M., Masaike, A., Masuda, Y., Matsuda, Y., Morgan, G., Morimoto, K., Morris, C., Nann, H., Penttilä, S., Pirozhkov, A., Pomeroy, V., Rich, D., Serebrov, A., Sharapov, E., Smith, D., Smith, T., Welsh, R., Wietfeldt, F., Wilburn, W., Yuan, V., and Zerger, J. (2000). Measurement of the parity violating asymmetry Aγ in n p d gamma. *Nucl. Instrum. Methods Phys. Res., Sect. A*, 440(3):729–735. 84

Sosnovsky, A., Spivak, P., Prokofiev, Y., Kutikov, I., and Dobrinin, Y. (1959). Measurement of the neutron life-time. *Nuclear Physics*, 10:395–404. 28

Souers, P. (1986). *Hydrogen Properties for Fusion Energy*. University of California Press, Oakland, CA. 155

Squires, G. L. and Stewart, A. T. (1955). The Scattering of Slow Neutrons by ortho- and para-Hydrogen. *Proc. R. Soc. A*, 230(1180):19–32. 158

Stelts, M., Chrien, R., Goldhaber, M., Kenny, M., and McCullagh, C. (1979). Angular distributions of the 6Li(n,t)4He and 10B(n,α)7Li reactions at 2 and 24 keV. *Phys. Rev. C*, 19(4):1159–1167. 45, 92

Steyerl, A., Pendlebury, J. M., Kaufman, C., Malik, S. S., and Desai, a. M. (2012). Quasielastic scattering in the interaction of ultracold neutrons with a liquid wall and application in a reanalysis of the Mambo I neutron-lifetime experiment. *Phys. Rev. C*, 85(6):065503. 30, 31, 32

Szymanski, J., Bowman, J., Delheij, P., Frankle, C., Knudson, J., Penttilä, S., Seestrom, S., Yoo, S., Yuan, V., and Zhu, X. (1994). Ion chamber system for neutron flux measurements. *Nucl. Instrum. Methods Phys. Res., Sect. A*, 340(3):564–571. 88

Tanaka, K. a., Yabuuchi, T., Sato, T., Kodama, R., Kitagawa, Y., Takahashi, T., Ikeda, T., Honda, Y., and Okuda, S. (2005). Calibration of imaging plate for high energy electron spectrometer. *Review of Scientific Instruments*, 76(1):013507. 53

Taniguchi, S., Yamadera, A., Nakamura, T., and Fukumura, A. (1998). Measurement of radiation tracks for particle and energy identification by using imaging plate. *Nucl. Instrum. Methods Phys. Res., Sect. A*, 413(1):119–126. 53

Wietfeldt, F. E. and Greene, G. L. (2011). Colloquium: The neutron lifetime. *Rev. Mod. Phys.*, 83(4):1173–1192. 18, 19

Wilburn, W., Bowman, J., Penttilä, S., and Gericke, M. (2005). A low-noise current-mode preamplifier for gamma asymmetry measurements. *Nuclear Instruments and Methods in Physics Research Section A: Accelerators, Spectrometers, Detectors and Associated Equipment*, 540(1):180–187. 89

Wilburn, W. S. (2007). Analysis of the Arithmetic and Geometric Mean Methods of Calculating Asymmetries. Technical report, Los Alamos National Laboratory. 93

Willendrup, P., Farhi, E., and Lefmann, K. (2004). McStas 1.7-a new version of the flexible Monte Carlo neutron scattering package. *Physica B: Condensed Matter*, 350(1):E735—-E737. 51

Williams, R. E. and Rowe, J. (2002). Developments in neutron beam devices and an advanced cold source for the NIST research reactor. *Physica B: Condensed Matter*, 311(1-2):117–122. 9

Wilson, F. (1968). Fermi's theory of beta decay. *Am. J. Phys.* 16

Wu, C. S., Ambler, E., Hayward, R. W., Hoppes, D. D., and Hudson, R. P. (1957). Experimental Test of Parity Conservation in Beta Decay. *Phys. Rev.*, 105(4):1413–1415. 1, 17

Wyckoff, R. (1963). *Crystal Structures*. Wiley, New York. 153

Young, J. and Koppel, J. (1964). Slow Neutron Scattering by Molecular Hydrogen and Deuterium. *Phys. Rev.*, 135(3A):A603–A611. 133

Yue, A. T. (2011). *Progress Towards a Redetermination of the Neutron Lifetime Through the Absolute Determination of Neutron Flux*. PhD thesis, University of Tennessee - Knoxville. 48

Yue, A. T., Dewey, M. S., Gilliam, D. M., Greene, G. L., Laptev, A. B., Nico, J. S., Snow, W. M., and Wietfeldt, F. E. (2013). Improved Determination of the Neutron Lifetime. *Phys. Rev. Lett.*, 111(22):222501. 2, 32, 48

Appendix

Appendix A

Equilibrium Concentration of Orthohydrgen and Parahydrogen

Molecular hydrogen is composed of two nuclear spin isomers, parahydrogen and orthohydrogen. The singlet parahydrogen state corresponds to even angular momentum quantum numbers ($J = even$) and the triplet orthohydrogen state corresponds to odd angular momentum quantum numbers ($J = odd$). The equilibrium concentrations of these two isomers depends on temperature.

The probability that a particular state, i, is occupied is given by the Boltzmann factor, $P_i = Ce^{-\beta E_i}$, where β is $\frac{1}{k_B T}$, C is a normalization constant, and E_i is the energy of the state. The normalization constant can be found by summing over all states, $1/C = \sum P_i = Z$, where Z is the called the partition function. The partition function is defined as the sum over all states of the Boltzmann factors,

$$Z = \sum_i e^{-\beta E_i}. \tag{A.1}$$

In the case of a system where the total energy depends on independent contributions, for instance if the energy of the state is given by the sum of two contributions a and b

$$E_{a,b} = E_a + E_b, \tag{A.2}$$

where E_a is energy due to contribution a and E_b is the energy due to contribution b. In this case, the partition function is

$$Z = \sum_a \sum_b e^{-\beta(E_a+E_b)} = \sum_a e^{-\beta E_a} \sum_b e^{-\beta E_b} = Z_a Z_b, \tag{A.3}$$

such that the partition functions of independent contributions multiply.

Hydrogen is a diatomic molecule with contributions to the total energy from translation, vibration, and rotation. The partition function is given by

$$Z_{\mathrm{H}_2} = Z_{\mathrm{vib}} Z_{\mathrm{trans}} Z_{\mathrm{rot}}. \tag{A.4}$$

The vibrational motion of a diatomic molecule, where each atom oscillates along the line connecting the atoms, can be approximated as a simple harmonic oscillator with energy levels $(n + \frac{1}{2})\hbar\omega$ for integer values of n. The vibrational partition function is then given by

$$Z_{\mathrm{vib}} = \sum_i e^{-\beta E_i} = \sum_{n=0}^{\infty} e^{-\beta(n+\frac{1}{2})\hbar\omega} = e^{-\beta\frac{1}{2}\hbar\omega} \sum_{n=0}^{\infty} e^{-\beta n\hbar\omega} = \frac{e^{-\frac{1}{2}\beta\hbar\omega}}{1 - e^{-\beta\hbar\omega}}. \tag{A.5}$$

The translational motion requires investigating a particle in a three dimensional box. Consider a three dimensional box of molecules of dimensions $L \times L \times L$ and volume $V = L^3$. The wave function of a molecule in the box with wave vector k is given by

$$\psi(x, y, z) = \frac{1}{V^{1/2}} \sin(k_x x) \sin(k_y y) \sin(k_z z). \tag{A.6}$$

The wave function goes to zero at the boundaries of the box, which occurs for

$$k_x = \frac{n_x \pi}{L}, \quad k_y = \frac{n_y \pi}{L}, \quad k_z = \frac{n_z \pi}{L}, \tag{A.7}$$

where n_x, n_y, and n_z are positive integers. A single point in k-space therefore occupies a volume

$$\frac{\pi}{L} \times \frac{\pi}{L} \times \frac{\pi}{L} = \left(\frac{\pi}{L}\right)^3. \tag{A.8}$$

The allowed states with a wave vector between k and $k + \mathrm{d}k$ lie in one octant of a spherical shell of radius k and thickness $\mathrm{d}k$, since only positive wave vectors are considered. The volume of this shell is given by

$$\frac{1}{8}4\pi k^2 \mathrm{d}k. \tag{A.9}$$

The number of states a wave vector between k and $k+\mathrm{d}k$ is described by the function $g(k)\mathrm{d}k$, where $g(k)$ is the density of states, and is given by

$$g(k)\mathrm{d}k = \frac{\frac{1}{8}4\pi k^2 \mathrm{d}k}{(\pi/L)^3} = \frac{Vk^2\mathrm{d}k}{2\pi^2}. \tag{A.10}$$

To determine the translational partition function, the summation is replaced by an integral

$$Z_{\mathrm{trans}} = \int_0^\infty e^{-\beta E(k)} g(k)\mathrm{d}k, \tag{A.11}$$

where the energy of a molecule is determined by the wave vector k such that

$$E(k) = \frac{\hbar^2 k^2}{2m}. \tag{A.12}$$

The partition function is then given by

$$Z_{\mathrm{trans}} = \int_0^\infty e^{-\beta\frac{\hbar^2k^2}{2m}} \frac{Vk^2\mathrm{d}k}{2\pi^2} = \frac{V}{\hbar^3}\big(\frac{m}{2\pi\beta}\big)^{3/2}. \tag{A.13}$$

This can be further simplified by defining the thermal wavelength, λ_{th} as

$$\lambda_{\mathrm{th}} = \frac{h}{\sqrt{2\pi m k_{\mathrm{B}T}}}, \tag{A.14}$$

and therefore

$$Z_{\mathrm{trans}} = \frac{V}{\lambda_{\mathrm{th}}^3}. \tag{A.15}$$

The rotational kinetic energy of a molecule with moment of inertia I is given by $\hat{\mathbf{J}}^2/2I$ where $\hat{\mathbf{J}}$ is the total angular momentum vector. The eigenvalues of $\hat{\mathbf{J}}^2$ are given by $\hbar^2 J(J+1)$, where the angular momentum quantum number J takes values $J = 0, 1, 2, \cdots$. The energy

levels are then given by

$$E_J = \frac{\hbar^2}{2I} J(J+1), \tag{A.16}$$

and have degeneracy $2J+1$. The rotation partition function is then given by

$$Z_{\text{rot}} = \sum_i e^{-\beta E_i} = \sum_{J=0}^{\infty} (2J+1) e^{-\beta \hbar^2 J(J+1)/2I}. \tag{A.17}$$

In the case of the hydrogen molecule, the total wave function must be antisymmetric because the protons are fermions. There are two forms of molecular hydrogen. If the protons are symmetric under exchange, the molecule is in the triplet state with $J = 1$ and is called orthohydrogen. If the protons are antisymmetric under exchange, the molecule is in the singlet state with $J = 0$ and is called parahydrogen. For orthohydrogen, the rotational part of the wave function must be antisymmetric and therefore has odd-integer values of J. Similarly, parahydrogen must have a symmetric rotational part of the wave function and has even-integer values of J. The partition function can then be further separated accordingly with

$$Z_{\text{ortho}} = \sum_{J=1,3,5,\cdots}^{\infty} 3(2J+1) e^{-\beta \hbar^2 J(J+1)/2I}, \tag{A.18}$$

$$Z_{\text{para}} = \sum_{J=0,2,4,\cdots}^{\infty} (2J+1) e^{-\beta \hbar^2 J(J+1)/2I}. \tag{A.19}$$

These expressions can then be used to express the equilibrium ratio of orthohydrogen to parahydrogen

$$f = \frac{Z_{\text{ortho}}}{Z_{\text{para}}} = \frac{\sum_{J=1,3,5,\cdots}^{\infty} 3(2J+1) e^{-\beta \hbar^2 J(J+1)/2I}}{\sum_{J=0,2,4,\cdots}^{\infty} (2J+1) e^{-\beta \hbar^2 J(J+1)/2I}}. \tag{A.20}$$

The molecule is represented as if it is two point masses of mass m connected by a massless rod of length l, which has a moment of inertia of $I = \frac{1}{2} m l^2$. The separation of the protons in the molecule is 7.4×10^{-11} m. The orthohydrogen and parahydrogen equilibrium concentrations are shown in figure A.1. Hydrogen at room temperature, commonly called normal hydrogen, is approximately 75% orthohydrogen while the equilibirum concentration of orthohydrogen at 15 Kelvin is about 0.01%. The energy separation between the $J = 0$ ground state and the first excited state is about 14.7 meV corresponding to about 85 Kelvin.

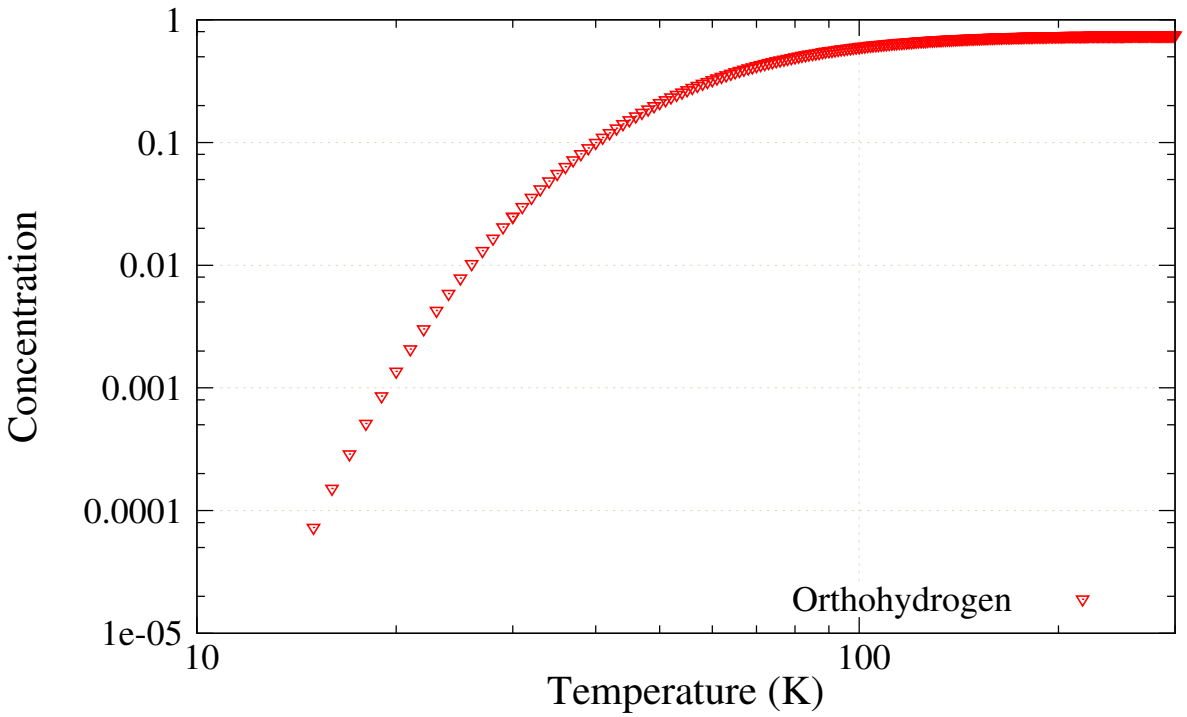

Figure A.1: Orthohydrogen concentration as a function of temperature. The parahydrogen concentration is $1 - x_{\mathrm{ortho}}$.

Appendix B

Geometrical factors and MCNPX model tables

Table B.1: Table of Materials used in MCNPX

Material	Density $g\,cm^{-3}$	Composition (by weight)
Air	0.001225	Nitrogen (75.5636%), Oxygen (23.1475%), Argon (1.2889%)
Aluminum at 293K or 20K	2.7	Aluminum (97.25%), Silicon (0.71%), Chromium (0.19%), Iron (0.5%), Zinc (0.24%), Copper (0.36%), Titanium (0.01%), Manganese (0.07%), Zirconium (0.24%), Magnesium (1%)
Carbon Tetrachloride	1.5867	Carbon (20%), Chlorine-35 (60%), Chlorine-37 (20%) (atomic fractions)
Cesium Iodide	4.51	Iodine (48.845%), Cesium (51.155%)
Concrete	2.2	Hydrogen (0.6488%), Oxygen (51.8069%), Sodium (1.6577%), Aluminum (3.5137%), Silicon (34.9085%), Potassium (1.5324%), Calcium (4.5057%), Iron (1.4411%)
Copper Metal	8.94	Copper-63 (69.15%), Copper-65 (30.85%)
Liquid para-Hydrogen at 20K	0.07093	para-Hydrogen (100%)
Natural Lead	11.35	Lead-206 (24.1%), Lead-207 (22.1%), Lead-208 (52.4%)
Lithium Carbonate	1.36	Hydrogen (4.2%), Carbon (21.898%), Silicon 27.888%), Oxygen (40.792%), Zinc (0.154%), Lithium-6 (4.498%), Lithium-7 (0.583%)
Lithium Fluoride	2.635	Hydrogen (2.2%), Fluorine (35.0%), Lithium-6 (31.5%), Lithium-7 (3.5%), Silicon (27.8%) (matrix composition unknown)
Nylon Plastic type 6	1.14	Hydrogen (9.7976%), Carbon (63.6856%), Nitrogen (12.3779%), Oxygen (14.1389%)
Steel (pure iron)	7.874	Iron (100%)

Table B.2: Table of Ideal Geometrical Factors and Absolute Statistical Uncertainties for the Chlorine Target

Detector	G_{LR}	G_{UD}	G_{Z}	σ_{LR}	σ_{UD}	σ_{Z}
0	-0.18268	0.66047	-0.66184	1.9160e-04	1.5890e-04	1.5179e-04
1	-0.4972	0.49667	-0.64675	1.9056e-04	1.7719e-04	1.9142e-04
2	-0.66078	0.18256	-0.661	1.6162e-04	1.8899e-04	1.7229e-04
3	-0.66132	-0.18211	-0.66095	1.6542e-04	2.1360e-04	1.6724e-04
4	-0.49689	-0.4966	-0.64696	1.8541e-04	1.8744e-04	1.8933e-04
5	-0.18247	-0.66047	-0.66162	2.0856e-04	1.5483e-04	1.7213e-04
6	0.18277	-0.6604	-0.66183	2.0046e-04	1.6886e-04	1.7841e-04
7	0.49688	-0.49667	-0.64748	1.7723e-04	1.8437e-04	1.7325e-04
8	0.66077	-0.18205	-0.66165	1.6781e-04	2.1944e-04	1.6685e-04
9	0.66097	0.18214	-0.66159	1.6033e-04	2.0962e-04	1.5974e-04
10	0.4971	0.49694	-0.64711	1.9177e-04	1.8111e-04	1.7193e-04
11	0.1826	0.66062	-0.66158	2.0193e-04	1.6688e-04	1.6162e-04
12	-0.22632	0.84456	-0.36918	1.8963e-04	1.0558e-04	1.4653e-04
13	-0.62495	0.62434	-0.35792	1.5352e-04	1.4950e-04	1.6892e-04
14	-0.84468	0.22562	-0.36867	1.0657e-04	1.8120e-04	1.5094e-04
15	-0.8446	-0.22541	-0.36888	1.1319e-04	1.9846e-04	1.6282e-04
16	-0.62496	-0.62426	-0.35785	1.5010e-04	1.3787e-04	1.7956e-04
17	-0.22609	-0.84463	-0.36916	1.9335e-04	1.0484e-04	1.6091e-04
18	0.22645	-0.8445	-0.36932	1.9174e-04	1.0221e-04	1.7260e-04
19	0.62499	-0.6243	-0.35796	1.5348e-04	1.3905e-04	1.8119e-04
20	0.84478	-0.22551	-0.36887	1.0727e-04	1.9142e-04	1.7273e-04
21	0.84451	0.22597	-0.36909	1.1003e-04	1.8433e-04	1.5754e-04
22	0.625	0.62442	-0.35828	1.5622e-04	1.5725e-04	1.7646e-04
23	0.22621	0.84456	-0.36935	1.7048e-04	1.0378e-04	1.5251e-04
24	-0.2415	0.90994	0.096158	1.9811e-04	9.4433e-05	1.8471e-04
25	-0.66977	0.66844	0.092741	1.5960e-04	1.6219e-04	1.8508e-04
26	-0.90962	0.24059	0.09593	8.9538e-05	1.8475e-04	1.8614e-04
27	-0.90979	-0.2406	0.096257	9.6138e-05	1.9419e-04	1.7429e-04
28	-0.66959	-0.66876	0.092784	1.4400e-04	1.5978e-04	1.8261e-04
29	-0.24159	-0.90959	0.096314	1.9375e-04	1.0025e-04	1.7036e-04
30	0.24107	-0.90988	0.0963	2.0024e-04	8.6794e-05	1.8158e-04
31	0.66969	-0.66863	0.092447	1.6335e-04	1.5586e-04	1.8276e-04
32	0.90977	-0.24073	0.095825	8.8589e-05	1.9087e-04	1.8898e-04
33	0.90977	0.24088	0.095953	9.1636e-05	1.9142e-04	1.7823e-04
34	0.66962	0.66866	0.092773	1.5370e-04	1.3413e-04	1.9008e-04
35	0.24111	0.90976	0.096313	2.2159e-04	9.8619e-05	1.7174e-04
36	-0.21069	0.77943	0.5055	1.9042e-04	1.2368e-04	1.4265e-04
37	-0.58014	0.57973	0.4914	1.7901e-04	1.6231e-04	1.6888e-04
38	-0.77939	0.21043	0.5051	1.3133e-04	1.9416e-04	1.4703e-04
39	-0.77945	-0.21039	0.50489	1.2385e-04	1.9870e-04	1.3768e-04
40	-0.58024	-0.57946	0.49125	1.5709e-04	1.6672e-04	1.7057e-04
41	-0.21065	-0.77957	0.50515	1.9517e-04	1.3336e-04	1.4890e-04
42	0.21097	-0.77943	0.50521	1.9802e-04	1.2480e-04	1.5695e-04
43	0.58032	-0.57962	0.49118	1.5286e-04	1.6230e-04	1.5180e-04
44	0.77958	-0.21053	0.5051	1.3262e-04	2.0377e-04	1.5917e-04
45	0.77984	0.21044	0.50491	1.3599e-04	1.9815e-04	1.4632e-04
46	0.57998	0.57976	0.49135	1.5671e-04	1.6347e-04	1.6100e-04
47	0.21097	0.77923	0.50542	1.9193e-04	1.2857e-04	1.5045e-04

Table B.3: Table of Ideal Geometrical Factors and Absolute Statistical Uncertainties for the Teflon Chlorine Target at the rear of the spin flipper

Detector	G_{LR}	G_{UD}	G_{Z}	σ_{LR}	σ_{UD}	σ_{Z}
0	-0.22932	0.83893	0.35018	3.1118e-04	1.7595e-04	2.7114e-04
1	-0.62284	0.62797	0.33138	2.5707e-04	2.5603e-04	2.8256e-04
2	-0.83358	0.22768	0.35334	1.9755e-04	3.4232e-04	3.1062e-04
3	-0.83304	-0.22764	0.35358	1.8486e-04	3.4519e-04	2.7887e-04
4	-0.62234	-0.62856	0.33122	2.6150e-04	2.5775e-04	3.1132e-04
5	-0.22898	-0.83891	0.35034	3.2241e-04	1.6879e-04	2.5558e-04
6	0.22857	-0.83937	0.35031	3.2449e-04	1.7329e-04	2.5479e-04
7	0.62298	-0.6278	0.33108	2.5340e-04	2.5954e-04	2.6440e-04
8	0.83351	-0.22799	0.35383	1.9215e-04	3.4662e-04	2.7922e-04
9	0.83348	0.22787	0.35334	1.9712e-04	3.6159e-04	3.0194e-04
10	0.62257	0.62803	0.33137	2.5049e-04	2.7079e-04	2.6988e-04
11	0.22925	0.83917	0.35016	3.3881e-04	1.7839e-04	2.5468e-04
12	-0.19379	0.70173	0.61546	2.2271e-04	1.7487e-04	1.7177e-04
13	-0.52581	0.52594	0.6013	2.2574e-04	2.3686e-04	1.7699e-04
14	-0.70194	0.19292	0.61529	1.7209e-04	2.5621e-04	1.7882e-04
15	-0.70187	-0.1931	0.61529	1.8112e-04	2.5672e-04	1.7811e-04
16	-0.52633	-0.52567	0.60067	2.2543e-04	2.2530e-04	1.9239e-04
17	-0.1931	-0.70173	0.61519	2.3807e-04	1.8248e-04	1.7505e-04
18	0.19347	-0.70181	0.61539	2.5760e-04	1.8375e-04	1.9356e-04
19	0.5259	-0.52579	0.60128	2.2516e-04	2.3045e-04	1.9260e-04
20	0.70191	-0.19299	0.61504	1.8362e-04	2.6609e-04	1.7604e-04
21	0.70191	0.19297	0.61522	1.7474e-04	2.8224e-04	1.7001e-04
22	0.52644	0.5253	0.60148	2.2149e-04	2.2719e-04	1.9027e-04
23	0.19334	0.70203	0.61503	2.4668e-04	1.7334e-04	1.8030e-04
24	-0.15217	0.53115	0.78259	2.9848e-04	2.4406e-04	1.8842e-04
25	-0.40517	0.40516	0.7703	3.1170e-04	2.8728e-04	2.0649e-04
26	-0.53129	0.15214	0.78217	2.6799e-04	3.0230e-04	1.9267e-04
27	-0.53078	-0.1525	0.7823	2.3264e-04	2.8992e-04	1.9183e-04
28	-0.40503	-0.40466	0.77059	2.8536e-04	2.7287e-04	2.1021e-04
29	-0.15266	-0.53096	0.7824	2.8546e-04	2.5666e-04	1.7669e-04
30	0.15242	-0.53149	0.78228	2.7714e-04	2.5183e-04	1.9979e-04
31	0.40445	-0.40509	0.77099	2.5835e-04	2.7173e-04	2.0287e-04
32	0.53139	-0.15202	0.78222	2.7692e-04	3.0178e-04	1.7638e-04
33	0.53135	0.15221	0.78219	2.6364e-04	3.1233e-04	1.6376e-04
34	0.40457	0.40502	0.77118	2.6956e-04	3.0895e-04	1.8094e-04
35	0.15159	0.53055	0.78292	2.6952e-04	2.3352e-04	1.9406e-04
36	-0.1212	0.4022	0.86271	3.9678e-04	3.6084e-04	2.2063e-04
37	-0.31172	0.31187	0.85452	3.9471e-04	3.9388e-04	2.4635e-04
38	-0.40288	0.12148	0.86249	3.5140e-04	3.8800e-04	2.1806e-04
39	-0.40336	-0.12027	0.863	3.4571e-04	3.9191e-04	2.1125e-04
40	-0.31289	-0.31143	0.8542	3.5903e-04	3.7274e-04	2.3024e-04
41	-0.12052	-0.40254	0.86308	3.7797e-04	3.6517e-04	2.2584e-04
42	0.12004	-0.40236	0.86353	3.5404e-04	3.5382e-04	2.3059e-04
43	0.31073	-0.31141	0.85514	3.7647e-04	3.9295e-04	2.2923e-04
44	0.40262	-0.12056	0.86304	3.7134e-04	3.9238e-04	2.2424e-04
45	0.40263	0.12183	0.86293	3.7848e-04	3.7426e-04	2.3553e-04
46	0.31093	0.31153	0.85507	3.7045e-04	3.8587e-04	2.1640e-04
47	0.12067	0.40208	0.86353	3.7562e-04	3.3709e-04	2.1557e-04

Table B.4: Table of Ideal Geometrical Factors and Absolute Statistical Uncertainties for the Aluminum Target

Detector	G_{LR}	G_{UD}	G_{Z}	σ_{LR}	σ_{UD}	σ_{Z}
0	-0.20424	0.75371	-0.49946	2.7718e-04	2.5343e-04	3.4185e-04
1	-0.56084	0.56035	-0.487	2.8167e-04	2.6014e-04	3.3579e-04
2	-0.75357	0.20348	-0.4994	2.5920e-04	3.1111e-04	3.5213e-04
3	-0.75365	-0.20325	-0.49924	2.3667e-04	2.8109e-04	3.4570e-04
4	-0.56103	-0.56013	-0.48568	2.7506e-04	2.4606e-04	3.9302e-04
5	-0.20399	-0.75334	-0.49985	2.8704e-04	2.3351e-04	3.5111e-04
6	0.20408	-0.75393	-0.49988	2.7448e-04	2.4124e-04	3.5726e-04
7	0.56146	-0.56063	-0.48659	2.4218e-04	2.8458e-04	3.3923e-04
8	0.75374	-0.20387	-0.49957	2.7557e-04	2.6474e-04	3.4280e-04
9	0.75379	0.20358	-0.49998	2.3370e-04	2.9397e-04	3.2979e-04
10	0.56156	0.56069	-0.48637	2.8367e-04	2.6198e-04	3.6435e-04
11	0.20316	0.75415	-0.50011	2.7557e-04	2.3182e-04	3.4556e-04
12	-0.23316	0.87604	-0.14385	2.6152e-04	1.4287e-04	3.6220e-04
13	-0.64694	0.64518	-0.14002	2.2286e-04	2.4190e-04	3.9201e-04
14	-0.87599	0.2326	-0.14411	1.5457e-04	2.8032e-04	4.0658e-04
15	-0.87638	-0.2324	-0.14348	1.6770e-04	2.6189e-04	3.5141e-04
16	-0.64638	-0.64598	-0.13971	2.3303e-04	2.2148e-04	4.0125e-04
17	-0.23281	-0.87622	-0.14377	2.6323e-04	1.7327e-04	3.6969e-04
18	0.2329	-0.87636	-0.14407	2.5405e-04	1.6147e-04	3.9623e-04
19	0.6464	-0.64597	-0.14053	2.1457e-04	2.1515e-04	3.9283e-04
20	0.87638	-0.23257	-0.14501	1.6192e-04	2.7116e-04	3.7557e-04
21	0.8763	0.23284	-0.14413	1.4944e-04	2.5891e-04	3.5893e-04
22	0.64717	0.64535	-0.14073	2.2875e-04	2.2541e-04	3.8377e-04
23	0.23316	0.87629	-0.14478	2.6532e-04	1.5581e-04	3.8313e-04
24	-0.22714	0.85173	0.26648	2.7174e-04	1.6610e-04	3.7065e-04
25	-0.62958	0.62849	0.25977	2.3423e-04	2.2330e-04	3.4783e-04
26	-0.85136	0.22606	0.26617	1.8033e-04	2.6733e-04	3.9340e-04
27	-0.85149	-0.22676	0.26551	1.7286e-04	2.8472e-04	3.7768e-04
28	-0.62973	-0.62845	0.25992	2.2549e-04	2.3548e-04	4.0746e-04
29	-0.22765	-0.85149	0.26539	2.5802e-04	1.7060e-04	3.7404e-04
30	0.22734	-0.85138	0.26628	2.7171e-04	1.7758e-04	3.9353e-04
31	0.62974	-0.62861	0.25893	2.1403e-04	2.0532e-04	3.7687e-04
32	0.85189	-0.22697	0.26472	1.6942e-04	2.5462e-04	3.7266e-04
33	0.85162	0.22643	0.26543	1.5483e-04	2.5733e-04	3.8860e-04
34	0.62966	0.629	0.25841	2.1878e-04	2.2349e-04	3.5443e-04
35	0.22712	0.85162	0.26629	2.6587e-04	1.8146e-04	4.1989e-04
36	-0.1931	0.7073	0.58177	3.3649e-04	2.9131e-04	3.6234e-04
37	-0.52934	0.52781	0.56934	2.8668e-04	3.0069e-04	3.4486e-04
38	-0.70703	0.19251	0.58158	2.7358e-04	3.0852e-04	3.2305e-04
39	-0.70698	-0.19272	0.58185	3.0540e-04	3.1560e-04	3.4025e-04
40	-0.52892	-0.52808	0.56916	2.9378e-04	3.1971e-04	3.5583e-04
41	-0.19246	-0.70681	0.5822	3.0696e-04	2.5917e-04	3.1757e-04
42	0.19272	-0.70674	0.58224	3.0023e-04	2.7700e-04	3.2914e-04
43	0.52883	-0.52864	0.56889	3.0111e-04	2.7768e-04	3.4776e-04
44	0.70743	-0.19236	0.58134	2.8493e-04	3.0501e-04	3.3460e-04
45	0.70752	0.19231	0.58118	2.8128e-04	3.0085e-04	3.4280e-04
46	0.52945	0.5285	0.56856	2.7375e-04	2.8939e-04	3.4136e-04
47	0.19273	0.70724	0.58166	2.8564e-04	2.7118e-04	3.1431e-04

Table B.5: Table of Ideal Geometrical Factors and Absolute Statistical Uncertainties for the Hydrogen Target

Detector	G_{LR}	G_{UD}	G_{Z}	σ_{LR}	σ_{UD}	σ_{Z}
0	-0.20568	0.75287	-0.51695	1.4376e-04	1.2775e-04	1.7326e-04
1	-0.56388	0.55893	-0.50176	1.3217e-04	1.3975e-04	1.7885e-04
2	-0.75539	0.20178	-0.51377	1.2312e-04	1.6153e-04	1.5515e-04
3	-0.75538	-0.20143	-0.51401	1.1676e-04	1.4107e-04	1.5904e-04
4	-0.564	-0.55878	-0.50216	1.4324e-04	1.5637e-04	1.6043e-04
5	-0.20594	-0.75291	-0.51689	1.4279e-04	1.2124e-04	1.5658e-04
6	0.20572	-0.75308	-0.51701	1.3819e-04	1.1244e-04	1.5118e-04
7	0.56384	-0.55887	-0.50231	1.3062e-04	1.3971e-04	1.6654e-04
8	0.75565	-0.2015	-0.51376	1.3361e-04	1.6896e-04	1.6563e-04
9	0.75547	0.20148	-0.51434	1.0348e-04	1.6199e-04	1.4680e-04
10	0.56399	0.55874	-0.50205	1.3073e-04	1.3299e-04	1.6989e-04
11	0.2058	0.75308	-0.51698	1.4420e-04	1.1177e-04	1.5123e-04
12	-0.23526	0.87727	-0.15589	1.3228e-04	7.4837e-05	1.6632e-04
13	-0.65148	0.64263	-0.15159	1.1331e-04	1.1747e-04	1.7244e-04
14	-0.87837	0.22822	-0.15453	8.2449e-05	1.3211e-04	1.6129e-04
15	-0.87853	-0.22819	-0.1545	7.5595e-05	1.4711e-04	1.7415e-04
16	-0.65149	-0.64259	-0.15165	1.1546e-04	1.1351e-04	1.7681e-04
17	-0.23537	-0.87718	-0.15637	1.1478e-04	6.9106e-05	1.6085e-04
18	0.23499	-0.87737	-0.15611	1.4031e-04	7.9104e-05	1.6812e-04
19	0.65159	-0.64267	-0.15152	1.1026e-04	1.1298e-04	1.7252e-04
20	0.87847	-0.22835	-0.15471	7.3614e-05	1.4035e-04	1.6712e-04
21	0.87852	0.22818	-0.15484	7.9059e-05	1.4605e-04	1.7472e-04
22	0.65172	0.64251	-0.1516	1.0367e-04	1.0852e-04	1.8783e-04
23	0.23541	0.87728	-0.15594	1.4641e-04	7.6414e-05	1.8142e-04
24	-0.22969	0.85227	0.2468	1.3169e-04	7.6428e-05	1.9149e-04
25	-0.63457	0.62601	0.23926	1.1770e-04	1.0986e-04	1.9081e-04
26	-0.85392	0.22258	0.24565	8.1626e-05	1.5431e-04	1.9169e-04
27	-0.85403	-0.22238	0.2453	7.3012e-05	1.4302e-04	1.8940e-04
28	-0.63465	-0.62589	0.2397	1.1888e-04	1.1574e-04	1.9804e-04
29	-0.22934	-0.85235	0.24682	1.4710e-04	7.9024e-05	1.8015e-04
30	0.22943	-0.85247	0.24663	1.4228e-04	7.8187e-05	1.8814e-04
31	0.63479	-0.62597	0.23927	1.2246e-04	1.1213e-04	1.9760e-04
32	0.85395	-0.22275	0.24548	7.9046e-05	1.5774e-04	1.8834e-04
33	0.85402	0.22267	0.24532	8.4659e-05	1.3564e-04	1.7536e-04
34	0.6348	0.62593	0.23932	1.1032e-04	1.0780e-04	1.9897e-04
35	0.22943	0.85245	0.2464	1.4015e-04	8.2798e-05	1.8094e-04
36	-0.19722	0.71887	0.55694	1.4934e-04	1.5265e-04	1.9746e-04
37	-0.53981	0.53494	0.54408	1.5292e-04	1.4323e-04	1.7740e-04
38	-0.72072	0.19296	0.55476	1.4389e-04	1.7129e-04	1.9201e-04
39	-0.72062	-0.1928	0.55509	1.2569e-04	1.6979e-04	1.8461e-04
40	-0.54009	-0.5351	0.54361	1.6396e-04	1.5447e-04	1.9899e-04
41	-0.19751	-0.7193	0.55657	1.5175e-04	1.3840e-04	1.8559e-04
42	0.19735	-0.7192	0.55681	1.6673e-04	1.3689e-04	1.7789e-04
43	0.53996	-0.53495	0.54441	1.4318e-04	1.4969e-04	2.0147e-04
44	0.72096	-0.19327	0.55456	1.3041e-04	1.4933e-04	1.8934e-04
45	0.72065	0.19292	0.55538	1.4375e-04	1.7449e-04	1.9949e-04
46	0.5401	0.53493	0.54388	1.5029e-04	1.5614e-04	2.1215e-04
47	0.19765	0.71882	0.55694	1.5823e-04	1.2863e-04	1.8933e-04

Table B.6: Table of δ_ϕ Angles and Uncertainties in radians.

Detector	δ_ϕ	σ_{δ_ϕ}
0	0.01735	0.003313
1	-0.005548	0.002477
2	-0.02734	0.006278
3	0.01874	0.005729
4	-0.003198	0.003487
5	-0.02321	0.003903
6	0.03346	0.004374
7	0.01246	0.002545
8	-0.01177	0.003931
9	0.03064	0.004608
10	-0.000883	0.00191
11	-0.02642	0.003797
12	0.01666	0.002787
13	-0.002647	0.002417
14	-0.02969	0.005557
15	0.01929	0.005326
16	-0.002863	0.003741
17	-0.01928	0.004821
18	0.02993	0.004601
19	0.0166	0.003154
20	-0.01674	0.003329
21	0.03609	0.004108
22	-0.00458	0.002405
23	-0.02715	0.003767
24	0.02237	0.00428
25	-0.0003962	0.001788
26	-0.02626	0.00444
27	0.02726	0.004367
28	-0.004062	0.002725
29	-0.02256	0.003867
30	0.03291	0.00385
31	0.01454	0.002108
32	-0.01561	0.00433
33	0.02924	0.00461
34	-0.007678	0.004789
35	-0.03061	0.004757
36	0.021	0.003861
37	-0.003253	0.004863
38	-0.03029	0.004079
39	0.021	0.004234
40	-0.0001232	0.003534
41	-0.02556	0.004581
42	0.02705	0.004007
43	0.01256	0.00346
44	-0.01666	0.00549
45	0.03251	0.007493
46	-0.00329	0.002208
47	-0.02672	0.004279

Table B.7: Table of Adjusted Geometrical Factors and Uncertainties for the Chlorine Target

Detector	G'_{LR}	G'_{UD}	$\sigma_{LR'}$	$\sigma_{UD'}$
0	-0.19411	0.65721	2.1856e-03	6.6240e-04
1	-0.49444	0.49942	1.2516e-03	1.2374e-03
2	-0.65554	0.20056	1.2695e-03	4.1201e-03
3	-0.65779	-0.19447	1.1263e-03	3.7744e-03
4	-0.49848	-0.49501	1.7360e-03	1.7483e-03
5	-0.19775	-0.65606	2.5692e-03	7.8721e-04
6	0.20476	-0.65391	2.8675e-03	9.1149e-04
7	0.50303	-0.49044	1.2605e-03	1.2932e-03
8	0.65858	-0.18981	7.6472e-04	2.5979e-03
9	0.65507	0.20231	9.4584e-04	3.0256e-03
10	0.49754	0.4965	9.6770e-04	9.6759e-04
11	0.19998	0.65556	2.4975e-03	7.7751e-04
12	-0.24036	0.84067	2.3505e-03	6.7813e-04
13	-0.62329	0.62599	1.5206e-03	1.5137e-03
14	-0.83761	0.25059	1.3968e-03	4.6586e-03
15	-0.84009	-0.24166	1.2920e-03	4.4786e-03
16	-0.62675	-0.62247	2.3337e-03	2.3489e-03
17	-0.24233	-0.84011	4.0552e-03	1.1731e-03
18	0.25162	-0.83734	3.8570e-03	1.1621e-03
19	0.63527	-0.61384	1.9422e-03	2.0085e-03
20	0.84088	-0.23962	8.0478e-04	2.8055e-03
21	0.8358	0.25629	1.0587e-03	3.4386e-03
22	0.62786	0.62155	1.5032e-03	1.5184e-03
23	0.24906	0.8381	3.1619e-03	9.4396e-04
24	-0.26179	0.90431	3.8758e-03	1.1245e-03
25	-0.6695	0.6687	1.2064e-03	1.2082e-03
26	-0.90299	0.2644	1.1775e-03	4.0139e-03
27	-0.9029	-0.26531	1.1627e-03	3.9481e-03
28	-0.6723	-0.66603	1.8207e-03	1.8391e-03
29	-0.26204	-0.90391	3.5010e-03	1.0184e-03
30	0.27088	-0.90145	3.4759e-03	1.0464e-03
31	0.67934	-0.65882	1.3984e-03	1.4405e-03
32	0.9059	-0.2549	1.1074e-03	3.9275e-03
33	0.90234	0.26737	1.2360e-03	4.1641e-03
34	0.67473	0.6635	3.1811e-03	3.2340e-03
35	0.26884	0.90196	4.2961e-03	1.2826e-03
36	-0.22702	0.77483	2.9977e-03	8.8521e-04
37	-0.57825	0.58161	2.8340e-03	2.8167e-03
38	-0.77266	0.23394	9.6334e-04	3.1579e-03
39	-0.77486	-0.22672	9.6781e-04	3.2865e-03
40	-0.58031	-0.57939	2.0537e-03	2.0577e-03
41	-0.23051	-0.77393	3.5504e-03	1.0642e-03
42	0.23197	-0.77343	3.1058e-03	9.3798e-04
43	0.58755	-0.57229	1.9861e-03	2.0395e-03
44	0.77597	-0.22349	1.2341e-03	4.2651e-03
45	0.77258	0.23568	1.7712e-03	5.7926e-03
46	0.58189	0.57785	1.2855e-03	1.2952e-03
47	0.23171	0.77331	3.3148e-03	9.9989e-04

Table B.8: Table of Adjusted Geometrical Factors and Uncertainties for the Chlorine Target

Detector	G'_{LR}	G'_{UD}	$\sigma_{LR'}$	$\sigma_{UD'}$
0	-0.24384	0.83482	2.7830e-03	8.2673e-04
1	-0.61934	0.63142	1.5850e-03	1.5553e-03
2	-0.82705	0.25038	1.5844e-03	5.2039e-03
3	-0.82863	-0.24321	1.4055e-03	4.7596e-03
4	-0.62435	-0.62657	2.2004e-03	2.1923e-03
5	-0.24839	-0.83337	3.2687e-03	9.8410e-04
6	0.25653	-0.83125	3.6506e-03	1.1355e-03
7	0.63076	-0.61998	1.5978e-03	1.6259e-03
8	0.83077	-0.23778	9.5416e-04	3.2838e-03
9	0.82611	0.2533	1.1836e-03	3.8234e-03
10	0.62312	0.62748	1.2246e-03	1.2208e-03
11	0.25133	0.83282	3.1805e-03	9.7094e-04
12	-0.20545	0.69841	1.9591e-03	5.9869e-04
13	-0.52442	0.52733	1.2942e-03	1.2893e-03
14	-0.6959	0.21367	1.1999e-03	3.8759e-03
15	-0.69802	-0.2066	1.1152e-03	3.7264e-03
16	-0.52783	-0.52416	1.9740e-03	1.9876e-03
17	-0.20659	-0.69788	3.3732e-03	1.0127e-03
18	0.21438	-0.6957	3.2109e-03	1.0032e-03
19	0.53455	-0.51699	1.6461e-03	1.7017e-03
20	0.69858	-0.20471	7.0570e-04	2.3405e-03
21	0.69449	0.21817	9.1320e-04	2.8670e-03
22	0.52884	0.52288	1.2771e-03	1.2922e-03
23	0.21233	0.69652	2.6355e-03	8.1847e-04
24	-0.16401	0.52761	2.2780e-03	7.4323e-04
25	-0.40501	0.40532	7.8899e-04	7.7914e-04
26	-0.52711	0.16604	7.8449e-04	2.3600e-03
27	-0.52643	-0.16691	7.6520e-04	2.3174e-03
28	-0.40667	-0.40301	1.1347e-03	1.1413e-03
29	-0.16459	-0.52738	2.0594e-03	6.8633e-04
30	0.16982	-0.52619	2.0444e-03	7.0056e-04
31	0.41029	-0.39917	8.8021e-04	9.0658e-04
32	0.52896	-0.16029	7.4733e-04	2.3104e-03
33	0.52667	0.16768	8.1673e-04	2.4479e-03
34	0.40767	0.4019	1.9434e-03	1.9765e-03
35	0.16776	0.52566	2.5149e-03	8.3147e-04
36	-0.12962	0.39957	1.5929e-03	6.1700e-04
37	-0.31071	0.31288	1.5719e-03	1.5615e-03
38	-0.39901	0.13362	6.4857e-04	1.6733e-03
39	-0.40075	-0.12871	6.4534e-04	1.7413e-03
40	-0.31293	-0.31139	1.1576e-03	1.1671e-03
41	-0.13077	-0.39933	1.8678e-03	7.0154e-04
42	0.13088	-0.39896	1.6376e-03	6.3268e-04
43	0.31461	-0.30748	1.1286e-03	1.1574e-03
44	0.40055	-0.12725	7.9120e-04	2.2339e-03
45	0.39846	0.13486	1.0791e-03	3.0091e-03
46	0.31195	0.3105	7.7929e-04	7.8953e-04
47	0.13137	0.39871	1.7471e-03	6.5550e-04

Table B.9: Table of Adjusted Geometrical Factors and Uncertainties for the Aluminum Target

Detector	G'_{LR}	G'_{UD}	$\sigma_{LR'}$	$\sigma_{UD'}$
0	-0.21729	0.75005	2.5002e-03	7.6313e-04
1	-0.55772	0.56345	1.4238e-03	1.4057e-03
2	-0.74773	0.22401	1.4301e-03	4.7049e-03
3	-0.74971	-0.21734	1.2674e-03	4.3041e-03
4	-0.56282	-0.55833	1.9662e-03	1.9779e-03
5	-0.22142	-0.7484	2.9352e-03	8.9523e-04
6	0.22918	-0.74668	3.2778e-03	1.0312e-03
7	0.56841	-0.55358	1.4293e-03	1.4741e-03
8	0.75129	-0.21272	8.8036e-04	2.9649e-03
9	0.7472	0.22658	1.0698e-03	3.4553e-03
10	0.56205	0.5602	1.1072e-03	1.1052e-03
11	0.22301	0.74852	2.8557e-03	8.7801e-04
12	-0.24773	0.87203	2.4443e-03	7.0502e-04
13	-0.64523	0.64689	1.5792e-03	1.5780e-03
14	-0.8687	0.2585	1.4449e-03	4.8359e-03
15	-0.87174	-0.24926	1.3381e-03	4.6502e-03
16	-0.64823	-0.64412	2.4211e-03	2.4353e-03
17	-0.24965	-0.87157	4.2105e-03	1.2161e-03
18	0.25902	-0.869	4.0059e-03	1.2025e-03
19	0.65703	-0.63516	2.0148e-03	2.0834e-03
20	0.87237	-0.24721	8.3864e-04	2.9164e-03
21	0.86733	0.2643	1.0961e-03	3.5726e-03
22	0.65012	0.64238	1.5620e-03	1.5799e-03
23	0.25686	0.86964	3.2868e-03	9.8013e-04
24	-0.24614	0.84644	3.6332e-03	1.0666e-03
25	-0.62933	0.62874	1.1485e-03	1.1473e-03
26	-0.84513	0.24834	1.1174e-03	3.7622e-03
27	-0.84499	-0.24988	1.1050e-03	3.7014e-03
28	-0.63228	-0.62588	1.7205e-03	1.7391e-03
29	-0.2468	-0.84613	3.2824e-03	9.6960e-04
30	0.25523	-0.84344	3.2582e-03	9.9844e-04
31	0.63881	-0.61938	1.3231e-03	1.3622e-03
32	0.84825	-0.24024	1.0540e-03	3.6820e-03
33	0.84464	0.25123	1.1685e-03	3.9022e-03
34	0.63447	0.62415	2.9969e-03	3.0466e-03
35	0.25308	0.84427	4.0248e-03	1.2174e-03
36	-0.20791	0.70308	2.7354e-03	8.5397e-04
37	-0.52762	0.52953	2.5910e-03	2.5834e-03
38	-0.70088	0.21383	9.1421e-04	2.8757e-03
39	-0.70277	-0.20753	9.3016e-04	2.9920e-03
40	-0.52899	-0.52801	1.8891e-03	1.8967e-03
41	-0.21046	-0.70166	3.2286e-03	9.9826e-04
42	0.21176	-0.70127	2.8263e-03	8.9270e-04
43	0.53543	-0.52195	1.8310e-03	1.8734e-03
44	0.70412	-0.20412	1.1563e-03	3.8778e-03
45	0.70089	0.21521	1.6370e-03	5.2606e-03
46	0.53118	0.52676	1.1949e-03	1.2081e-03
47	0.21156	0.70183	3.0169e-03	9.4510e-04

Table B.10: Table of Adjusted Geometrical Factors and Uncertainties for the Hydrogen Target

Detector	G'_{LR}	G'_{UD}	$\sigma_{LR'}$	$\sigma_{UD'}$
0	-0.21871	0.74919	2.4861e-03	7.3571e-04
1	-0.56077	0.56205	1.3984e-03	1.3960e-03
2	-0.7496	0.22235	1.4014e-03	4.7091e-03
3	-0.75148	-0.21555	1.2404e-03	4.3074e-03
4	-0.56578	-0.55697	1.9474e-03	1.9791e-03
5	-0.22336	-0.74793	2.9228e-03	8.8021e-04
6	0.2308	-0.74578	3.2652e-03	1.0159e-03
7	0.57077	-0.5518	1.4101e-03	1.4591e-03
8	0.75322	-0.21038	8.3764e-04	2.9654e-03
9	0.74894	0.22453	1.0397e-03	3.4546e-03
10	0.56449	0.55824	1.0744e-03	1.0866e-03
11	0.22562	0.74738	2.8416e-03	8.6402e-04
12	-0.24984	0.87323	2.4372e-03	7.0029e-04
13	-0.64978	0.64435	1.5613e-03	1.5747e-03
14	-0.87121	0.25419	1.4151e-03	4.8436e-03
15	-0.87397	-0.2451	1.3076e-03	4.6570e-03
16	-0.65333	-0.64073	2.3999e-03	2.4469e-03
17	-0.25223	-0.87248	4.2082e-03	1.2181e-03
18	0.26114	-0.86995	4.0047e-03	1.2040e-03
19	0.66217	-0.63177	1.9957e-03	2.0916e-03
20	0.87453	-0.24302	8.1226e-04	2.9144e-03
21	0.86972	0.25973	1.0700e-03	3.5760e-03
22	0.65465	0.63952	1.5418e-03	1.5784e-03
23	0.25914	0.87057	3.2828e-03	9.7920e-04
24	-0.2487	0.84692	3.6275e-03	1.0673e-03
25	-0.63432	0.62627	1.1261e-03	1.1396e-03
26	-0.84778	0.24492	1.0906e-03	3.7677e-03
27	-0.84765	-0.24557	1.0750e-03	3.7048e-03
28	-0.63719	-0.6233	1.7027e-03	1.7403e-03
29	-0.24851	-0.84696	3.2787e-03	9.6430e-04
30	0.25736	-0.84446	3.2539e-03	9.9378e-04
31	0.64383	-0.61668	1.3057e-03	1.3618e-03
32	0.85037	-0.23605	1.0252e-03	3.6858e-03
33	0.84715	0.24755	1.1443e-03	3.9076e-03
34	0.63959	0.62104	2.9761e-03	3.0648e-03
35	0.25541	0.84503	4.0220e-03	1.2178e-03
36	-0.21227	0.71457	2.7630e-03	8.3368e-04
37	-0.53806	0.53669	2.6144e-03	2.6205e-03
38	-0.71455	0.2147	8.8759e-04	2.9199e-03
39	-0.71641	-0.2079	8.8909e-04	3.0378e-03
40	-0.54016	-0.53503	1.8980e-03	1.9152e-03
41	-0.21583	-0.71401	3.2741e-03	9.9827e-04
42	0.21673	-0.7136	2.8646e-03	8.7927e-04
43	0.54663	-0.52812	1.8330e-03	1.8974e-03
44	0.71764	-0.20526	1.1345e-03	3.9429e-03
45	0.71399	0.21624	1.6267e-03	5.3530e-03
46	0.54186	0.53315	1.1868e-03	1.2066e-03
47	0.21678	0.71328	3.0565e-03	9.3658e-04

Appendix C

Data Acquisition System Code

The data acquisition system was written in LabWindows/CVI using the C language. The DAQ contains multiple separate threads that communication with each other via Windows "events". The CAMAC and GaGe systems operate in separate threads during a data acquisition run. There is a slow DAQ system in a separate thread that monitors various apparatus systems such as temperature and voltage as well as controls the high voltage supply.

There are two primary windows in the DAQ system. The main window is the data taking window where histograms and run stats messages are display and runs can be started and stopped. The second window has the monitoring DAQ.

C.1 Data Acquisition Code

The monitoring DAQ operates at a sample frequency of 1 Hz, and all sampling is inhibited while the CAMAC system is being written to or read from so as to not interfere with CAMAC communication.

The High Voltage (Fig. C.1) tab controls the ramping up of the high voltage system as well as displaying readout of the voltage and leakage current. The leakage current limit is specified by the user and if the current rises above this limit, the high voltage supply trips off and an email is sent to a mailing list as an alert.

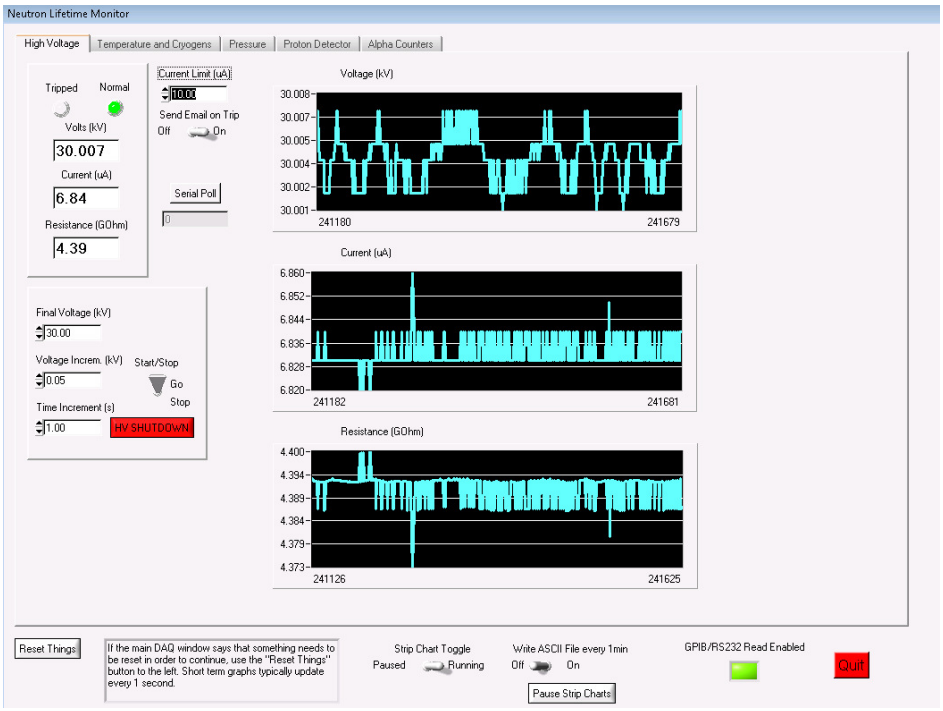

Figure C.1: Monitoring DAQ: High Voltage tab.

The high voltage system can be ramped up separately from the 1 Hz polling of the monitoring systems. The default ramp rate is also 1 Hz, with user specified voltage increments. The system can also be gracefully turned off without sending an alert email.

A separate tab (Fig. C.2) displays the three diode thermometer readings from the inside of the bore volume. The helium diode is mounted on the 4K vessel inside the bore, while the nitrogen diode is mounted on one of the heat shields on the downstream end of the apparatus. The trap diode is mounted on the downstream end of the trap. All of these temperatures are read via a SIM-9000 mainframe.

Liquid levels are read via a Keithley 2900 DVM. Nominally, the level readings are a linear voltage scale with 0 V corresponding to full and 0.5 V corresponding to empty. After a rough calibration to get more accuracy from these readings, it was found that each has an offset of about 10 mV and that the scale is 0.53 V rather than 0.5 V. The correct conversion functions to level percentages are:

$$LN2(\%) = (1 - (V - 0.01)/0.53) * 100.0 \tag{C.1}$$

Figure C.2: Monitoring DAQ: Temperature and Cryogens.

$$LHe(\%) = (1 - (V - 0.0165)/0.53) * 100.0. \tag{C.2}$$

These level readings allow for the capability to trigger a cryogen level alert email.

This tab (Fig. C.3) shows the Pfeiffer Dual-gauge readings of the pressure measured for the OVC and the bore. There is possibility to send a pressure trip email. These readings are read via a USB to RS232 converter.

This tab (Fig. C.4) contains recent history of the proton detector as well as the settings to specify the proton "speed limit", a feature that attempts to protect a detector by shutting down the high voltage if the proton rate exceeds the specified level. The top left plot is updated frequently from the GaGe card data and gives an indication of the 0.5 s average proton trigger rate, with no threshold set in the code on energy windows. The middle left plot shows the number of triggers from the previous 500 runs, and the bottom left plot shows whether the ADC has been behaving or has been giving permanent busy signals. The plots to the right are energy and time window bin counts for the last 500 runs. The energy and time windows are specified in the Run Parameters dialog box that can be reached from the main window.

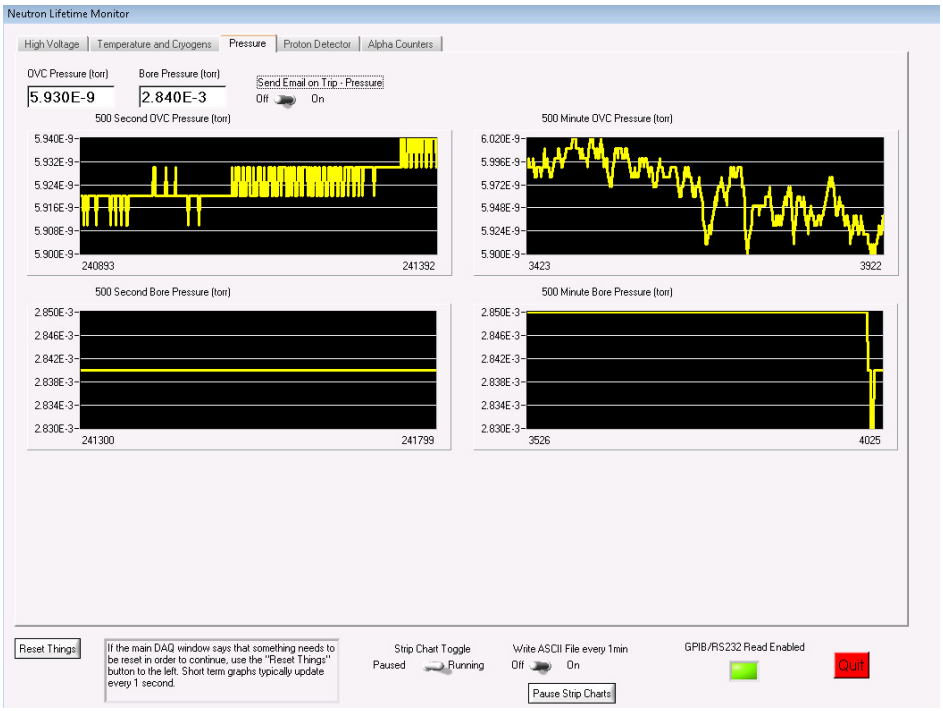

Figure C.3: Monitoring DAQ: Pressure.

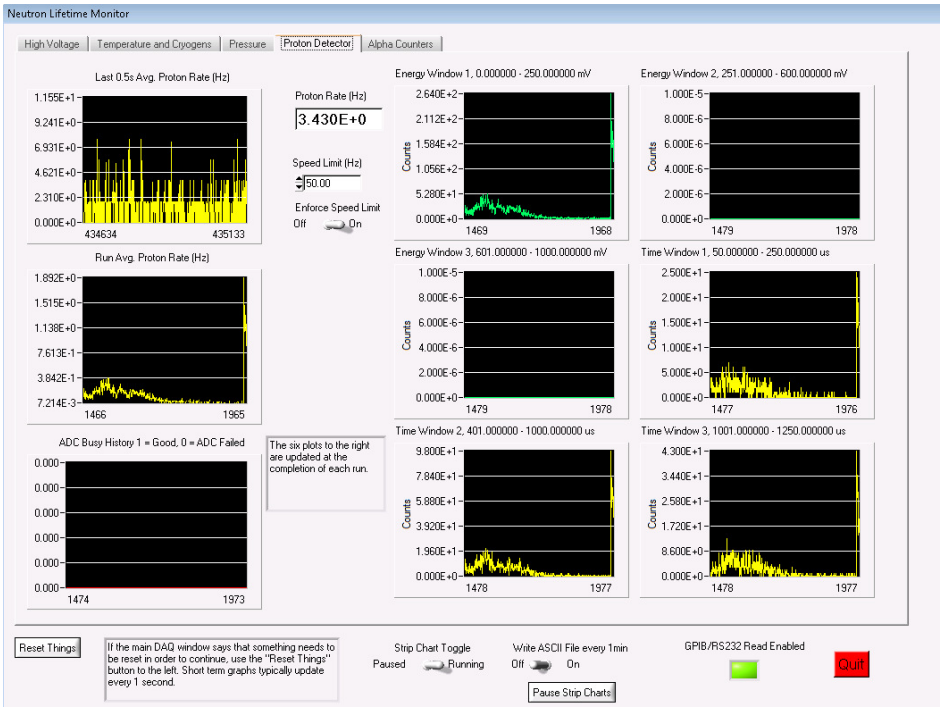

Figure C.4: Monitoring DAQ: Proton Detector

This tab (Fig. C.5) shows the counter result for the last 500 runs from a single hex counter in the CAMAC crate. At present, these counters are the proton gate signal, the

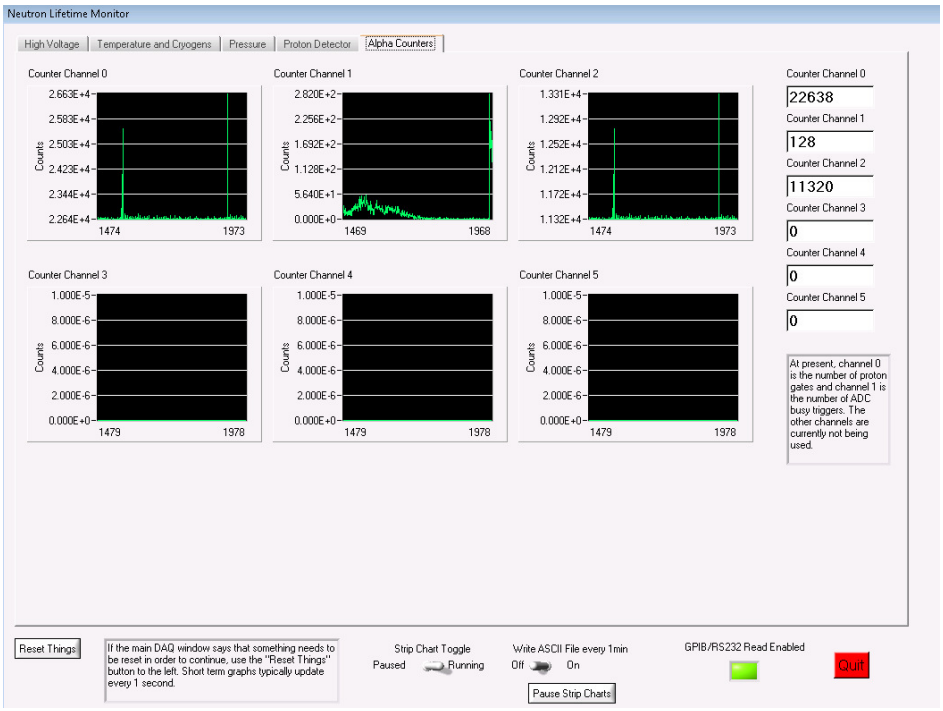

Figure C.5: Monitoring DAQ: Alpha Counters

CAMAC ADC Busy signal, and a dummy timer. In the future, this tab could contain as many counters as are desired.

The main window (Fig. C.6) contains two tabs, one of which shows the cumulative peak height and timing histograms and the other shows the histograms from the last run only. There is a message box below the histograms showing the current status of the DAQ along with a progress bar showing the progress of the current run. The Run Comments text is appended to a comments file named runcomments.dat at the end of each run.

When a run is started, the DAQ first resets several Windows events that indicate whether each system is ready to acquire data to their default state. Any previous asynchronous timer for the data acquisition thread is terminated. The amount of free space on the current local data hard drive is checked to make sure there is space for the next run, otherwise the data will be written to the next hard drive. The DAQ is now ready to trigger the CAMAC and GaGe threads for setup and acquisition, and the acquisition thread waits for three Windows event triggers.

The CAMAC acquisition thread begins by inhibiting the CAMAC line. The memory modules are then cleared, and then setup commands are sent to the CAMAC modules. The

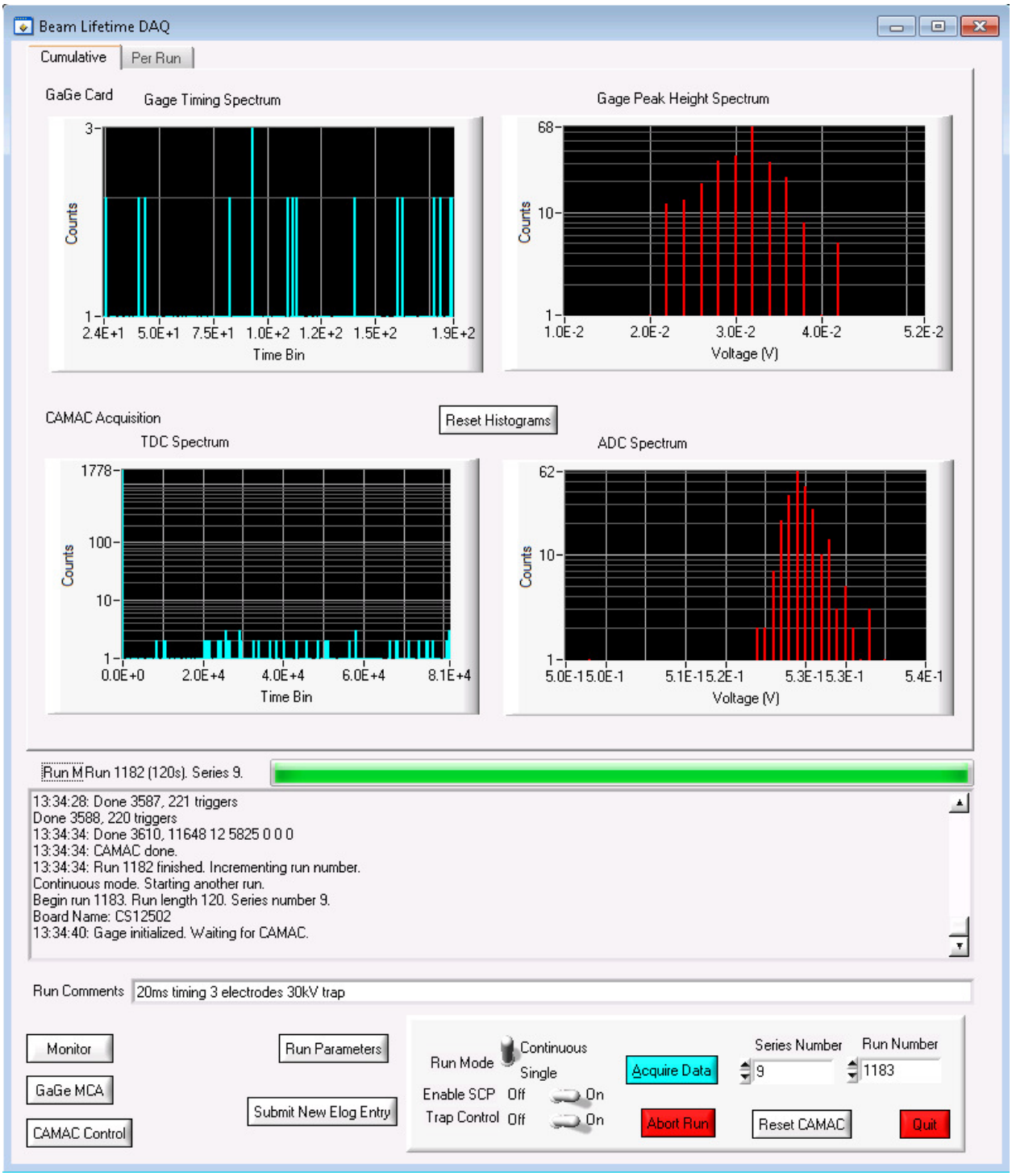

Figure C.6: Main DAQ Window.

Kinetic Systems 3655 module that controls the trap timing signals is cleared and finally the data enable logic signals are reset in order to set the gate flipflops for the trap signals, α counting gate, and proton gate. A Windows event is then triggered to indicate that the

CAMAC setup is complete and the thread waits for a similar signal from the GaGe card, or times out after 30 s if the signal never arrives.

The GaGe digitizer setup occurs simultaneous to the CAMAC setup and in a separate thread. Setup parameters are read from an .ini file that contains the sampling rate, sample size, and other parameters of the digitizer card. When this has completed, the GaGe thread sets another Windows event that indicates that it is ready for acquisition and similarly waits for the CAMAC thread to be ready, and it times out after 50 s.

Once both threads signal that they are ready, the CAMAC 3655 timer starts generating trap timing signals and a third Windows event is triggered to indicate that data acquisition has begun. The GaGe card can operate in one of two modes; one in which the GaGe card data is written to a file every trap opening and another in which the GaGe card stores waveforms in internal memory which is read out at the completion of the run.

The DAQ then begins an asynchronous timer once the GaGe and CAMAC setup events and the acquisition event have all triggered. This asynchronous timer determines the duration of a single run and is typically 120 s long. When the timer ticks to indicate that the run is complete, the GaGe card is triggered to abort its current operation, write data to a file, and begin an upload of the data via SSH to the remote analysis server. The CAMAC system is inhibited and the timers are disabled. The CAMAC system then reads the timing and peak height spectra from the memory modules as well as the α counter data. The system then takes another run if it is in continuous run mode.

The DAQ has a where the GaGe card is used in singles mode to function as a multi-channel analyzer for quick collection of calibration spectra. The MCA program acquires data from the GaGe card for a specified amount of time, with a histogram update every few hundred counts. The MCA code acquires data at 10 MHz for 51.2 μs per trigger, with the trigger specified in an .ini file separate from the main DAQ .ini file. The program steps through each waveform and record the maximum value and stores it in a histogram that is updated much less frequently than the trigger rate due to the overhead of updating a plot in Labwindows/CVI. The data can then be written to a text file for analysis later.

The run parameters can be changed via a separate window, with all changes saved in the DAQ .ini file. The first tab controls the ADC and TDC set up parameters, which ordinarily don't need to be changed.

The Timing Signals tab controls the trapping time in microseconds and the timer delays for the trap signals. A single timing sequence is as follows:

1. T=0uS, ramp is grounded, door and mirror at 800V.
2. T=Trapping Time (10000uS) + T1, gate the proton detector on, ramp is grounded, door and mirror at 800V.
3. T=Trapping Time + T2, open door, turn on ramp, mirror maintained at 800V.
4. T=Trapping Time + T3, lower mirror, ramp and door state maintained.
5. T=Trapping Time + T4, raise mirror and door, ground the ramp.
6. T=Trapping Time + T5, gate off the proton detector.
7. T=Trapping Time + T6, this is the dummy timer currently recorded in the counter.

Timers T7 and T8 are unused, so a trapping cycle has a length of Trapping Time + T6.

The Gage tab controls the inputs to the GaGe card.

The Trap tab contains information about the trap configuration as well as the length of the run in seconds. The switches to the right show the configuration of the trap electrodes with the ramp electrodes shown at 0 V and the door/mirror electrodes shown at 800 V. This trap configuration is printed in the ini file as a string of ones and zeros, with the configuration shown in the figure being 1110000000001111. The number of electrodes is forced to be the same as the number of ramp electrodes shown in the switches. The Ramp Max and Door/Mirror Max should be changed depending on the current settings of the respective voltage supplies for the trap.

The Detectors tab contains information about the proton and alpha detectors. The Windows tab controls the window binning that is shown in the right six plots of the proton monitoring tab in figure C.4.

C.2 Data Storage Format

The data is stored in several binary files for ease of reading and to minimize storage requirements. The GaGe card digitized waveforms are recorded in a single file (run_XXXXX_1.dat) sequentially with 2048 time bins per waveform as well as a timestamp in microseconds for the arrival time of the event since the start of the run. Each time bin is a signed short integer, requiring 2 bytes per time bin. Two channels are recorded for each event, the first is the digitized detector signal from the amplifier and the second is a digitized detector signal from the preamplifier. The binary format for each event is:

```
double (8 bytes) - timestamp in microseconds
short (2 bytes) - time bin 0 for channel 1
   ...
short (2 bytes) - time bin 2047 for channel 1
double (8 bytes) - timestamp in microseconds
short (2 bytes) - time bin 0 for channel 2
   ...
short (2 bytes) - time bin 2047 for channel 2
```

There is an indeterminate number of such traces per run, so the file is read to completion in a loop after determining the file size. Waveforms are appened to the file (run_XXXXX_1.dat) only if the amplified signal rose above a user specified trigger threshold and therefore represents an abridged version of the data stream. Every trap opening is appened to the fifth file, (run_XXXXX_5.dat).

Data from the list-mode CAMAC module is stored in a single file (run_XXXXX_2.dat), consisting of (usually) 2 signed short integers (2 bytes each) per recorded pulse. One of these is the ADC pulse height and the other is the TDC arrival time. At present, these numbers can occur in any order and the ADC will digitize two numbers if multiple peaks satisfying the LLD arrive in a trapping cycle. This file also has an indeterminate size and is read similar to the GaGe card file.

Data from the histogramming CAMAC module is stored in a single file, (run_XXXXX_3.dat), and consists of 16384 signed short integers (2 bytes each). The first 8192 entries contain the

ADC pulse height spectrum and the second 8192 entries contain the TDC timing spectrum. The total size of this file will always be 32768 bytes.

Data from the slow monitoring system is stored in a small file (`run_XXXXX_4.dat`), which currently contains 9 doubles occupying 8 bytes each followed by 6 integers. These are the high voltage supply leakage current in microamperes, the high voltage supply voltage in kilovolts, the three thermometers in Kelvin, two Pfieffer pressure gauge channels, and the Keithley DVM recording the cryogen levels. The six integers are read at the end of each run and correspond to the CAMAC hex-counter. At present, these are counts of the proton gate signal, the ADC busy signal, and a dummy timer signal. In the future, these will be counters from the neutron monitor. The format for each run is:

```
double (8 bytes) - High voltage leakage current (uA)
double (8 bytes) - High voltage level (kV)
double (8 bytes) - Temperature channel 1 (4K surface)
double (8 bytes) - Temperature channel 2 (77K surface)
double (8 bytes) - Temperature channel 3 (downstream end of trap)
double (8 bytes) - Pfieffer pressure channel 1
double (8 bytes) - Pfieffer pressure channel 2
double (8 bytes) - Keithley cryogen level channel 1
double (8 bytes) - Keithley cryogen level channel 2
int (4 bytes) - CAMAC Counter channels 0-5
```

C.3 Reading Data for Analysis

The ROOT library [Brun and Rademakers, 1996] is used for reading and analyzing data for the lifetime experiment. Data is read into a series of trees and branches for ease of plotting and analysis. A wrapper class called TauData reads the data and stores it in memory for plotting or analysis. There are four trees, one for each file, because it is undesirable for a tree to have a different number of entries in each branch. An entry corresponds to the pulse/waveform number. For instance, if there are 200 GaGe traces in a run, then the GaGe file will have 400 sets of 4104 byte blocks and likewise the list-mode file will have 200-ish

sets of 4 byte blocks. However, the histogram file and the monitoring file will only contain 32768 and 96 bytes, respectively. This poses an issue if all four files are read into the same tree and causes undefined behavior for the non-existent second entry of the monitoring and histogramming data, or if the list and GaGe files contain different numbers of entries. For this reason, the ROOT library reads each file into separate trees.

A run is read on the ROOT command line as follows:

```
root -l
.L TauData.cc++g
TauData t(x, y)
```

This loads ROOT, loads and compiles the library file into a shared object file, and declares an instance of *TauData* named t using the run number x from series number y. Four files described above will be read into memory into trees, in the ROOT parlance.

The first tree containing data is called `g_tree`, and it contains all data in the "`_1`" file as well as this data processed into volts rather than ADC bits. There are five branches in this tree. The first, known as "`g`", contains the raw digitized amplifier waveform data in ADC bits. The second, known as "`g_v`", contains the GaGe waveform converted to volts by the function

$$g_v = \frac{-16.0 - g}{-16384.0}. \tag{C.3}$$

The third, known as "`g_b`", contains the ADC busy signal converted to volts. The fourth, "`ts`", contains a single number per event corresponding to the time stamp for each event. The fifth, called "t", is the integer sequence 0 to 2047 for indexing the time bins. An event recorded in a tree is known as an "Entry", so if the ADC LLD triggered 150 times in a run, there will be 150 Entries in the tree, `g_tree`, numbered from 0 to 149.

This allows the use of the following for plotting the GaGe data:

```
t.g_tree->Draw("what branch:against what", "some boolean", "options")
t.g_tree->Draw("g:t","Entry$ == 5")
t.g_tree->Draw("g_v:t","")
t.g_tree->Draw("g:t+Entry$*2048","")
t.g_tree->Draw("ts:Entry$","")
```

The first line is an example of the structure of a draw line in ROOT's CINT (C-interpreter). The second and third options in quotation marks can be empty, but should always be present in the function call. The second line plots the GaGe raw digitized amplifier data for the sixth waveform in the data file as a function of time bins. The third plots the GaGe signal converted to volts as a function of time bin for all waveforms in the file, which piles each waveform on top of each other. The fourth plots the raw data for all waveforms as a function of time bin but shifts each entry by 2048 from the previous one, which results in each waveform plotted sequentially. The last one plots the timestamp since the initialization of the Gage card for the trigger of waveform.

The second tree contains the list-mode data and is called `c_tree`. There is a single branch in this tree, called "`list`", which contains 2 shorts per entry. Commands to plot the list-mode data include:

```
t.c_tree->Draw("list:Entry$","")
t.c_tree->Draw("list:Entry$"," list < 8192")
t.c_tree->Draw("list:Entry$","list >=8192")
t.c_tree->Draw("list[0]:list[1]-8192","")
```

The first plots the TDC and ADC entries all together as a function of the entry number. The second plots only the ADC values, since these are all stored as numbers between 0 and 8192. The third plots the TDC values only, since these are always offset by 8192 such that the ADC and TDC numbers do not overlap. The last plots the ADC pulse height as a function of the TDC arrival time minus the TDC bin shift of 8192.

The third tree contains the histograms from the ADC and TDC and is called `h_tree`. There are three branches in this tree, called "`adch`", "`tdch`", and "`hb`". These are the adc histogram, tdc histogram, and an index of the histogram bin number respectively. This tree contains only one entry for each branch, and each branch is composed of 8192 elements. Plot commands include:

```
t.h_tree->Draw("adch:hb","")
t.h_tree->Draw("tdch:hb","")
t.h_tree->Draw("tdch:hb","hb > 50 && hb < 500")
```

The first and second plot the ADC and TDC histograms, respectively, as a function of bin number. The third plots the TDC histogram as a function of bin number for histogram bins between 50 and 500.

The fourth tree contains the monitoring data and is called `m_tree`. There are two branches in this tree, called "`m`" and "`alpha`", containing 9 doubles and 6 integers, respectively. It is not especially useful to plot this branch, but it can be done.

```
t.m_tree->Draw("m","")
t.m_tree->Draw("alpha[1]","")
```

The first plots all elements of the branch, "`m`", and the second plots only the first element of the branch,"`alpha`".

This structure also allows for straightforward access to the entries within each tree for analysis at code level by using "`C++`" arrays.

A copy of the code required to read data from Beam Lifetime 2 is located at `/home/lifetime/analysis`, as well as a simple program (detsigave) that reads a set of runs and saves pulse height spectra to a ROOT file. Required files are:

```
TauData.h
TauData.cc
taun_vars.h
Makefile
detsigave.cc
```

Running `make detsigave` compiles the detsigave code into a program for running. In order to run it, use:

```
./detsigave 4038 4040 0.005 1 savefile
```

which specifies the first run, last run, histogram bin size in mV, the run stepsize, and the filename for saving the resulting histograms. In order to plot the results, use:

```
root -l
TFile f("savefile")
```

```
GaGe_spectrum.Draw()
camac_spectrum.Draw()
```

C.4 DAQ Parameters

The DAQ program includes a dialog box for editing the parameters of various aspects of the data acquisition electronics as well as recording the run configuration in a human readable format. These parameters are saved locally in the LifetimeDAQ folder in an .ini file. The file is copied at the end of each run to a new file in the data folder named `Lifetime_s_XXXX_r_YYYYYY.ini` which is then copied to hodor at the end of each run.

This file originated as the GaGe digitizer parameters file and then had everything else added to it. The GaGe parameters are saved in sections titled Acquisition, Application, Channel1, Channel2, and Trigger1.

- Acquisition
- Depth = 1792 - The amount in time bins of post trigger data to record.
- Mode = "Dual" - The number of channels.
- SampleRate = 10000000 - The sample rate in hertz.
- SegmentCount = 1 - The number of waveforms to record before in internal memory before dumping to the DAQ program.
- SegmentSize = 2048 - The length of each waveform in time bins, of 204.8 microseconds.
- TimeStampClock = "Fixed" - A timestamping parameter for the GaGe card.
- TimeStampMode = "Free" - A timestamping parameter for the GaGe card.
- TriggerHoldoff = 256 - The amount in time bins of pre-trigger data to save, which gives us a measure of the background.
- TriggerTimeout = 1000000000 - The time in units of 100ns to wait for a trigger before forcing a trigger.

- Application
- SaveFileFormat = "`TYPE_DEC`" - Flag for the DAQ loop to convert data.
- SaveFileName = "`run_`" - Currently ignored since it's a relic from the original file.
- SegmentCount = 1 - Number of waveforms to record.
- SegmentStart = 1
- StartPosition = -256 - Amount of pre-trigger data to save.
- TransferLength = 2048 - Full length in time bins of a waveform.
- Channel1 and Channel2
- Coupling = "DC" - We use DC coupling on each channel.
- DcOffset = 1750 - Amount in mV to offset the channel. Channel 1 is offset by 1750mV to give a range of -250mV to 3750mV. Channel 2 has an offset of zero.
- Impedance = 50 - Input impedance of the channel. I believe the device only supports 50 Ohms.
- Range = 4000 - Full range in mV of each channel.

Trigger on rising edge at a level of 60% of the full range on the external source line (which is the proton gate signal):

- Trigger1
- Condition = "Rising"
- Level = 60
- Source = "External"

The CAMAC sections are titled CAMAC and Timers, the former controlling the parameters of the ADC and TDC and the latter controlling the trap timer.

- Camac
- Gain3512 = 8000 - ADC's internal gain, corresponding to 8192 bins per 8V.
- LLD3512 = 0.3 - Level of the ADC's Lower Level Discriminator, which is set manually with a potentiometer and should be updated in the DAQ manually.
- Offset3512 = 0 - Amount to add to the ADC peak height in order to separate it from the TDC results, currently this is zero.
- Offset4204 = 8192 - Amount to add to the TDC digitized arrival time to separate it from the ADC results, currently 8192.
- Resolution4204 = 40 - Resolution flag for the TDC.
- Timers
- Delay3655 = 10000 - Length of a trapping cycle in microseconds, after which T1 will tick.
- T1 = 0 - Time after Delay3655 in which T1 ticks, currently trapping is exactly 10000 microseconds. Proton detector gated on.
- T2 = 22 - Door grounded and ramp applied.
- T3 = 98 - Mirror grounded, ramp still applied and door still grounded.
- T4 = 128 - Ground the trapping region, raise door and mirror.
- T5 = 160 - Proton detector gated off.
- T6 = 600 - Dummy timer that is recorded in one of the hex counter channels.
- T7 = 700 - Recorded in ini file, but this channel isn't used.
- T8 = 999 - Recorded in ini file, but this channel isn't used.

There are four sections defining parameters for the apparatus and DAQ, named Summing Windows, TauN, Alpha Detector, and Proton Detector. Most of these settings are either flags for the DAQ plotting window or tags for detector IDs, voltages, etc. in a human readable format for deciphering what the run configuration was for a given series of runs.

12 numbers that correspond to DAQ plotting bounds for recording the run averaged number of hits in 3 different energy windows and 3 different timing windows. These plots are shown in one of the tabs of the monitoring DAQ window.

- TauN
- Door Mirror max voltage = 800 - This is set manually with a power supply and should be updated in the DAQ manually as well.
- Electrode configuration = "1110000000001111" - This is set with switches in the DAQ and corresponds to the trap electrode pattern, 1 being 800V and 0 being grounded during a trap cycle.
- Ramp max voltage = 15 - Set in the same way as the door and mirror voltage.
- RunLength = 120 - This is the length of a run in seconds, which controls an asynchronous timer that stops the run and reads data.
- Trap length = 9 - The length of the trapping region.

Currently gibberish since we don't have these in place.

- Alpha Detector
- Alpha detectors = "PIPs"
- Alpha structure = 1
- Foil = "hello"
- Proton Detector
- Detector area = 300

- Detector depletion depth = 300
- Detector gold thickness = 20
- Detector ID = “38-173D”
- Detector position = 520
- Detector type = “surface barrier”

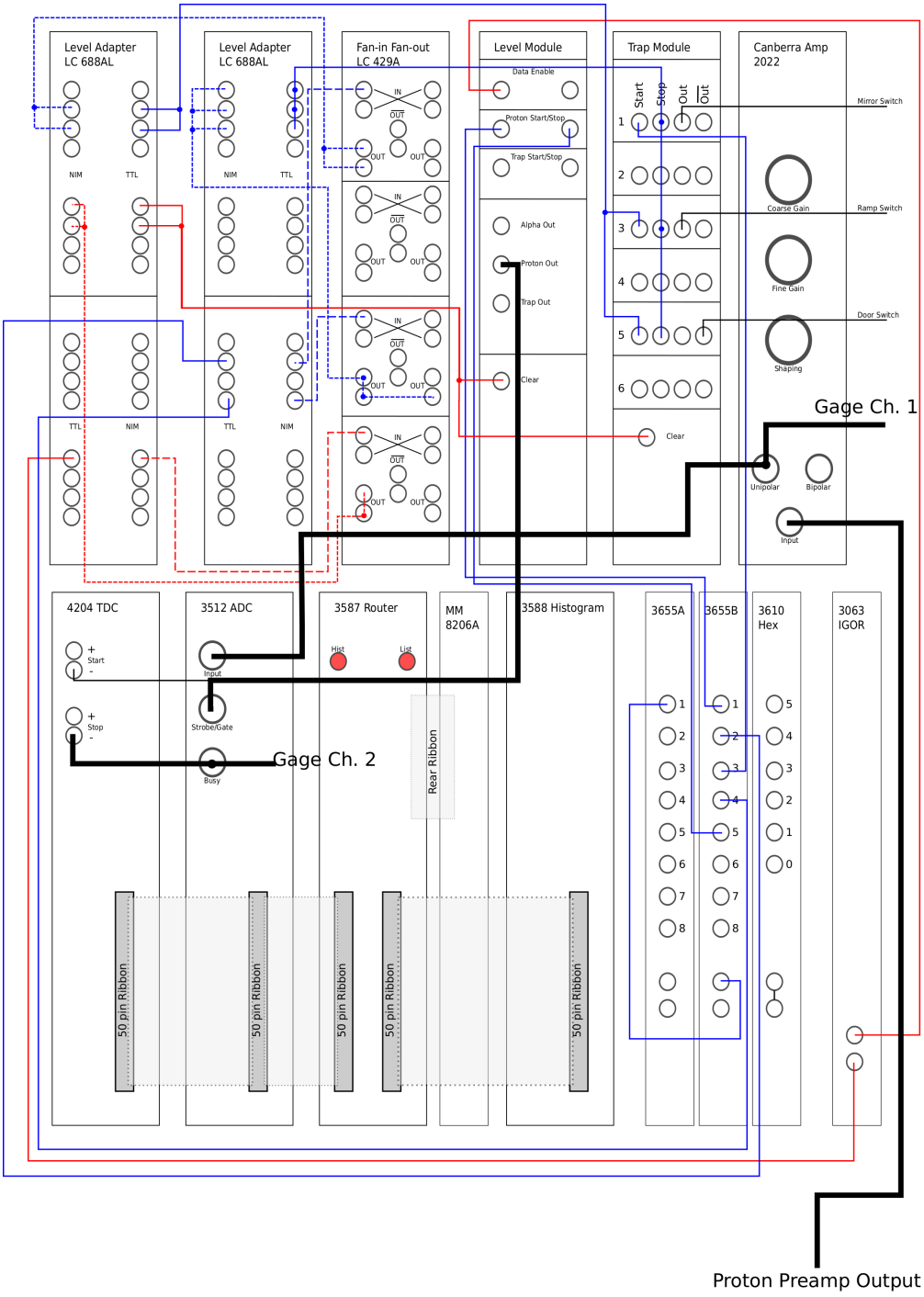

Figure C.7: Wiring schematic of the lifetime DAQ electronics.

Vita

Kyle Brandon Grammer was born in Missouri to Scott and Jan Grammer. He moved to Ohio in 1990 and graduated from Lakota East High School in 2004. He earned a backelor's degree in physics and astronomy with a minor in economics from The Ohio State University in 2009. He then enrolled at the University of Tennessee at Knoxille in Fall 2009 and will graduate with a PhD in physics in May 2016.